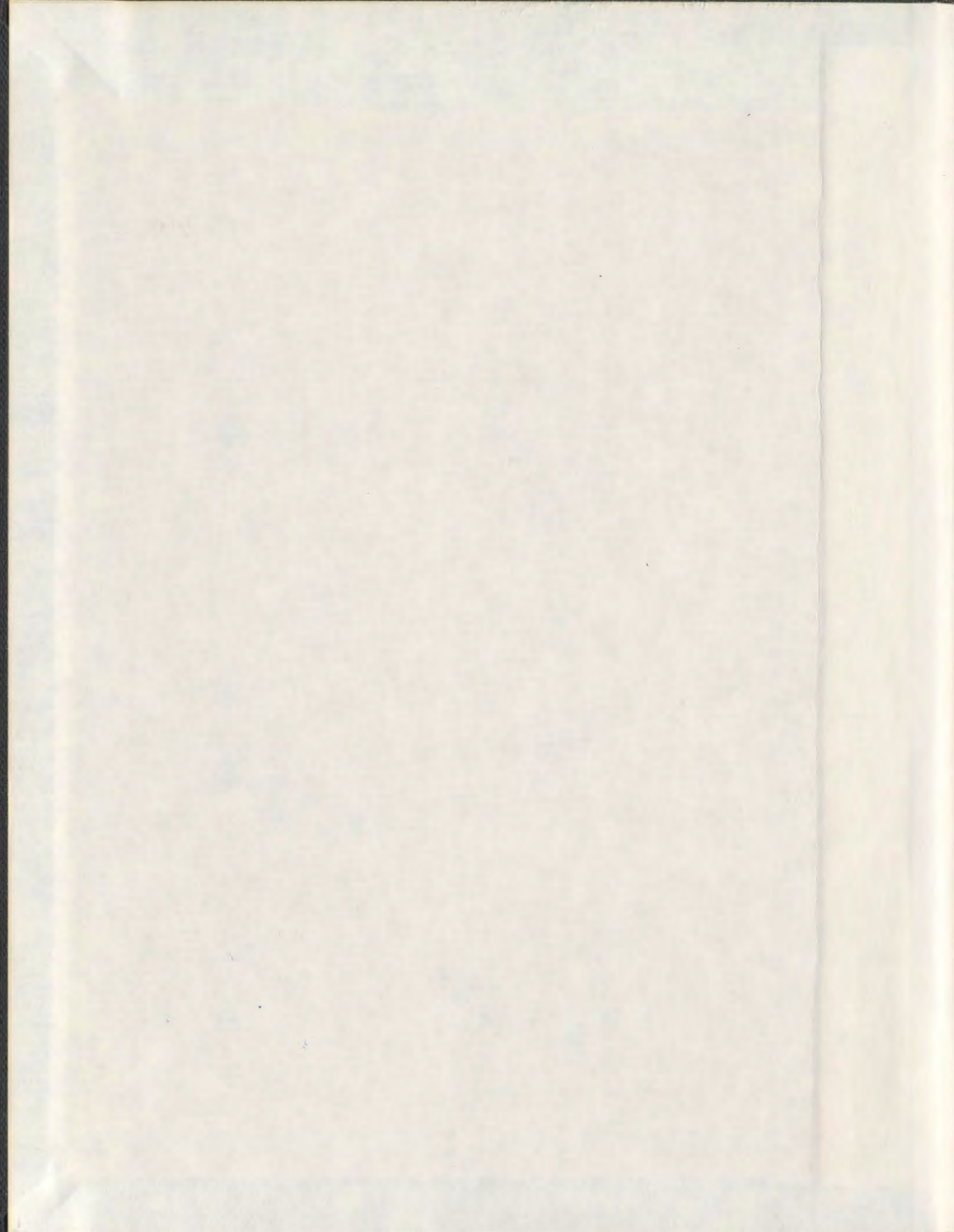


ANALYSIS OF SLIP FLOW IN MICROCHANNELS

ZHIPENG DUAN



001311



Analysis of Slip Flow in Microchannels

by

©Zhipeng Duan

A thesis submitted to the
School of Graduate Studies
in partial fulfillment of the
requirements for the degree of
Doctor of Philosophy

Faculty of Engineering and Applied Science
Memorial University of Newfoundland

November 2007

St. John's

Newfoundland

Abstract

Fluid flow in microchannels has emerged as an important research area. This has been motivated by their various applications in microfluidic systems, such as Micro-Electro-Mechanical Systems (MEMS). The advent of MEMS has opened up a new research area where non-continuum behavior is important. Microchannels are the fundamental part of microfluidic systems. Understanding the flow characteristics of microchannel flows is very important in determining friction factor, pressure distribution, heat transfer, and transport properties of the flow. The non-circular cross sections such as rectangular, triangular, and trapezoidal, are common channel shapes that may be produced through a variety of microfabrication techniques. These cross sections have extensive practical applications in MEMS.

Developing and fully developed slip flow in non-circular microchannels has been investigated and models are proposed to predict the friction factor Reynolds product f/Re for slip flow in most non-circular microchannels. It is found that the linearization method to solve the Navier-Stokes equations is an accurate approximation for developing slip flows.

Compressibility effects on slip flow in non-circular microchannels have been examined and simple models are proposed to predict the pressure distribution and mass flow rate for slip flow in most non-circular microchannels.

The effects of corrugated surface roughness on fully developed laminar flow in microtubes are investigated. Novel analytical models are developed to predict friction factor and pressure drop in corrugated roughness microtubes for continuum flow and slip flow. The developed model for slip flow illustrates the coupled effects between velocity slip and corrugated roughness.

Slip flow heat transfer in annular microchannels has been examined. The effects of Knudsen number, radii ratio and heat flux ratio on heat transfer characteristics are discussed.

Analytical models have been developed to provide a means of predicting slip flow characteristics, such as friction factor, mass flow rate, and pressure distribution for fluids operating in microchannels. These models are general and robust, and can be used by the research community for practical engineering design of microchannel flow systems. This study may help understand the behavior of fluids in microchannels.

Acknowledgments

I would like to express my appreciation to my supervisor Dr. Yuri Muzychka for his enthusiastic guidance and support of this work. He has opened my eyes to the art of fluid dynamics and heat transfer through many enlightening discussions. He stimulated my interests in microflows and provided many useful insights over the duration of my exciting graduate research. The experience of working with him has been more than rewarding.

Thanks are also due to my supervisory committee members Dr. Abdi and Dr. Kocabiyik for the time they were willing to spend in helping me on this project.

I would like to thank my parents, Guiqin Wang and Yongda Duan. Your untiring and loving support, for all the endeavors I have chosen to undertake, has made all my dreams come true. I love you both. I certainly cannot repay them for the many sacrifices they endured by allowing me to pursue my scientific career in North America. The important thanks however, go to my wife. She has put up with, among other things, more than her fair share of my late nights and weekends at the office, and has done so with love and understanding. Thank you, Wen.

Table of Contents

| | |
|---|-----|
| Abstract..... | i |
| Acknowledgements | iii |
| List of Tables | vii |
| List of Figures..... | ix |
| Nomenclature | xiv |
| Chapter 1 Introduction..... | 1 |
| 1.1 Introduction..... | 1 |
| 1.2 Objectives | 6 |
| Chapter 2 Literature Review | 8 |
| 2.1 Review of Currently Available Experimental Data..... | 8 |
| 2.2 Summary of Currently Available Experimental Data..... | 30 |
| 2.3 Proposed Explanation | 32 |
| 2.4 Summary | 40 |
| Chapter 3 Methodology | 41 |
| 3.1 Theoretical Background..... | 41 |
| 3.1.1 Continuum Assumption | 42 |
| 3.1.2 Continuum Breakdown | 43 |
| 3.1.3 Governing Equations | 44 |
| 3.1.4 Pressure-Driven Flow in Channels | 48 |
| 3.1.5 Flow in Circular Tubes | 49 |
| 3.1.6 Entrance Length Effects..... | 52 |
| 3.1.7 Noncircular Channels..... | 53 |
| 3.2 Scale Analysis..... | 54 |
| 3.3 Asymptotic Analysis..... | 56 |

| | |
|--|------------|
| 3.4 Characteristic Length Scale | 58 |
| 3.5 Numerical Simulation | 60 |
| Chapter 4 Slip Flow in Long Microchannels..... | 63 |
| 4.1 Introduction..... | 63 |
| 4.2 Slip Flow in Elliptic Microchannels | 66 |
| 4.2.1 Theoretical Analysis | 67 |
| 4.2.2 Results and Discussion | 77 |
| 4.3 Slip Flow in Other Non-Circular Microchannels..... | 83 |
| 4.3.1 Rectangular Ducts..... | 83 |
| 4.3.2 Annular Ducts | 92 |
| 4.3.3 Trapezoidal and Double-trapezoidal Ducts | 93 |
| 4.4 Modelling Slip Flow in Long Microchannels..... | 94 |
| 4.4.1 Effect of Characteristic Length Scale | 96 |
| 4.4.2 Mass Flow Rate and Pressure Distribution..... | 102 |
| 4.5 Compressibility Effects on Slip Flow in Microchannels | 105 |
| 4.5.1 Theoretical Analysis | 106 |
| 4.5.2 Results and Discussion | 116 |
| 4.6 Summary | 121 |
| Chapter 5 Slip Flow in the Hydrodynamic Entrance of Microchannels | 122 |
| 5.1 Introduction..... | 122 |
| 5.2 Circular Tubes..... | 123 |
| 5.3 Parallel Plates..... | 135 |
| 5.4 General Model | 153 |
| 5.5 Results and Discussion | 156 |
| 5.6 Summary | 157 |
| Chapter 6 Effects of Corrugated Roughness on Laminar Flow in Microtubes ... | 160 |
| 6.1 Introduction..... | 160 |
| 6.2 Circumferential Corrugated Roughness..... | 163 |
| 6.2.1 Continuum Flow | 164 |

| | |
|---|-----|
| 6.2.2 Slip Flow | 168 |
| 6.3 Axial Corrugated Roughness | 176 |
| 6.3.1 Introduction..... | 176 |
| 6.3.2 Theoretical Analysis | 177 |
| 6.4 Summary | 191 |
| Chapter 7 Slip Flow Heat Transfer in Annular Microchannels with Constant Heat | |
| Flux..... | 192 |
| 7.1 Introduction..... | 192 |
| 7.2 Theoretical Analysis | 192 |
| 7.2.1 Case (i) uniform wall heat flux on the inner wall, adiabatic on the outer wall ($q_i = q, q_o = 0$) | 194 |
| 7.2.2 Case (ii) uniform wall heat flux on the outer wall, adiabatic on the inner wall ($q_i = 0, q_o = q$) | 198 |
| 7.2.3 Case (iii) uniform wall heat flux on both walls ($q_i \neq 0, q_o \neq 0$) | 202 |
| 7.3 Results and Discussion | 212 |
| 7.4 Summary | 213 |
| Chapter 8 Summary | 215 |
| 8.1 Summary | 215 |
| 8.2 Future Research | 217 |
| References..... | 219 |

List of Tables

| | | |
|-----------|---|-----|
| Table 2.1 | Experimental results for liquid flows in microchannels | 33 |
| Table 2.2 | Experimental results for gas flows in microchannels | 36 |
| Table 3.1 | Classification of flow regimes based on Knudsen number..... | 44 |
| Table 3.2 | Definition of aspect ratio | 53 |
| Table 3.3 | Flow regimes and fluid models..... | 61 |
| Table 4.1 | A comparison of the Po using one to four terms of binomial series approximation | 78 |
| Table 4.2 | Poiseuille number results for elliptic ducts..... | 78 |
| Table 4.3 | The constants α for the Poiseuille number ratio | 81 |
| Table 4.4 | Comparison of single term approximation for fRe | 90 |
| Table 4.5 | $fRe_{\sqrt{A}}$ ($b/a=0.1$) results for elliptical and rectangular ducts using three characteristic length ℓ respectively..... | 96 |
| Table 4.6 | fRe results for elliptical and rectangular ducts..... | 97 |
| Table 4.7 | Definitions of aspect ratio [94] | 100 |
| Table 4.8 | Experimental conditions for microchannel flows | 119 |
| Table 5.1 | Eigenvalues obtained from Eq. (5.24) | 155 |
| Table 6.1 | fRe for developed laminar flow in corrugated microtubes | 168 |
| Table 7.1 | Fully developed Nusselt numbers (i) for different Knudsen numbers..... | 198 |
| Table 7.2 | Fully developed Nusselt numbers (ii) for different Knudsen numbers | 202 |

| | |
|--|-----|
| Table 7.3 Fully developed Nusselt numbers at the inner walls (iii)(A) for different Kn | 210 |
| Table 7.4 Fully developed Nusselt numbers at the inner walls (iii)(B) for different Kn | 210 |
| Table 7.5 Fully developed Nusselt numbers at the outer walls (iii)(A) for different Kn | 211 |
| Table 7.6 Fully developed Nusselt numbers at the outer walls (iii)(B) for different Kn | 211 |

List of Figures

| | |
|--|----|
| Figure 1.1 Typical MEMS and nanotechnology applications in standard atmospheric conditions span the entire Knudsen regime [1]..... | 2 |
| Figure 1.2 Micro heat exchanger constructed from rectangular channels machined in metal [2]..... | 4 |
| Figure 1.3 Design of filter microchannels [3]..... | 5 |
| Figure 2.1 Comparison of C^* vs. Reynolds number for some experimental results for liquid flows in microchannel | 28 |
| Figure 2.2 Comparison of C^* vs. Reynolds number for some experimental results for gas flows in microchannel | 29 |
| Figure 3.1 Summary of simulation methods for liquid and gas microflows [1]..... | 61 |
| Figure 4.1 An elliptic duct | 66 |
| Figure 4.2 Normalized Po results as a function of aspect ratio ϵ and Kn | 79 |
| Figure 4.3 The pressure distribution for different pressure ratios [107]..... | 82 |
| Figure 4.4 A rectangular duct | 83 |
| Figure 4.5 Normalized Po results as a function of aspect ratio ϵ and Kn for rectangular ducts | 91 |
| Figure 4.6 A concentric circular annular duct | 92 |
| Figure 4.7 Trapezoidal and double-trapezoidal microchannels [108] | 93 |
| Figure 4.8 $f \text{Re}_{\sqrt{A}}$ for elliptic and rectangular ducts | 98 |
| Figure 4.9 $f \text{Re}_{\sqrt{A}}$ for elliptic and rectangular ducts | 99 |

| | | |
|-------------|--|-----|
| Figure 4.10 | $f \text{Re}_{\sqrt{A}}$ for annular ducts | 100 |
| Figure 4.11 | $f \text{Re}_{\sqrt{A}}$ for trapezoidal ducts, data from Morini et al. [108] | 101 |
| Figure 4.12 | $f \text{Re}_{\sqrt{A}}$ for double-trapezoidal ducts, data from Morini et al. [108] | 101 |
| Figure 4.13 | The pressure distribution for different pressure ratios | 104 |
| Figure 4.14 | Momentum flux correction factor for circular tubes | 111 |
| Figure 4.15 | Momentum flux correction factor for rectangular ducts | 111 |
| Figure 4.16 | Normalized mass flow rate comparison for Arkilic et al. [27] experimental data..... | 117 |
| Figure 4.17 | Pressure distribution comparison for Pong et al. [29] experimental data. | 117 |
| Figure 4.18 | Pressure distribution comparison for Liu et al. [30] experimental data ... | 118 |
| Figure 4.19 | Pressure distribution comparison for Jang and Wereley [111] experimental data..... | 118 |
| Figure 4.20 | Deviation from linear pressure distribution comparison for Karniadakis et al. [1] numerical data | 120 |
| Figure 5.1 | Effect of ξ on development of velocity profiles for $Kn^*=0.01$ for circular tubes | 130 |
| Figure 5.2 | Entrance length for which $U(0,\xi)=0.99U_{fd}(0)$ for circular tubes | 131 |
| Figure 5.3 | Effect of Kn^* on excess pressure drop for circular tubes..... | 133 |
| Figure 5.4 | Effect of Kn^* on $f_{app}Re$ for developing laminar flow for circular tubes | 134 |
| Figure 5.5 | Effect of ξ on development of velocity profiles for $Kn^*=0.005$ for parallel plates | 142 |
| Figure 5.6 | Entrance length for which $U(0,\xi)=0.99U_{fd}(0)$ for parallel plates | 142 |

| | | |
|-------------|---|-----|
| Figure 5.7 | Entrance length comparison for Barber and Emerson numerical model.... | 143 |
| Figure 5.8 | Effect of Kn^* on excess pressure drop for parallel plates | 146 |
| Figure 5.9 | Effect of Kn^* on $f_{app}Re$ for developing laminar flow for parallel plates..... | 147 |
| Figure 5.10 | Comparison of $f_{app}Re$ for different Kn^* between circular tube and parallel plates | 149 |
| Figure 5.11 | Comparison of $f_{app}Re$ for Renksizbulut et al. [117] numerical data for $Re=1$ | 150 |
| Figure 5.12 | Comparison of $f_{app}Re$ for Renksizbulut et al. [117] numerical data for $Re=10$ | 151 |
| Figure 5.13 | Comparison of $f_{app}Re$ for Renksizbulut et al. [117] numerical data for $Re=100$ | 152 |
| Figure 5.14 | Comparison of $f Re_{\sqrt{A}}$ for Muzychka and Yovanovich [94] model.... | 158 |
| Figure 5.15 | Comparison of $f Re_{\sqrt{A}}$ for circular tubes..... | 159 |
| Figure 5.16 | Comparison of $f Re_{\sqrt{A}}$ for Niazmand et al. [118] numerical data..... | 159 |
| Figure 6.1 | SEM image of the cross-section of a roughness microtube with a nominal internal diameter of 75 μm [62] | 161 |
| Figure 6.2 | A sinusoidal wave roughness microtube | 163 |
| Figure 6.3 | Effect of relative roughness ε and wave number λ on pressure drop of microtubes..... | 167 |
| Figure 6.4 | Effect of relative roughness ε and wave number λ on pressure drop of microtubes..... | 168 |
| Figure 6.5 | Effect of relative roughness ε , wave number λ and Knudsen number Kn on | |

| | |
|--|-----|
| pressure drop of microtubes..... | 173 |
| Figure 6.6 An axial sinusoidal wave rough microtube | 177 |
| Figure 6.7 $B(\lambda, Kn^*)$ as a function of λ and Kn^* | 185 |
| Figure 6.8 Effect of relative roughness ε and wave number λ on pressure drop of microtubes for continuum flow..... | 187 |
| Figure 6.9 Effect of relative roughness ε and wave number λ on pressure drop of microtubes for continuum flow..... | 187 |
| Figure 6.10 Effect of relative roughness ε , wave number λ and Knudsen number Kn on pressure drop of microtubes for slip flow | 188 |
| Figure 7.1 A concentric circular annular duct with uniform wall heat flux on the inner wall, adiabatic on the outer wall | 195 |
| Figure 7.2 Variation of Nusselt number for uniform wall heat flux on the inner wall, adiabatic on the outer wall | 197 |
| Figure 7.3 A concentric circular annular duct with uniform wall heat flux on the outer wall, adiabatic on the inner wall | 199 |
| Figure 7.4 Variation of Nusselt number for uniform wall heat flux on the outer wall, adiabatic on the inner wall | 201 |
| Figure 7.5 A concentric circular annular duct with uniform wall heat flux on both walls | 203 |
| Figure 7.6 Variation of Nu_i for uniform wall heat flux on both walls | 206 |
| Figure 7.7 Effects of q_i/q_o for Nu_i for uniform wall heat flux on both walls | 207 |
| Figure 7.8 Variation of Nu_o for uniform wall heat flux on both walls..... | 207 |

Figure 7.9 Effects of q_i/q_o for Nu_o for uniform wall heat flux on both walls 208

Nomenclature

| | |
|-----------------|---|
| A | = flow area, m^2 |
| a | = major semi-axis of ellipse or rectangle, m |
| a | = base width of a trapezoidal or double-trapezoidal duct, m |
| b | = minor semi-axis of ellipse or rectangle, m |
| b | = height of a trapezoidal or double-trapezoidal duct, m |
| c | = half focal length of ellipse, m |
| c | = short side of a trapezoidal or double-trapezoidal duct, m |
| C^* | = normalized friction coefficient |
| c_p | = specific heat at constant pressure, $J/\text{kg}^\circ\text{C}$ |
| D | = diameter of circular tubes, m |
| D_h | = hydraulic diameter, $= 4A/P$ |
| $E(e)$ | = complete elliptical integral of the second kind |
| e | = eccentricity, $= \sqrt{1 - b^2/a^2}$ |
| F | = external body force per unit mass, N/kg |
| f | = Fanning friction factor, $= \tau / (\frac{1}{2} \rho \bar{u}^2)$ |
| f_{app} | = apparent friction factor |
| g | = gravitational acceleration, $= 9.81 \text{m/s}^2$ |
| g_1, g_2, g_3 | = metric coefficients |
| H | = height, m |
| h | = half height of parallel plate channel, m |
| h | = local fully developed heat transfer coefficient, $\text{W/m}^2\text{ }^\circ\text{C}$ |
| K | = incremental pressure drop factor |
| K_L | = minor loss factor |
| k | = thermal conductivity, $\text{W/m}^\circ\text{C}$ |

| | |
|----------------|---|
| Kn | = Knudsen number, $= \lambda/\ell$ |
| Kn^* | = modified Knudsen number, $= Kn(2-\sigma)/\sigma$ |
| L | = channel length, m |
| L^+ | = dimensionless channel length, $= L/D_h \text{Re}_{D_h}$ |
| ℓ | = arbitrary length scale |
| Ma | = Mach number, $= u/V_s$ |
| \dot{m} | = mass flow rate, kg/s |
| Nu | = fully developed Nusselt number |
| Nu_c | = fully developed Nusselt number for continuum flow |
| P | = perimeter, m |
| Po | = Poiseuille number, $= \bar{\tau} \ell / \mu \bar{u}$ |
| Pr | = Prandtl number, $\mu c_p / k$ |
| p | = pressure, N/m^2 |
| Δp | = pressure drop, N/m^2 |
| Q | = volume flow rate, m^3/s |
| q | = heat flux per unit area, W/m^2 |
| R | = radius of a microtube, m |
| R | = specific gas constant, J/kgK |
| \mathfrak{R} | = specific gas constant, J/kgK |
| Re | = Reynolds number, $= \ell \bar{u} / \nu$ |
| r | = dimensionless radius ratio, $= r_i/r_o$ |
| r_i | = inner radius of a concentric duct, m |
| r_o | = outer radius of a concentric duct, m |
| r, θ, z | = cylindrical polar coordinates |
| S_{ij} | = rate of deformation tensor |
| T | = temperature, K |
| T_b | = bulk temperature, K |
| T_w | = wall temperature, K |

| | |
|-----------|--|
| t | = time, s |
| U | = velocity scale, m/s |
| u, v, w | = velocity components, m/s |
| \bar{u} | = average velocity, m/s |
| V | = dimensionless developing velocity |
| V_s | = speed of sound, $= \sqrt{\gamma RT}$ |
| W | = width, m |
| X_n | = function of x/α |
| x, y | = Cartesian coordinates, m |
| z | = coordinate in flow direction, m |

Greek Symbols

| | |
|---------------------|--|
| α | = constants |
| α | = eigenvalue |
| β | = dimensionless variable |
| γ | = ratio of specific heats |
| δ_{ij} | = Kronecker delta or identity tensor |
| δ_n | = eigenvalues |
| ε | = aspect ratio |
| ε | = relative surface roughness |
| ε_{ijk} | = alternating unit tensor |
| η, ψ, z | = elliptic cylinder coordinates |
| η_0 | = parameter of elliptic cylinder coordinates |
| λ | = molecular mean free path, m |
| λ | = wave number |
| λ_f | = molecular mean free path, m |
| μ | = dynamic viscosity, Ns/m^2 |
| ν | = kinematic viscosity, m^2/s |

| | |
|-------------|--|
| ξ | = dimensionless duct length, $= x/\ell \text{Re}_\tau$ |
| ρ | = gas density, kg/m^3 |
| σ | = tangential momentum accommodation coefficient |
| σ_T | = thermal accommodation coefficient |
| τ | = wall shear stress, N/m^2 |
| τ_{ij} | = stress tensor, N/m^2 |
| Φ | = viscous dissipation, $\text{N/m}^2\text{s}$ |
| Φ | = half angle, rad |
| ψ | = dimensionless stream function |
| ψ | = momentum flux correction factor |

Subscripts

| | |
|------------|---|
| \sqrt{A} | = based upon the square root of flow area |
| app | = apparent |
| c | = continuum |
| $crit$ | = critical |
| D_h | = based upon the hydraulic diameter |
| fd | = fully developed |
| i | = inlet |
| ℓ | = based upon the arbitrary length ℓ |
| o | = outlet |
| sm | = smooth |
| w | = wall |

Superscripts

| | |
|-----|-----------|
| E | = ellipse |
|-----|-----------|

h = homogeneous

p = particular

R = rectangle

Chapter 1

Introduction

1.1 Introduction

Fluid flow in microchannels has emerged as an important area of research. This has been motivated by their various applications such as medical and biomedical use, computer chips, and chemical separations. Over the past 15 years, micromachining technology has been used to develop a number of microfluidic systems in silicon, glass, quartz, or plastics, such as biochemical lab-on-a-chip systems and microelectromechanical systems (MEMS). The advent of MEMS has opened up a new research area where non-continuum behavior is important. MEMS are one of the major advances of industrial technologies in the past decades. MEMS refer to devices which have a characteristic length of less than 1 mm but more than 1 μm , which combine electrical and mechanical components and which are fabricated using integrated circuit (IC) fabrication technologies. Now, microfabrication is a diverse spectrum of processing techniques that involve a wide range of disciplines from chemical sciences to plastic molding. Compared with conventional mechanical and electrical systems, these MEMS devices are several orders of magnitude smaller in size. In fact, these dimensions are in the same range as the average diameter of human hair (about 50 μm). A MEMS device can be a single piece of hardware that produces outputs directly based on the inputs from

external sources. The outputs can be mechanical and fluidic movement, electrical charges, analog signals, and digital signals. Often several microcomponents are integrated, such as the lab-on-a-chip device, which performs the multistage processing of the inputs and produces several different types of outputs, all in one single miniature device. A current emphasis in microfluidics research is the development of lab-on-a-chip devices for biological and chemical analysis. MEMS and lab-on-a-chip devices, therefore, offer opportunities to many areas of application, such as biomedical and information technology, that were thought not achievable using conventional devices. Micron- and submicron-size mechanical and biochemical devices are becoming more prevalent both in commercial applications and in scientific research. Estimates of the potential commercial market size are as high as billions of U.S. dollars.

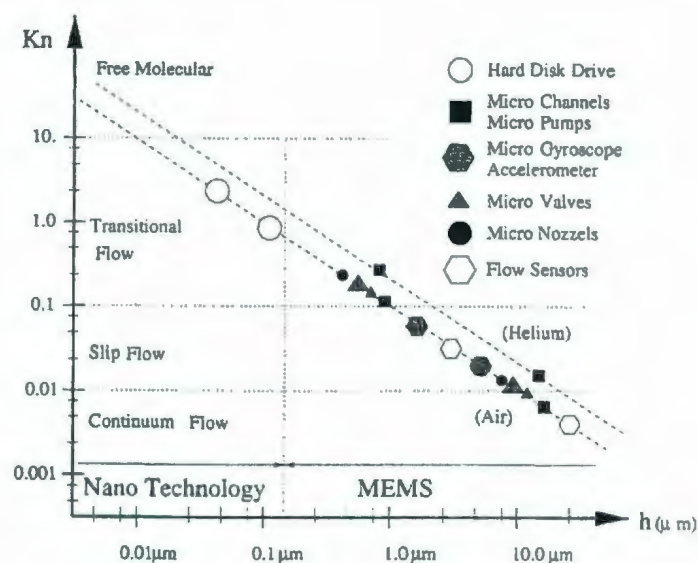


Figure 1.1 Typical MEMS and nanotechnology applications in standard atmospheric conditions span the entire Knudsen regime [1].

The operational regimes of typical Microsystems at standard temperature and pressure are shown in Figure 1.1. MEMS devices operate in a wide range of flow regimes covering the continuum, slip, and transition flow. It is necessary to study mass, momentum, and energy transport in these flow regimes.

As more new applications are proposed and new MEMS devices designed, it was often found that measured quantities could not be interpreted by using conventional correlations developed for macro scale devices. It has become increasingly apparent that the physical mechanisms at work in these small scale devices are different from what can be extrapolated from what is known from experience with macroscaled devices. Many fundamental issues that are not observed in macro flows are prominent in microscale fluid dynamics. There is a need to either reexamine or replace the modeling developed from observations of macro scale devices.

Microchannels are the fundamental part of microfluidic systems. In addition to connecting different devices, microchannels are also utilized as biochemical reaction chambers, in physical particle separation, in inkjet print heads, in infrared detector, in diode lasers, in miniature gas chromatographs, or as heat exchangers for cooling computer chips. The non-circular cross sections such as rectangular, triangular, and trapezoidal, are common channel shapes that may be produced by microfabrication. These cross sections have wide practical applications in MEMS [1-5]. For example, Figure 1.2 shows a micro heat exchanger constructed from rectangular channels machined in metal. Reduced heat exchanger dimensions of 50 μm to 500 μm result in more effective heat transfer due to decreased thermal diffusion lengths. The tremendous

enhancement in heat transport obtained by employing microchannels has provided an effective alternative to conventional heat dissipation methods. Figure 1.3 shows typical microchannel designs for fabricating membrane microfilters. Understanding the flow characteristics of microchannel flows is very important in determining pressure distribution, heat transfer, and transport properties of the flow.

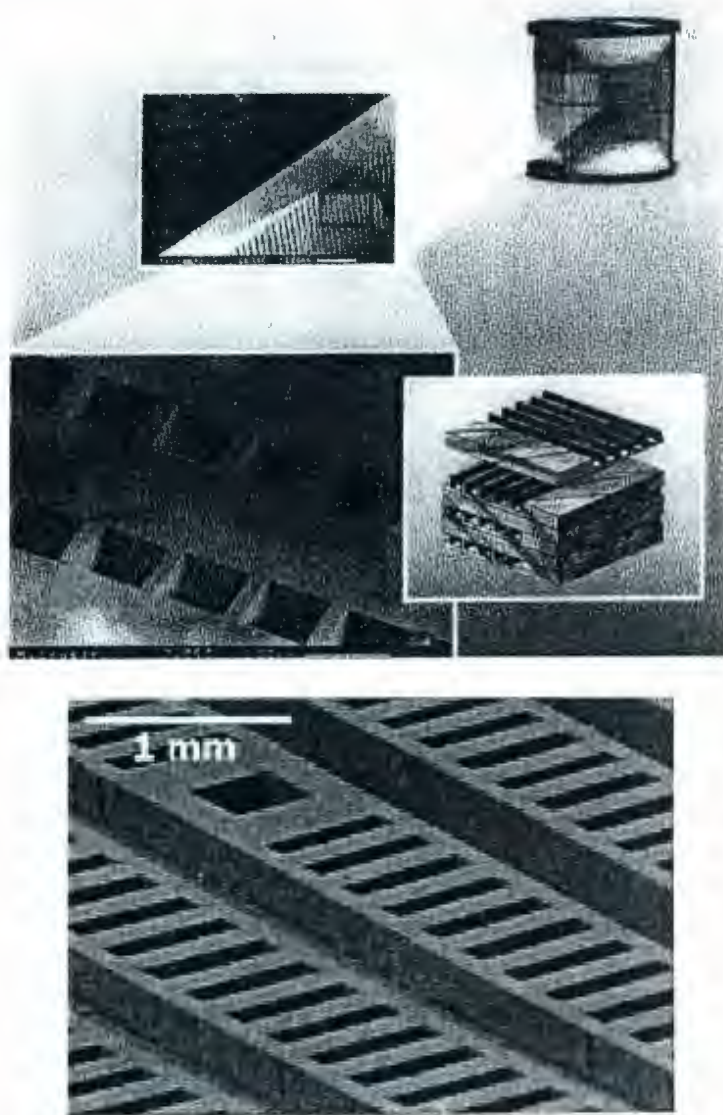


Figure 1.2 Micro heat exchanger constructed from rectangular channels machined in metal [2].

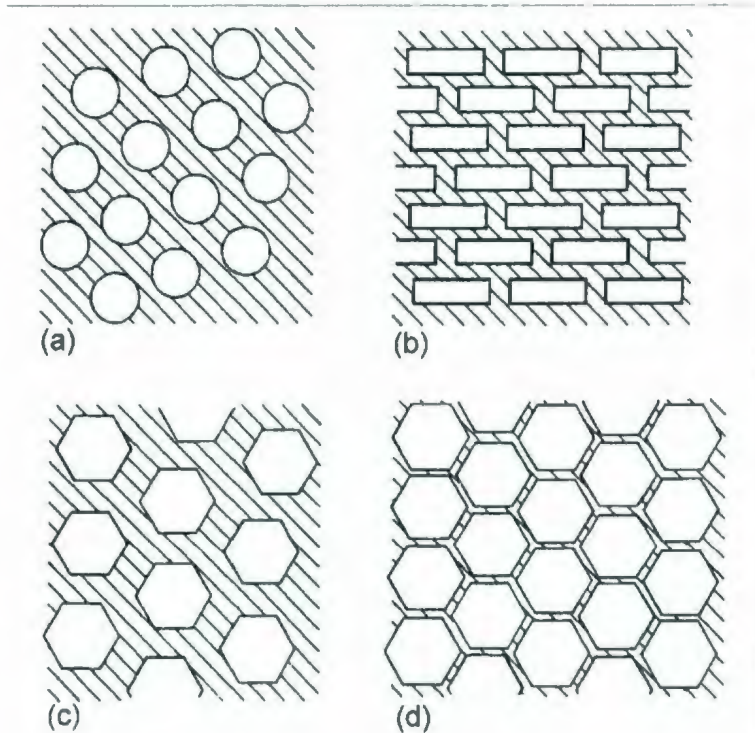


Figure 1.3 Design of filter microchannels: (a) circular; (b) rectangular; and (c) and (d) hexagonal [3].

The characteristic dimension associated with the term “microchannels” is ambiguous. Nominally, microchannels may be defined as channels whose dimensions are from one micron to one millimeter. Typical applications may involve characteristic dimensions in the range of approximately 10 to 200 μm . Above one millimeter the flow exhibits behavior that is the same as macroscopic continuum flows. A statistical approach is used when modeling flows on the nanoscale. Advances in microtechnologies have required the use of microcomponents, which are often interconnected by channels. The need to cool or heat very small devices such as microelectronics has appeared as an application of flow through microchannels. Channels etched in silicon chips have been used to cool

microprocessors as well as other computer components. Microchannels have also seen application in chemical separations where the chemist is able to take advantage of the small scales in obtaining more efficient performance. Research into micro heat exchangers, micro power generation, and other micro devices has made the understanding of transport phenomena in microchannels necessary.

Some researchers have reported on discrepancies between microchannel flow behavior and macroscale theory. A number of publications indicate that flows on the microscale are different from that on macroscale and that the conventional theories are incapable of explaining the occurring phenomena. For laminar flow through microchannels, researchers have observed both significant increases and decreases in the pressure drop from the expected value based on macroscale flow theory, as data appears both up to 60% above and up to 80% below the theoretical values. The reported deviations from macroscale laminar flow theory have been significant for many investigations when the hydraulic diameter decreases below approximately 200 μm . The results from limited prior work have varied greatly resulting in significant confusion concerning the causes of the observed phenomenon. Several theories and models have been presented in an attempt to explain the observed phenomena, but an unquestionable conclusion has not yet been reached.

1.2 Objectives

The objectives of present research are:

- (i) consider slip effects in fully developed microchannel flow;

- (ii) consider compressibility for flows in microchannels with slip;
- (iii) consider entrance effects for microchannel flow;
- (iv) consider microchannel shape effects;
- (v) consider the effects of corrugated surface roughness for microchannel flow;
- (vi) develop robust models for predicting flow characteristics, such as flow rate or average velocity, pressure distribution, and friction factor for fluid flows through microchannels.

The remainder of this document describes the literature that has previously reported on the topic, presents the methodology of the present work, and provides many new models.

Chapter 2

Literature Review

2.1 Review of Currently Available Experimental Data

As microscale fluid transport applications become more numerous, an understanding of the fundamental flow physics becomes more important. A review of the literature indicated that this basic understanding has not yet been achieved. Particularly, many investigators have reported anomalous behavior in the laminar flow regime.

Flow through microchannels is a relatively new area of research. The number of applications is growing with technological advances in the field. Microchannel flows have been the most widely studied. The manufacturability and broad use of microchannels in industry has fueled this research. However, the amount of experimental data is still limited.

To assist in evaluating the results of these studies, a normalized friction factor, the experimental value of fRe is non-dimensionalized using theoretical value of fRe , is defined as:

$$C^* = \frac{(fRe)_{\text{exp}}}{(fRe)_{\text{theo}}} \quad (2.1)$$

Tuckerman and Pease [6] studied flow through an array of microchannels with approximately rectangular cross sections (high range 50-56 μm , width range 287-320 μm). This is the first experimental investigation of flow through microchannels. The large surface-to-volume ratios of microchannels make them excellent candidates for efficient heat transfer devices. Although this study was concentrated primarily on heat transfer characteristics, they proved that the flow rate obeyed conventional theory.

Shortly thereafter, Wu and Little [7,8] conducted experiments measuring the friction factors for both laminar and turbulent nitrogen and hydrogen gas flows in microchannels. Silicon and glass microchannels were used, having a trapezoidal cross section with hydraulic diameters ranging from 55 μm to 73 μm and for Reynolds numbers ranging between 200 and 15000. The glass had a larger surface roughness than did the silicon. The measured values of the friction factor were larger than those predicted by the conventional theory. The glass channels show the greatest deviation from the macroscale theory, which is most likely due to roughness effects caused by the fabrication technique. The results showed that the friction factor for the glass was 3 to 5 times higher than the friction factor for the silicon channels. Overall, the data were in the shape of the Moody chart. The data showed the transition from laminar to turbulent flow to be at a Reynolds number of approximately 400.

Pfahler et al. [9-11] and Harley et al. [12-14] presented a number of papers on microscale fluid flow. The channels tested are approximately 100 μm wide with depths ranging from 0.5 to 50 μm . The majority of the channels tested had a low aspect ratio. The cross-sections of the channels were either trapezoidal or rectangular. The authors

acknowledged that their results depend heavily on channel size measurement, which was extremely difficult to measure accurately for the shallowest channels.

Pfahler et al. [9] reported on flow through micromachined rectangular and trapezoidal shaped channels of various aspect ratios and hydraulic diameters ranging from 0.5–40 μm . They utilized isopropanol and silicon oil as working fluid, and the Reynolds number was less than 100 for all of their data. The amount of measured friction factor deviation from laminar flow theory for the polar isopropanol was observed to increase with decreasing hydraulic diameter. The deviation was toward a smaller friction factor and the deviation varied from 0–30% as the hydraulic diameter decreased from 40 to 1 μm . The measured friction factor was approximately 15% lower than theoretical predicts for the silicon oil. The depth was measured with a surface profilometer within 2% [9,10]. The surface of these channels was rough, with roughness of approximately 0.01.

Fluids tested by Pfahler et al. [9-11] and Harley et al. [12-14] included alcohols (n-propanol and isopropanol), silicon oil, and helium, nitrogen, and argon. The overall Reynolds number range is from 0.0001 to 1000. These investigations showed a decrease in the friction factor on the order of 10% to 30% when compared to macroscale theory. While surface roughness may have an effect, similar to the effects seen in the Wu and Little [7,8] data, most likely the uncertainty in the channel dimensions causes these discrepancies.

Pfahler et al. [9-11] and Harley et al. [12] tested three gases—nitrogen, helium, and argon. Harley et al. [12] showed that the data for $Re < 500$ is entirely 5% below the theoretical values, while the remaining data points for $Re > 500$ are 5% above the

theoretical values. This may be the transition to turbulent flow, which agrees with the studies of Wu and Little [7]. The data by Pfahler et al. [9,10] are for the flow of nitrogen $0.8 \leq C^* \leq 0.9$ for $0.01 \leq Re \leq 100$.

Choi et al. [15] conducted experiments on the friction characteristics of nitrogen gas in circular tubes with diameters ranging from 3 to 81 μm . Tubes used by Choi et al. [15] were smooth with relative roughness from 0.00017 to 0.0116. The data showed the friction factors to be as much as 30% lower than that predicted by conventional theory for $10 \leq Re \leq 500$. However, friction factor increased by 15% for $Re > 500$. This is similar to the data presented by Harley et al. [12], and may be due to a transition to turbulent flow. In addition, the microtubes that produced $C^* > 1$ had relative roughness 0.01, which is the same as the roughness of channels used by Harley et al. [12].

Yu et al. [16] extended the work of Choi et al. [15] by conducting experimental and theoretical studies of flow and heat transfer characteristics in microtubes. Yu et al. [16] determined the friction factors of nitrogen gas and water in microtubes with diameters ranging from 19 μm to 102 μm and Reynolds number ranging from 100 to 20000. The relative roughness of the inner surface measured using a laser interferometer was found to be approximately 0.003. The laminar friction constant is 60% to 90% of the theoretical value. This behavior is consistent with data of Choi et al. [15]. The average friction coefficient ranged from 49 to 52, which is somewhat lower than that obtained by Choi et al. ($fRe = 53$) [15]. The turbulent flow friction factor was observed to be about 5% lower than macroscale empirical turbulent correlations.

Several papers have also appeared by Peng et al. [17-20]. They conducted studies in stainless steel channels of hydraulic diameter ranged between 133 and 367 μm . They report frictional behavior that was correlated empirically as $f=C/Re^2$. This is in contrast to the inversely proportional relationship $f=C/Re$, and what all other researchers have reported. Transition also occurred in their channels at $Re \approx 300$ -400. The authors proposed empirical correlations in order to calculate the friction factor in laminar and in turbulent regime, namely, $f \sim Re^{-1.98}$ and $f \sim Re^{-1.72}$ respectively. In addition, Peng et al. [19] suggested that the regions themselves must be redefined depending upon the geometry of the microchannel. As in Moody chart for macroscale flows, two distinct relationships between f and Re were observed, one in the lower Re region and one in the higher Re region. The area between the two trends represents the transition region. The critical Reynolds number, Re_{crit} , decreased as the hydraulic diameter was reduced. Re_{crit} was estimated at 200 for $D_h < 220 \mu\text{m}$, 400 for $D_h = 240 \mu\text{m}$, and 700 for $260 < D_h < 360 \mu\text{m}$, indicating the occurrence of early transition to turbulence in these microchannels.

Wang and Peng [21] analyzed the forced convection of water or methanol through stainless steel rectangular microchannels. They found that the transition from laminar to turbulent regime occurs for Reynolds numbers ranging between 300 and 800. A further analysis was conducted by Peng and Peterson [22] using the same test sections analyzed in [21]. The effect of the variation of the fluid properties with the temperature for forced convection of water and methanol through metallic rectangular microchannels was investigated. They observed the laminar region for Reynolds numbers lower than 400.

Wilding et al. [23] analyzed flow of water and various biological fluids (saline, serum, plasma, and whole blood) in silicon microchannels having a trapezoidal cross-section with dimensions ranging between 40 and 150 μm in width and between 20 and 40 μm in height. The experimental data of this study are for $17 < Re < 126$ and indicate a 30% increase in the normalized friction coefficient from the theoretical values.

Jiang et al. [24] investigated flow of water through rectangular, trapezoidal, or triangular microchannels. The microchannel dimensions ranged from 35 μm to 110 μm in width and from 13.4 μm to 46 μm in height, where the lengths varied from 2.5 mm to 10 mm. For the 10 mm long microchannel, the experimental data are $0.1 < Re < 10$ and the normalized friction coefficient is 15-30% above the theoretical values. This is in close agreement with the data presented by Wilding et al. [23]. In a later work, Jiang et al. [25] studied flow of water through trapezoidal microchannels with the hydraulic diameter ranging from 35 to 120 μm and Reynolds numbers from 1 to 30. Their experimental results were from 50 to 100% lower than theoretical predicts. They also suggested that the development length may be different than macroscale theory suggests.

Arkilic et al. [26,27] investigated helium flow through microchannels for pressure drops of 1.2 to 4.2 atm. The microchannels were 52.25 μm wide, 1.33 μm deep, 7.5 mm long. The results showed that the pressure drop over the channel length was less than the continuum flow results. The friction coefficient was only about 40% of the theoretical values. The significant reduction in the friction coefficient may be due to the slip flow regime, as according to the flow regime classification by Schaaf and Chambre [28], the flows studied by Arkilic et al. [26,27] are mostly within the slip flow regime, only

bordering the transition flow near the outlet. When using the Navier-Stokes equations with slip flow boundary condition, the slip model with full tangential momentum accommodation fit the experimental data well.

Pong et al. [29] investigated helium and nitrogen gas flows through rectangular microchannels with a depth of 1.2 μm and a width of 5-40 μm . Pressure sensors were fabricated as an integral part of the flow channels, allowing measurements of not only the overall pressure drop and flow rate, but also pressure distribution along the microchannel. They found that the pressure distribution was not linear as suggested by a continuum flow analysis. Pressure drop required is less than that in a conventional channel. The deviations of the pressure distribution from the linear distribution become more pronounced as Knudsen number decreases. Pong et al. suggested that such nonlinearity is due to the compressibility and the rarefaction effects.

Liu et al. [30] used the same flow system described by Pong et al. [29] to further study microscale gaseous flow by employing helium as testing fluid. They also found the pressure drop distribution was nonlinear. This is consistent with the results found by Pong et al. [29]. Due to very low Reynolds numbers in the experiment, the inertial effects were neglected in the model. Liu et al. also proved that the solution to the Navier-Stokes equation combined with slip flow boundary conditions showed good agreement with the experimental data in microchannel flow.

Shih et al. [31] continued the experimental work of Liu et al. [30] and Pong et al. [29]. Shih et al. not only measured the overall pressure drop and flow rate, but also the pressure distribution along the microchannel. The microchannel used in the study was the

same as the one used by Liu et al. The only difference was the reduced channel length. The reduction in channel length resulted from the fact that two of the integrated pressure sensors closest to the channel ends were not used due to entrance and exit effects. Shih et al. used helium and nitrogen for the flow experiments over a Reynolds number range of 0.001–0.1. The friction coefficient is only 30-45% of the theoretical values. This significant reduction in the friction coefficient may be due to the slip and transition flow regimes, as the Knudsen number for the data ranges from 0.02 to 0.16. This is consistent with the results of Liu et al. and Arkilic et al. [26,27]. Shih et al. conducted that the mass flow rate for helium was greater than conventional no-slip theory predicted. The data agreed very well with a first-order slip flow model.

Ho and Tai [32] presented a review of progress in microscale fluid flow research. They suggested possible explanations of the observed deviation. All of the proposed theories dealt with surface forces and surface interactions. In the microscale flows studied, the surface phenomena may become quite significant in comparison to other forces.

Wu et al. [33] investigated fluid flow and heat transfer in microchannels. The microchannels used in this study were 19 μm in width, 1.85 μm in height, and 4.4 mm in length. Wu et al. [33] used water and nitrogen gas as working fluids over a Reynolds number range of 0.1–1. For water, the values of the normalized friction coefficient are 10-30% above the theoretical values, which is consistent with the results of Wilding et al. [23] and Jiang et al. [24]. For nitrogen gas flow, while the normalized friction factor is $0.3 < C^* < 0.4$ and is consistent with the results of Liu et al. [30] and Arkilic et al. [26,27].

Urbanek et al. [34] investigated the flow of three isomers of alcohol in triangular and trapezoidal microchannels of hydraulic diameter of 5 and 25 μm . They reported an increase in the frictional pressure drop, in contrast to the decrease observed by other investigators in similar channels.

Papautsky et al. [35,36] conducted experiments of water flow in a rectangular microchannel over a Reynolds number range of 1–20. The channel was metallic with dimensions of $3,000 \times 600 \times 30 \mu\text{m}^3$. The experimental data showed an increase in the friction factor above that predicted by conventional theory. Papautsky et al. [37] extended their work on metallic microchannels with water as the working fluid. They tested rectangular channels of widths ranging between 150 and 600 μm and heights ranging between 23 and 26 μm . Over a Reynolds number range of 0.001–10, an increase in the friction factor was observed. The normalized friction factor was as high as 1.4. Papautsky et al. proposed a model based upon micropolar fluid theory. The model predicts an increase in flow resistance, in better agreement with their data than conventional predictions.

Choquette et al. [38] studied helium gas flow in a microchannel with a hydraulic diameter of 3 μm . A numerical model was introduced which allowed for slip at the wall. The model predicted the flow accurately.

Harms et al. [39] reported on experiments characterizing pressure drop and heat transfer characteristics in a rectangular microchannel. The channel was 251 μm wide and 1030 μm deep and the working fluid was deionized water. The experimental results

agreed reasonably well with conventional theory for both frictional and heat transfer effects. The critical Reynolds number was found to be 1500.

Webb and Zhang [40] studied refrigerant R-134a in rectangular microchannels with a hydraulic diameter of 133 μm . They observed that the friction factor and heat transfer properties agreed well with macroscale empirical correlations.

Using water as the working fluid, Pfund et al. [41] measured pressure drop in rectangular channels of hydraulic diameter ranging from 200 to 900 μm for Reynolds numbers between 40 and 4000. For $Re \leq 1300$ their data also showed good agreement with the conventional theory. They observed that the friction factor increased as the surface roughness increased. Similar behavior was observed in gas flows by Wu and Little [7]. Transitional behavior was observed at $Re \approx 1300$, which is similar to the Reynolds number observed for transition by Harms et al. [39]. Later, Pfund et al. [42] measured the friction factor for water flowing in high aspect ratio smooth and rough rectangular channels over a Reynolds number range of 60–3450. They found that the friction factor in laminar flow were significantly greater than the classical theoretical value, in particular when the rough channel ($\varepsilon/D_h = 3\%$) was tested.

Mala et al. [43,44] proposed a theory to account for the increase in friction factor for microchannels. They argue that the cause of the deviation is due to the electric double layer (EDL) of the fluid. They developed a model that explains the increase in the friction factor by solving the Poisson-Boltzmann equation for microchannel flow. Mala et al. [45] reported testing water and an aqueous solution between two parallel plates of silicon and glass. The tests were conducted in order to validate the EDL theory. The results agreed

well with their proposed theory. Qu et al. [46] also studied flow characteristics of water in silicon trapezoidal microchannels with a hydraulic diameter ranging between 51.3 and 169 μm . The Reynolds number range was 10–1500. At small Reynolds numbers ($Re \leq 100$), the friction factor agreed with conventional theory. The results showed an increase in the friction factor from theory as Re increased above 100. The greatest deviation was approximately 40%. The authors proposed a roughness-viscosity model to explain the experimental data.

Mala and Li [47] studied a flow of water through microtubes of fused silica and stainless steel. They observed nonlinear trends between pressure drop and flow rate for low Reynolds numbers. At small Reynolds numbers ($Re < 100$) the measured friction factors were in agreement with conventional theory, but for all other Re (up to 2500), the friction factors were consistently higher with respect to conventional theory.

Kolinsky et al. [48] also performed studies on microchannel flows. They proposed an electrokinetic theory to model microflows. Their theory dealt with the electrokinetic retardation of polar liquids in microchannels due to the charge separation principle. The model accounted for the increase in the friction factor from conventional theory. They also conducted experiments in rectangular microchannels with a hydraulic diameter ranging between 39 and 100 μm to further validate the model. Some polar liquids were tested including deionized water and ethyl and propyl alcohols. The experimental results agreed well with the proposed electrokinetic theory.

Migun and Prokhorenko [49] argued that the effective viscosity of polar fluids such as water increases as the hydraulic diameter decreases. In contrast, they argued that the same phenomenon does not occur for non-polar liquids.

Beskok et al. [50] studied gas microflows numerically. They concluded that for pressure driven flows the pressure distribution is nonlinear due to compressibility effects. This is consistent with the results of Pong et al. [29].

Ameel and Warrington [51] also presented a model for compressible flow in microtubes. The model was derived from the Navier-Stokes equations using a slip boundary condition. The experimental data they cited from other researchers corresponded well with the model.

Guo and Wu [52] presented a numerical model studying the effects of compressibility on gas flows in microtubes. They argued that due to compressibility effects, the flow cannot be considered fully developed and f/Re does not remain constant and is a function of Re .

Flockhart and Dhariwal [53] performed an experimental and numerical work to determine the flow characteristics of a series of trapezoidal channels with a hydraulic diameter ranging from 50 to 120 μm . This trapezoidal geometry is very common in microfluidic applications. Distilled water was used as the testing fluid. The flow was kept within laminar flow regime with the experimental results not exceeding a Reynolds number of 600. They found a good agreement with the theoretical predictions on the friction factor in macrochannels.

Xu et al. [54] carried out experimental investigations on water flow in microchannels with hydraulic diameters ranging from 50 to 300 μm . They found that the flow characteristics deviated from conventional theory when channels dimensions were below 100 μm . The friction factor was smaller than that predicted by the conventional theory. Later, Xu et al. [55] compared the experimental data obtained with rectangular aluminum microchannels and silicon microchannels. The hydraulic diameters investigated ranged from 46.8 to 344.3 μm for aluminum microchannels and from 29.59 to 79.08 μm for silicon microchannels. They concluded that for liquid flow through microchannels with a hydraulic diameter greater than 30 μm the experimental results in the laminar regime agree very well with the conventional theory.

Microscale measurements of friction factor by Sharp et al. [56] agree with the macroscale laminar theory for water flowing through circular fused silica microchannels with a diameter ranging between 75 and 242 μm over a Reynolds number range of 50–2000. Similar agreement was also obtained using a 20% solution of glycerol and 1-propanol. They observed that there is no evidence that transition to turbulence occurs for $Re < 2000$.

Using R134a and R12 as the working fluids, Ding et al. [57] conducted experiments to investigate the pressure drop through stainless steel microchannels with a triangular and a rectangular cross-section having a hydraulic diameter of 400 and 600 μm . The friction factor was higher than the conventional macroscale prediction. The experimental results demonstrated that the wall roughness effects on the friction factor were strong. In particular, they found that the Poiseuille number in the laminar regime does not remain

constant but depends on the Reynolds number. The proposed correlation for the friction factor in the laminar regime is similar to the correlation proposed by Peng et al. [18,19].

Araki et al. [58] studied frictional characteristics of nitrogen and helium flows through trapezoidal microchannels whose hydraulic diameter is from 3 to 10 μm . The measured friction factor was lower than that predicted by the conventional theory. They concluded that this deviation was caused by the rarefaction effects. In the later studies, the friction resistance of gas flow in microtubes of diameter ranging 5 to 100 μm was observed by Kim et al. [59] to be smaller about 20% than that in the conventional sized tubes.

Celata et al. [60] reported the results of R114 flowing in capillary tubes with a diameter of 130 μm . Experimental tests were performed in a wide range of Reynolds numbers (100-8000) and provided insights into the fluid flow in the transition region. They found that the friction factor was in good agreement with the conventional theory in the laminar flow regime. They observed that the laminar-to-turbulent transition occurred for Reynolds number in the range 1880-2480. The authors evidenced the role that the high relative roughness could play on the transition.

Judy et al. [61] measured the friction factor of water, hexane and isopropanol flowing in fused silica circular microtubes with a diameter ranging between 20 and 150 μm in order to study the effects of the fluid polarity. For diameters lower than 100 μm the friction factor deviated from the conventional theory. The friction factor was lower than expected and the deviations were higher as the diameter decreased. Later, they [62] investigated a pressure driven flow through circular and square microchannels in fused silica and stainless steel with hydraulic diameters in the range of 47-101 μm and for

Reynolds numbers ranging between 8 and 2300. The experimental results on the pressure drop demonstrated no distinguishable deviation from the classical theory.

Li et al. [63] investigated the friction factor of a nitrogen flow through microtubes with diameters ranging from 80 to 166.6 μm . They observed that the pressure drop along the tube became nonlinear when Mach numbers were higher than 0.3. The friction factor is higher than the prediction of the conventional theory. Later, Li et al. [64] utilized glass, silicon and stainless steel microtubes with diameters ranging from 79.9 to 166.3 μm , from 100.25 to 205.3 μm , from 128.8 to 179.8 μm , respectively, in order to measure the friction factors of a deionized water flow and verify the effect of surface roughness. The experimental results showed that for smooth glass and silicon microtubes the classical theory in the laminar regime holds. For rough stainless steel microtubes ($\varepsilon/D = 3\text{-}4\%$) the friction factors were higher than the predictions of the conventional theory. They concluded that the relative roughness cannot be neglected for microtubes also in the laminar regime. The transition from laminar to turbulent occurred at Reynolds numbers between 1700 and 2000 and no early transition effects were observed.

Yang et al. [65] performed a test of the friction characteristic of air, water and refrigerant R134a through microtubes with a diameter ranging between 173 and 4010 μm . The experimental results demonstrated that the friction factor for water and refrigerant R134a agree well with the conventional theory. In contrast, for air flow the measured friction factors were significantly lower than those predicted by the conventional theory.

Turner et al. [66] conducted an experimental investigation on nitrogen, helium and air flow through rough and smooth rectangular microchannels with hydraulic diameters in

the range of 4–100 μm . The measurements were made over a Reynolds number range of 0.02 to 1000. The test results showed that the friction factor for both smooth and rough microchannels agreed with the conventional theory.

Kandlikar et al. [67] investigated experimentally the effects of the relative roughness on the pressure drop in two microtubes with a diameter of 1067 and 620 μm . They found that for the 1067 μm diameter tube with a relative roughness 0.003, the effects of the relative roughness on pressure drop are negligible and the tube can be considered smooth. However, for the 620 μm tube, the same relative roughness increases the pressure drop; in other words, the pressure drop is dependent of relative roughness even in the laminar region. The relative roughness could play an important role in microchannels than in macrochannels.

Gao et al. [68] performed an experimental investigation of the frictional characteristics of demineralized water through rectangular microchannels with a hydraulic diameter from 199 to 1923 μm . They found that the friction factor agreed with the prediction of the conventional theory.

Warrier et al. [69] reported experimental results on pressure drop for FC-84 through an aluminum rectangular microchannel with a hydraulic diameter of 750 μm . The experimental results in the laminar regime were in good agreement with the conventional predictions.

Hegab et al. [70] investigated experimentally the fluid flow and the heat transfer of R134a in rectangular aluminum microchannels with hydraulic diameters in the range of 112 and 210 μm and relative roughness from 0.0016 to 0.0089. The experimental data in

the laminar regime were very close to the predictions using the classical theory. The experimental results in the transition region and in the turbulent regime indicated that the friction factor was lower than the values predicted by the conventional theory. They evidenced that the aspect ratio of the channels and the relative roughness did not influence the transition region.

Experiments were performed to study the flow behavior of deionized water and nitrogen gas through round capillary tubes by Chung et al. [71]. The pressure drop measurements at Re less than 2000 showed good agreement with the conventional correlations for flows of both gas and liquid in a 100 μm microchannel. For gas flows in a microchannel, a compressibility effect was found to be important, even under flow conditions that are traditionally described as being incompressible.

Bucci et al. [72] measured the friction factor for water flowing in a 290 μm microtube with a relative roughness of 0.0075. They observed that the friction factor agreed with the prediction of the conventional theory up to a Reynolds number equals to 1500.

Wu and Cheng [73] focused on the influence of aspect ratio in smooth trapezoidal silicon microchannels with hydraulic diameters ranging between 25.9 and 291 μm . The experimental data were in good agreement with the predictions of the conventional theory. The authors concluded that the Navier-Stokes equations are still valid for the laminar flow of deionized water in microchannels with hydraulic diameters as small as 25.9 μm .

Maurer et al. [74] conducted experiments for helium and nitrogen flow in 1.14 μm deep 200 μm wide shallow microchannels. Flowrate and pressure drop measurements in the slip and early transition regimes were performed for averaged Knudsen numbers

extending up to 0.8 for helium and 0.6 for nitrogen. The authors also provided estimates for second-order effects and found the upper limit of slip flow regime as the averaged Knudsen number equals 0.3 ± 0.1 .

Teng et al. [75] investigated experimentally and numerically the fluidic behavior of the liquid flowing through the triangular microchannels. The triangular microchannels have the transverse dimensions from 50–100 μm ; the fluid flowing through these channels has Reynolds numbers from 0.1 to 35. They concluded that a linear relation exists between pressure drop and flow rate.

Tu and Hrnjak [76] investigated experimentally single-phase flow frictional pressure drop in five rectangular microchannels with hydraulic diameters ranging from 69.5 to 304.7 μm . The measured friction factors were compared with the conventional correlations. The results support such an agreement in the literature that the flow friction in microchannels may be different from the conventional results. However, when the channel surface roughness was low, both the laminar friction factor and the critical Reynolds number approach the conventional values. In the turbulent region, the surface roughness has great effect on the flow friction even for the smoothest channel tested.

Jung and Kwak [77] measured forced convective heat transfer coefficients and friction factor for flow of water in microchannels. The obtained friction factors are close to the theoretical value.

Bari et al. [78] experimentally investigated frictional characteristics of high velocity air flow in microchannels with diameters ranging from 266 to 1090 μm . The

experimental data depart significantly from macroscale correlations when $Re > 1400$ suggesting earlier transition to turbulence.

Brutin and Tadrist [79] experimentally investigated the friction factor of water flow through fused silica microtubes with diameters ranging from 50 to 530 μm . The experimental results for tap water indicate a disparity from the conventional theory. The experiments show that the surface roughness cannot explain such an increase. Fluid-surface interaction can be put forward as an explanation of the Poiseuille number increase by the fluid ionic coupling with the surface.

Baviere et al. [80] presented experimental results of water flow in smooth and rough rectangular microchannels. Friction is correctly predicted by the Navier-Stokes equations in the smooth case. Roughness considerably increases the friction coefficient in the laminar regime. However, the Poiseuille number remains independent of the Reynolds number.

Pressure drop and mass flow rate measurements were experimentally studied in a microchannel with hydraulic diameter of 146 μm by Hsieh et al. [81]. Deionized water served as working medium. The authors proposed empirical correlations in order to calculate the friction factor in laminar and in turbulent regime, namely, $f \sim Re^{-0.94}$ and $f \sim Re^{-0.23}$ respectively. The transition was found at $Re = 240$ which is a little bit lower than the value reported by Peng et al. [19].

Liquid flow in microchannels was investigated both experimentally and numerically by Liu and Garimella [82]. The experiments are carried out in microchannels with hydraulic diameters from 244 to 974 μm at Reynolds numbers ranging from 230 to 6500.

Results show that conventional theory may be used to predict successfully the flow behavior in microchannels.

In recent studies, Kohl et al [83] investigated experimentally liquid and gas flow in rectangular microchannels with hydraulic diameters ranging from 25 to 100 μm . Gas flow results for $6.8 < \text{Re} < 18814$ and liquid flow results for $4.9 < \text{Re} < 2068$ have been obtained. The results suggest that friction factors for microchannels can be accurately determined from data for large channels.

Aubert and Colin [84] studied slip flow in rectangular microchannels using the second-order boundary conditions proposed by Deissler [85]. In a later study, Colin et al. [86] presented experimental results for nitrogen and helium flows in a series of silicon rectangular microchannels. The authors proposed that the second-order slip flow model is valid for Knudsen numbers up to about 0.25.

A variety of researchers have attempted to develop second-order slip models which can be used in the transition regime. However, there are large variations in the second-order slip coefficient. The lack of a universally accepted second-order slip coefficient is a major problem in extending Navier-Stokes equations into the transition regime [87].

The wide variability of experimental results is illustrated in Figures 2.1 and 2.2. There is also broad variability in experimental conditions, microchannel geometries and material, surface roughness and methodology. The inconsistencies demonstrate the need for further work in order to elucidate potential microscale effects and mechanisms in these microchannels.

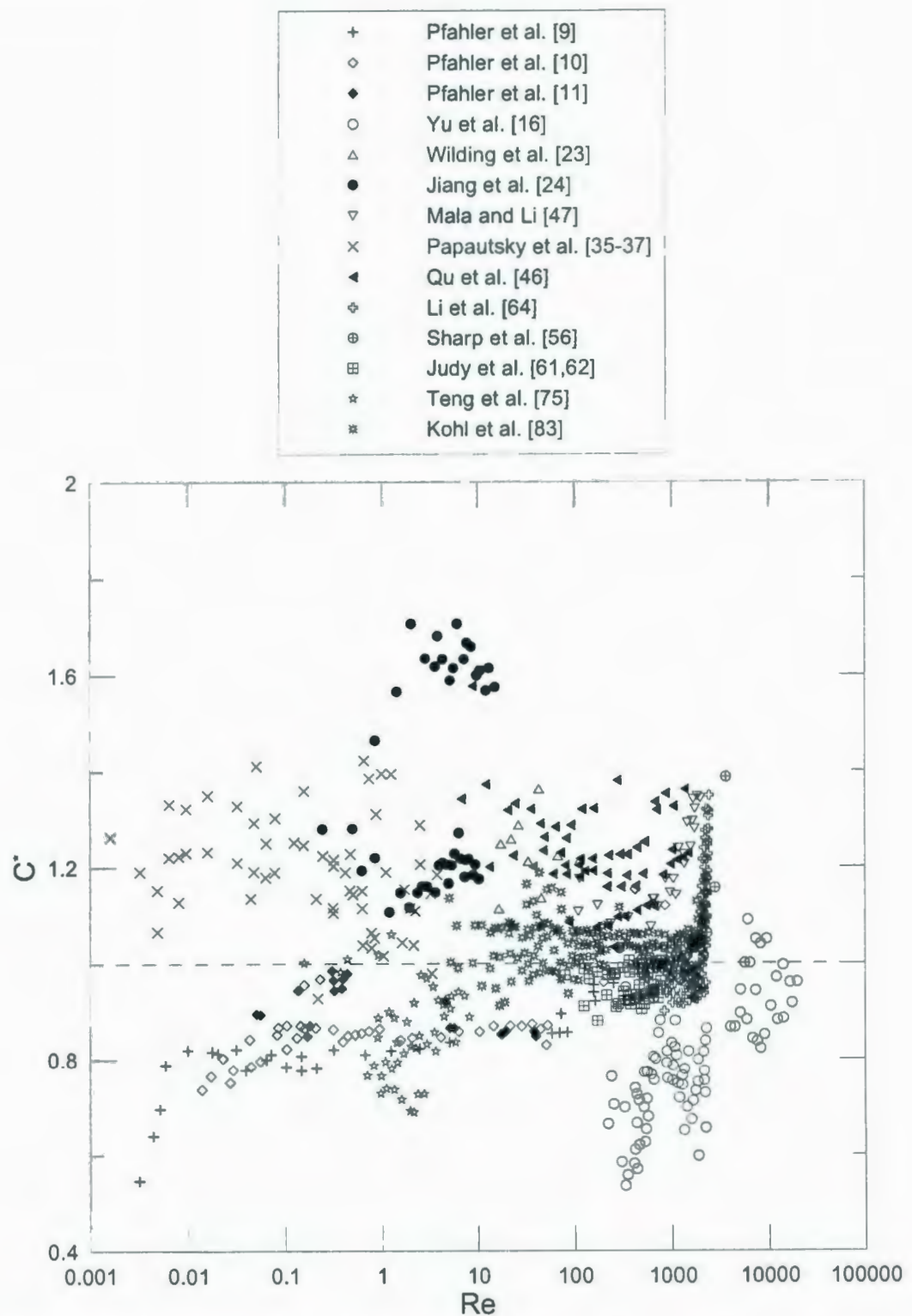


Figure 2.1 Comparison of C^* vs. Reynolds number for some experimental results for liquid flows in microchannel.

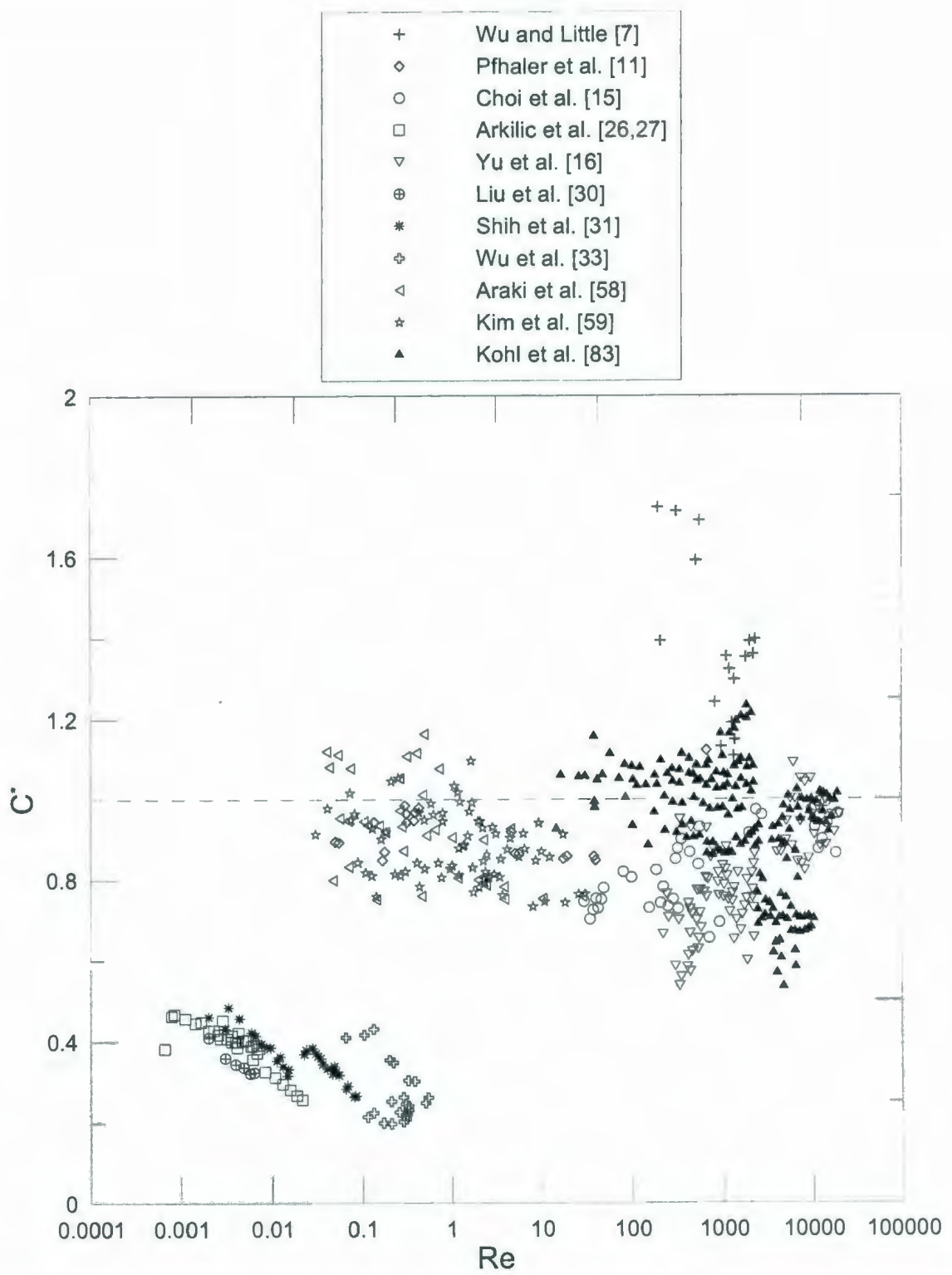


Figure 2.2 Comparison of C^* vs. Reynolds number for some experimental results for gas flows in microchannel.

2.2 Summary of Currently Available Experimental Data

Although the laminar flow in ducts is one of the most fundamental problems in fluid dynamics, experimental studies of microchannel flow attempting to reveal the frictional characteristics have often failed to demonstrate the expected relationship between friction factor and Reynolds number. Furthermore, the deviations are neither consistently higher nor lower than macroscale theory predictions. Tables 2.1 and 2.2 present a summary of the experiments that have been performed to investigate the behavior of fluid flow in microchannels over a large range of Reynolds numbers, geometries, and experimental conditions.

Tables 2.1 and 2.2 illustrate the varied and conflicting results that have been obtained by researchers. Many important factors have been varied and explored by these researchers. It is noted that, if we want to demonstrate the validity of the conventional theory for microchannel flows using the experimental results, the answer obtained is not univocal. Some researchers found that the predictions of the conventional theory agree with the experimental results; on the other hand, some researchers found the opposite conclusion with only slight differences in experimental conditions.

It is important to summarize the main results cited in the open literature on the friction factor with respect to the conventional theory:

- The friction factor for laminar fully developed flow is found to follow the conventional theory [39-41,53,55-56,60,62,64,68-69,71,73,75,77,80,82-83];
- The friction factor for laminar fully developed flow is found to be higher than the conventional prediction [7-8,14,18-19,23,33-37,41-48,57,63-64,67,79,81];

- The friction factor and Reynolds product for laminar fully developed flow does not remain constant and depends on the Reynolds number [9-11,18-19,52,57,70];
- The friction factor for laminar fully developed flow is found to be lower than the conventional prediction [9-12,15-16,25-27,29-33,38,54,58-59,61,65-66,70,76]; this result has been demonstrated especially for gas microchannel flow experiments;
- The friction factor for gaseous laminar fully developed flow decreases as the Knudsen number increases due to the effect of rarefaction [12,26-27, 29-31,58-59,74,86];
- The friction factor for gaseous laminar fully developed flow increases when the Mach number increases [12,29,63] due to the effect of compressibility;
- The friction factor depends on the material of the microchannel walls (conductivity) and the working fluid (polarity). The effect of electrokinetics phenomena for microchannel liquid flows is not negligible [9-11,43-48,61-62];
- In laminar regime, the friction factor also depends on the relative roughness of the walls of the microchannels [7,16,41-42,46,57,60,63-64,67,72,76,80];
- The critical Reynolds numbers depend on the microchannel wall roughness [7,47,60,72];
- The critical Reynolds numbers decrease when the microchannel hydraulic diameter decreases [15,19,65].
- An early laminar-to-turbulent transition with respect to the conventional predictions has been observed [7,12,15,19-22,25,39,43-45,47,54,57,65,78,81];

The flow of liquids in microchannels differs from that of gases in microchannels, due to the effects of compressibility and rarefaction in gases. In reviewing the results quoted in Tables 2.1 and 2.2, it is noted that generally for gases the friction factor is found to be smaller than the prediction of the conventional theory for continuum flows; for liquids, the friction factor is found to be larger than or obey the prediction of the conventional theory.

2.3 Proposed Explanation

Figures 2.1 and 2.2 show the currently available experimental results. The data are either above or below the theoretical predictions. Some of these anomalous results may be attributed to roughness of the channels and to uncertainty in the determination of the channel dimensions. Part of the discrepancy may also be due to the lack of a well-controlled surface structure.

Based on the available experimental data in the literature it has been suggested that phenomena occur at the microscale that are not described by conventional theory. It is also evident that significantly different behavior has been observed in the previous investigations with similar experimental design conditions. No universally accepted physical interpretation of the microscale effects has been proposed.

Table 2.1 Experimental results for liquid flows in microchannels.

| Researcher | Channel (μm) | Fluids | D_h (μm) | Re | Difference in f from Theory | % Diff |
|--------------------------|--|-------------------------------------|-----------------------------|------------|--|-----------------------------|
| Pfahler et al. [9-11] | Rectangular, Trapezoidal; silicon H=0.48-38.7, W=55-115 | Isopropyl, isopropanol, silicon oil | 0.5-40, 2.5-25, silicon oil | <100 | Decrease Proposed $f=C/Re$ with C given as C vs Re graphs | 15% |
| Urbanet et al. [34] | Rectangular | Propanol pentanol | 5,12,25 | - | Increase | 5-20% |
| Wang and Peng [21] | Rectangular | Water and methanol | 311-747 | - | Transition to turbulent flow was initiated at Re of 300-800. | - |
| Peng et al. [18,19] | Rectangular, Rough stainless steel, H=100-300, W=200-400, L=50mm | Water | 133-367 | 50-4000 | Flow transition occurred for Re=200-700. Transition Re decreased as D_h was reduced. $f = C_{f,l}/Re^{1.98}$ Laminar flow $f = C_{f,v}/Re^{1.72}$ Turbulent flow $Re=200 \quad D_h < 220$ $Re=400 \quad D_h = 240$ $Re=700 \quad 260 < D_h < 360$ | - |
| Papautsky et al. [35,36] | Rectangular , metallic, H=30, W=600, L=3mm | Water | 57 | 1-20 | Increase | 12% |
| Papautsky et al. [37] | Rectangular , metallic, H=22.71-26.35, W=150-600, L=7.75mm | Water | 44 | 0.001-10 | Increase | 20% |
| Jiang et al. [25] | Circular,Rectangular , Trapezoidal, Triangular,silicon | Water | 35-120 | 1-30 | Decrease Flow transition occurred for Re=600-2800. | 15-30% short 50-75% long |
| Wu et al. [33] | Rectangular , silicon, W=19, H=1.85, L=4.4mm | Water | 3.5 | 0.1-1 | Increase | 10-30% |
| Harms et al. [39] | Rectangular , silicon, W=251, H=1030, L=2.5cm | Water | 403-1923 | - | Transitional Re was 1500. | 0% |
| Webb & Zhang [40] | Rectangular , Silicon | R-134a | 133 | 6000-30000 | None | 0% |
| Pfund et al. [41] | Rectangular, Silicon | Water | 200-900 | 40-1300 | Re<1300 agreement with laminar theory. When roughness increased, friction factor also increased. | 0% |
| Pfund et al. [42] | Rectangular, Rough, Silicon | Water | 128-521 | 60-3450 | Increase. Flow transition occurred for Re=1700. | - |
| Mala et al. [43-45] | Circular, Parallel plate, Silicon , Rough | Water | 51-169 | 0-1500 | Argue that the increase in friction factor is due to the electric double layer(EDL). | 0-39% |

| | | | | | Transition to turbulent at Re 300- 900 | |
|---------------------------|--|------------------------------|-------------|------------|--|--------|
| Kolinsky et al. [48] | Rectangular, Silicon | Polar Liquids | 39-100 | - | Increase Proposed an electrokinetic theory to model microflows. | - |
| Harley et al. [14] | Rectangular, Trapezoidal, Silicon | Isopropylol, | 45,67 | - | Increase | - |
| Flockhart & Dhariwal [53] | Trapezoidal, Silicon, H=27-63 W=100-1000 L=12-36mm | Water | 50-120 | <600 | None | 0% |
| Qu et al. [46] | Trapezoidal, Rough, Silicon, H=28-114 W=148-523 L=28mm | Water | 51-169 | 10-1450 | Increase The authors proposed a roughness-viscosity model. | 8-38% |
| Yu et al. [16] | Circular, fused silica | Water | 52,102 | 250-20000 | Decrease $f = 50.13/Re$ Re<2000 $f = 0.302/Re^{0.25}$ 6000<Re<20000 Transition from laminar to turbulent flow occurred for 2000<Re<6000. | 10-40% |
| Sharp et al. [56] | Circular | Water | 75-242 | 50-2500 | None | 0% |
| Wilding et al. [23] | Trapezoidal, Silicon, H=20-40 W=40-150 L=11.7mm | Water, Biological fluids | 26-63 | 17-126 | Increase | 30% |
| Guo & Wu [52] | Circular, numerical | - | - | - | $f Re$ product not constant; dependent on Re . f will increase along the flow direction. | - |
| Hegab et al. [70] | Rectangular, aspect ratio 1.0-1.5 | R-134a | 112-210 | 1280-13000 | Decrease in the transition and turbulent region. Transition from laminar to turbulent flow occurred for 2000<Re<4000. $f = 0.000173Re^{0.646}$ 2000<Re<4000 $f = 0.611Re^{-0.35}$ 4000<Re<15000 | 9-23% |
| Xu et al. [54] | Rectangular, | Water | 50-300 | 50-1500 | Decrease from theory for channel dimensions below 100 μm . | - |
| Xu et al. [55] | Rectangular, aluminum, silicon | Water | 29.59-344.3 | 5-4620 | None | 0% |
| Celata et al. [60] | Circular | R 114 | 130 | 100-8000 | Laminar to turbulent transition for 1880<Re<2480. Laminar flow regime f is in good agreement with conventional theory. | - |
| Judy et al. [61] | Circular | Water, methanol isopropylol, | 20-150 | 8-2300 | Decrease No evidence of transition to turbulent flow in the range $Re<2000$ as reported by other works. | - |
| Judy et al. [62] | Circular and square, Silica and Stainless steel | Water, methanol isopropylol, | 47-101 | 8-2300 | None | 0% |

| | | | | | | |
|-------------------------|--|-------------------------|------------|-----------|---|----|
| Wu and Cheng [73] | Trapezoidal, silicon | Water | 25.9-291 | 11-3060 | None | 0% |
| Li et al. [64] | Circular, rough, glass, silicon, stainless steel | Water | 79.9-205.3 | - | None Flow transition occurred for Re=2000. Relative roughness can not be neglected in the laminar regime. | 0% |
| Brutin and Tadrist [79] | Circular, fused silica | Distilled and tap water | 50-530 | - | Increase Deviation observed only for tap water. | - |
| Baviere et al. [80] | Smooth and rough rectangular | Water | 7-300 | 0.01-8000 | None Roughness increases in laminar regime. However, P_o remains independent of Re. | 0% |
| Jung and Kwak [77] | Rectangular | Water | 100-200 | 50-400 | None | 0% |
| Bucci et al. [72] | Circular, stainless steel | Water | 172-520 | 200-6000 | None for Re<1000 Increase for Re>1000, transition occurs for 1800<Re<3000. | - |
| Ding et al. [57] | Triangular and rectangular | R-134a, R-12 | 400-600 | 200-3500 | Increase. $f=C/Re^m$ Transition from laminar to turbulent are small than macro size. Surface roughness is an important factor. | - |
| Yang et al. [65] | Circular | Water, R134a | 173-4010 | - | None Early transition to turbulence | - |
| Hsieh et al. [81] | Rectangular | water | 146 | 0-900 | Increase $f = 48.1/Re^{0.94}$ for laminar $f = 1.03/Re^{0.23}$ for turbulent Transition from laminar to turbulent flow occurred at Re=240. | - |
| Liu and Garimella [82] | Rectangular | Deionized water | 244-974 | 230-6500 | None | 0% |
| Tu and Hrnjak [76] | Rectangular | R134a | 69.5-304.7 | 112-9180 | Decrease Surface roughness is an important factor. | - |
| Chung et al. [71] | Circular | Deionized water | 100 | 0-2000 | None | 0% |
| Kandlikar et al. [67] | Circular, rough | Water | 620, 1032 | 500-3000 | Increase Surface roughness is an important factor. | - |
| Gao et al. [68] | Rectangular | Water | 199-1923 | | None | 0% |
| Warrier et al. [69] | Rectangular | FC-84 | 750 | | None | 0% |
| Teng et al. [75] | Triangular | Water | 50-100 | 0.1-35 | None | 0% |
| Kohl et al. [83] | Rectangular | Water | 25-100 | 4.9-2068 | None | 0% |

Table 2.2 Experimental results for gas flows in microchannels.

| Researcher | Channel (μm) | Fluids | D_h (μm) | Re | Difference in f from Theory | % Diff |
|---------------------------|---|-------------------------------|-------------------------|------------------|--|-----------------------------|
| Wu & Little [7] | Trapezoidal; silicon and glass $W=130-300$, $H=30-60$ | Nitrogen, Helium | 55-76 | 200- 15000 | Friction factor for rough glass channel 3-5 times larger than smooth-pipe predictions. Flow transition occurred at Re=400. Correlation for f : $(110 \pm 8)/Re$ Re<900 $0.165(3.48-\log Re)^{0.24} + (0.081 \pm 0.007)$ 900<Re<3000 $(0.195 \pm 0.017)/Re^{0.11}$ 3000<Re<15000 | 0% for smooth channel |
| Choi et al. [15] | Circular silica | Nitrogen gas | 3-81 | 10-3000 | Decrease $f = 64/Re[1+30(v/Dc_a)]^{-1}$ Re<2000 $f = 0.140Re^{-0.182}$ 2500<Re<20000 $fRe=53$ Flow transition occurred for Re=500- 2000. | 0-30% |
| Harley et al. [12] | Rectangular, Trapezoidal, Silicon | Nitrogen, Hydroge n gas | 0.51 | 12-430 | Decrease | 12-20% |
| Pfalher et al. [9-11] | Rectangular, Trapezoidal, Silicon | Nitrogen, Hydroge n gas | 1.6-65 | 0.01- 1000 | Decrease | 10-20% |
| Ho & Tai [32] | Rectangular, Silicon | Nitrogen | 1.2 | 0.02- 0.07 | Decrease The surface phenomena is quite significant in microscale flow. | - |
| Wu et al. [33] | Rectangular , silicon, $W=19$, $H=1.85$, $L=4.4\text{mm}$ | Nitrogen | 3.5 | 0.1-1 | Decrease | 60-70% |
| Choquette et al. [38] | Rectangular, Silicon | Helium | 3 | - | Decrease | - |
| Guo & Wu [52] | Circular, numerical | - | - | - | fRe product not constant, dependent on Re . f will increase along the flow direction. | |
| Arkilic et al. [26,27] | Rectangular silicon, $H=1.33$, $W=52.25$, $L=7.5\text{mm}$ | Helium | 2.6 | 0.0005- 0.004 | Decrease Flow pressure relationship accurately modeled by including a slip flow B.C. | 55-65% |
| Pong et al. [29] | Rectangular silicon, $H=1.2$, $W=5$, 40 $L=3\text{mm}$ | Helium, Nitrogen | 1.94-2.33 | - | Decrease Pressure distribution was not linear as suggested by a continuum flow analysis. | - |
| Liu et al. [30] | Rectangular silicon, $H=1.2$, $W=40$ $L=4.5\text{mm}$ | Helium, Nitrogen | 2.33 | 0.001- 0.01 | Decrease The pressure drop distribution was shown to be nonlinear. | - |
| Shih et al. [31] | Rectangular silicon, $H=1.2$, $W=40$ $L=4\text{mm}$ | Helium Nitrogen | 2.33 | 0.001- 0.009 | Decrease Pressure distribution was not linear. | 55-70% |
| Araki et al. [58] | Trapezoidal; | Helium, Nitrogen | 3-10 | | Decrease Rarefaction effects could be | - |

| | | | | | | |
|--------------------|-------------|-------------------------|----------|------------|---|-----|
| | | | | | significant. | - |
| Yu et al. [16] | Circular | Nitrogen | 19-102 | 100-20000 | Decrease Flow transition occurred for Re=1700-6000. Roughness effects | - |
| Li et al. [63] | Circular | Helium | 80-166.6 | - | Increase Flow transition occurred for Re=1700-2300. | - |
| Bari et al. [78] | Rectangular | Air | 266-1090 | 250-430 | Higher for Re<1400 Lower when Re>1400 Earlier transition to turbulence | - |
| Turner et al. [66] | Rectangular | Helium, Nitrogen | 9.7-46.6 | 0.2-1000 | Decrease Entrance pressure loss is significant. Rarefaction and compressibility effects could be significant. | - |
| Yang et al. [65] | Circular | Air | 173-4010 | - | Decrease | - |
| Chung et al. [71] | Circular | Nitrogen | 100 | 0-2000 | None Compressibility effects could be significant. | 0% |
| Kim et al. [59] | Circular | Helium, Nitrogen, Argon | 5-100 | 0.03-29.7 | Decrease | 20% |
| Kohl et al. [83] | Rectangular | Air | 25-100 | 6.8-18814 | None | 0% |
| Maurer et al. [74] | Rectangular | Helium, Nitrogen | 2.28 | 0.001-0.07 | Decrease Estimated second-order slip effects | - |
| Colin et al. [86] | Rectangular | Helium, Nitrogen | 1-9 | - | Decrease Proposed a second-order slip model | - |

The theories attempting to explain the observed deviation are various. Table 2.2 demonstrates that the friction factor is lower than conventional prediction for gas microchannel flow experiments. It has been widely accepted that the deviation observed in gas flows may be attributed to velocity slip at the wall. However, the deviation experienced in liquid flows cannot be attributed to slip effects. There are many unanswered questions to be explored and a few of these are briefly discussed below.

Some effects, which are normally neglected for macroscale flows, may exist on the microscale. For example, the temperature variations in the transport fluid can cause a significant variation in fluid viscosity through a microchannel.

Viscous dissipation becomes significant when the diameter decreases and the average velocities increase. Energy generated by friction raise the average temperature of the fluid, which will result in a lower viscosity. Viscous dissipation effects may cause deviation in the friction factor from theoretical expectations. The fRe should be calculated by basing the viscosity on the average of the inlet and exit temperature. If the fRe is calculated by basing the viscosity only on the inlet temperature, the lower temperature will heighten the viscosity resulting in a lower Reynolds number than what is representative of the flow. Some researchers have reported the decrease in fRe with increasing Reynolds number. It is possible that viscous dissipation could contribute to the deviation observed by some researchers.

Many researchers believe the polarity of the fluid and the wall material is a factor in the deviation. The electrokinetic effects occur at the interface between the channel and the fluid due to chemical interactions. The EDL theory addresses these types of

phenomena [43,44]. However, the electrokinetic effects have not been adequately addressed in the microchannel flow studies.

In macroscale flows, the surface roughness does not affect the flow resistance relationships in the laminar regime. However, many microscale experimental results are opposite regarding the effects of surface roughness on friction factor in the laminar region.

Early transition to turbulence has often been offered as an explanation for the increase of flow resistance in microchannels. The evidence suggesting early transition to turbulence has been based solely on the trends in the experimental data.

Neglecting the entrance effects could affect the accuracy of the measured friction factor. The entrance lengths at the higher Reynolds numbers could become quite significant for comparatively short microchannels. The entrance length is estimated at half the length of the test section for the higher Reynolds number in some experiments in the literature. Furthermore, microscale effects could possibly lengthen the entrance region. In addition, neglecting the inlet and outlet pressure losses may cause inaccuracies in the prediction of the friction factor.

It is extremely difficult to accurately measure the dimensions of these microchannels, particularly when one of the dimensions is on the order of several microns. The uncertainty in the fRe calculation is very dependent upon the diameter. The diameter is to the fourth power in the fRe calculation. Any uncertainty associated with the diameter measurement will be multiplied four times, enough to explain the majority of the

discrepancies between the conventional predictions and the observed results in Figures 2.1 and 2.2.

2.4 Summary

The explanations offered for this anomalous behavior in the literature included rarefaction effects, compressibility effects, electrokinetic effects, surface roughness effects, variations in viscosity, micro-rotational effects of individual fluid molecules (micropolar flow theory), early transition to turbulence, entrance effects, and inaccuracies in measuring channel dimensions.

The currently available experimental data suggest the presence of microscale phenomena. However, they do not unequivocally identify the effects. There is a clear need for additional experimental investigations over a wider Reynolds number range using microchannels with well characterized dimensions and surface roughness in order to understand microscale internal fluid flow.

Chapter 3

Methodology

3.1 Theoretical Background

The emphasis was on the development of efficient microfabrication techniques in the early years of microfluidic devices. However, with the successful design and fabrication of various microfluidic devices with complex microstructures, the interest has shifted towards the prediction of device performance (e.g., microchannel flow) as microdevices tend to behave differently than the macroscale devices.

The two approaches that are typically utilized to study fluid behavior in microfluidic devices are continuum approach and molecular approach. In molecular approach, the molecular models recognize the fluid as a myriad of discrete particles. In this statistical approach, every particle in the flow must be accounted for. Therefore, this method is computationally intensive and is predominantly used when modeling nanoscale flows with the channel characteristic dimension up to approximately 100 nm. In continuum approach, the focus is on small groups of particles with smooth variations in properties so that differential calculus can be used in the analysis. This approach is much less computationally intensive than the molecular approach and is typically used in investigation of flows in channels with characteristic dimensions above approximately 1 mm. Some researchers have used the continuum approach to investigate microscale flows

and demonstrated a deviation of the experimentally observed results from the theoretical predictions. A possible explanation of this phenomenon is the breakdown of the continuum assumption.

3.1.1 Continuum Assumption

The concept of a continuum is the basis of classical fluid mechanics. The foundation of the continuum originated in the works of Euler (1707-1783). The continuum assumption simply means that physical properties are imagined to be distributed throughout space. We can consider a small volume element ΔV possessing mass density ρ defined by

$$\rho = \lim_{\Delta V \rightarrow 0} \frac{\Delta m}{\Delta V} \quad (3.1)$$

where Δm is the total mass contained in ΔV . This equation assumes that ρ is independent of the size of ΔV . As the size of ΔV approaches zero, a critical volume is reached when ρ begins to show increasing dependence on ΔV . In other words, as the size of the volume element approaches a characteristic dimension, the continuity assumption for mass density is no longer valid.

As a consequence of the continuum assumption, all properties of interest such as density, velocity, stress, pressure, temperature are assumed to be defined everywhere in space and to vary continuously from point to point within a flow. Therefore, fluid properties are considered continuous functions of position and time. Properties may change from one point to the next. Conversely, the continuum assumption does not allow

properties to become infinite or to jump discontinuously at a single isolated point. Continuum properties may be interpreted as the average of a large number of microscopic particles.

3.1.2 Continuum Breakdown

The continuum assumption is valid in considering the behavior of fluid under macroscale conditions. When the molecular spacing and mean free path of the fluid are comparable to the smallest characteristic dimension, the continuum assumption becomes no longer valid.

The Knudsen number (Kn) relates the molecular mean free path of gas to a characteristic dimension [88]:

$$Kn = \frac{\lambda}{L} \quad (3.2)$$

where λ is the mean free path of the molecules and L is a characteristic dimension. Knudsen number is very small for continuum flows. However, for microscale gas flows where the gas mean free path becomes comparable with the characteristic dimension of the duct, the Knudsen number may be greater than 10^{-3} . Schaaf and Chambre [28] have proposed the use of the Knudsen number to classify flow regimes of gases as presented in Table 3.1. Thus, microchannels with characteristic lengths on the order of 100 μm would produce flows inside the slip regime ($Kn > 10^{-3}$) for gas with a typical mean free path of approximately 100 nm at standard conditions.

Table 3.1 Classification of flow regimes based on Knudsen number.

| Regime | Lower Limit | Upper Limit |
|---------------------|-------------|-------------|
| Continuum Flow | 0 | 0.001 |
| Slip Flow | 0.001 | 0.1 |
| Transition Flow | 0.1 | 10 |
| Free Molecular Flow | 10 | ∞ |

The density of liquids is 100 to 800 times that of the typical gaseous state. The molecules are closely packed and surrounded by other molecules. Since the molecules are continuously in collision, the concept of a mean free path is not used for liquids. When considering liquids, it is typical to talk about molecular lengths. For many liquids, the molecular lengths are on the order of 1 nm. This means that the microchannel characteristic length must be at least on the order of 1 μm or less to produce flows outside the continuum regime. Furthermore, the nature of liquid flows near walls is more complex than that of gases. The physical and chemical nature of the walls and liquids are significant. Beskok and Karniadakis [89] attempted to define a flow regime scale for liquids, similar to gases. However, such an empirical scale requires further experimental validation.

3.1.3 Governing Equations

The most important equations of fluid mechanics are the continuity equation, momentum equation, and energy equation. The continuity equation, also known as the law of conservation of mass, states that for a unit volume there is a balance between the

masses entering and leaving per unit time, and the change in density. Using symbolic notation, the differential continuity equation is written as

$$\frac{\partial \rho}{\partial t} + \nabla \cdot (\rho \mathbf{V}) = 0 \quad (3.3)$$

where ρ is the fluid density, \mathbf{V} is the fluid velocity vector, and t is time.

The momentum equation is essentially Newton's second law applied to a continuum. The momentum equation states that the time rate of change of linear momentum of a continuum is equal the sum of the forces on the continuum. Two types of forces are typically present: body forces which act on the bulk of the material inside the continuum, and surface forces which act at the boundary surface. Using symbolic notation, the differential momentum equation is written as

$$\rho \frac{D\mathbf{V}}{Dt} = \rho \frac{\partial \mathbf{V}}{\partial t} + \rho(\mathbf{V} \cdot \nabla) \mathbf{V} = \rho \mathbf{F} + \nabla \cdot \tau_{ij} \quad (3.4)$$

where D/Dt is the material derivative, \mathbf{F} is the external body force per unit mass (e.g., gravity), p is the pressure, and τ_{ij} is the stress tensor.

For an isotropic Newtonian fluid, the stress tensor is proportional to the rate of shearing strain and can be expressed in terms of velocity gradient and fluid properties as

$$\tau_{ij} = -p \delta_{ij} - \frac{2}{3} \mu (\nabla \cdot \mathbf{V}) \delta_{ij} + 2\mu S_{ij} \quad (3.5)$$

where δ_{ij} is the Kronecker delta or identity tensor, μ is the fluid viscosity, and S_{ij} is the rate of deformation tensor. The identity tensor δ_{ij} equals unity if $i = j$ and zero if $i \neq j$. The rate of deformation is defined as

$$S_{ij} = \frac{1}{2} \left(\frac{\partial u_i}{\partial x_j} + \frac{\partial u_j}{\partial x_i} \right) \quad (3.6)$$

Equation (3.5) is Newton's viscosity law and must be satisfied by all Newtonian fluids. For a Newtonian fluid, the viscous stresses are proportional to the rate of shearing strain. The stresses can be expressed in terms of velocity gradients and fluid properties in rectangular coordinates as (constitutive equation)

$$\begin{aligned} \tau_{xx} &= -p - \frac{2}{3} \mu (\nabla \cdot \mathbf{V}) + 2\mu \frac{\partial u}{\partial x} & \tau_{yy} = \tau_{yx} = \mu \left(\frac{\partial u}{\partial y} + \frac{\partial v}{\partial x} \right) \\ \tau_{yy} &= -p - \frac{2}{3} \mu (\nabla \cdot \mathbf{V}) + 2\mu \frac{\partial v}{\partial y} & \tau_{xz} = \tau_{zx} = \mu \left(\frac{\partial w}{\partial x} + \frac{\partial u}{\partial z} \right) \\ \tau_{zz} &= -p - \frac{2}{3} \mu (\nabla \cdot \mathbf{V}) + 2\mu \frac{\partial w}{\partial z} & \tau_{yz} = \tau_{zy} = \mu \left(\frac{\partial v}{\partial z} + \frac{\partial w}{\partial y} \right) \end{aligned} \quad (3.7)$$

where u , v , and w are components of the velocity vector \mathbf{V} in x , y , and z directions.

Introducing Newton's viscosity law into the momentum equations yields the differential equations of motion for a Newtonian fluid

$$\rho \frac{D\mathbf{V}}{Dt} = -\nabla p + \rho \mathbf{F} - \frac{2}{3} \nabla (\mu \nabla \cdot \mathbf{V}) + 2\nabla \cdot (\mu S_{ij}) \quad (3.8)$$

These equations of motion are commonly referred to as the Navier-Stokes equations. The equations are greatly simplified when applied to incompressible flows in which variations

in fluid viscosity and density can be neglected. Under these conditions the equations reduce to

$$\rho \frac{D\mathbf{V}}{Dt} = -\nabla p + \rho\mathbf{F} + \mu\nabla^2\mathbf{V} \quad (3.9)$$

The corresponding energy equation is

$$\rho \frac{Dh}{Dt} = \frac{Dp}{Dt} - \nabla \cdot \mathbf{q} + \Phi \quad (3.10)$$

where h is the enthalpy and \mathbf{q} is the vector heat flux given by Fourier's law of heat conduction,

$$\mathbf{q} = -k\nabla T \quad (3.11)$$

The rate of conversion of mechanical energy into heat due to internal viscous dissipation is

$$\Phi = \mu \left(\frac{\partial u_i}{\partial x_j} + \frac{\partial u_j}{\partial x_i} - \frac{2}{3} (\nabla \cdot \mathbf{V}) \delta_{ij} \right) \frac{\partial u_i}{\partial x_j} \quad (3.12)$$

The detailed derivations of the continuity equation, the momentum equation, and the energy equation, as well as the more detailed description of the continuum assumption are provided in a number of available texts. Advanced readers are referred to White [90], Panton [91], and Schlichting [92].

3.1.4 Pressure-Driven Flow in Channels

For incompressible Newtonian fluid flow with no body forces other than gravity, the continuity and momentum equations reduce to

$$\nabla \cdot \mathbf{V} = 0 \quad (3.13)$$

$$\rho \left(\frac{\partial u_i}{\partial t} + u_j \frac{\partial u_i}{\partial x_j} \right) = \frac{\partial \tau_{ij}}{\partial x_j} + \rho F_i \quad (3.14)$$

where F_i is the body force per unit mass (often $F_i = g_i$, the gravitational acceleration).

Consider a long straight duct with the x direction along the axis of the duct and the coordinates y and z in the plane perpendicular to the axis of the duct. When the velocity becomes purely axial and varies only with the lateral coordinates, $\mathbf{u} = (u(y, z), 0, 0)$, the flow is then called fully developed. Thus, for fully developed flow with gravitational body force g the equations become very simply

$$\rho \frac{\partial u}{\partial t} = - \frac{dp}{dx} + \rho g_x + \frac{\partial}{\partial y} \left(\mu \frac{\partial u}{\partial y} \right) + \frac{\partial}{\partial z} \left(\mu \frac{\partial u}{\partial z} \right) \quad (3.15)$$

$$\rho c_p \left(\frac{\partial T}{\partial t} + u(y, z) \frac{\partial T}{\partial x} \right) = k \left(\frac{\partial^2 T}{\partial y^2} + \frac{\partial^2 T}{\partial z^2} \right) + \Phi \quad (3.16)$$

Furthermore, if the flow is steady and the properties are constant, then the momentum equation for streamwise velocity profiles reduces to a simple Poisson equation

$$\frac{\partial^2 u}{\partial y^2} + \frac{\partial^2 u}{\partial z^2} = \frac{1}{\mu} \left(\frac{dp}{dx} - \rho g_x \right) \quad (3.17)$$

3.1.5 Flow in Circular Tubes

The circular tube is the geometry most commonly used in fluid flow and heat transfer devices. While microfabrication characteristically yields noncircular channels, the circular cross section is a useful and familiar archetype. Extensive macroscale research on pipe flows dates back to the original studies by Hagen (1839), and Poiseuille (1840). Hagen and Poiseuille respectively observed the relation between pressure head and velocity, and its inverse proportionality to the fourth power of tube diameter.

For fully developed laminar flow, the continuum momentum equation takes the form

$$\mu \left(\frac{d^2 u}{dr^2} + \frac{1}{r} \frac{du}{dr} \right) = \frac{dp}{dx} \quad (3.18)$$

After applying both the boundary condition of finite centerline velocity and the no slip boundary condition at the wall, the following velocity distribution is obtained

$$u = - \frac{dp}{dx} \frac{(R^2 - r^2)}{4\mu} \quad (3.19)$$

where R is the radius of the pipe, r is the radial coordinate, μ is the fluid viscosity, and dp/dx is the constant pressure gradient. The volume flow rate (Q) is then determined by integrating the axial velocity over the pipe cross sectional area

$$Q = \int_0^R 2\pi u r dr \quad (3.20)$$

Using the volume flow rate, the average velocity (\bar{u}) can be determined by dividing by the area, and gives the following form

$$\bar{u} = -\frac{D^2}{32\mu} \frac{dp}{dx} \quad (3.21)$$

D is the pipe diameter. After integrating Eq. (3.21), the pressure difference along the length of the pipe (L) is given by

$$\Delta p = \frac{32\mu L \bar{u}}{D^2} = \frac{8\mu L Q}{\pi R^4} \quad (3.22)$$

To find a nondimensional relationship for the pressure drop, both sides of Eq. (3.22) are divided by the dynamic pressure $\rho \bar{u}^2 / 2$ to yield

$$\frac{2\Delta p}{\rho \bar{u}^2} = \frac{64}{Re} \left(\frac{L}{D} \right) \quad (3.23)$$

where $Re = \rho \bar{u} D / \mu$. The Fanning friction factor (f) is defined as

$$f = \frac{\tau_w}{\frac{1}{2} \rho \bar{u}^2} = -\frac{dp}{dx} \frac{D}{2\rho \bar{u}^2} \quad (3.24)$$

and turns out to be the classic relation $16/Re$ for laminar incompressible flow.

The Poiseuille number is conveniently used to describe flow resistance in ducts of arbitrary cross section as the Poiseuille number is a pure constant. It is defined by

$$Po = \frac{\tau_w D}{\mu \bar{u}} = \frac{f Re}{2} \quad (3.25)$$

Therefore, the friction factor can be calculated by measuring the pressure drop along a specified length, the flow rate through the tube, and the diameter of the tube. With these measurements it is possible to determine the friction factor or friction factor Reynolds product using the following relations

$$f = \frac{\pi^2 \Delta p D^5}{32 \rho Q^2 L} - \sum K_L \left(\frac{D}{4L} \right) \quad (3.26)$$

$$f Re = \frac{\pi \Delta p D^4}{8 \mu Q L} - \sum K_L \frac{\rho Q}{\pi \mu L} \quad (3.27)$$

where the second term represents minor losses that exist due to the tube inlet, exit, and developing length. The measured friction factor can then be compared to the theoretical value of $16/Re$ for circular pipe flow. For flows in non-circular ducts, a relationship $f=C/Re$, where C is a constant based on the channel geometry, is determined by following the similar procedure as above. Measurements of f and Re are made, and then the product fRe is compared with the corresponding constant obtained from macroscale laminar flow theory. This has been the standard approach of most research in this area.

The inverse relationship between friction factor and Reynolds number has been well documented on the macroscale laminar flow. The pressure drop is linearly proportional to

the flow rate, Q . When the Reynolds number increases above 2300 in a circular tube, the flow begins to transition to turbulence. At this point, the friction factor increases strikingly, and the pressure drop ultimately becomes proportional to Q^2 .

3.1.6 Entrance Length Effects

The hydrodynamic entrance region of the duct is that region where the velocity boundary layer is developing. In this region the flow looks like a boundary layer that grows as it progresses downstream. In this region, the fluid velocity profile changes from the initial profile at the entrance to an invariant form downstream. This transition occurs in the entrance length of the duct. Ultimately, the viscously retarded layers meet in the center of the duct at the end of the entrance length.

The pressure drop from the beginning of the duct to a location x is given by

$$p_0 - p(x) = \left(4f \frac{x}{D_h} + K(x) \right) \frac{\rho \bar{u}^2}{2} \quad (3.28)$$

where $K(x)$ is the excess pressure drop coefficient. Schmidt and Zeldin [93] numerically calculated the parameter, K , for circular ducts and parallel plates. The apparent friction factor, f_{app} , is defined as

$$f_{app} = f + \frac{K}{4L/D_h} \quad (3.29)$$

Muzychka and Yovanovich [94] developed a simple model for the apparent friction factor in the entrance region for non-circular ducts.

$$f_{app} \text{Re}_{\sqrt{A}} = \left[\left(\frac{12}{\sqrt{\varepsilon}(1+\varepsilon) \left[1 - \frac{192\varepsilon}{\pi^5} \tanh\left(\frac{\pi}{2\varepsilon}\right) \right]} \right)^2 + \left(\frac{3.44}{\sqrt{z^+}} \right)^2 \right]^{1/2} \quad (3.30)$$

where ε is the aspect ratio and the dimensionless position for hydrodynamically developing flows $z^+ = z/(\ell \text{Re}_\ell)$. The definition of aspect ratio is summarized in Table 3.2 for a number of geometries. It predicts most of the non-circular friction data within $\pm 10\%$.

Table 3.2 Definition of aspect ratio.

| Geometry | Aspect Ratio |
|-------------------|---|
| Regular Polygons | $\varepsilon = 1$ |
| Singly-Connected | $\varepsilon = \frac{b}{a}$ |
| Trapezoid | $\varepsilon = \frac{2b}{a+c}$ |
| Annular Sector | $\varepsilon = \frac{1-r^*}{(1+r^*)\Phi}$ |
| Circular Annulus | $\varepsilon = \frac{1-r^*}{\pi(1+r^*)}$ |
| Eccentric Annulus | $\varepsilon = \frac{(1+e^*)(1-r^*)}{\pi(1+r^*)}$ |

3.1.7 Noncircular Channels

Most microfluidic channels have noncircular cross-sections. Fully developed flow in noncircular ducts can be found by solving the Poisson equation (3.17). Muzychka and

Yovanovich [94] developed a pretty simple model for predicting the friction factor Reynolds number product in non-circular ducts for fully developed laminar flow.

$$f \text{Re}_{\sqrt{A}} = \frac{12}{\sqrt{\varepsilon}(1+\varepsilon) \left[1 - \frac{192\varepsilon}{\pi^5} \tanh\left(\frac{\pi}{2\varepsilon}\right) \right]} \quad (3.31)$$

Yovanovich and Muzychka [95] showed an important result that the characteristic length scale for non-circular ducts in laminar flows should not be the hydraulic diameter, but rather, the square root of the cross-sectional area of the duct.

3.2 Scale Analysis

Scale analysis is the art of examining the order of magnitude of terms appearing in the governing equations of transport problems. It is also referred to as order of magnitude analysis or scaling. The objective of scale analysis is to use the basic principles to produce order of magnitude estimates for the quantities of interest. Scale analysis may be used to simplify governing equations through the determination and elimination of terms which have little effects on the flow, and it may be used to obtain crude solutions which are correct within an order of magnitude. It is indicative of the relative magnitudes of the various physical mechanisms in each problem. Scale analysis is remarkable when the exact analytical solution is not available.

Scale analysis is recommended as the premier method for determining the most knowledge for the least effort. There are five essential rules which must be followed when undertaking a scale analysis. These are discussed in the text by Bejan [96].

Rule 1 – Always define the spatial extent of the problem under consideration. This could be a physical dimension associated with the system or another region such as a boundary layer when the system or region of interest is not finite.

Rule 2 – Any equation constitutes an equivalence between the scales of two dominant terms appearing in the equation. Other terms in the equation of interest may dominate under certain conditions. The reasoning for selecting the dominant scales is the basis of rules 3-5.

Rule 3 – If in the sum of two terms in which the order of magnitude of one term is greater than the order or magnitude of the other term, then the order of magnitude of the sum is dictated by the dominant term. i.e. given $c = a+b$, then if

$$O(a) > O(b) \quad \text{then} \quad O(c) = O(a) \quad (3.32)$$

Rule 4 – If in the sum of two terms, the order of magnitude is the same for each term, then the sum is of the same order of magnitude. i.e. given $c = a+b$, then if

$$O(a) = O(b) \quad \text{then} \quad O(c) \sim O(a) \sim O(b) \quad (3.33)$$

Rule 5 – In any product or quotient of two terms, the order of magnitude of the product or quotient is given by the product or quotient of the order of magnitudes of each term. i.e. given $c = ab$, then if

$$O(c) = O(a)O(b) \quad (3.34)$$

or if given $c = a/b$, then

$$O(c) = O(a)/O(b) \quad (3.35)$$

Successful application of scale analysis can provide much of the information and insight about the nature of a given fluid mechanics or transport process without the need to solve the governing differential equations.

3.3 Asymptotic Analysis

In many problems found in the field of transport phenomena, there exists an asymptotic behaviour of a general solution for small and large values of a particular parameter. For example, in the case of fluid flow, the first type of behaviour which may come to mind is the flow of fluid at small and large Reynolds numbers. However, in this type of situation, there usually exists a transition region which may or may not be smooth. On the other hand if we confine ourselves to a particular flow regime such as laminar flow, there exist many fundamental problems which display smooth transition for flow from small to large Reynolds number, from short to long tubes, for small to large Prandtl numbers. This smooth transition indicates that there is no sudden change in slope and no discontinuity within the transition region.

Many of these problems lend themselves to asymptotic analysis. That is, we may develop a composite solution by considering only the asymptotic or limiting behaviour of these problems. It is easier to obtain exact or approximate solutions for limiting conditions of a particular variable of interest, than it is to find a solution which is exact over a wide range of that particular variable.

Once these asymptotic limits are determined we may develop a composite model by combining the asymptotes in one of two ways:

$$y(x) = \left[\{y_0(x \rightarrow 0)\}^n + \{y_\infty(x \rightarrow \infty)\}^n \right]^{1/n} \quad (3.36)$$

or

$$y(x) = \left[\{y_0(x \rightarrow 0)\}^{-n} + \{y_\infty(x \rightarrow \infty)\}^{-n} \right]^{-1/n} \quad (3.37)$$

where y_0 and y_∞ are asymptotic solutions for small and large values of the independent variable x . The parameter n is a fitting coefficient determined using data which should be distributed in the transition region of the asymptotes. These data may be either experimental or numerical, and in some situations may be analytical. The value of the parameter n is only important in the transition region. The results for small and large values of the independent parameter x , remain unchanged with changing the parameter n . The parameter n may be chosen using a number of methods as discussed by Churchill and Usagi [97]. This method was proposed by Churchill and Usagi [97] as a means of combining asymptotic solutions to develop a model which is valid over a wide range of the parameter of interest.

Asymptotic techniques provides a way to generate approximate solutions of the nonlinear differential equations of fluid mechanics, as well as the corresponding thermal energy (or species transport) equations. They demand an extremely close interplay between the mathematics and the physics, and in this way contribute a very powerful

understanding of the physical phenomena that characterize a particular problem or process.

Thus, the power and impact of asymptotic techniques is not mainly because they provide approximate solutions of complex problems but rather because they provide a framework to understand the essential features from a qualitative physical point of view.

3.4 Characteristic Length Scale

In the fluid flow and heat transfer literature the convention is to use the hydraulic diameter $4A/P$. This characteristic length arises naturally from a simple control volume balance on an arbitrary shaped straight duct. For non-circular geometries, it is desirable to eliminate or reduce the effects of geometry such that the general trends for all duct shapes may be easily modeled. It is better to choose a “reasonable” characteristic length scale to non-dimensionalize the fluid flow and heat transfer data.

Dimensional analysis using Buckingham theorem was undertaken for fully developed flow by Muzychka [98]. It was shown that only the perimeter or the square root of the flow area result as possible choices for the characteristic length.

All three possibilities for characteristic length L ($L = P$, $L = \sqrt{A}$, and $L = A/P$) have a number potential flaws. First, the perimeter and area are not definable for a parallel plate. This is not a problem for singly or doubly connected regions having finite area and perimeter. This aspect does not pose a problem for the definition of the hydraulic diameter. However, a number of deficiencies in the hydraulic diameter concept should be addressed, namely, that the hydraulically equivalent circular area and perimeter based

upon the hydraulic diameter are not the same as the true area and perimeter of the non-circular duct. This mismatch in area and perimeter is the probable cause in the mismatch of dimensionless laminar flow data. Finally, the hydraulic diameter concept produces results which are in contradiction of correct physical behaviour. In a number of cases where a duct shape varies with aspect ratio, the dimensionless results decrease with decreasing aspect ratio, which is contradictory to observation that fluid friction and heat transfer generally increase with a decrease in aspect ratio.

All three length scales have been critically examined by Muzychka [98]. It was observed that $L = P$ and $L = \sqrt{A}$ succeeded in bringing the dimensionless results closer together for similar ducts, i.e. rectangular and elliptical or polygonal. In both cases, better correlation of the laminar flow data was achieved versus the duct aspect ratio. For low aspect ratio ducts, $L = P$ provided better correlation than $L = \sqrt{A}$. For high aspect ratio ducts such as the polygonal ducts, $L = \sqrt{A}$ provided better correlation than $L = P$. Overall, $L = \sqrt{A}$ was found to be more effective at collapsing the data over a wide range of duct aspect ratios.

It may also be argued on physical grounds that the square root of the flow area is essentially the same as preserving the duct area or maintaining a constant mass flow rate. That is

$$(\rho \bar{u} A)_{cir} = (\rho \bar{u} A)_{ncir} \quad (3.38)$$

Now if both the circular and non-circular ducts have the same mass flux $G = \rho \bar{u}$ then,

$$A_{cir} = A_{ncir} \quad (3.39)$$

And the effective circular diameter becomes

$$D_{eff} = \sqrt{\frac{4A_{ncir}}{\pi}} \quad (3.40)$$

In other words, the characteristic length $L = \sqrt{A} \sim D_{eff}$.

Finally, the characteristic length should also be representative of a direction parallel to a vector normal to the duct wall. Since this length changes around the perimeter of many ducts, $L = \sqrt{A}$ appears to represent the geometric mean value. Consider the rectangular and elliptical cross-sections having semi-axes of length a and b . The square root of the cross-sectional area for each ducts gives $\sqrt{4ab}$ and $\sqrt{\pi ab}$ for the rectangle and ellipse, respectively. Both a and b are directions normal to the duct wall.

3.5 Numerical Simulation

A summary of possible simulation approaches at the continuum and molecular levels for both gas and liquid microflows is shown in Figure 3.1. MD refers to molecular dynamics, DPD refers to dissipative particle dynamics, and DSMC refers to direct simulation Monte Carlo method.

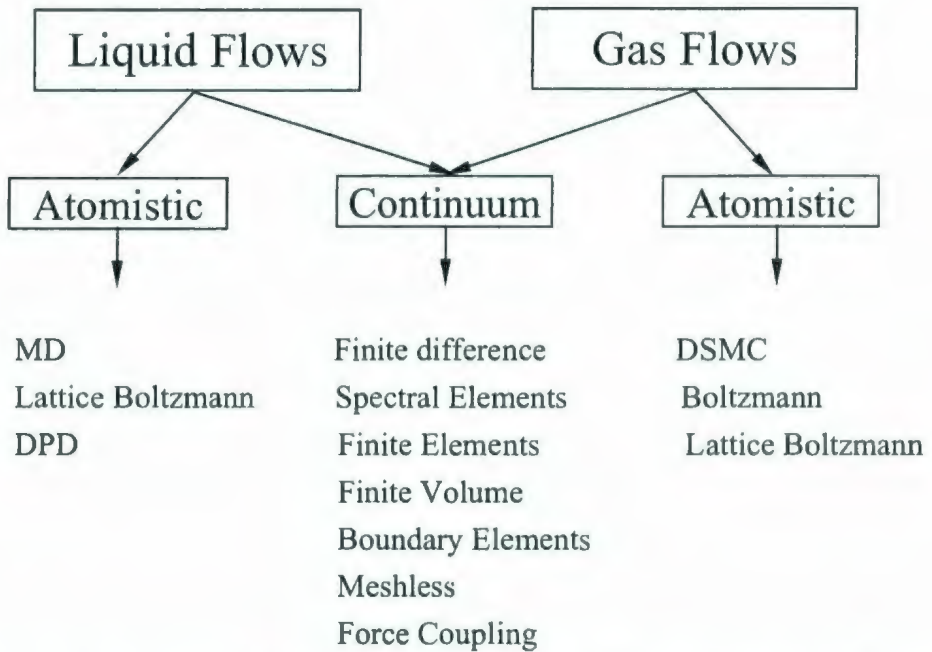


Figure 3.1 Summary of simulation methods for liquid and gas microflows[1].

Table 3.3 Flow regimes and fluid models.

| Kn | Fluid Model |
|--|--|
| $Kn \leq 10^{-3}$ (continuum) | Navier-Stokes equations with no-slip boundary conditions |
| $10^{-3} \leq Kn \leq 10^{-1}$ (slip) | Navier-Stokes equations with first-order slip boundary conditions |
| $10^{-1} \leq Kn \leq 10$ (transition) | Navier-Stokes equations with second-order slip boundary conditions, Burnett equations with slip boundary conditions, DSMC, Lattice Boltzmann |
| $Kn \geq 10$ (free molecular) | Collisionless Boltzmann, DSMC, Lattice Boltzmann |

Various regimes of fluid flows and appropriate fluid models are shown in Table 3.3.

The flow regime for $Kn < 0.001$ is known as the continuum regime, where the Navier-Stokes equations with no-slip boundary conditions govern the flow. In the slip flow

regime ($0.001 \leq Kn \leq 0.1$) the assumed no-slip boundary conditions seem to fail. This results in a finite velocity slip value at the wall, and the corresponding flow regime is known as the slip flow regime. In the slip flow regime the flow is governed by the Navier-Stokes equations, and rarefaction effects are modeled by using Maxwell's velocity slip and von Smoluchowski's temperature jump boundary conditions at the wall.

Chapter 4

Slip Flow in Long Microchannels

4.1 Introduction

Rarefaction effects must be considered in gases in which the molecular mean free path is comparable to the channel's characteristic dimension. The continuum assumption is no longer valid and the gas exhibits non-continuum effects such as velocity slip and temperature jump at the channel walls. Traditional examples of non-continuum gas flows in channels include low-density applications such as high-altitude aircraft or vacuum technology. The recent development of microscale fluid systems has motivated great interest in this field of study. Microfluidic systems must take into account non-continuum effects. There is strong evidence to support the use of Navier-Stokes and energy equations to model the slip flow problem, while the boundary conditions are modified by including velocity slip and temperature jump at the channel walls.

Traditionally, the no-slip condition at a fluid-solid interface is enforced in the momentum equation, and an analogous no-temperature-jump condition is applied in the energy equation. The interaction between a fluid particle and a wall is similar to that between neighboring fluid particles, and therefore no discontinuities are allowed at the fluid-solid interface. In other words, the fluid velocity must be zero relative to the surface,

and the fluid temperature must be equal to that of the surface. However, strictly speaking those two boundary conditions are valid only if the fluid flow adjacent to the surface is in thermodynamic equilibrium. This requires an infinitely high frequency of collisions between the fluid and the solid surface. In practice, the no-slip and no-temperature-jump conditions lead to fairly accurate predictions as long as Knudsen numbers are less than 0.001. Beyond that, the collision frequency is simply not high enough to ensure equilibrium, and a certain degree of velocity slip and temperature jump must be allowed. The non-continuum effects become important gradually with increased Knudsen number. The no-slip and no-temperature-jump boundary conditions are just an empirical finding. These boundary conditions are generally valid for macroscopic flows in which the continuum holds and the molecular nature of the fluid is not apparent at the length scales of the flow.

One of the most fundamental problems in fluid dynamics is that of laminar flow in circular and non-circular channels under constant pressure gradient. Upon obtaining the velocity distribution $u(x, y)$ and mean velocity \bar{u} , the friction factor Reynolds number parameter may be defined using the simple expression denoted in some texts as the Poiseuille number:

$$Po_\ell = \frac{\tau_\ell}{\mu \bar{u}} = \frac{\left(-\frac{A}{P} \frac{dp}{dz} \right)_\ell}{\mu \bar{u}} = \frac{f \text{Re}_\ell}{2} \quad (4.1)$$

The above grouping Po is interpreted as the dimensionless average wall shear. The mean wall shear stress may also be related to the pressure gradient by means of the force balance $\bar{\tau} = -A/P dp/dz$.

Using the method of scale analysis, we examine the momentum equation and consider the various force balances. Considering the force balance between the friction and pressure forces for a long microchannel:

$$\frac{\Delta p}{L} \sim \frac{\mu U}{D_h^2} \quad (4.2)$$

then, the incompressible flow criterion for microchannel flows can be obtained:

$$\frac{\Delta p}{p} = \frac{\Delta \rho}{\rho} \sim \frac{\mu UL}{\rho RT D_h^2} \sim \frac{LMa^2}{D_h Re_{D_h}} \sim \frac{L}{D_h} Kn^2 Re_{D_h} \ll 1 \quad (4.3)$$

where we have employed ideal gas equation of state $p=\rho RT$ and $Kn \approx Ma/Re$ and assumed that the flow is isothermal. As the pressure drop is owing to viscous effects and not to any free expansion of the gas, the isothermal assumption should be reasonable. Therefore, in microchannel flows which are dominated by viscous effects, density changes may be significant even though the Mach number is very small. The gas flow through a microchannel can be considered incompressible when the Reynolds number is very low with comparatively high Knudsen numbers or the Knudsen number is small with moderate Reynolds numbers.

Comparing the scale between friction and inertial forces we obtain the following relation:

$$\frac{\mu \frac{\partial^2 u}{\partial y^2}}{\rho u \frac{\partial u}{\partial x}} \sim \frac{\mu \frac{U}{D_h^2}}{\frac{\rho U^2}{L}} = \frac{L}{D_h \text{Re}_{D_h}} = L^+ \quad (4.4)$$

This analysis demonstrates that inertial forces are only important for short ducts $L^+ \ll 1$.

4.2 Slip Flow in Elliptic Microchannels

Kennard [88] studied internal flows with slip in the circular tube and parallel-plate channel. Ebert and Sparrow [99] performed an analysis to determine the velocity and pressure drop characteristics of slip flow in rectangular and annular ducts. No attempt has been made for solving the same problem in elliptic microchannels. With the development of microscale thermal fluid systems, there is a need to investigate slip flow in elliptic microchannels. Slip flow in elliptic microchannels will be examined first and a detailed theoretical analysis will be performed. Later a simple model for many duct shapes will be developed.

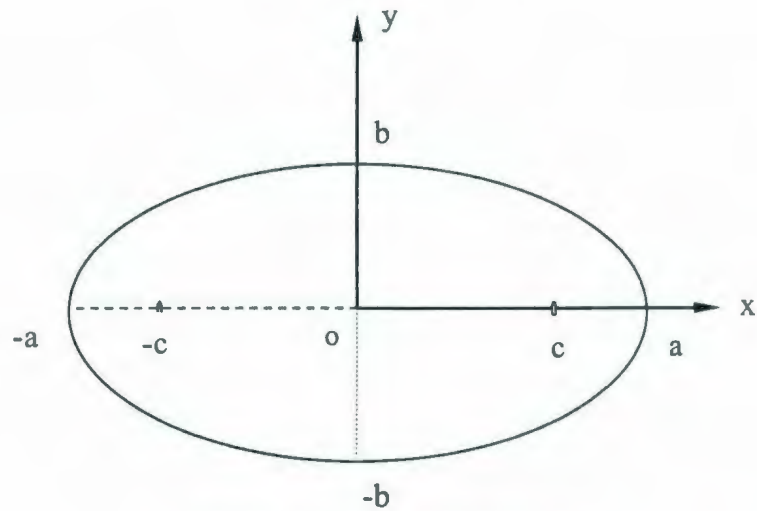


Figure 4.1 An elliptic duct.

4.2.1 Theoretical Analysis

A schematic diagram of the elliptic cross section with coordinates and other dimensional nomenclature is shown in Figure 4.1. The starting point of the analysis is the law of conservation of momentum. When $L^+ \gg 1$, the continuum flow momentum equation reduces to the form

$$\frac{\partial^2 u}{\partial x^2} + \frac{\partial^2 u}{\partial y^2} = \frac{1}{\mu} \frac{dp}{dz} \quad (4.5)$$

It is convenient to use elliptic cylinder coordinates [100,101] to facilitate the solution process. The metric coefficients for this system of coordinates are

$$g_1 = g_2 = c^2 (\cosh^2 \eta - \cos^2 \psi) \quad (4.6)$$

$$g_3 = 1 \quad (4.7)$$

The elemental distance for this coordinate system is [100,101]

$$ds_1 = c(\cosh^2 \eta - \cos^2 \psi)^{1/2} d\eta \quad (4.8)$$

$$ds_2 = c(\cosh^2 \eta - \cos^2 \psi)^{1/2} d\psi \quad (4.9)$$

In elliptic cylinder coordinates, the momentum equation becomes

$$\frac{\partial^2 u}{\partial \eta^2} + \frac{\partial^2 u}{\partial \psi^2} = \frac{c^2}{\mu} \frac{dp}{dz} (\cosh^2 \eta - \cos^2 \psi) \quad (4.10)$$

The velocity distribution must satisfy the slip boundary condition at the walls. The local slip velocity is proportional to the local velocity gradient normal to the wall. In elliptic cylinder coordinates, the boundary conditions assuming a one quarter basic cell, are:

$$\frac{1}{\sqrt{g_2}} \frac{\partial u}{\partial \psi} = 0 \quad \text{at } \psi = 0 \quad (4.11)$$

$$\frac{1}{\sqrt{g_2}} \frac{\partial u}{\partial \psi} = 0 \quad \text{at } \psi = \frac{\pi}{2} \quad (4.12)$$

$$\frac{1}{\sqrt{g_1}} \frac{\partial u}{\partial \eta} = 0 \quad \text{at } \eta = 0 \quad (4.13)$$

$$u = -\frac{\lambda \frac{2-\sigma}{\sigma}}{\sqrt{g_1}} \frac{\partial u}{\partial \eta} \quad \text{at } \eta = \eta_0 \quad (4.14)$$

where λ is the molecular mean free path. The constant σ denotes tangential momentum accommodation coefficient, which has values that typically lie between 0.87 and 1 [102]. Although the nature of the tangential momentum accommodation coefficients is still an active research problem, almost all evidence indicates that for most gas-solid interactions the coefficients are approximately 1.0. The same procedure is valid even if $\sigma \neq 1$, defining a modified Knudsen number as $Kn^* = Kn(2-\sigma)/\sigma$.

The parameter η_0 is related to the major and minor axes through

$$\eta_0 = \ln \frac{1 + \frac{b}{a}}{\sqrt{1 - \left(\frac{b}{a}\right)^2}} \quad (4.15)$$

The half focal length of an ellipse c , is defined such that

$$c = \frac{a}{\cosh \eta_0} = \frac{b}{\sinh \eta_0} \quad (4.16)$$

Equation (4.10) may be solved using the separation of variables method [100], assuming that

$$u(\eta, \psi) = \phi(\eta, \psi) + F(\eta) + G(\psi) \quad (4.17)$$

After differentiating twice with respect to η and ψ we get

$$\begin{aligned} \frac{\partial^2 u}{\partial \eta^2} &= \frac{\partial^2 \phi}{\partial \eta^2} + \frac{\partial^2 F}{\partial \eta^2} \\ \frac{\partial^2 u}{\partial \psi^2} &= \frac{\partial^2 \phi}{\partial \psi^2} + \frac{\partial^2 G}{\partial \psi^2} \end{aligned} \quad (4.18)$$

Substitution of Eq. (4.18) into Eq. (4.10) gives

$$\frac{\partial^2 \phi}{\partial \eta^2} + \frac{\partial^2 \phi}{\partial \psi^2} + \frac{\partial^2 F}{\partial \eta^2} + \frac{\partial^2 G}{\partial \psi^2} = \frac{c^2}{\mu} \frac{dp}{dz} (\cosh^2 \eta - \cos^2 \psi) \quad (4.19)$$

Laplace's equation, $\nabla^2 \phi = 0$, can be obtained by letting

$$\begin{aligned}\frac{\partial^2 F}{\partial \eta^2} &= \frac{c^2}{2\mu} \frac{dp}{dz} \cosh 2\eta \\ \frac{\partial^2 G}{\partial \psi^2} &= -\frac{c^2}{2\mu} \frac{dp}{dz} \cos 2\psi\end{aligned}\tag{4.20}$$

Integrating both expressions of Eq. (4.20) twice yields the following substitutions for $F(\eta)$ and $G(\psi)$:

$$\begin{aligned}F(\eta) &= \frac{c^2}{8\mu} \frac{dp}{dz} \cosh 2\eta \\ G(\psi) &= \frac{c^2}{8\mu} \frac{dp}{dz} \cos 2\psi\end{aligned}\tag{4.21}$$

After applying separation of variables to $\phi(\eta, \psi)$, the solution of the Laplace equation is

$$\phi(\eta, \psi) = [A \cos(\delta\psi) + B \sin(\delta\psi)][C \cosh(\delta\eta) + D \sinh(\delta\eta)]\tag{4.22}$$

The solution for $u(\eta, \psi)$ is the sum of the solution of the Laplace equation, $\nabla^2 \phi = 0$, and of Eq. (4.21); therefore we have

$$u = [A \cos(\delta\psi) + B \sin(\delta\psi)][C \cosh(\delta\eta) + D \sinh(\delta\eta)] + \frac{c^2}{8\mu} \frac{dp}{dz} (\cosh 2\eta + \cos 2\psi)\tag{4.23}$$

According to the boundary condition, Eq. (4.11)

$$B = 0$$

In terms of the boundary condition, Eq. (4.13)

$$D = 0$$

From the boundary condition, Eq. (4.12)

$$\delta_n = n \quad n = 0, 2, 4, 6 \dots (\text{even})$$

in which the δ_n are a set of eigenvalues. Therefore, the solution of this problem becomes

$$u = \sum_{n=0, \text{even}}^{\infty} C_n \cos(n\psi) \cosh(n\eta) + \frac{c^2}{8\mu} \frac{dp}{dz} (\cosh 2\eta + \cos 2\psi) \quad (4.24)$$

and

$$\frac{\partial u}{\partial \eta} = \sum_{n=1}^{\infty} C_n n \cos(n\psi) \sinh(n\eta) + \frac{c^2}{8\mu} \frac{dp}{dz} 2 \sinh 2\eta$$

Applying the final boundary condition, Eq. (4.14)

$$\begin{aligned} & \sum_{n=0, \text{even}}^{\infty} C_n \cos(n\psi) \left[\cosh(n\eta_0) + \frac{\lambda \frac{2-\sigma}{\sigma}}{c(\cosh^2 \eta_0 - \cos^2 \psi)^{1/2}} n \sinh(n\eta_0) \right] \\ &= -\frac{c^2}{8\mu} \frac{dp}{dz} \left(\cosh 2\eta_0 + \cos 2\psi + 2 \frac{\lambda \frac{2-\sigma}{\sigma}}{c(\cosh^2 \eta_0 - \cos^2 \psi)^{1/2}} \sinh(2\eta_0) \right) \end{aligned}$$

a solution for C_n may be obtained by means of a Fourier expansion.

In order to overcome the difficulty caused by the metric coefficient, we use a binomial series to approximate the metric coefficient and take the first three terms:

$$(1+x)^a = 1 + \sum_{n=1}^{\infty} \frac{a(a-1)(a-2)\cdots(a-n+1)}{n!} x^n \quad -1 < x < 1$$

The metric coefficient may now be written as:

$$\frac{1}{\sqrt{g_1}} = \frac{1}{c(\cosh^2 \eta_0 - \cos^2 \psi)^{1/2}} = \frac{1}{c \cosh(\eta_0) \left(1 - \frac{\cos^2 \psi}{\cosh^2 \eta_0}\right)^{1/2}} \approx \frac{1 + \frac{1}{2} \frac{\cos^2 \psi}{\cosh^2 \eta_0} + \frac{3}{8} \frac{\cos^4 \psi}{\cosh^4 \eta_0}}{c \cosh(\eta_0)} \quad (4.25)$$

assuming a three term expansion.

From orthogonality principles, we get

$$C_n' = \frac{\int_0^{2\pi} -\frac{c^2}{8\mu} \frac{dp}{dz} \left(\cosh 2\eta_0 + \cos 2\psi + 2\lambda \frac{2-\sigma}{\sigma} \frac{1 + \frac{1}{2} \frac{\cos^2 \psi}{\cosh^2 \eta_0} + \frac{3}{8} \frac{\cos^4 \psi}{\cosh^4 \eta_0}}{c \cosh(\eta_0)} \sinh(2\eta_0) \right) \cos(n\psi) d\psi}{\int_0^{2\pi} \left[\cosh(n\eta_0) + \lambda \frac{2-\sigma}{\sigma} \frac{1 + \frac{1}{2} \frac{\cos^2 \psi}{\cosh^2 \eta_0} + \frac{3}{8} \frac{\cos^4 \psi}{\cosh^4 \eta_0}}{c \cosh(\eta_0)} n \sinh(n\eta_0) \right] \cos^2(n\psi) d\psi}$$

and

$$C_0' = -\frac{c^2}{8\mu} \frac{dp}{dz} \left[\cosh 2\eta_0 + 2\lambda \frac{2-\sigma}{\sigma} \frac{1 + \frac{1}{4} \frac{\cos^2 \psi}{\cosh^2 \eta_0} + \frac{9}{64} \frac{\cos^4 \psi}{\cosh^4 \eta_0}}{c \cosh(\eta_0)} \sinh(2\eta_0) \right]$$

$$C_2' = -\frac{c^2}{8\mu} \frac{dp}{dz} \frac{\frac{1+2\lambda}{\sigma} \left[\frac{1}{4c \cosh^3(\eta_0)} + \frac{3}{16c \cosh^5(\eta_0)} \right] \sinh(2\eta_0)}{\cosh(2\eta_0) + 2\lambda \frac{2-\sigma}{\sigma} \frac{1+\frac{1}{4 \cosh^2 \eta_0} + \frac{21}{128 \cosh^4 \eta_0}}{c \cosh(\eta_0)} \sinh(2\eta_0)}$$

$$C_4' = -\frac{c^2}{8\mu} \frac{dp}{dz} \frac{\lambda \frac{2-\sigma}{\sigma} \frac{3}{32c \cosh^5(\eta_0)} \sinh(2\eta_0)}{\cosh(4\eta_0) + 4\lambda \frac{2-\sigma}{\sigma} \frac{1+\frac{1}{4 \cosh^2 \eta_0} + \frac{9}{64 \cosh^4 \eta_0}}{c \cosh(\eta_0)} \sinh(4\eta_0)}$$

$$C_6' = C_8' = C_{10}' = \dots = 0$$

The solution of this problem becomes:

$$\begin{aligned} u = & -\frac{c^2}{8\mu} \frac{dp}{dz} \left[\cosh 2\eta_0 + 2\lambda \frac{2-\sigma}{\sigma} \frac{1+\frac{1}{4 \cosh^2 \eta_0} + \frac{9}{64 \cosh^4 \eta_0}}{c \cosh(\eta_0)} \sinh(2\eta_0) \right] \\ & -\frac{c^2}{8\mu} \frac{dp}{dz} \frac{\frac{1+2\lambda}{\sigma} \left[\frac{1}{4c \cosh^3(\eta_0)} + \frac{3}{16c \cosh^5(\eta_0)} \right] \sinh(2\eta_0)}{\cosh(2\eta_0) + 2\lambda \frac{2-\sigma}{\sigma} \frac{1+\frac{1}{4 \cosh^2 \eta_0} + \frac{21}{128 \cosh^4 \eta_0}}{c \cosh(\eta_0)} \sinh(2\eta_0)} \cos(2\psi) \cosh(2\eta) \\ & -\frac{c^2}{8\mu} \frac{dp}{dz} \frac{\lambda \frac{2-\sigma}{\sigma} \frac{3}{32c \cosh^5(\eta_0)} \sinh(2\eta_0)}{\cosh(4\eta_0) + 4\lambda \frac{2-\sigma}{\sigma} \frac{1+\frac{1}{4 \cosh^2 \eta_0} + \frac{9}{64 \cosh^4 \eta_0}}{c \cosh(\eta_0)} \sinh(4\eta_0)} \cos(4\psi) \cosh(4\eta) \\ & + \frac{c^2}{8\mu} \frac{dp}{dz} (\cosh 2\eta + \cos 2\psi) \end{aligned} \tag{4.26}$$

The eccentricity of the ellipse is defined as:

$$e = \sqrt{1 - \left(\frac{b}{a}\right)^2} \quad (4.27)$$

and the hydraulic diameter as:

$$D_h = \frac{\pi b}{E(e)} \quad (4.28)$$

where $E(e)$ is the complete elliptical integral of the second kind [103]. The characteristic length scale in the present analysis is defined as the hydraulic diameter ($2b < D_h \leq \pi b$), such that:

$$Kn = \frac{\lambda}{D_h} = \frac{\lambda}{\frac{\pi b}{E(e)}} \quad (4.29)$$

Finally, the velocity distribution is as follows:

$$\begin{aligned}
u = & -\frac{c^2}{8\mu} \frac{dp}{dz} \left[\cosh 2\eta_0 + 2 \frac{\pi b K n_{D_h}}{E(e)} \frac{2-\sigma}{\sigma} \frac{1 + \frac{1}{4 \cosh^2 \eta_0} + \frac{9}{64 \cosh^4 \eta_0}}{c \cosh(\eta_0)} \sinh(2\eta_0) \right] \\
& - \frac{c^2}{8\mu} \frac{dp}{dz} \frac{1 + 2 \frac{\pi b K n_{D_h}}{E(e)} \frac{2-\sigma}{\sigma} \left[\frac{1}{4c \cosh^3(\eta_0)} + \frac{3}{16c \cosh^5(\eta_0)} \right] \sinh(2\eta_0)}{\cosh(2\eta_0) + 2 \frac{\pi b K n_{D_h}}{E(e)} \frac{2-\sigma}{\sigma} \frac{1 + \frac{1}{4 \cosh^2 \eta_0} + \frac{21}{128 \cosh^4 \eta_0}}{c \cosh(\eta_0)} \sinh(2\eta_0)} \cos(2\psi) \cosh(2\eta) \\
& - \frac{c^2}{8\mu} \frac{dp}{dz} \frac{\frac{\pi b K n_{D_h}}{E(e)} \frac{2-\sigma}{\sigma} \frac{3}{32c \cosh^5(\eta_0)} \sinh(2\eta_0)}{\cosh(4\eta_0) + 4 \frac{\pi b K n_{D_h}}{E(e)} \frac{2-\sigma}{\sigma} \frac{1 + \frac{1}{4 \cosh^2 \eta_0} + \frac{9}{64 \cosh^4 \eta_0}}{c \cosh(\eta_0)} \sinh(4\eta_0)} \cos(4\psi) \cosh(4\eta) \\
& + \frac{c^2}{8\mu} \frac{dp}{dz} (\cosh 2\eta + \cos 2\psi)
\end{aligned} \tag{4.30}$$

In the limit of $Kn \rightarrow 0$, Eq. (4.30) reduces to its continuum flow solution [104]:

$$u = -\frac{c^2}{8\mu} \frac{dp}{dz} \left[\cosh 2\eta_0 + \frac{1}{\cosh 2\eta_0} \cos(2\psi) \cosh(2\eta) - \cosh(2\eta) - \cos(2\psi) \right] \tag{4.31}$$

The mean velocity is found by integration of Eq. (4.30) across the section of the duct

$$\bar{u} = \frac{1}{A} \int u dA = \frac{\int u ds_1 ds_2}{\int ds_1 ds_2} = \frac{\int_0^{\eta_0} \int_0^{2\pi} u c^2 (\cosh^2 \eta - \cos^2 \psi) d\eta d\psi}{\int_0^{\eta_0} \int_0^{2\pi} c^2 (\cosh^2 \eta - \cos^2 \psi) d\eta d\psi} = \frac{\int_0^{\eta_0} \int_0^{2\pi} u c^2 (\cosh^2 \eta - \cos^2 \psi) d\eta d\psi}{\pi ab} \tag{4.32}$$

We can define the Poiseuille number using the above equations:

$$Po_{D_h} = \frac{\bar{r}D_h}{\mu \bar{u}} = \frac{\left(-\frac{A}{P} \frac{dp}{dz} \right) D_h}{\mu \bar{u}} = \frac{-\frac{dp}{dz} \left(\frac{\pi b}{E(e)} \right)^2}{4\mu \bar{u}} \quad (4.33)$$

The solution can be obtained using commercially available algebraic software tools, such as Maple 9 [105].

The mass flow rate in the microchannel is given by using the equation of state and assuming $Po = Po_c / (1 + \alpha Kn^*)$ which is discussed later in this section:

$$\dot{m} = \rho \bar{u} A = -\frac{\pi ab \left(\frac{\pi b}{E(e)} \right)^2}{4\mu Po_c RT} \frac{dp}{dz} \left(p + \alpha \frac{2-\sigma}{\sigma} pKn \right) \quad (4.34)$$

We can use $pKn = p_o Kn_o$ since pKn is constant for isothermal flow. Integrating Eq. (4.34), we obtain

$$\dot{m} = \rho \bar{u} A = \frac{\pi ab p_o^2 \left(\frac{\pi b}{E(e)} \right)^2}{8\mu Po_c RT z} \left[\frac{p_i^2}{p_o^2} - \frac{p_z^2}{p_o^2} + 2\alpha \frac{2-\sigma}{\sigma} Kn_o \left(\frac{p_i}{p_o} - \frac{p_z}{p_o} \right) \right] \quad (4.35)$$

Letting $z = L$ gives:

$$\dot{m} = \rho \bar{u} A = \frac{\pi ab p_o^2 \left(\frac{\pi b}{E(e)} \right)^2}{8\mu Po_c R T L} \left[\frac{p_i^2}{p_o^2} - 1 + 2\alpha \frac{2-\sigma}{\sigma} Kn_o \left(\frac{p_i}{p_o} - 1 \right) \right] \quad (4.36)$$

The continuum flow mass flow rate is given by:

$$\dot{m}_c = \rho \bar{u} A = \frac{\pi ab p_o^2 \left(\frac{\pi b}{E(e)} \right)^2}{8\mu P o_c R T L} \left(\frac{p_i^2}{p_o^2} - 1 \right) \quad (4.37)$$

The effect of slip may be illustrated clearly by dividing the slip flow mass flow Eq. (4.36) by the continuum mass flow Eq. (4.37)

$$\frac{\dot{m}}{\dot{m}_c} = 1 + \frac{\frac{2\alpha \frac{2-\sigma}{\sigma} Kn_o}{\frac{p_i}{p_o} + 1}}{\frac{p_i}{p_o}} \quad (4.38)$$

It is seen that the rarefaction increases the mass flow and that the effect of rarefaction becomes more significant when the pressure ratio decreases. By including the slip velocity at the wall, one adds another term to the mass flow equation; therefore, the mass flow rate for a given inlet and outlet pressure always increases due to the effect of slip. This could be interpreted as a decrease of the gas viscosity.

Combining Eq. (4.35) and Eq. (4.36), we obtain the expression for pressure distribution:

$$\frac{p_z}{p_o} = -\alpha \frac{2-\sigma}{\sigma} Kn_o + \sqrt{\left(\alpha \frac{2-\sigma}{\sigma} Kn_o + \frac{p_i}{p_o} \right)^2 - \left[\frac{p_i^2}{p_o^2} - 1 + 2\alpha \frac{2-\sigma}{\sigma} Kn_o \left(\frac{p_i}{p_o} - 1 \right) \right] \frac{z}{L}} \quad (4.39)$$

4.2.2 Results and Discussion

Table 4.1 presents a comparison of the Poiseuille number results using one to four terms of the binomial series approximation respectively. For the practical application

range $\varepsilon > 0.1$, taking first three terms to obtain the Poiseuille number is accurate enough.

More terms should be used when aspect ratio ε is comparatively small and Knudsen number is comparatively large.

Table 4.1 A comparison of the Po using one to four terms of binomial series approximation.

| ε | Po ($Kn^* = 0.1$) | | | | Po ($Kn^* = 0.01$) | | | |
|---------------|-----------------------|---|---|---|------------------------|---|---|---|
| | 1 term 1 | 2 terms $1 + \frac{1}{2} \frac{\cos^2 \psi}{\cosh^2 \eta_0}$ | 3 terms $1 + \frac{1}{2} \frac{\cos^2 \psi}{\cosh^2 \eta_0} + \dots$ | 4 terms $1 + \frac{1}{2} \frac{\cos^2 \psi}{\cosh^2 \eta_0} + \dots$ | 1 term 1 | 2 terms $1 + \frac{1}{2} \frac{\cos^2 \psi}{\cosh^2 \eta_0}$ | 3 terms $1 + \frac{1}{2} \frac{\cos^2 \psi}{\cosh^2 \eta_0} + \dots$ | 4 terms $1 + \frac{1}{2} \frac{\cos^2 \psi}{\cosh^2 \eta_0} + \dots$ |
| 0.1 | 5.03 | 4.66 | 4.49 | 4.38 | 8.84 | 8.72 | 8.66 | 8.62 |
| 0.2 | 4.96 | 4.61 | 4.46 | 4.36 | 8.54 | 8.43 | 8.38 | 8.34 |
| 0.3 | 4.91 | 4.58 | 4.44 | 4.36 | 8.25 | 8.16 | 8.11 | 8.08 |
| 0.4 | 4.86 | 4.56 | 4.44 | 4.37 | 8.01 | 7.92 | 7.88 | 7.86 |
| 0.5 | 4.82 | 4.54 | 4.44 | 4.39 | 7.82 | 7.74 | 7.71 | 7.69 |
| 0.6 | 4.77 | 4.52 | 4.44 | 4.41 | 7.67 | 7.60 | 7.58 | 7.57 |
| 0.7 | 4.70 | 4.49 | 4.44 | 4.42 | 7.57 | 7.51 | 7.50 | 7.49 |
| 0.8 | 4.63 | 4.47 | 4.44 | 4.43 | 7.57 | 7.45 | 7.44 | 7.44 |
| 0.9 | 4.54 | 4.45 | 4.44 | 4.44 | 7.44 | 7.42 | 7.42 | 7.41 |
| 1 | 4.44 | 4.44 | 4.44 | 4.44 | 7.41 | 7.41 | 7.41 | 7.41 |

Table 4.2 Poiseuille number results for elliptic ducts.

| ε | Po | | | |
|---------------|------------|---------------|---------------|--------------|
| | $Kn^* = 0$ | $Kn^* = 0.01$ | $Kn^* = 0.05$ | $Kn^* = 0.1$ |
| 0.1 | 9.657 | 8.657 | 6.125 | 4.490 |
| 0.2 | 9.301 | 8.379 | 6.012 | 4.457 |
| 0.3 | 8.948 | 8.110 | 5.917 | 4.443 |
| 0.4 | 8.647 | 7.884 | 5.846 | 4.440 |
| 0.5 | 8.412 | 7.709 | 5.795 | 4.440 |
| 0.6 | 8.239 | 7.582 | 5.759 | 4.440 |
| 0.7 | 8.122 | 7.496 | 5.735 | 4.439 |
| 0.8 | 8.049 | 7.442 | 5.721 | 4.440 |
| 0.9 | 8.011 | 7.415 | 5.715 | 4.443 |
| 1 | 8.000 | 7.407 | 5.714 | 4.444 |

Table 4.2 shows the Poiseuille number results for different aspect ratio ε and Kn . The Po values decrease with an increase of Kn for the same aspect ratio. The Po values decrease with an increase of ε for the same Kn .

The Poiseuille number results can be presented conveniently in terms of normalized Poiseuille number. Furthermore, the effects of slip are illustrated clearly by plotting the ratio Po/Po_c as a function of the Knudsen number and aspect ratio, where Po_c represents the continuum flow value. Figure 4.2 shows the normalized Poiseuille number results for elliptic ducts as a function of aspect ratio ε and Kn . From an inspection of the graphs, it is seen that Po decreases as the rarefaction becomes greater.

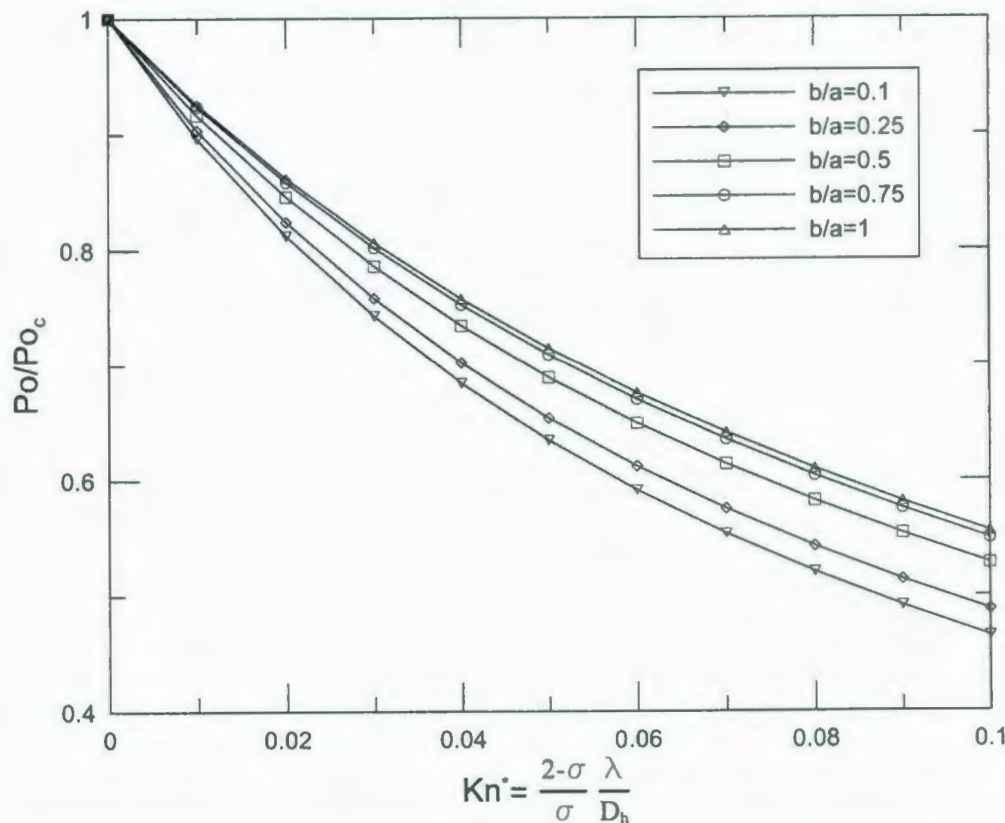


Figure 4.2 Normalized Po results as a function of aspect ratio ε and Kn .

The Poiseuille number reduction depends on the geometry of the cross-section. It is convenient that the Poiseuille number results are expressible to good accuracy by the relation

$$\frac{Po}{Po_c} = \frac{1}{1 + \alpha \frac{2 - \sigma}{\sigma} Kn} \quad (4.40)$$

in which α depends on the duct geometry. For other geometries, $\alpha = 12$ for the parallel plate and $\alpha = 8$ for the circular tube.

For an elliptic duct, the constants, α , are derived from a least-square fit of the Poiseuille number results (Figures 4.2). It is found that the maximum error incurred by using these constants in Eq. (4.40) is less than 0.3 %. The error is much smaller and negligible for most cases i.e. < 0.05%. The constants α are listed in Table 4.3 and the data points are fitted to a simple correlation:

$$\alpha = 12.53 - 9.41\varepsilon + 4.87\varepsilon^2 \quad (4.41)$$

then

$$\frac{Po}{Po_c} = \frac{1}{1 + (12.53 - 9.41\varepsilon + 4.87\varepsilon^2) \frac{2 - \sigma}{\sigma} Kn} \quad (4.42)$$

where $Po_c = (1 + \varepsilon^2) (\pi/E(e))^2$, see Shah and London [106].

Table 4.3 The constants α for the Poiseuille number ratio.

| ε | α |
|---------------|----------|
| 0.1 | 11.522 |
| 0.15 | 11.242 |
| 0.2 | 10.911 |
| 0.25 | 10.556 |
| 0.3 | 10.196 |
| 0.4 | 9.531 |
| 0.5 | 8.989 |
| 0.6 | 8.587 |
| 0.75 | 8.211 |
| 0.85 | 8.076 |
| 1 | 8 |

Therefore, using the simple expression Eq. (4.42), the Poiseuille number results can be easily obtained. As a further proof of the reliability of the proposed solution, Eq. (4.33), all the numerical results obtained in slip flow reduce to their continuum flow limits in the limit of $Kn \rightarrow 0$ [106]. Moreover, the limit of Eq. (4.33) for $b/a \rightarrow 1$ corresponds to the circular tube solution.

Figure 4.3 shows the pressure distribution with and without rarefaction predicted by Eq. (4.39) for different pressure ratios. The pressure distribution exhibits a nonlinear behavior due to the compressibility effect. The pressure drop required is less than that in a conventional channel. The deviations of the pressure distribution from the linear distribution decrease with an increase in Knudsen number. The nonlinearity increases as the pressure ratio increases. The effects of compressibility and rarefaction are opposite as Karniadakis et al. [1] demonstrated.

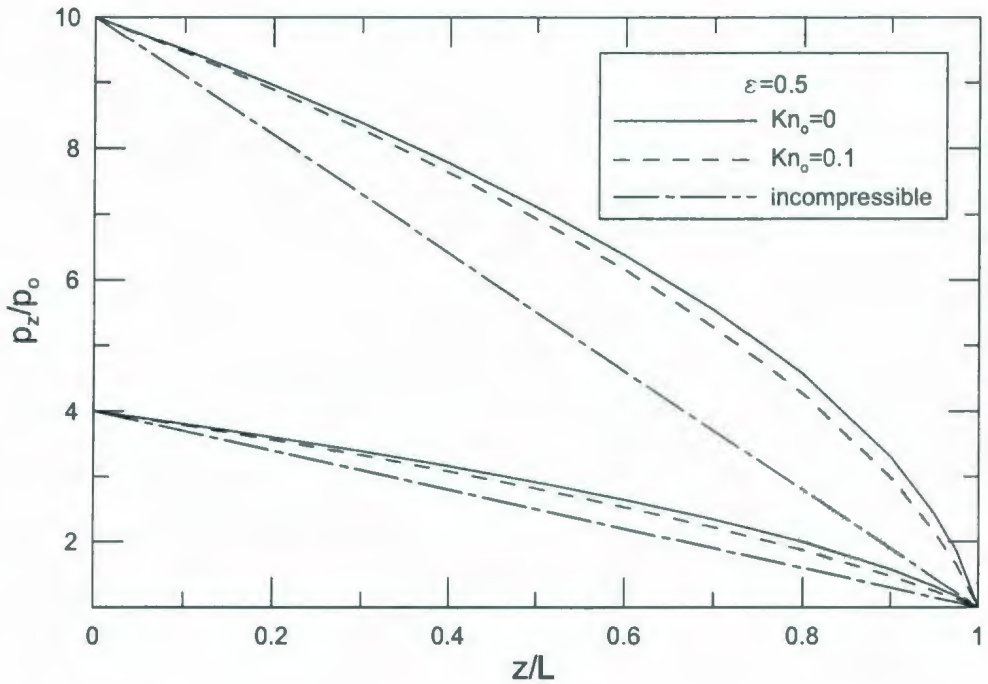


Figure 4.3 The pressure distribution for different pressure ratios [107].

Slip flow in elliptic microchannels has been examined and a detailed theoretical analysis has been performed. An analytical solution of Poiseuille number was obtained using separation of variables in elliptic cylinder coordinates. A simple model [Eq. (4.42)] was developed for predicting the Poiseuille number in elliptic microchannels for slip flow. The accuracy of the proposed simple model was found to be within 2 percent of exact values. The developed model may be used to predict mass flow rate and pressure distribution of slip flow in elliptic microchannels.

4.3 Slip Flow in Other Non-Circular Microchannels

The non-circular cross sections such as rectangular, triangular, and trapezoidal, are common channel shapes that may be produced by microfabrication. These cross sections have extensive practical applications in MEMS [1-5]. Muzychka and Yovanovich [94] developed a simple model for predicting the friction factor Reynolds number product in non-circular ducts for fully developed laminar continuum flow. Later, we will show that Muzychka and Yovanovich's approach can be extended to the slip flow regime.

4.3.1 Rectangular Ducts

We may now examine the solution for rectangular ducts for slip flow. A schematic diagram of the rectangular cross section is shown in Figure 4.4. When $L^+ \gg 1$, the continuum flow momentum equation in Cartesian coordinates reduces to the form

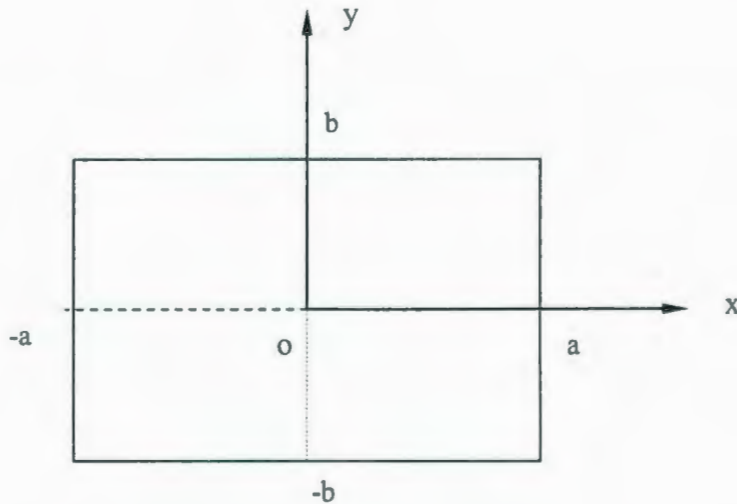


Figure 4.4 A rectangular duct.

$$\frac{\partial^2 u}{\partial x^2} + \frac{\partial^2 u}{\partial y^2} = \frac{1}{\mu} \frac{dp}{dz} \quad (4.43)$$

The velocity distribution must satisfy the slip boundary condition at the walls. The local slip velocity is proportional to the local velocity gradient normal to the wall. Due to symmetry, the boundary conditions are

$$u = -\lambda \frac{2-\sigma}{\sigma} \frac{\partial u}{\partial y} \quad \text{at } y = b, \quad 0 \leq x < a \quad (4.44)$$

$$u = -\lambda \frac{2-\sigma}{\sigma} \frac{\partial u}{\partial x} \quad \text{at } x = a, \quad 0 \leq y < b \quad (4.45)$$

$$\frac{\partial u}{\partial y} = 0 \quad \text{at } y = 0, \quad 0 \leq x \leq a \quad (4.46)$$

$$\frac{\partial u}{\partial x} = 0 \quad \text{at } x = 0, \quad 0 \leq y \leq b \quad (4.47)$$

It is convenient to rewrite the momentum equation and the boundary conditions

$$\varepsilon^2 \frac{\partial^2 u}{\partial \left(\frac{x}{a}\right)^2} + \frac{\partial^2 u}{\partial \left(\frac{y}{b}\right)^2} = \frac{b^2}{\mu} \frac{dp}{dz} \quad (4.48)$$

where $\varepsilon = b/a$, the ratio of minor and major axes.

$$u = -\frac{\lambda}{b} \frac{2-\sigma}{\sigma} \frac{\partial u}{\partial \left(\frac{y}{b}\right)} \quad \text{at } \frac{y}{b} = 1, \quad 0 \leq \frac{x}{a} < 1 \quad (4.49)$$

$$u = -\frac{\lambda}{a} \frac{2-\sigma}{\sigma} \frac{\partial u}{\partial \left(\frac{x}{a} \right)} \quad \text{at} \quad \frac{x}{a} = 1, \quad 0 \leq \frac{y}{b} < 1 \quad (4.50)$$

$$\frac{\partial u}{\partial \left(\frac{y}{b} \right)} = 0 \quad \text{at} \quad \frac{y}{b} = 0, \quad 0 \leq \frac{x}{a} \leq 1 \quad (4.51)$$

$$\frac{\partial u}{\partial \left(\frac{x}{a} \right)} = 0 \quad \text{at} \quad \frac{x}{a} = 0, \quad 0 \leq \frac{y}{b} \leq 1 \quad (4.52)$$

Following Ebert and Sparrow [99], using Method of Eigenfunction Expansions, a solution of the velocity may be assumed as follows:

$$u = \frac{b^2}{\mu} \frac{dp}{dz} \sum_{n=1}^{\infty} X_n \left(\frac{x}{a} \right) \cos \left(\delta_n \frac{y}{b} \right) \quad (4.53)$$

in which the δ_n are a set of eigenvalues, the X_n are a set of functions of x/a , and the $\cos(\delta_n y/b)$ are a set of eigenfunctions. This solution satisfies the boundary condition, Eq. (4.51). Furthermore, substituting the velocity solution into the boundary condition, Eq. (4.49), we obtain

$$\delta_n \tan \delta_n = \frac{b}{\frac{2-\sigma}{\sigma} \lambda} \quad (4.54)$$

The characteristic length scale in the present analysis is defined as the hydraulic diameter.

$$Kn_{D_h} = \frac{\lambda}{D_h} = \frac{\lambda}{\frac{4b}{1+\varepsilon}} \quad (4.55)$$

Thus,

$$\delta_n \tan \delta_n = \frac{1}{\frac{2-\sigma}{\sigma} \frac{4}{1+\varepsilon} Kn_{D_h}} \quad (4.56)$$

The eigenvalues, δ_n , can be obtained from Eq. (4.56).

In order to determine unknown $X_n(x/a)$, the right-hand side of Eq. (4.48) should also expand in terms of eigenfunctions $\cos(\delta_n y/b)$

$$\frac{b^2}{\mu} \frac{dp}{dz} = \sum_1^\infty C_n \cos\left(\delta_n \frac{y}{b}\right) \quad (4.57)$$

Therefore, the Fourier coefficient becomes:

$$C_n = \frac{\frac{b^2}{\mu} \frac{dp}{dz} \int_0^1 \cos\left(\delta_n \frac{y}{b}\right) d\frac{y}{b}}{\int_0^1 \cos^2\left(\delta_n \frac{y}{b}\right) d\frac{y}{b}} = \frac{2 \frac{b^2}{\mu} \frac{dp}{dz} \sin \delta_n}{\delta_n + \sin \delta_n \cos \delta_n} \quad (4.58)$$

and Eq. (4.48) becomes

$$\varepsilon^2 \frac{\partial^2 u}{\partial \left(\frac{x}{a}\right)^2} + \frac{\partial^2 u}{\partial \left(\frac{y}{b}\right)^2} = \sum_{n=1}^\infty C_n \cos\left(\delta_n \frac{y}{b}\right) \quad (4.59)$$

Introducing Eq. (4.53) into Eq. (4.59), we find

$$X_n'' - \frac{1}{\varepsilon^2} \delta_n^2 X_n - \frac{1}{\varepsilon^2} \frac{2 \sin \delta_n}{\delta_n + \sin \delta_n \cos \delta_n} = 0 \quad (4.60)$$

The solution for X_n is

$$X_n = A_n \cosh\left(\frac{\delta_n x}{\varepsilon a}\right) + B_n \sinh\left(\frac{\delta_n x}{\varepsilon a}\right) - \frac{2 \sin \delta_n}{\delta_n^2 (\delta_n + \sin \delta_n \cos \delta_n)} \quad (4.61)$$

Substituting Eq. (4.61) into Eq. (4.53), we obtain

$$u = \frac{b^2}{\mu} \frac{dp}{dz} \sum_{n=1}^{\infty} \left[A_n \cosh\left(\frac{\delta_n x}{\varepsilon a}\right) + B_n \sinh\left(\frac{\delta_n x}{\varepsilon a}\right) - \frac{2 \sin \delta_n}{\delta_n^2 (\delta_n + \sin \delta_n \cos \delta_n)} \right] \cos\left(\delta_n \frac{y}{b}\right) \quad (4.62)$$

According to the boundary conditions Eqs. (4.50) and (4.52), we obtain

$$A_n = \frac{\frac{2 \sin \delta_n}{\delta_n^2 (\delta_n + \sin \delta_n \cos \delta_n)}}{\cosh\left(\frac{\delta_n}{\varepsilon}\right) + \frac{2-\sigma}{\sigma} \frac{\lambda}{b} \delta_n \sinh\left(\frac{\delta_n}{\varepsilon}\right)}$$

$$B_n = 0$$

Finally, the velocity distribution is as follows:

$$u = \frac{b^2}{\mu} \frac{dp}{dz} \sum_{n=1}^{\infty} \frac{2 \sin \delta_n \cos\left(\delta_n \frac{y}{b}\right)}{\delta_n^2 (\delta_n + \sin \delta_n \cos \delta_n)} \left[\frac{\cosh\left(\frac{\delta_n x}{\varepsilon a}\right)}{\cosh\left(\frac{\delta_n}{\varepsilon}\right) + \frac{2-\sigma}{\sigma} \frac{4}{1+\varepsilon} K n_{D_h} \delta_n \sinh\left(\frac{\delta_n}{\varepsilon}\right)} - 1 \right] \quad (4.63)$$

The mean velocity is found by integration of Eq. (4.63) across the section of the duct

$$\begin{aligned}\bar{u} &= \frac{1}{A} \int u dA = \int_0^1 \int_0^1 u d\frac{x}{a} d\frac{y}{b} \\ &= \frac{b^2}{\mu} \frac{dp}{dz} \sum_{n=1}^{\infty} \frac{2\varepsilon \sin^2 \delta_n}{\delta_n^4 (\delta_n + \sin \delta_n \cos \delta_n)} \left[\frac{\sinh\left(\frac{\delta_n}{\varepsilon}\right)}{\cosh\left(\frac{\delta_n}{\varepsilon}\right) + \frac{2-\sigma}{\sigma} \frac{4}{1+\varepsilon} Kn_{D_h} \delta_n \sinh\left(\frac{\delta_n}{\varepsilon}\right)} - \frac{\delta_n}{\varepsilon} \right] \quad (4.64)\end{aligned}$$

We can define the friction factor and Reynolds product from the above equations

$$\begin{aligned}f \text{Re}_{D_h} &= \frac{2 \left(-\frac{A}{P} \frac{dp}{dz} \right) D_h}{\mu \bar{u}} \\ &= \frac{4}{(1+\varepsilon)^2 \sum_{n=1}^{\infty} \frac{\varepsilon \sin^2 \delta_n}{\delta_n^4 (\delta_n + \sin \delta_n \cos \delta_n)} \left[\frac{\delta_n}{\varepsilon} - \frac{\sinh\left(\frac{\delta_n}{\varepsilon}\right)}{\cosh\left(\frac{\delta_n}{\varepsilon}\right) + \frac{2-\sigma}{\sigma} \frac{4}{1+\varepsilon} Kn_{D_h} \delta_n \sinh\left(\frac{\delta_n}{\varepsilon}\right)} \right]} \quad (4.65)\end{aligned}$$

The limit of Eq. (4.65) corresponds to a parallel-plate channel for $\varepsilon \rightarrow 0$:

$$f \text{Re}_{D_h} = \frac{24}{1 + \frac{2-\sigma}{\sigma} 12 Kn_{D_h}}$$

It can also be demonstrated that Eq. (4.65) reduces to its continuum flow limits as $Kn \rightarrow 0$:

$$\delta_n = (2n-1) \frac{\pi}{2} \quad \text{when } Kn \rightarrow 0$$

$$(f \text{Re}_{D_h})_c = \frac{24}{(1+\varepsilon)^2 \left[1 - 6 \sum_{n=1}^{\infty} \frac{\varepsilon}{\delta_n^5} \tanh\left(\frac{\delta_n}{\varepsilon}\right) \right]} \quad (4.66)$$

Moreover, the limit of Eq. (4.66) which corresponds to a parallel-plate channel for $\varepsilon \rightarrow 0$ is:

$$(f \text{Re}_{D_h})_c = 24 \quad \text{when} \quad \varepsilon \rightarrow 0$$

The friction factor Reynolds product fRe for slip flow in rectangular microchannels, considering only the first term of the series Eq. (4.65) gives

$$f \text{Re}_{D_h} = \frac{4}{(1+\varepsilon)^2 \frac{\varepsilon \sin^2 \delta_1}{\delta_1^4 (\delta_1 + \sin \delta_1 \cos \delta_1)} \left[\frac{\delta_1}{\varepsilon} - \frac{\sinh\left(\frac{\delta_1}{\varepsilon}\right)}{\cosh\left(\frac{\delta_1}{\varepsilon}\right) + \frac{2-\sigma}{\sigma} \frac{4}{1+\varepsilon} Kn_{D_h} \delta_1 \sinh\left(\frac{\delta_1}{\varepsilon}\right)} \right]} \quad (4.67)$$

Examination of the single term solution reveals that the greatest error occurs when $Kn=0.001$ and $\varepsilon=1$ in slip regime, which gives a fRe value 2.6 percent above the exact value. Table 4.4 presents a comparison of the exact values with the single term approximation, Eq. (4.65) and Eq. (4.67).

The friction factor results can be presented conveniently in terms of normalized Poiseuille number. Furthermore, the effects of slip are illustrated clearly by plotting the ratio Po/Po_c as a function of the Knudsen number and aspect ratio, where Po_c represents the continuum flow value. Figure 4.5 shows the normalized Poiseuille number results for rectangular ducts as a function of aspect ratio ε and Kn .

The Poiseuille number reduction depends on the geometry of the cross-section. It is convenient that the Poiseuille number results are expressible to good accuracy by the relation

$$\frac{Po}{Po_c} = \frac{f Re}{(f Re)_c} = \frac{1}{1 + \alpha \frac{2 - \sigma}{\sigma} Kn_{D_h}} \quad (4.68)$$

in which α depends on the duct geometry. For the common duct shapes, $\alpha=12$ for the parallel plate and $\alpha=8$ for the circular tube.

Table 4.4 Comparison of single term approximation for fRe .

| $\varepsilon = b/a$ | $f Re_{D_h}$ ($Kn^*=0.001$) | | Eq.(4.67)/Exact | $f Re_{D_h}$ ($Kn^*=0.1$) | | Eq.(4.67)/Exact |
|---------------------|-------------------------------|------------|-----------------|-----------------------------|------------|-----------------|
| | Exact | Eq. (4.67) | | Exact | Eq. (4.67) | |
| 0.001 | 23.70 | 24.03 | 1.014 | 10.90 | 10.94 | 1.004 |
| 0.01 | 23.41 | 23.74 | 1.014 | 10.82 | 10.86 | 1.004 |
| 0.05 | 22.24 | 22.55 | 1.014 | 10.47 | 10.52 | 1.005 |
| 0.1 | 20.95 | 21.26 | 1.015 | 10.09 | 10.14 | 1.005 |
| 0.2 | 18.89 | 19.18 | 1.015 | 9.46 | 9.52 | 1.006 |
| 0.3 | 17.36 | 17.64 | 1.016 | 9.00 | 9.06 | 1.007 |
| 0.4 | 16.24 | 16.51 | 1.017 | 8.66 | 8.72 | 1.007 |
| 0.5 | 15.43 | 15.71 | 1.018 | 8.41 | 8.49 | 1.010 |
| 0.6 | 14.87 | 15.16 | 1.020 | 8.25 | 8.33 | 1.010 |
| 0.7 | 14.50 | 14.81 | 1.021 | 8.14 | 8.23 | 1.011 |
| 0.8 | 14.28 | 14.61 | 1.023 | 8.08 | 8.18 | 1.012 |
| 0.9 | 14.17 | 14.52 | 1.025 | 8.04 | 8.16 | 1.015 |
| 1 | 14.14 | 14.51 | 1.026 | 8.04 | 8.16 | 1.015 |

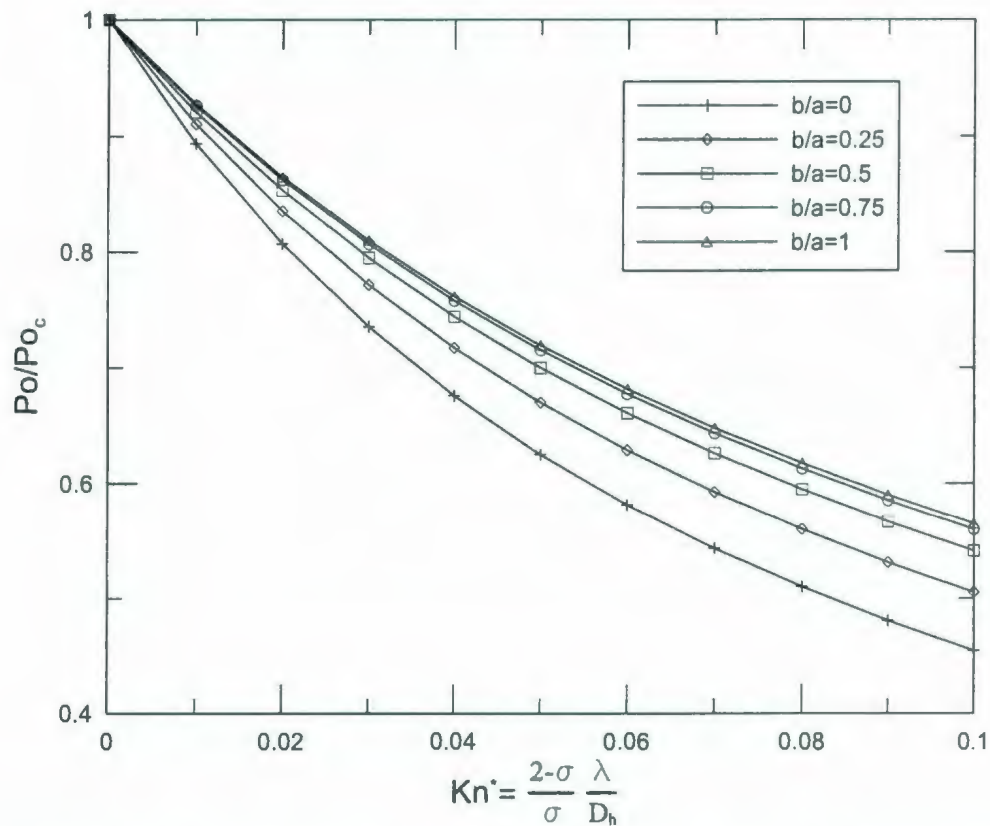


Figure 4.5 Normalized Po results as a function of aspect ratio ε and Kn for rectangular ducts.

For rectangular ducts, the constants α are derived from a least-square fit of the Poiseuille number results (Figure 4.5). It is found that the maximum error caused by using these constants in Eq. (4.68) is less than 0.3 %. The error is much smaller and negligible for most cases. The constants α are a function of aspect ratio and the data points are fitted to a simple correlation:

$$\alpha = 11.97 - 10.59\varepsilon + 8.49\varepsilon^2 - 2.11\varepsilon^3 \quad (4.69)$$

then

$$\frac{Po}{Po_c} = \frac{1}{1 + (11.97 - 10.59\epsilon + 8.49\epsilon^2 - 2.11\epsilon^3) \frac{2-\sigma}{\sigma} Kn_{D_h}} \quad (4.70)$$

Therefore, using the simple expression Eq. (4.70), the Poiseuille number results can be easily obtained.

4.3.2 Annular Ducts

A schematic diagram of the annular cross section is pictured in Figure 4.6. Using the similar procedure as for rectangular ducts, it is not difficult to show that the friction factor Reynolds product for an annular duct is as follows:

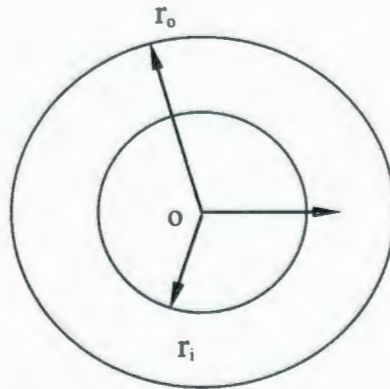


Figure 4.6 A concentric circular annular duct.

$$f \text{Re}_{D_h} = \frac{8(1-r)^2}{1+r^2 + 8(r^2 - r + 1) \frac{2-\sigma}{\sigma} Kn_{D_h} + \frac{r(1-r^2) \left(1 + 4 \frac{2-\sigma}{\sigma} Kn_{D_h} \right)^2}{r \ln r - 2(1-r^2) \frac{2-\sigma}{\sigma} Kn_{D_h}}} \quad (4.71)$$

where $r = r_i/r_o$, the dimensionless radius ratio.

4.3.3 Trapezoidal and Double-trapezoidal Ducts

Morini et al. [108] numerically studied the velocity distribution in microchannels with trapezoidal ($\alpha=54.74^\circ$) and hexagonal (double-trapezoidal) cross-section typical of microchannels. A schematic diagram of the trapezoidal and hexagonal cross-sections is depicted in Figure 4.7. Morini et al. [108] showed that the normalized Poiseuille number can be expressed as Eq. (4.68). The appropriate value of α for trapezoidal and double-trapezoidal microchannels was numerically determined and reported for different aspect ratio.

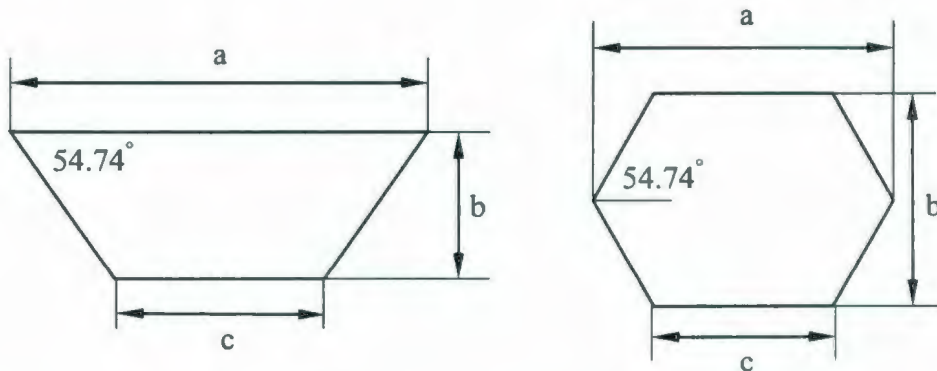


Figure 4.7 Trapezoidal and double-trapezoidal microchannels [108].

4.4 Modelling Slip Flow in Long Microchannels

We will now examine the rectangular, elliptical and annular friction factor Reynolds product results employing characteristic length \sqrt{A} as Muzychka and Yovanovich [94] showed that the square root of cross-sectional area was a more effective characteristic length scale than the hydraulic diameter for non-dimensionalizing the laminar continuum flow data. If the solution for rectangular duct is recast using \sqrt{A} as a characteristic length scale in $f \text{Re}_{\sqrt{A}}$, the following relationship is obtained:

$$f \text{Re}_{\sqrt{A}} = \frac{2}{\sqrt{\varepsilon}(1+\varepsilon) \sum_{n=1}^{\infty} \frac{\varepsilon \sin^2 \delta_n}{\delta_n^4 (\delta_n + \sin \delta_n \cos \delta_n)} \left[\frac{\delta_n}{\varepsilon} - \frac{\sinh\left(\frac{\delta_n}{\varepsilon}\right)}{\cosh\left(\frac{\delta_n}{\varepsilon}\right) + \frac{2-\sigma}{\sigma} \frac{4}{1+\varepsilon} Kn_{D_h} \delta_n \sinh\left(\frac{\delta_n}{\varepsilon}\right)} \right]} \quad (4.72)$$

considering only the first term of the series gives:

$$f \text{Re}_{\sqrt{A}} = \frac{2}{\sqrt{\varepsilon}(1+\varepsilon) \frac{\varepsilon \sin^2 \delta_1}{\delta_1^4 (\delta_1 + \sin \delta_1 \cos \delta_1)} \left[\frac{\delta_1}{\varepsilon} - \frac{\sinh\left(\frac{\delta_1}{\varepsilon}\right)}{\cosh\left(\frac{\delta_1}{\varepsilon}\right) + \frac{2-\sigma}{\sigma} \frac{4}{1+\varepsilon} Kn_{D_h} \delta_1 \sinh\left(\frac{\delta_1}{\varepsilon}\right)} \right]} \quad (4.73)$$

In the limit of $Kn \rightarrow 0$, Eq. (4.73) reduces to its corresponding continuum flow solution [94]:

$$f \text{Re}_{\sqrt{A}} = \frac{12}{\sqrt{\varepsilon}(1+\varepsilon) \left[1 - \frac{192\varepsilon}{\pi^5} \tanh\left(\frac{\pi}{2\varepsilon}\right) \right]} \quad (4.74)$$

Furthermore, using the above developed correlation Eq. (4.70), Eq. (4.72) can be simplified to provide the following model for practical applications:

$$f \text{Re}_{\sqrt{A}} = \frac{1}{1 + (11.97 - 10.59\varepsilon + 8.49\varepsilon^2 - 2.11\varepsilon^3) \frac{2-\sigma}{\sigma} Kn_{D_h}} \frac{12}{\sqrt{\varepsilon}(1+\varepsilon) \left[1 - \frac{192\varepsilon}{\pi^5} \tanh\left(\frac{\pi}{2\varepsilon}\right) \right]} \quad (4.75)$$

The maximum difference between Eq. (4.72) and Eq. (4.75) is less than 1%.

If the solutions for elliptical and annular ducts are also recast using \sqrt{A} as a characteristic length scale in $f \text{Re}_{\sqrt{A}}$, the following relationships are obtained respectively:

$$f \text{Re}_{\sqrt{A}} = \frac{E(e)}{\sqrt{\varepsilon\pi}} f \text{Re}_{D_h} \quad (4.76)$$

for the elliptic duct, where $f \text{Re}_{D_h}$ is found from Eq. (4.33), and

$$f \text{Re}_{\sqrt{A}} = \frac{8(1-r)\sqrt{\pi(1-r^2)}}{1+r^2 + 8(r^2-r+1) \frac{2-\sigma}{\sigma} Kn_{D_h} + \frac{r(1-r^2) \left(1 + 4 \frac{2-\sigma}{\sigma} Kn_{D_h} \right)^2}{r \ln r - 2(1-r^2) \frac{2-\sigma}{\sigma} Kn_{D_h}}} \quad (4.77)$$

for the annular duct using Eq. (4.71).

4.4.1 Effect of Characteristic Length Scale

There are three possibilities for characteristic length ℓ ($\ell = D_h$, $\ell = \sqrt{A}$ and $\ell = 2b$) to define Knudsen number. All three length scales have been critically examined in the slip regime over a wide range of duct aspect ratios. It was observed that using $\ell = D_h$ to define Knudsen number and $\ell = \sqrt{A}$ to define Reynolds number succeeded in bringing the dimensionless results closer together for similar ducts, i.e. rectangular and elliptical or trapezoidal. Overall, using $\ell = D_h$ to define Knudsen number was found to be more effective at collapsing the data in the slip regime over a wide range of duct aspect ratios. For example, Table 4.5 presents the solutions $f \text{Re}_{\sqrt{A}}$ ($b/a=0.1$) for elliptical and rectangular ducts using the three characteristic length scales, ℓ , respectively.

Table 4.5 $f \text{Re}_{\sqrt{A}}$ ($b/a=0.1$) results for elliptical and rectangular ducts using three characteristic length ℓ respectively.

| Kn^* | $\frac{f \text{Re}_{\sqrt{A}}^R}{f \text{Re}_{\sqrt{A}}^E}, \quad Kn = \frac{\lambda}{D_h}$ | $\frac{f \text{Re}_{\sqrt{A}}^R}{f \text{Re}_{\sqrt{A}}^E}, \quad Kn = \frac{\lambda}{\sqrt{A}}$ | $\frac{f \text{Re}_{\sqrt{A}}^R}{f \text{Re}_{\sqrt{A}}^E}, \quad Kn = \frac{\lambda}{2b}$ |
|--------|---|--|--|
| 0 | 1.052 | 1.052 | 1.052 |
| 0.01 | 1.057 | 1.068 | 1.066 |
| 0.02 | 1.061 | 1.079 | 1.079 |
| 0.03 | 1.064 | 1.087 | 1.090 |
| 0.04 | 1.067 | 1.094 | 1.099 |
| 0.05 | 1.070 | 1.099 | 1.109 |
| 0.06 | 1.072 | 1.103 | 1.117 |
| 0.07 | 1.074 | 1.107 | 1.124 |
| 0.08 | 1.075 | 1.110 | 1.131 |
| 0.09 | 1.077 | 1.113 | 1.138 |
| 0.1 | 1.078 | 1.115 | 1.144 |

Table 4.6 fRe results for elliptical and rectangular ducts.

| b/a | fRe_{D_h} ($Kn^*=0.1$) | | | $fRe_{\sqrt{A}}$ ($Kn^*=0.1$) | | |
|------|----------------------------|--------|-----------------------|---------------------------------|--------|-----------------------|
| | Rect. | Ellip. | $\frac{fRe^R}{fRe^E}$ | Rect. | Ellip. | $\frac{fRe^R}{fRe^E}$ |
| 0.05 | 10.472 | 9.023 | 1.161 | 24.586 | 22.817 | 1.078 |
| 0.1 | 10.080 | 8.979 | 1.123 | 17.532 | 16.277 | 1.078 |
| 0.2 | 9.447 | 8.913 | 1.060 | 12.674 | 11.812 | 1.073 |
| 0.3 | 8.971 | 8.886 | 1.010 | 10.646 | 10.037 | 1.061 |
| 0.4 | 8.621 | 8.881 | 0.971 | 9.542 | 9.116 | 1.047 |
| 0.5 | 8.372 | 8.880 | 0.943 | 8.880 | 8.581 | 1.035 |
| 0.6 | 8.201 | 8.879 | 0.924 | 8.470 | 8.255 | 1.026 |
| 0.7 | 8.089 | 8.879 | 0.911 | 8.218 | 8.056 | 1.020 |
| 0.8 | 8.019 | 8.880 | 0.903 | 8.069 | 7.944 | 1.016 |
| 0.9 | 7.978 | 8.885 | 0.898 | 7.989 | 7.891 | 1.012 |
| 1 | 7.957 | 8.889 | 0.895 | 7.957 | 7.878 | 1.010 |

| b/a | fRe_{D_h} ($Kn^*=0.01$) | | | $fRe_{\sqrt{A}}$ ($Kn^*=0.01$) | | |
|------|-----------------------------|--------|-----------------------|----------------------------------|--------|-----------------------|
| | Rect. | Ellip. | $\frac{fRe^R}{fRe^E}$ | Rect. | Ellip. | $\frac{fRe^R}{fRe^E}$ |
| 0.05 | 20.163 | 17.540 | 1.150 | 47.340 | 44.471 | 1.065 |
| 0.1 | 19.066 | 17.314 | 1.101 | 33.161 | 31.384 | 1.057 |
| 0.2 | 17.298 | 16.758 | 1.032 | 23.208 | 22.209 | 1.045 |
| 0.3 | 15.976 | 16.219 | 0.985 | 18.959 | 18.319 | 1.035 |
| 0.4 | 15.000 | 15.767 | 0.951 | 16.602 | 16.185 | 1.026 |
| 0.5 | 14.296 | 15.418 | 0.927 | 15.163 | 14.898 | 1.018 |
| 0.6 | 13.805 | 15.164 | 0.910 | 14.258 | 14.097 | 1.011 |
| 0.7 | 13.477 | 14.991 | 0.899 | 13.692 | 13.603 | 1.007 |
| 0.8 | 13.273 | 14.884 | 0.892 | 13.355 | 13.314 | 1.003 |
| 0.9 | 13.160 | 14.830 | 0.887 | 13.178 | 13.170 | 1.001 |
| 1 | 13.114 | 14.815 | 0.885 | 13.114 | 13.129 | 1.000 |

A comparison is now made between the rectangular and elliptical duct solutions, Eqs. (4.75, 4.76). Muzychka and Yovanovich [94] showed that the square root of cross-sectional area is more appropriate than the hydraulic diameter for non-dimensionalizing the laminar continuum flow data. Table 4.6 demonstrates that the same conclusion can be extended to the slip flow regime. Figures 4.8 and 4.9 show the solutions $fRe_{\sqrt{A}}$ as a

function of aspect ratio and Knudsen number. As seen in these Figures, the results for the elliptical duct and the rectangular duct come closer together. From these Figures it is seen that the maximum difference which is 7.8% between the values for fRe occur in the limit of $\varepsilon \rightarrow 0$. The difference is smaller than 1% and negligible for large aspect ratio ($\varepsilon = 0.6 \sim 1.0$). Therefore, we may use the simpler expression, Eq. (4.75), to compute values for the elliptical duct. This way, we do not need to use elliptic cylinder coordinates and the complicated solution proposed in Section 4.2, unless greater accuracy is desired.

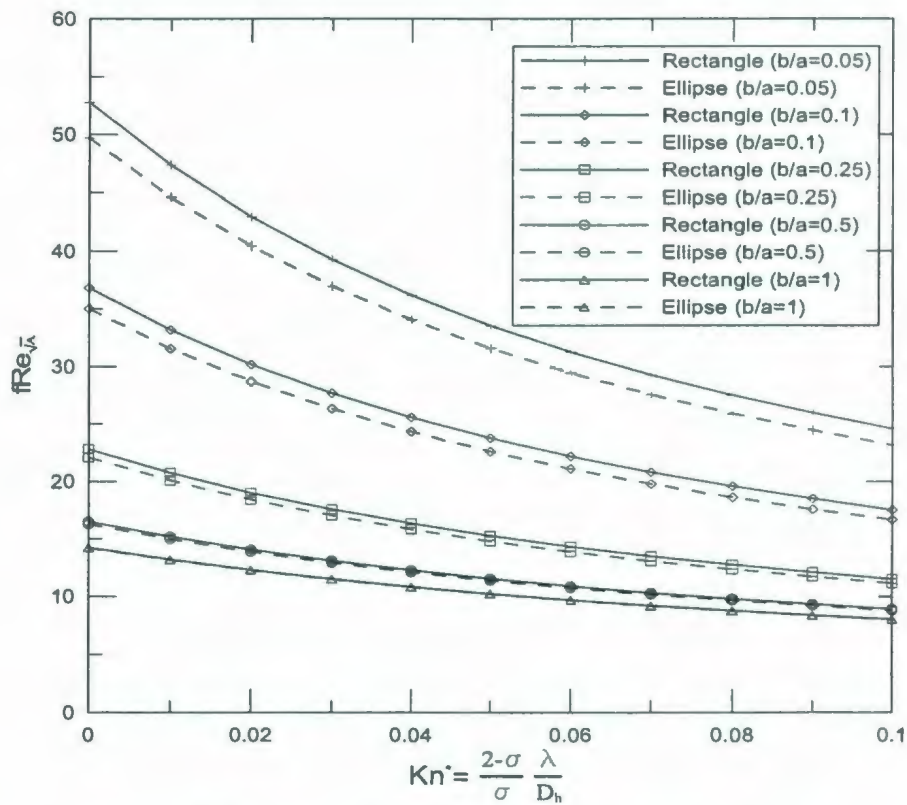


Figure 4.8 $fRe_{\sqrt{\lambda}}$ for elliptic and rectangular ducts.

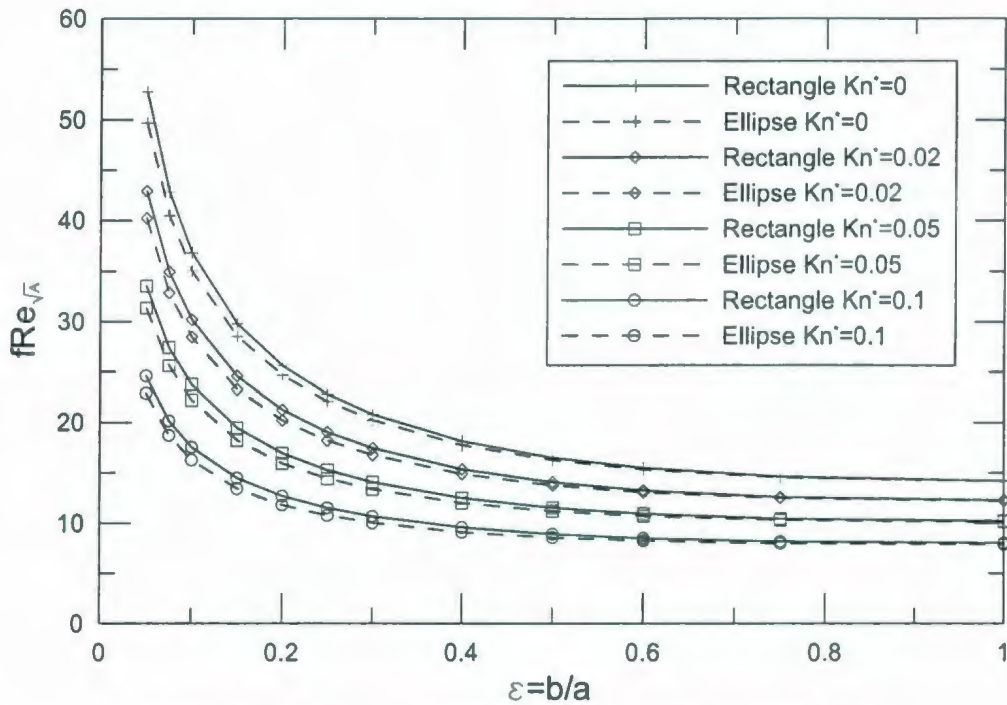


Figure 4.9 $fRe_{\sqrt{A}}$ for elliptic and rectangular ducts.

In addition, from an inspection of the graphs, it is seen that $fRe_{\sqrt{A}}$ decreases as the Knudsen number increases for the same aspect ratio. The $fRe_{\sqrt{A}}$ values decrease with an increase of ε for the same Kn . Moreover, it is obvious that the pressure gradient for a slip flow is less than the corresponding continuum flow.

The simple expression, Eq. (4.75), can also be extended to other common geometries. The definition of aspect ratio proposed by Muzychka and Yovanovich [94] is summarized in Table 4.7 for a number of geometries. The aspect ratio for regular polygons is unity. The aspect ratio for all singly connected ducts is taken as the ratio of the maximum width to maximum length such that $0 < \varepsilon < 1$. For the trapezoid and double-trapezoid ducts, simple expressions can be used to relate the characteristic dimensions of the duct to a width to length ratio.

Table 4.7 Definitions of aspect ratio [94].

| Geometry | Aspect Ratio |
|------------------|---------------------------------------|
| Regular Polygons | $\varepsilon = 1$ |
| Singly-Connected | $\varepsilon = \frac{b}{a}$ |
| Trapezoid | $\varepsilon = \frac{2b}{a+c}$ |
| Double-Trapezoid | $\varepsilon = \frac{2b}{a+c}$ |
| Annular Sector | $\varepsilon = \frac{1-r}{(1+r)\Phi}$ |
| Circular Annulus | $\varepsilon = \frac{1-r}{\pi(1+r)}$ |

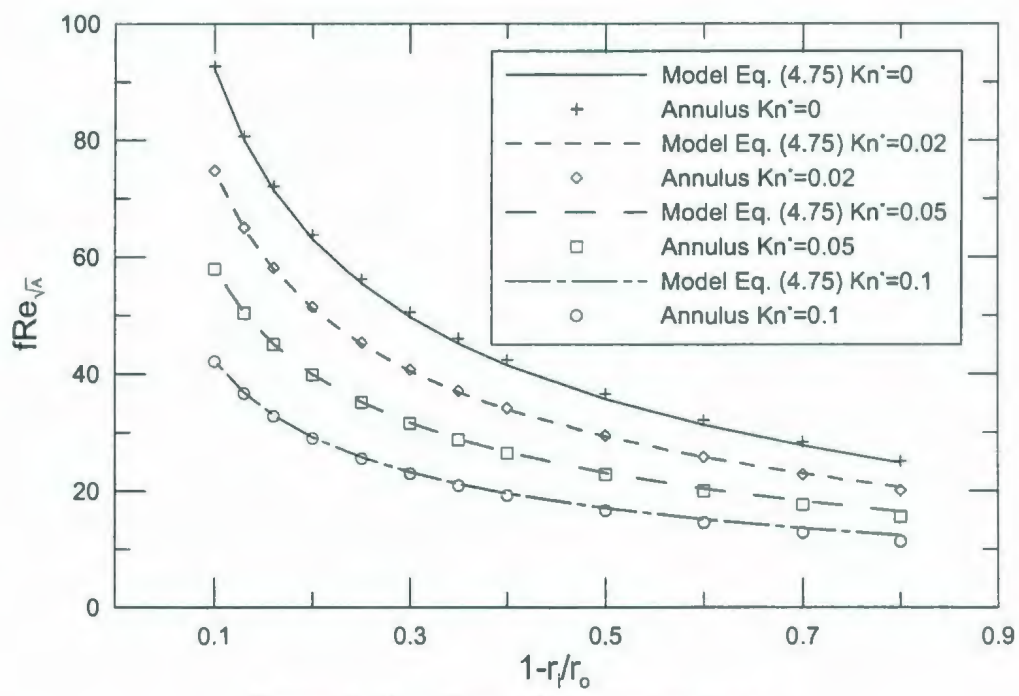


Figure 4.10 $f \text{Re}_{\sqrt{\lambda}}$ for annular ducts.

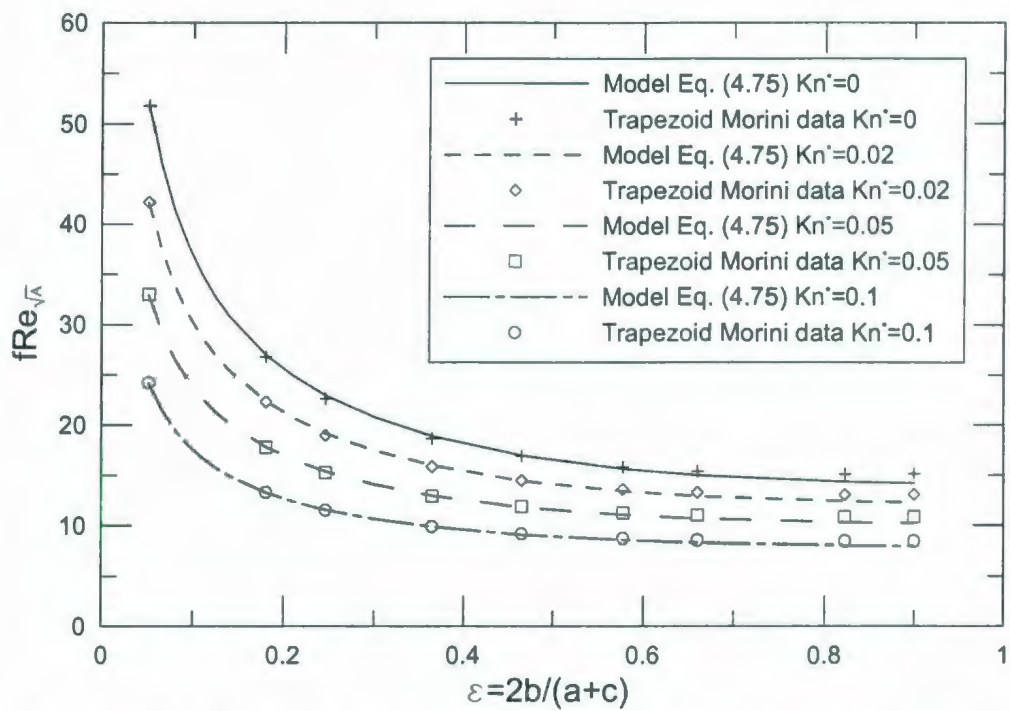


Figure 4.11 $f Re_{\sqrt{A}}$ for trapezoidal ducts, data from Morini et al. [108].

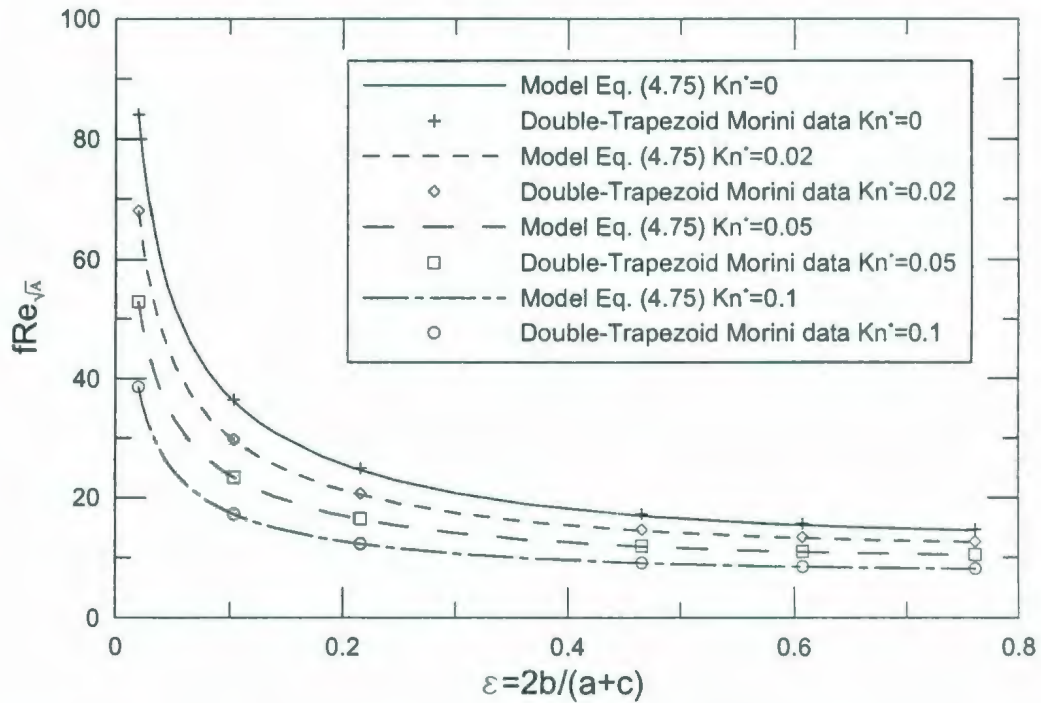


Figure 4.12 $f Re_{\sqrt{A}}$ for double-trapezoidal ducts, data from Morini et al. [108].

Figure 4.10 presents the comparison between the proposed model Eq. (4.75) and the analytical solution of annular ducts Eq. (4.77). The model predictions are in agreement with analytical solution within 8.7%.

Figure 4.11 demonstrates the comparison between the proposed model Eq. (4.75) and Morini et al. [108] numerical data for trapezoidal ducts. It is found that the model predictions agree with Morini et al. numerical data within 6.5%.

Figure 4.12 presents the comparison between the proposed model Eq. (4.75) and Morini et al. [108] numerical data for double-trapezoidal ducts. The model predictions are in agreement with Morini et al. numerical data within 1.8%.

It is clear that Eq. (4.75) characterizes the non-circular microchannel slip flow. The maximum deviation of exact values is less than 10 percent. The friction factor Reynolds product may be predicted from Eq. (4.75), provided an appropriate definition of the aspect ratio is chosen. Thus, Muzychka and Yovanovich's approach [94] may be extended to the slip flow regime.

4.4.2 Mass Flow Rate and Pressure Distribution

The mass flow rate in the microchannel is given by using the equation of state, Eq. (4.75), and $f \text{Re}_{\sqrt{A}} = (f \text{Re}_{\sqrt{A}})_c / (1 + \alpha Kn^*)$

$$\dot{m} = \rho \bar{u} A = \rho A \frac{2 \left(-\frac{A}{P} \frac{dp}{dz} \right) \sqrt{A}}{\mu f \text{Re}_{\sqrt{A}}} = - \frac{2 \frac{A^{5/2}}{P}}{\frac{12 \mu R T}{\sqrt{\varepsilon} (1 + \varepsilon) \left[1 - \frac{192 \varepsilon}{\pi^5} \tanh \left(\frac{\pi}{2 \varepsilon} \right) \right]}} \frac{dp}{dz} \left(p + \alpha \frac{2 - \sigma}{\sigma} p Kn \right) \quad (4.78)$$

We can use $pKn = p_oKn_o$ since pKn is constant for isothermal flow. Integrating Eq. (4.78), we obtain

$$\dot{m} = \rho \bar{u} A = \frac{p_o^2 \frac{A^{5/2}}{P}}{12\mu RT_z} \left[\frac{p_i^2}{p_o^2} - \frac{p_z^2}{p_o^2} + 2\alpha \frac{2-\sigma}{\sigma} Kn_o \left(\frac{p_i}{p_o} - \frac{p_z}{p_o} \right) \right] \frac{\sqrt{\varepsilon}(1+\varepsilon)}{\sqrt{\varepsilon}(1+\varepsilon) \left[1 - \frac{192\varepsilon}{\pi^5} \tanh\left(\frac{\pi}{2\varepsilon}\right) \right]} \quad (4.79)$$

Letting $z=L$ gives:

$$\dot{m} = \rho \bar{u} A = \frac{p_o^2 \frac{A^{5/2}}{P}}{12\mu R T L} \left[\frac{p_i^2}{p_o^2} - 1 + 2\alpha \frac{2-\sigma}{\sigma} Kn_o \left(\frac{p_i}{p_o} - 1 \right) \right] \frac{\sqrt{\varepsilon}(1+\varepsilon)}{\sqrt{\varepsilon}(1+\varepsilon) \left[1 - \frac{192\varepsilon}{\pi^5} \tanh\left(\frac{\pi}{2\varepsilon}\right) \right]} \quad (4.80)$$

The continuum flow mass flow rate is given by:

$$\dot{m}_c = \rho \bar{u} A = \frac{p_o^2 \frac{A^{5/2}}{P}}{12\mu R T L} \left(\frac{p_i^2}{p_o^2} - 1 \right) \frac{\sqrt{\varepsilon}(1+\varepsilon)}{\sqrt{\varepsilon}(1+\varepsilon) \left[1 - \frac{192\varepsilon}{\pi^5} \tanh\left(\frac{\pi}{2\varepsilon}\right) \right]} \quad (4.81)$$

The effect of slip may be illustrated clearly by dividing the slip flow mass flow Eq.(4.80) by the continuum flow mass flow Eq. (4.81)

$$\frac{\dot{m}}{\dot{m}_c} = 1 + \frac{2\alpha \frac{2-\sigma}{\sigma} Kn_o}{\frac{p_i}{p_o} + 1} \quad (4.82)$$

It is seen that the rarefaction increases the mass flow and that the effect of rarefaction becomes more significant when the pressure ratio decreases. This could also be interpreted as a decrease in effective gas viscosity.

Combining Eq. (4.79) and Eq. (4.80), we obtain the expression for pressure distribution in non-circular microchannels:

$$\frac{p_z}{p_o} = -\alpha \frac{2-\sigma}{\sigma} Kn_o + \sqrt{\left(\alpha \frac{2-\sigma}{\sigma} Kn_o + \frac{p_i}{p_o}\right)^2 - \left[\frac{p_i^2}{p_o^2} - 1 + 2\alpha \frac{2-\sigma}{\sigma} Kn_o \left(\frac{p_i}{p_o} - 1\right)\right] \frac{z}{L}} \quad (4.83)$$

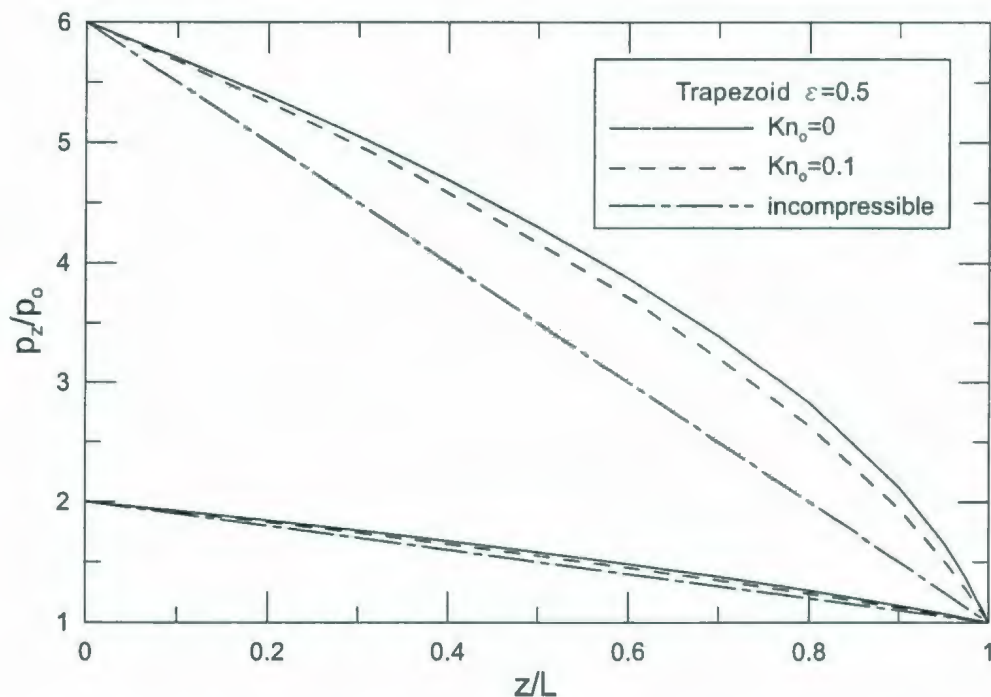


Figure 4.13 The pressure distribution for different pressure ratios.

Figure 4.13 shows the pressure distribution with and without rarefaction predicted by Eq. (4.83) for non-circular microchannels. The pressure distribution exhibits a nonlinear behavior due to the compressibility effect. The nonlinearity increases as the pressure ratio increases. The incompressibility assumption (linear pressure distribution) is valid for small pressure drop in the microchannels.

In the present analysis for the pressure distribution and mass flow rate, momentum changes are neglected. The effect of the momentum changes will become important when Reynolds number is increased.

Slip flow in non-circular microchannels has been investigated and a simple model was developed for predicting the friction factor Reynolds product in non-circular microchannels for slip flow. The present model took advantage of the selection of a more appropriate characteristic length scale square root of flow area to develop a simple model. The accuracy of the developed model was found to be within 10 percent, with most data for practical configurations within 5 percent. As for slip flow no solutions or tabulated data exist for most geometries, this developed model may be used to predict mass flow rate and pressure distribution of slip flow in non-circular microchannels.

4.5 Compressibility Effects on Slip Flow in Microchannels

As Mach number is increased, the effects of momentum changes should be taken into account. The effects of momentum changes on pressure variation along the duct and mass flow rate will be investigated in detail in this section.

4.5.1 Theoretical Analysis

In Section 4.4, we examined slip flow in non-circular microchannels and presented the unified modes for pressure distribution and mass flow rate in non-circular microchannels. In addition, some mass flow rate analytical expressions for simple geometric forms are given as follows [109].

Using Eq. (4.64), the mass flow rate in the rectangular microchannel was given by

$$\dot{m} = \rho \bar{u} A = -\frac{4ab^3\rho}{\mu} \frac{dp}{dz} \sum_{n=1}^{\infty} \frac{2\varepsilon \sin^2 \delta_n}{\delta_n^4 (\delta_n + \sin \delta_n \cos \delta_n)} \left[\frac{\delta_n}{\varepsilon} - \frac{\sinh\left(\frac{\delta_n}{\varepsilon}\right)}{\cosh\left(\frac{\delta_n}{\varepsilon}\right) + \frac{2-\sigma}{\sigma} \frac{4}{1+\varepsilon} Kn \delta_n \sinh\left(\frac{\delta_n}{\varepsilon}\right)} \right] \quad (4.84)$$

Taking derivative of the Eq. (4.83) and substituting into Eq. (4.84) and evaluating at outlet $z=L$, we obtain

$$\dot{m} = \frac{\frac{2ab^3 p_o^2}{\mu L R T} \left[\frac{p_i^2}{p_o^2} - 1 + 2\alpha \frac{2-\sigma}{\sigma} Kn_o \left(\frac{p_i}{p_o} - 1 \right) \right]}{1 + \alpha \frac{2-\sigma}{\sigma} Kn_o} \sum_{n=1}^{\infty} \frac{2\varepsilon \sin^2 \delta_n}{\delta_n^4 (\delta_n + \sin \delta_n \cos \delta_n)} \left[\frac{\delta_n}{\varepsilon} - \frac{\sinh\left(\frac{\delta_n}{\varepsilon}\right)}{\cosh\left(\frac{\delta_n}{\varepsilon}\right) + \frac{2-\sigma}{\sigma} \frac{4}{1+\varepsilon} Kn_o \delta_n \sinh\left(\frac{\delta_n}{\varepsilon}\right)} \right] \quad (4.85)$$

Examination of the single term and two terms of the series solutions reveals that the greatest error occurs when $Kn=0.001$ and $\varepsilon=1$ in slip regime, which gives a value 2.6 and 0.3 percent below the exact value respectively. Therefore, using the first term of the series or two terms at most is accurate enough to obtain the mass flow rate.

It can be demonstrated that the limit of Eq. (4.85) for $\varepsilon \rightarrow 0$ corresponds to parallel plates channel

$$\dot{m} = \frac{2ab^3 p_o^2}{3\mu LRT} \left[\frac{p_i^2}{p_o^2} - 1 + 24 \frac{2-\sigma}{\sigma} Kn_o \left(\frac{p_i}{p_o} - 1 \right) \right] \quad (4.86)$$

Similarly, using Eq. (4.71), the mass flow rate in the annular microchannel was given by

$$\dot{m} = -\frac{\pi(r_o^2 - r_i^2)r_o^2 \rho}{8\mu} \frac{dp}{dz} \left[1 + r^2 + 8(r^2 - r + 1) \frac{2-\sigma}{\sigma} Kn + \frac{r(1-r^2) \left(1 + 4 \frac{2-\sigma}{\sigma} Kn \right)^2}{r \ln r - 2(1-r^2) \frac{2-\sigma}{\sigma} Kn} \right] \quad (4.87)$$

Taking derivative of the Eq. (4.83) and substituting into Eq. (4.87), we get

$$\dot{m} = \frac{\pi(r_o^2 - r_i^2)r_o^2 p_o^2}{16\mu LRT} \left[\frac{p_i^2}{p_o^2} - 1 + 2\alpha \frac{2-\sigma}{\sigma} Kn_o \left(\frac{p_i}{p_o} - 1 \right) \right] \left[1 + r^2 + 8(r^2 - r + 1) \frac{2-\sigma}{\sigma} Kn_o + \frac{r(1-r^2) \left(1 + 4 \frac{2-\sigma}{\sigma} Kn_o \right)^2}{r \ln r - 2(1-r^2) \frac{2-\sigma}{\sigma} Kn_o} \right] \quad (4.88)$$

where $\alpha=8$ when $r=0$ and $\alpha \approx 12$ for $r > 0.1$. The limit of Eq. (4.88) for $r \rightarrow 0$ reduces to circular tubes

$$\dot{m} = \frac{r_o^4 \pi p_o^2}{16\mu LRT} \left[\frac{p_i^2}{p_o^2} - 1 + 16 \frac{2-\sigma}{\sigma} Kn_o \left(\frac{p_i}{p_o} - 1 \right) \right] \quad (4.89)$$

In the above analysis for the pressure distribution and mass flow rate in microchannel flows, momentum changes are neglected as the pressure force is mostly utilized to

overcome the friction force against the walls, very little is spent in accelerating the flow. The effect of the momentum changes will become important when Mach number is increased. The effects of momentum changes on pressure distribution and mass flow rate will be discussed as follows. A similar analysis on pressure distribution was done by Ebert and Sparrow [99] for flow in annular tubes and Sreekanth [110] for flow in circular tubes.

As it is exceedingly difficult to solve the Navier-Stokes equations to determine the actual velocity distribution of the compressible gas flow in non-circular microchannels, the flow is assumed to be locally fully developed and isothermal. Because the pressure drop is due to viscous effects and not to any free expansion of the gas, the isothermal assumption should be reasonable. The locally fully developed flow assumption means that the velocity field at any cross section is the same as that of a fully developed flow at the local density and the wall shear stress also takes on locally fully developed values.

The momentum balance on a control volume with axial length dz is given by:

$$-Adp - \bar{\tau}_w P dz = d\left(\int_A \rho u^2 dA\right) \quad (4.90)$$

The momentum flux may be written as

$$d\left(\int_A \rho u^2 dA\right) = \frac{Re^2 \mu^2 A}{D_h^2} d\left(\frac{1}{\rho} \int_A \left(\frac{u}{\bar{u}}\right)^2 \frac{dA}{A}\right) \quad (4.91)$$

The wall shear force can be expressed as follows:

$$\bar{\tau}_w = f \frac{1}{2} \rho \bar{u}^2 = \frac{Po \operatorname{Re} \mu^2}{\rho D_h^2} \quad (4.92)$$

Substituting Eqs. (4.91) and (4.92) into (4.90) and utilizing the perfect gas equation of state $p=\rho RT$, with some algebraic manipulation, we get

$$\frac{P}{P_o} d \frac{p}{p_o} + \operatorname{Re}^2 \beta \frac{p}{p_o} d \left(\frac{\psi}{p/p_o} \right) + 4 Po_c \operatorname{Re} \beta \frac{Po}{Po_c} d \frac{z}{D_h} = 0 \quad (4.93)$$

where

$$\psi = \frac{1}{A} \int_A \left(\frac{u}{\bar{u}} \right)^2 dA \quad (4.94)$$

The Knudsen number may be calculated based on the following formula

$$Kn = \frac{\lambda}{D_h} = \frac{\mu}{\rho D_h} \sqrt{\frac{\pi}{2RT}} \quad (4.95)$$

therefore

$$\beta = \frac{\mu^2 RT}{p_o^2 D_h^2} = \frac{2}{\pi} Kn_o^{-2} \quad (4.96)$$

The Poiseuille number reduction depends on the geometry of the cross-section. It is convenient that the Poiseuille number results are expressible by the relation

$$\frac{Po}{Po_c} = \frac{1}{1 + \alpha \frac{2-\sigma}{\sigma} Kn} \quad (4.97)$$

It is clear that Po/Po_c and ψ depend on the Knudsen number, or on the pressure. The derivation of ψ is fairly complicated and the expressions for ψ are also very lengthy. The resulting expressions for circular tubes and rectangular microchannels are given as follows respectively:

$$\psi = \frac{4 \left[1 + 12 \frac{2-\sigma}{\sigma} Kn + 48 \left(\frac{2-\sigma}{\sigma} Kn \right)^2 \right]}{3 \left(1 + 8 \frac{2-\sigma}{\sigma} Kn \right)^2} \quad (4.98)$$

$$\psi = \frac{\frac{1}{2} \left(1 + \frac{\varepsilon}{2\delta_n} \sinh \frac{2\delta_n}{\varepsilon} \right) - \frac{2\varepsilon}{\delta_n}}{\sum_{n=1}^{\infty} \frac{\left(\cosh \frac{\delta_n}{\varepsilon} + \frac{4}{1+\varepsilon} \frac{2-\sigma}{\sigma} Kn \delta_n \sinh \frac{\delta_n}{\varepsilon} \right)}{\delta_n^6 \left(\frac{4}{1+\varepsilon} \frac{2-\sigma}{\sigma} Kn + \csc^2 \delta_n \right)} + 1} \quad (4.99)$$

$$2\varepsilon^2 \left[\sum_{n=1}^{\infty} \frac{1}{\delta_n^5} \left(\frac{1}{\frac{4}{1+\varepsilon} \frac{2-\sigma}{\sigma} Kn \delta_n + \csc^2 \delta_n} \right) \left(\frac{1}{\frac{4}{1+\varepsilon} \frac{2-\sigma}{\sigma} Kn \delta_n + \coth \frac{\delta_n}{\varepsilon}} - \frac{\delta_n}{\varepsilon} \right) \right]^2$$

Figures 4.14 and 4.15 show the values of ψ as a function of Knudsen number for circular tubes and rectangular microchannels respectively. It is seen that the variation of ψ with Knudsen number is very gentle. It is reasonable that the approximation $\psi = \text{constant}$ as ψ is a weak function of Knudsen number. Figures 4.14 and 4.15 may be used to choose an estimated value of ψ for most non-circular microchannels for practical application calculation.

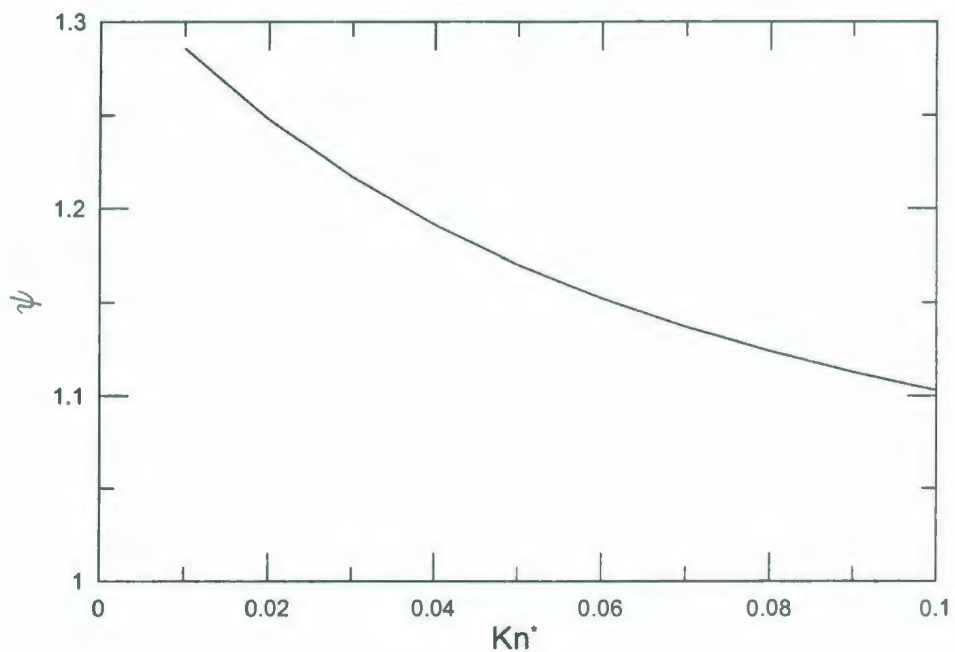


Figure 4.14 Momentum flux correction factor for circular tubes.

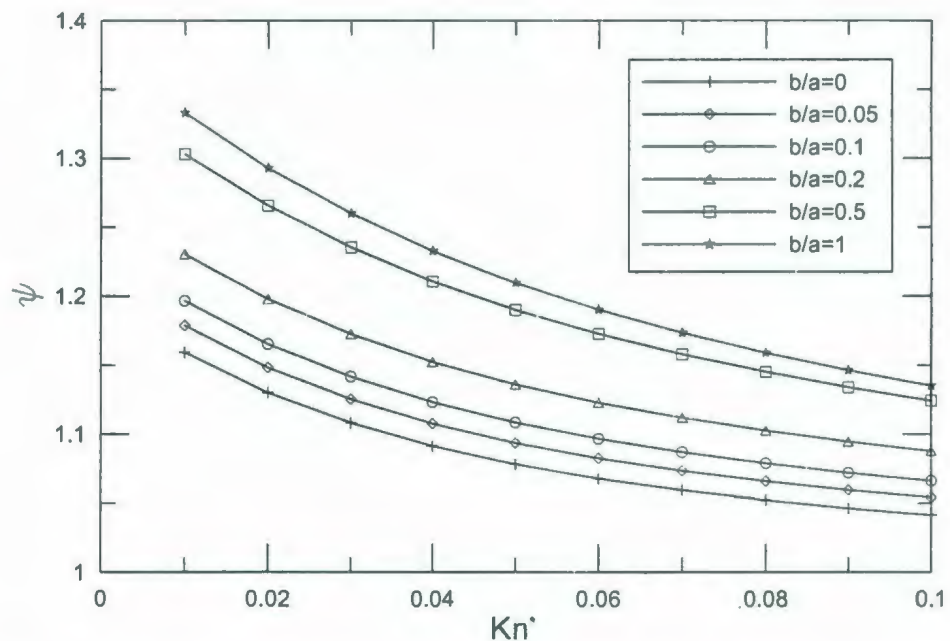


Figure 4.15 Momentum flux correction factor for rectangular ducts.

By noting that pKn is constant for isothermal flow, a reference state which is taken at the outlet can be introduced

$$Kn = \frac{Kn_o p_o}{p} \quad (4.100)$$

Equation (4.93) may be rearranged to

$$\left[-\frac{p}{p_o} - \alpha \frac{2-\sigma}{\sigma} Kn_o + Re^2 \frac{2}{\pi} Kn_o^2 \psi \left(\frac{1}{p/p_o} + \frac{\alpha \frac{2-\sigma}{\sigma} Kn_o}{(p/p_o)^2} \right) \right] d \frac{p}{p_o} = 4 Po_c Re \frac{2}{\pi} Kn_o^2 d \frac{z}{D_h} \quad (4.101)$$

An expression of the pressure difference between some upstream position z and the outlet position $z=L$ can be found by integration Eq. (4.101) (known outlet conditions)

$$\begin{aligned} & \left[\left(\frac{p}{p_o} \right)^2 - 1 \right] + 2\alpha \frac{2-\sigma}{\sigma} Kn_o \left(\frac{p}{p_o} - 1 \right) + \frac{4}{\pi} Re^2 Kn_o^2 \psi \left[\alpha \frac{2-\sigma}{\sigma} Kn_o \left(\frac{p_o}{p} - 1 \right) - \ln \frac{p}{p_o} \right] \\ &= \frac{16}{\pi} Po_c Re Kn_o^2 \frac{L-z}{D_h} \end{aligned} \quad (4.102)$$

Similarly, taking a reference state at the inlet, the pressure difference between some downstream position z and the inlet location $z = 0$ is (known inlet conditions)

$$\begin{aligned} & \left[\left(\frac{p}{p_i} \right)^2 - 1 \right] + 2\alpha \frac{2-\sigma}{\sigma} Kn_i \left(\frac{p}{p_i} - 1 \right) + \frac{4}{\pi} Re^2 Kn_i^2 \psi \left[\alpha \frac{2-\sigma}{\sigma} Kn_i \left(\frac{p_i}{p} - 1 \right) - \ln \frac{p}{p_i} \right] \\ &= -\frac{16}{\pi} Po_c Re Kn_i^2 \frac{z}{D_h} \end{aligned} \quad (4.103)$$

Equations (4.102) and (4.103) may be applied to any duct.

It is seen that variations of ψ does not bring obvious difference of pressure distribution in practical microchannel flows application range that $\text{Re } Kn \approx Ma$ is small. Sreekanth [110] also showed that the approximation $\psi = \text{constant}$ had little effect on pressure distribution covered in his experiments. Taking ψ as a constant is completely reasonable for practical microchannel flow applications.

Substituting Eq. (4.90) into Eq. (4.78) and integrating, with some algebraic manipulation, we obtain

$$\dot{m} = \frac{p_o^2 \frac{A^{5/2}}{P} \left[\frac{p_i^2}{p_o^2} - \frac{p^2}{p_o^2} + 2\alpha \frac{2-\sigma}{\sigma} Kn_o \left(\frac{p_i}{p_o} - \frac{p}{p_o} \right) + \frac{4}{\pi} \text{Re}^2 Kn_o^2 \psi \left[\alpha \frac{2-\sigma}{\sigma} Kn_o \left(\frac{p_o}{p_i} - \frac{p_o}{p} \right) - \ln \frac{p_i}{p} \right] \right]}{12 \mu R T z} \frac{1}{\sqrt{\varepsilon(1+\varepsilon)} \left[1 - \frac{192\varepsilon}{\pi^5} \tanh \left(\frac{\pi}{2\varepsilon} \right) \right]} \quad (4.104)$$

Letting $z=L$ gives:

$$\dot{m} = \frac{p_o^2 \frac{A^{5/2}}{P} \left[\frac{p_i^2}{p_o^2} - 1 + 2\alpha \frac{2-\sigma}{\sigma} Kn_o \left(\frac{p_i}{p_o} - 1 \right) + \frac{4}{\pi} \text{Re}^2 Kn_o^2 \psi \left[\alpha \frac{2-\sigma}{\sigma} Kn_o \left(\frac{p_o}{p_i} - 1 \right) - \ln \frac{p_i}{p_o} \right] \right]}{12 \mu R T L} \frac{1}{\sqrt{\varepsilon(1+\varepsilon)} \left[1 - \frac{192\varepsilon}{\pi^5} \tanh \left(\frac{\pi}{2\varepsilon} \right) \right]} \quad (4.105)$$

It is seen that, in microchannel flows, compressibility affects the pressure distribution and mass flow rate primarily through the viscous shear rather than through momentum flux. However, when $\text{Re } Kn \approx Ma$ increases, the effect of the momentum flux becomes

gradually significant. Especially for low pressure ratio, the effect of the momentum flux is comparatively pronounced.

The continuum flow mass flow rate is given by:

$$\dot{m}_c = \rho \bar{u} A = \frac{\frac{p_o^2 A^{5/2}}{P}}{\frac{12\mu R T L}{\sqrt{\varepsilon}(1+\varepsilon) \left[1 - \frac{192\varepsilon}{\pi^5} \tanh\left(\frac{\pi}{2\varepsilon}\right) \right]}} \left(\frac{p_i^2}{p_o^2} - 1 \right) \quad (4.106)$$

The effect of slip may be illustrated clearly by dividing the slip flow mass flow Eq.(4.105) by the continuum flow mass flow Eq. (4.106)

$$\frac{\dot{m}}{\dot{m}_c} = 1 + \frac{\frac{2\alpha \frac{2-\sigma}{\sigma} Kn_o \left(\frac{p_i}{p_o} - 1 \right) + \frac{4}{\pi} Re^2 Kn_o^2 \psi \left[\alpha \frac{2-\sigma}{\sigma} Kn_o \left(\frac{p_o}{p_i} - 1 \right) - \ln \frac{p_i}{p_o} \right]}{\frac{p_i^2}{p_o^2} - 1}}{(4.107)}$$

It is seen that the rarefaction increases the mass flow for low Mach number microchannel flows and that the effect of rarefaction becomes more significant when the pressure ratio decreases. For comparatively high Mach number microchannel flows, the rarefaction may decrease the mass flow.

Combining Eq. (4.104) and Eq. (4.105), we obtain the implicit expression for pressure distribution:

$$\begin{aligned} \frac{p_i^2}{p_o^2} - \frac{p^2}{p_o^2} + 2\alpha \frac{2-\sigma}{\sigma} Kn_o \left(\frac{p_i}{p_o} - \frac{p}{p_o} \right) + \frac{4}{\pi} Re^2 Kn_o^2 \psi \left[\alpha \frac{2-\sigma}{\sigma} Kn_o \left(\frac{p_o}{p_i} - \frac{p_o}{p} \right) - \ln \frac{p_i}{p_o} \right] = \\ \frac{z}{L} \left[\frac{p_i^2}{p_o^2} - 1 + 2\alpha \frac{2-\sigma}{\sigma} Kn_o \left(\frac{p_i}{p_o} - 1 \right) + \frac{4}{\pi} Re^2 Kn_o^2 \psi \left[\alpha \frac{2-\sigma}{\sigma} Kn_o \left(\frac{p_o}{p_i} - 1 \right) - \ln \frac{p_i}{p_o} \right] \right] \end{aligned} \quad (4.108)$$

In the limit of $ReKn \rightarrow 0$, Eq. (4.108) reduces to the explicit form Eq. (4.83). The deviations of the nonlinear pressure distribution from the linear distribution is given by

$$\begin{aligned} \frac{p}{p_o} - \left[\frac{p_i}{p_o} - \left(\frac{p_i}{p_o} - 1 \right) \frac{z}{L} \right] = -\alpha \frac{2-\sigma}{\sigma} Kn_o + \sqrt{\left(\alpha \frac{2-\sigma}{\sigma} Kn_o + \frac{p_i}{p_o} \right)^2 - \left[\frac{p_i^2}{p_o^2} - 1 + 2\alpha \frac{2-\sigma}{\sigma} Kn_o \left(\frac{p_i}{p_o} - 1 \right) \right] \frac{z}{L}} \\ - \frac{p_i}{p_o} + \left(\frac{p_i}{p_o} - 1 \right) \frac{z}{L} \end{aligned} \quad (4.109)$$

Taking derivative of the Eq. (4.109) and letting it equals zero, we obtain the location of maximum deviation from linearity as

$$\frac{z}{L} = \frac{3 \frac{p_i}{p_o} + 4\alpha \frac{2-\sigma}{\sigma} Kn_o + 1}{4 \left(\frac{p_i}{p_o} + 2\alpha \frac{2-\sigma}{\sigma} Kn_o + 1 \right)} \quad (4.110)$$

It is seen that the location of maximum deviation from linearity is between 0.5 and 0.75. The location approaches to 0.5 for low pressure ratio and approaches to 0.75 for high pressure ratio.

4.5.2 Results and Discussion

The mass flow rate models Eq. (4.85) and Eq. (4.105) have been examined using Arkilic et al. [27] experimental data. Figure 4.16 presents the normalized mass flow rate

$$m^* = \frac{\dot{m}\mu R T L}{2ab^3 p_o^2}$$

as a function of the pressure ratio. It is found that the predictions agree with Arkilic et al. [27] experimental data within 9.8%. It is seen that there is a significant mass flow rate increase from this Figure. The experimental data and model predictions are in good agreement.

Figure 4.17 demonstrates the pressure distribution comparison between the proposed model Eq. (4.108) and Pong et al. [29] experimental data. It is found that the model predictions agree with Pong et al. experimental data within 2.2%.

Figure 4.18 presents the pressure distribution comparison between the proposed model Eq. (4.108) and Lui et al. [30] experimental results. The model predictions are in agreement with Lui et al. experimental results within 1.6%.

Jang and Wereley [111] experimentally investigated pressure distributions of slip flow in uniform rectangular microchannels. Figure 4.19 shows the pressure distribution comparison between the proposed model Eq. (4.108) and Jang and Wereley [111] experimental data. The model predictions are in agreement with Jang and Wereley experimental data within 0.4%.

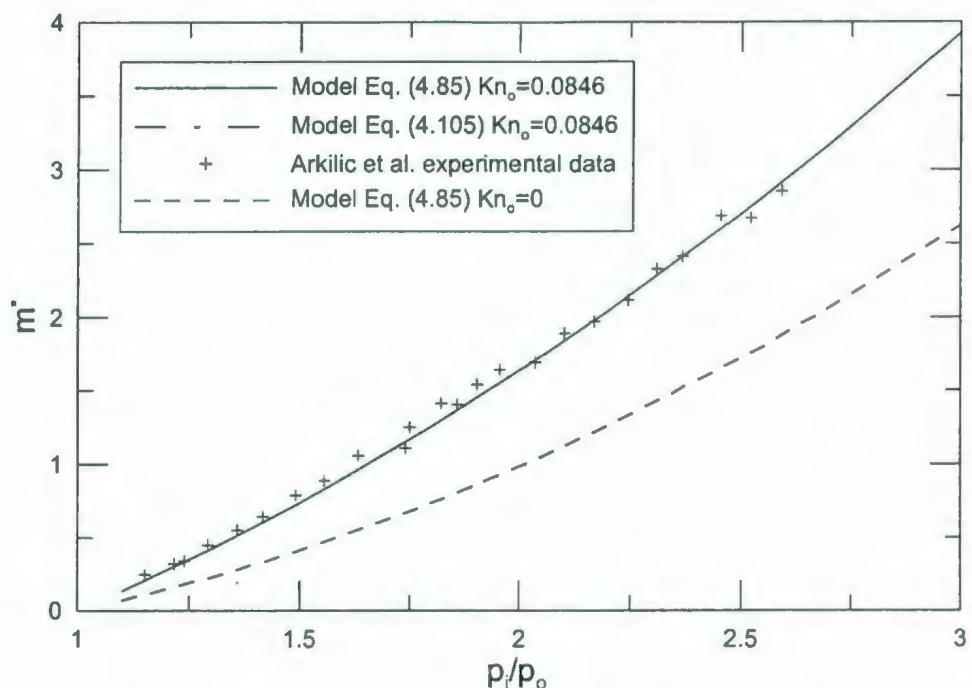


Figure 4.16 Normalized mass flow rate comparison for Arkilic et al. [27] experimental data.

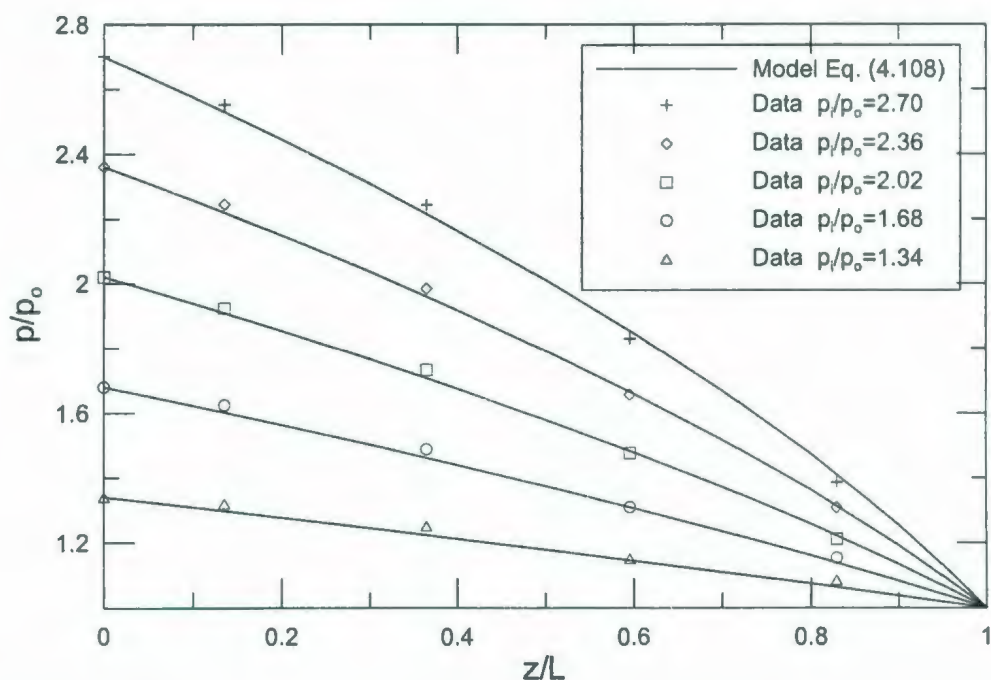


Figure 4.17 Pressure distribution comparison for Pong et al. [29] experimental data.

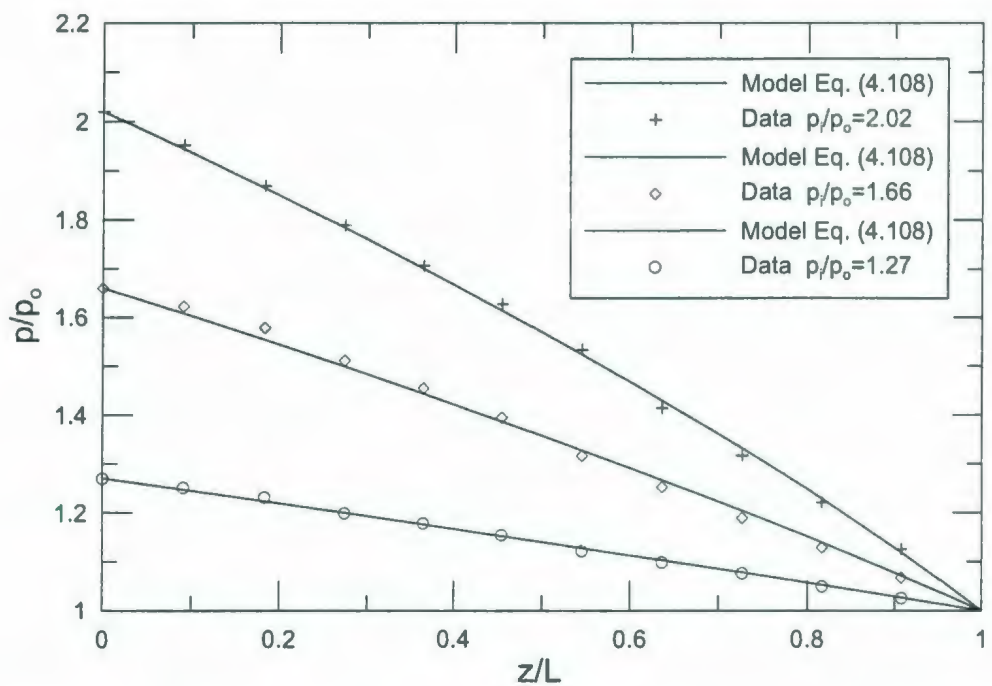


Figure 4.18 Pressure distribution comparison for Liu et al. [30] experimental data.

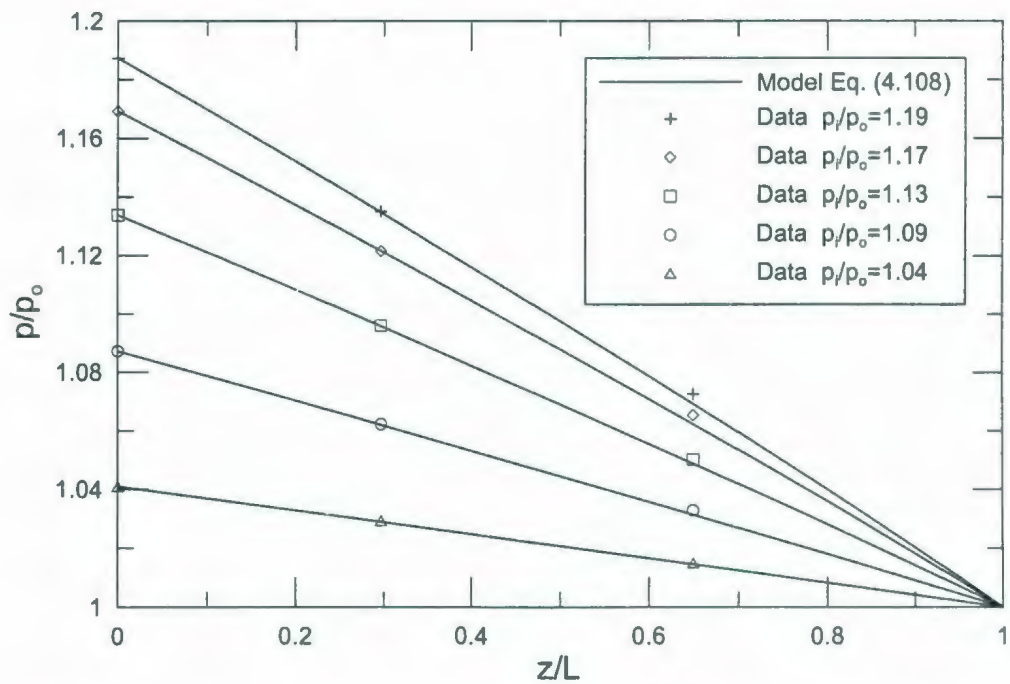


Figure 4.19 Pressure distribution comparison for Jang and Wereley [111] experimental data.

The corresponding experimental conditions for Arkilic et al., Pong et al., Liu et al., and Jang and Wereley are given in Table 4.8.

Table 4.8 Experimental conditions for microchannel flows.

| Parameter | Arkilic et al. | Pong et al. | Liu et al. | Jang and Wereley |
|--------------------------|----------------|-------------|------------|------------------|
| Length (μm) | 7500 | 3000 | 4500 | 5020 |
| Width (μm) | 52.25 | 40 | 40 | 104.63 |
| Height (μm) | 1.33 | 1.2 | 1.2 | 38.57 |
| Gas | Helium | Nitrogen | Helium | Air |
| Kn_o | 0.08460 | 0.02833 | 0.05665 | 0.001232 |
| p_o (kPa) | 100.8 | 100 | 100 | 98.7 |
| T (K) | 314 | 298 | 298 | 296 |

From an inspection of the above Figures, it is seen that the pressure distribution exhibits a nonlinear behavior due to the compressibility effect. Pressure drop required is less than that in a conventional channel. The deviations of the pressure distribution from the linear distribution decrease with an increase in Knudsen number. The nonlinearity increases as the pressure ratio increases. The effects of compressibility and rarefaction are opposite as Karniadakis et al. [1] demonstrated. When the pressure ratio is very small, the pressure distribution is nearly linear, which is close to an incompressible flow.

Karniadakis et al. [1] simulated nitrogen flow in a microchannel. The microchannel is 1.25 μm high and 40 μm wide. Figure 4.20 shows the deviation from linear pressure distribution comparison between the proposed model Eq. (4.109) and Karniadakis et al. [1] simulation results. Equation (4.109) agrees with Karniadakis et al. [1] simulation results very well.

It is clear that the pressure distribution may be predicted from Eq. (4.102), Eq. (4.103) or Eq.(4.108) according to different known conditions. The pressure distribution models

can provide quite accurate results. The mass flow rate may be predicted from Eq. (4.105) for most non-circular microchannels, provided an appropriate definition of the aspect ratio is chosen. The maximum deviation of exact values is less than 10 percent.

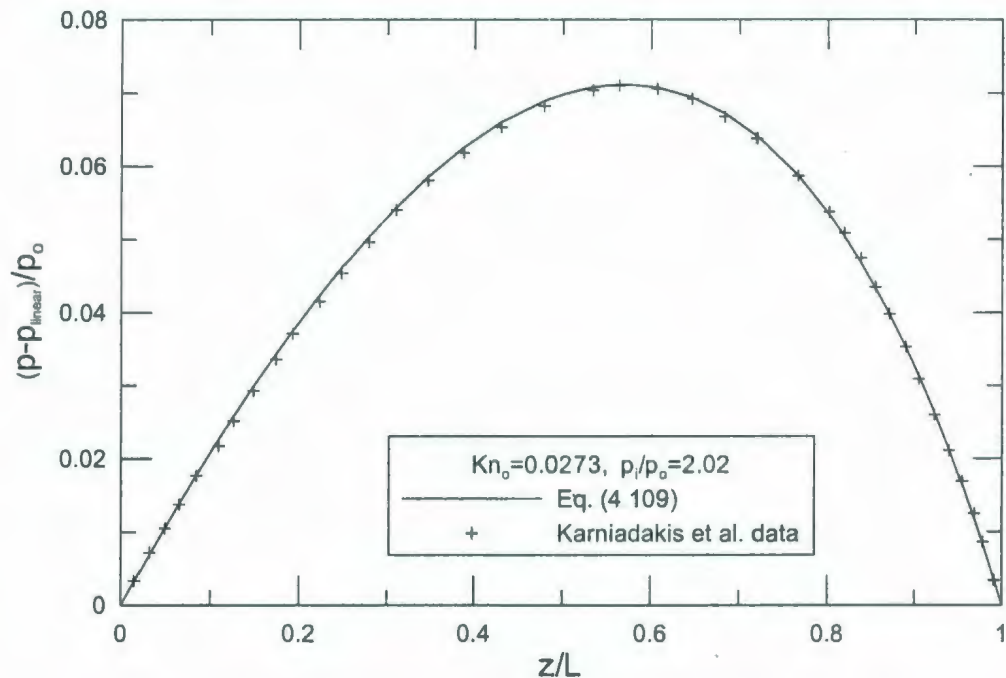


Figure 4.20 Deviation from linear pressure distribution comparison for Kariadakis et al. [1] numerical data.

Compressibility effects on slip flow in non-circular microchannels have been examined. Simple models were developed for predicting the pressure distribution and mass flow rate in non-circular microchannels for slip flow. The effects of momentum changes were considered in the models. The effect of the momentum flux becomes gradually significant with an increase in Mach number. The developed pressure distribution and mass flow rate models can provide very accurate results. The accuracy of the developed models has been examined with some experimental measurements and

numerical analysis. As for slip flow no solutions exist for most geometries, the developed models may be used to predict mass flow rate and pressure distribution of slip flow in non-circular microchannels.

4.6 Summary

This chapter investigated fully developed slip flow in microchannels. Microchannel shape effects and compressibility effects were considered. Some robust models for predicting slip flow characteristics were developed. An analytical solution of Poiseuille number was obtained using separation of variables in elliptic cylinder coordinates. Slip flow in non-circular microchannels has been investigated and a simple model was proposed to predict the friction factor Reynolds product in non-circular microchannels. The developed model took advantage of the selection of a more appropriate characteristic length scale square root of flow area to develop a simple model. The accuracy of the developed model was found to be within 10 percent, with most data for practical configurations within 5 percent. Compressibility effects on slip flow in non-circular microchannels have been examined and simple models were developed to predict the pressure distribution and mass flow rate. The effects of momentum changes were taken into account in the models.

Chapter 5

Slip Flow in the Hydrodynamic Entrance of Microchannels

5.1 Introduction

For developing continuum flow ($Kn=0$), some solutions or tabulated data exist for some geometries [106]. However, for developing slip flow, only parallel plates and circular duct are considered in the literature due to the slip boundary conditions which make this particular hydrodynamically developing flow problem, even more complicated. A survey of the available literature indicates a shortage of information for three dimensional entrance flows in the slip regime, such as short non-circular microchannels where the entrance region plays a very important role. There currently is no published model or tabulated data which can be utilized by the research community.

When a viscous fluid enters a duct with the uniform velocity distribution at the entrance, boundary layers develop along the walls and the velocity is gradually redistributed due to the viscosity. Eventually the fluid will reach a location where the velocity is independent of the axial direction, and under such conditions the flow is termed hydrodynamically fully developed. The hydrodynamic entrance length is defined as the duct length required to achieve a maximum velocity of 99% of that for fully developed flow. Following Sparrow et al. [112], slip flow in the entrance of circular and

parallel plate microchannels is first considered by solving a linearized momentum equation respectively. Sparrow et al. only considered the channel using the linearization method. In this analysis the compressibility effects can be neglected.

5.2 Circular Tubes

The equations of continuity and momentum in Cartesian coordinates are

$$\frac{1}{r} \frac{\partial}{\partial r} (rv) + \frac{\partial u}{\partial x} = 0 \quad (5.1)$$

$$v \frac{\partial u}{\partial r} + u \frac{\partial v}{\partial x} = -\frac{1}{\rho} \frac{dp}{dx} + \nu \frac{\partial}{\partial r} \left(r \frac{\partial u}{\partial r} \right) \quad (5.2)$$

assuming that dp/dx is independent of r .

By using the continuity Eq. (5.1), Eq. (5.2) can be rewritten as

$$\frac{\partial}{\partial x} (ru^2) + \frac{\partial}{\partial r} (ruv) = -\frac{r}{\rho} \frac{dp}{dx} + \nu \frac{\partial}{\partial r} \left(r \frac{\partial u}{\partial r} \right) \quad (5.3)$$

Integrating Eq. (5.3) with respect to r from 0 to R , there is obtained

$$-\frac{1}{\rho} \frac{dp}{dx} = \frac{2}{R^2} \frac{\partial}{\partial x} \int_0^R ru^2 dr - \frac{2\nu}{R} \left(\frac{\partial u}{\partial r} \right)_{r=R} \quad (5.4)$$

Eliminating dp/dx from Eqs. (5.2) and (5.4) and rearranging

$$\bar{u} \frac{\partial u}{\partial x} + \frac{2\nu}{R} \left(\frac{\partial u}{\partial r} \right)_{r=R} - \frac{\nu}{r} \frac{\partial}{\partial r} \left(r \frac{\partial u}{\partial r} \right) = (\bar{u} - u) \frac{\partial u}{\partial x} - \nu \frac{\partial u}{\partial r} + \frac{2}{R^2} \frac{\partial}{\partial x} \int_0^R ru^2 dr \quad (5.5)$$

The cross-sectional average of the terms on the right side of Eq. (5.5) is zero. This follows by integrating Eq. (5.5) across the section and employing that $\partial/\partial x \left(\int_0^R r u dr \right)$ is zero from continuity equation. Hence, the right side is equated to zero as a linearizing approximation. The equation to be solved becomes

$$\frac{v}{r} \frac{\partial}{\partial r} \left(r \frac{\partial u}{\partial r} \right) = \bar{u} \frac{\partial u}{\partial x} + \frac{2v}{R} \left(\frac{\partial u}{\partial r} \right)_{r=R} \quad (5.6)$$

From the above analysis we obtain Targ's linearization results [106]:

$$v \frac{\partial u}{\partial r} + u \frac{\partial u}{\partial x} = \bar{u} \frac{\partial u}{\partial x}$$

$$\frac{1}{\rho} \frac{dp}{dx} = \frac{2v}{R} \left(\frac{\partial u}{\partial r} \right)_{r=R}$$

Introducing the dimensionless variables $\xi = (x/D)/(\bar{u}D/v)$, $\eta = r/R$, and $U = u/\bar{u}$, Eq. (5.6) becomes

$$\frac{1}{\eta} \frac{\partial}{\partial \eta} \left(\eta \frac{\partial U}{\partial \eta} \right) = \frac{1}{4} \frac{\partial U}{\partial \xi} + 2 \left(\frac{\partial U}{\partial \eta} \right)_{\eta=1} \quad (5.7)$$

The velocity distribution must satisfy the slip boundary condition at the walls. The local slip velocity is proportional to the local velocity gradient normal to the wall. The appropriate boundary conditions are

$$U(1, \xi) = -\frac{2-\sigma}{\sigma} 2Kn(\partial U / \partial \eta)_{\eta=1} \quad (5.8)$$

$$\left(\frac{\partial U}{\partial \eta} \right)_{\eta=0} = 0 \quad (5.9)$$

$$U(\eta, 0) = 1 \quad (5.10)$$

$$U(\eta, \infty) = U_{fd}(\eta) \quad (5.11)$$

The Knudsen number is defined as $Kn = \lambda/D_h$ and λ is the molecular mean free path.

We can write a solution of the form

$$U(\eta, \xi) = U_{fd}(\eta) + V(\eta, \xi) \quad (5.12)$$

where $V(\eta, \xi)$ essentially represents the deviation from the fully developed flow velocity distribution. It is obvious that V approaches zero for large ξ .

Substituting Eq. (5.12) into Eq. (5.7), we find that $U_{fd}(\eta)$ satisfies the equation

$$\frac{1}{\eta} \frac{\partial}{\partial \eta} \left(\eta \frac{dU_{fd}}{d\eta} \right) = 2 \left(\frac{dU_{fd}}{d\eta} \right)_{\eta=1} \quad (5.13)$$

and $V(\eta, \xi)$ satisfies the equation

$$\frac{1}{\eta} \frac{\partial}{\partial \eta} \left(\eta \frac{\partial V}{\partial \eta} \right) = \frac{1}{4} \frac{\partial V}{\partial \xi} + 2 \left(\frac{\partial V}{\partial \eta} \right)_{\eta=1} \quad (5.14)$$

A solution of Eq. (5.13) may be obtained using Eqs. (5.8) and (5.9) and the continuity

$$\text{condition } \int_0^1 \eta U_{fd}(\eta) d\eta = 1/2$$

$$U_{fd}(\eta) = \frac{8 \frac{2-\sigma}{\sigma} Kn}{1 + 8 \frac{2-\sigma}{\sigma} Kn} + \frac{2}{1 + 8 \frac{2-\sigma}{\sigma} Kn} (1 - \eta^2) \quad (5.15)$$

Equation (5.14) can be solved using separation of variables method. Thus,

$$V(\eta, \xi) = F(\xi)G(\eta) \quad (5.16)$$

Substituting Eq. (5.16) into Eq. (5.14), we obtain

$$F_i(\xi) = C_i \exp(-4\alpha_i^2 \xi) \quad (5.17)$$

$$\frac{1}{\eta} \frac{d}{d\eta} \left(\eta \frac{dG_i}{d\eta} \right) + \alpha_i^2 G_i = 2 \left(\frac{dG_i}{d\eta} \right)_{\eta=1} \quad (5.18)$$

where α_i are the eigenvalues.

We find that a particular solution of Eq. (5.18) is

$$G_i^p(\eta) = \frac{2}{\alpha_i^2} \left(\frac{dG_i}{d\eta} \right)_{\eta=1} \quad (5.19)$$

The homogeneous equation is Bessel's equation of zero order and the solution is

$$G_i^h(\eta) = A_i J_0(\alpha_i \eta) + B_i Y_0(\alpha_i \eta) \quad (5.20)$$

In terms of Eq. (5.9), $B_i = 0$, and thus the solution of Eq. (5.18) is

$$G_i(\eta) = G_i^p(\eta) + G_i^h(\eta) = A_i J_0(\alpha_i \eta) + \frac{2}{\alpha_i^2} \left(\frac{dG_i}{d\eta} \right)_{\eta=1} \quad (5.21)$$

then

$$\left(\frac{dG_i}{d\eta} \right)_{\eta=1} = -\alpha_i A_i J_1(\alpha_i) \quad (5.22)$$

Therefore, the solution for $G_i(\eta)$ is obtained

$$G_i(\eta) = \frac{A_i}{\alpha_i} [\alpha_i J_0(\alpha_i \eta) - 2J_1(\alpha_i)] \quad (5.23)$$

According to boundary condition Eq. (5.8), we find the eigenvalue α_i satisfies the following equation

$$\alpha_i J_0(\alpha_i) - 2 \left(1 + \frac{2-\sigma}{\sigma} Kn \alpha_i^2 \right) J_1(\alpha_i) = 0 \quad (5.24)$$

In addition, the coefficients A_i can be chosen so as to normalize the G_i in terms of the Sturm-Liouville orthogonality conditions, that is $\int_0^1 \eta G_i^2 d\eta = 0.5$

$$A_i = \left[\frac{2\alpha_i^2}{\alpha_i^2 J_0^2(\alpha_i) + (\alpha_i^2 - 4) J_1^2(\alpha_i)} \right]^{1/2} \quad (5.25)$$

Thus, the G_i form a complete orthonormal set.

Applying the entrance condition, Eq. (5.10),

$$V(\eta, 0) = 1 - U_{fd}(\eta) = \sum_{i=1}^{\infty} C_i G_i(\eta)$$

Using the orthonormality properties of G_i , the coefficients C_i can be determined

$$C_i = \frac{2}{1 + 8 \frac{2-\sigma}{\sigma} Kn} \int_0^1 \eta^3 G_i(\eta) d\eta \quad (5.26)$$

Substituting Eq. (5.23) into Eq. (5.26), we obtain

$$C_i = \frac{A_i}{\alpha_i^3 \left(1 + 8 \frac{2-\sigma}{\sigma} Kn \right)} \left[4\alpha_i J_0(\alpha_i) + (\alpha_i^2 - 8) J_1(\alpha_i) \right] \quad (5.27)$$

Therefore,

$$\begin{aligned} V(\eta, \xi) &= \sum_{i=1}^{\infty} \frac{C_i A_i}{\alpha_i} \exp(-4\alpha_i^2 \xi) \left[\alpha_i J_0(\alpha_i \eta) - 2 J_1(\alpha_i) \right] = \sum_{i=1}^{\infty} \frac{4 \left(1 + \alpha_i^2 \frac{2-\sigma}{\sigma} Kn \right)}{\alpha_i^2 \left[1 + 8 \frac{2-\sigma}{\sigma} Kn + 4 \left(\alpha_i \frac{2-\sigma}{\sigma} Kn \right)^2 \right]} \\ &\quad \left[\frac{J_0(\alpha_i \eta)}{J_0(\alpha_i)} - \frac{2}{2 + 2\alpha_i^2 \frac{2-\sigma}{\sigma} Kn} \right] \exp(-4\alpha_i^2 \xi) \end{aligned} \quad (5.28)$$

Finally, the complete velocity solution is

$$U(\eta, \xi) = \frac{8 \frac{2-\sigma}{\sigma} Kn}{1 + 8 \frac{2-\sigma}{\sigma} Kn} + \frac{2}{1 + 8 \frac{2-\sigma}{\sigma} Kn} (1 - \eta^2) \\ + \sum_{i=1}^{\infty} \frac{4 \left(1 + \alpha_i^2 \frac{2-\sigma}{\sigma} Kn \right)}{\alpha_i^2 \left[1 + 8 \frac{2-\sigma}{\sigma} Kn + 4 \left(\alpha_i \frac{2-\sigma}{\sigma} Kn \right)^2 \right]} + \left[\frac{J_0(\alpha_i \eta)}{J_0(\alpha_i)} - \frac{2}{2 + 2\alpha_i^2 \frac{2-\sigma}{\sigma} Kn} \right] \exp(-4\alpha_i^2 \xi) \quad (5.29)$$

Figure 5.1 shows the effect of ξ on the development of the velocity for $Kn^*=0.01$.

Figure 5.2 illustrates the dimensionless entrance development length $L^+ (L/D_h \text{Re}_{D_h})$ as a function of Kn ($0.001 \leq Kn \leq 0.1$). The values of L^+ corresponding to the point where $U(0, \xi) = 0.99 U_{fd}(0)$. They are fitted a simple correlation:

$$L^+ = 0.0396 \left[1 + 3.7 \frac{2-\sigma}{\sigma} Kn - 15 \left(\frac{2-\sigma}{\sigma} Kn \right)^2 \right] \quad (5.30)$$

For the continuum flow entrance length, Atkinson et al. [113] presented a simple relationship

$$\frac{L}{D} = 0.59 + 0.056 \text{Re} \quad (5.31)$$

Chen et al. [114] suggested a form using the development length data of Friedmann et al. [115]:

$$\frac{L}{D} = \frac{0.60}{0.035 \text{Re} + 1} + 0.056 \text{Re} \quad (5.32)$$

The entrance length does not vanish as Re approaches zero. It still takes about 0.6 tube diameter. Finally, we present a relationship for slip flow entrance length:

$$\frac{L}{D} = \frac{0.60}{0.035 Re + 1} + 0.0396 Re \left[1 + 3.7 \frac{2-\sigma}{\sigma} Kn - 15 \left(\frac{2-\sigma}{\sigma} Kn \right)^2 \right] \quad (5.33)$$

where we use the first term of Chen's development length formula, Eq. (5.32). Sreekanth [110] calculated the entrance lengths of his experiments and found that they agree with values predicted by the expression $L^+ = K/4$, where K has a value between 0.15 and 0.2 depending on the Kn . Therefore, Sreekanth's experiments approximately agree with Eq. (5.30).

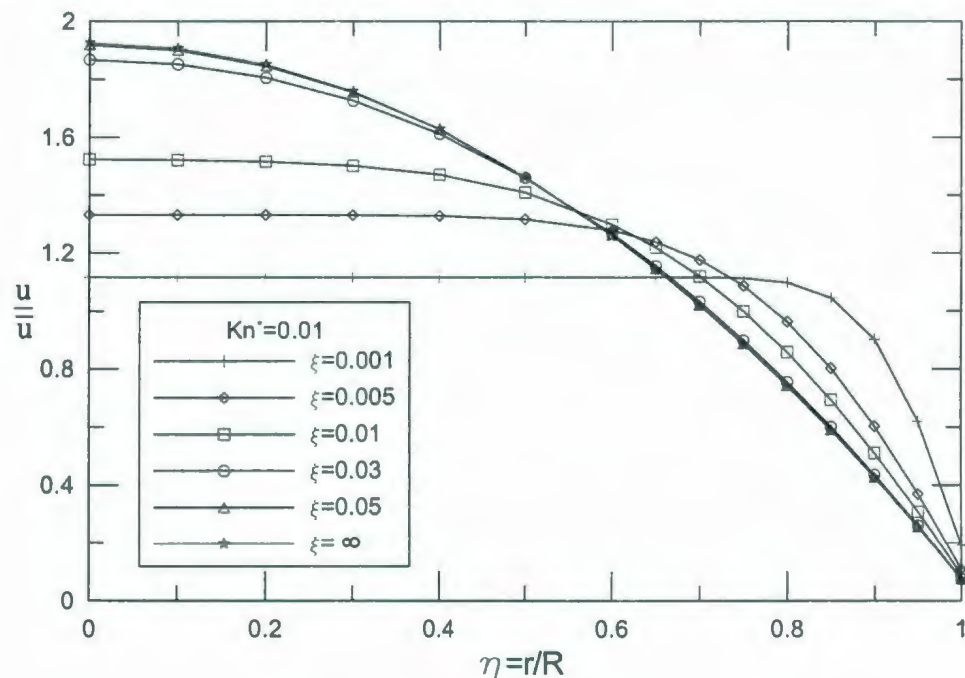


Figure 5.1 Effect of ξ on development of velocity profiles for $Kn^* = 0.01$ for circular tubes.

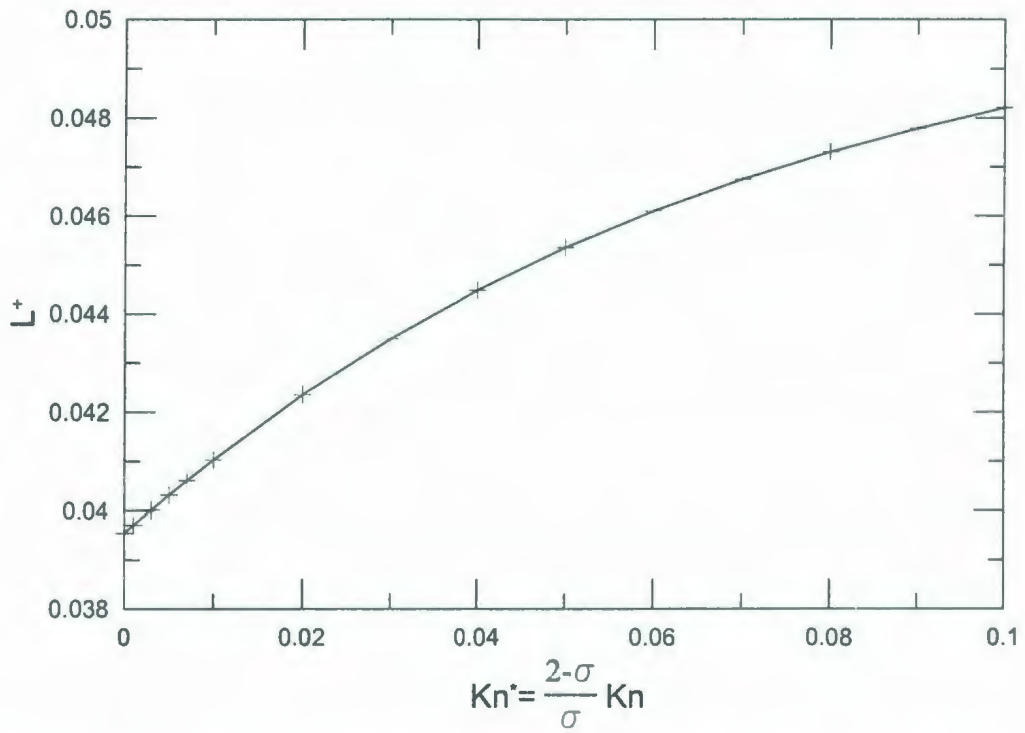


Figure 5.2 Entrance length for which $U(0, \xi) = 0.99 U_{fd}(0)$ for circular tubes.

The pressure drop between the entrance and any station downstream can be found by integrating the momentum equation. Equation (5.4) can be written as

$$-\frac{1}{4\left(\frac{1}{2}\rho\bar{u}^2\right)}\frac{dp}{d\xi} = \frac{\partial}{\partial\xi} \int_0^1 \eta U^2(\eta, \xi) d\eta - 4\left(\frac{\partial U}{\partial\eta}\right)_{\eta=1} \quad (5.34)$$

Under fully developed conditions, the inertia terms in Eq. (5.34) disappear. Therefore,

$$\frac{1}{4\left(\frac{1}{2}\rho\bar{u}^2\right)}\frac{dp}{d\xi} = 4\left(\frac{\partial U_{fd}}{\partial\eta}\right)_{\eta=1} \quad (5.35)$$

Equation (5.35) is integrated between 0 and ξ , giving

$$\frac{[p(0) - p(\xi)]_{fd}}{\frac{1}{2} \rho \bar{u}^2} = -16 \int_0^\xi \left(\frac{\partial U_{fd}}{\partial \eta} \right)_{\eta=1} d\xi = \frac{64\xi}{1 + 8 \frac{2-\sigma}{\sigma} Kn} \quad (5.36)$$

It is convenient to report the pressure drop in a developing flow as equal to that for a fully-developed flow plus a correction term $K(\xi)$ representing additional pressure drop which exceeds the fully developed pressure drop. Thus,

$$\frac{p(0) - p(\xi)}{\frac{1}{2} \rho \bar{u}^2} = \frac{64\xi}{1 + 8 \frac{2-\sigma}{\sigma} Kn} + K(\xi) \quad (5.37)$$

Integrating Eq. (5.34) between 0 and ξ , we can obtain the following expression

$$\frac{p(0) - p(\xi)}{\frac{1}{2} \rho \bar{u}^2} = 4 \left[\int_0^1 \eta U^2 d\eta - \frac{1}{2} - 4 \int_0^\xi \left(\frac{\partial U}{\partial \eta} \right)_{\eta=1} d\xi \right] \quad (5.38)$$

Thus,

$$\begin{aligned} K(\xi) &= 4 \left[\int_0^1 \eta U^2 d\eta - \frac{1}{2} - 4 \int_0^\xi \left(\frac{\partial V}{\partial \eta} \right)_{\eta=1} d\xi \right] \\ &= \frac{4}{3 \left(1 + 8 \frac{2-\sigma}{\sigma} Kn \right)^2} - 8 \sum_{i=1}^{\infty} \frac{[3 - \exp(-4\alpha_i^2 \xi)] \exp(-4\alpha_i^2 \xi)}{\alpha_i^2 \left(1 + 8 \frac{2-\sigma}{\sigma} Kn + 4 \left(\alpha_i \frac{2-\sigma}{\sigma} Kn \right)^2 \right)} \end{aligned} \quad (5.39)$$

From an inspection of Eq. (5.39), it is found that $K(0)$ is zero and $K(\infty)$ is given by

$$K(\infty) = \frac{4}{3 \left(1 + 8 \frac{2-\sigma}{\sigma} Kn \right)^2} \quad (5.40)$$

which is the fully-developed value of incremental pressure drop factor.

Figure 5.3 shows the variation of the excess pressure drop function $K(\xi)$ with ξ for various values of Kn . It is seen that the effect of increasing Kn is to decrease $K(\xi)$. The excess pressure drop function for continuum flow and finite difference solutions from White [90] are in agreement.

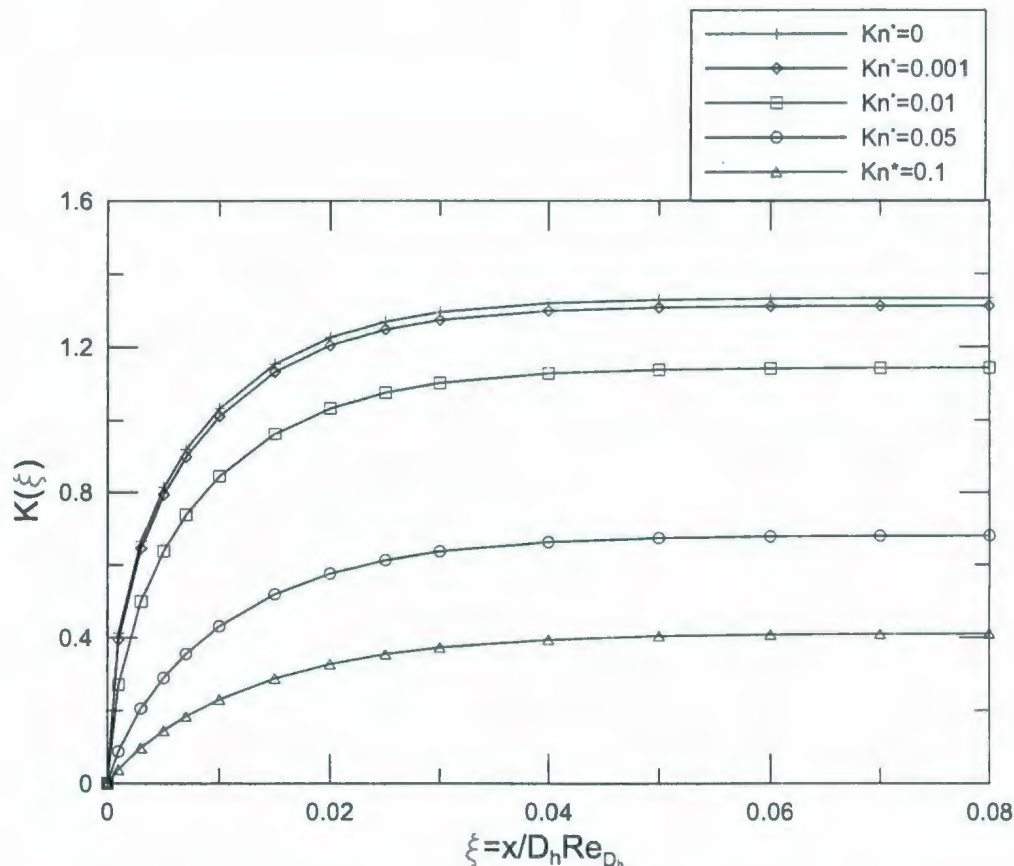


Figure 5.3 Effect of Kn^* on excess pressure drop for circular tubes.

Substituting Eq. (5.39) into Eq. (5.37), the apparent friction factor Reynolds product for circular tubes can be obtained

$$f_{app} Re_{D_h} = \frac{16}{1 + 8 \frac{2-\sigma}{\sigma} Kn} + \frac{1}{3\xi \left(1 + 8 \frac{2-\sigma}{\sigma} Kn\right)^2} - 2 \sum_{i=1}^{\infty} \frac{(3 - \exp(-4\alpha_i^2 \xi)) \exp(-4\alpha_i^2 \xi)}{\alpha_i^2 \xi \left(1 + 8 \frac{2-\sigma}{\sigma} Kn + 4 \left(\alpha_i \frac{2-\sigma}{\sigma} Kn\right)^2\right)} \quad (5.41)$$

The effects of Kn on $f_{app}Re$ for developing laminar flow is illustrated in Figure 5.4. It is seen that the effect of increasing Kn is to decrease apparent friction factor.

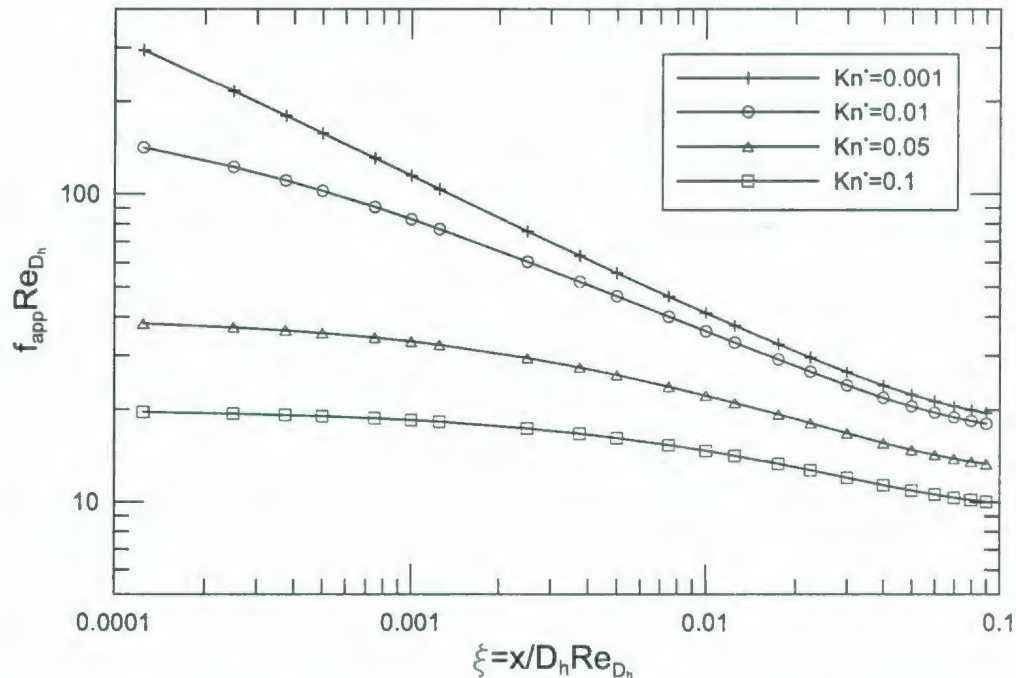


Figure 5.4 Effect of Kn^* on $f_{app}Re$ for developing laminar flow for circular tubes.

5.3 Parallel Plates

Next, following Sparrow et al. [112], we consider the flow in hydrodynamic entrance region under slip conditions between parallel plate microchannels. The solution is considered in detail as Sparrow et al. only showed the developing velocity profiles. The microchannel height is $2h$ and there is symmetry about $y=0$. The equations of continuity and momentum in Cartesian coordinates are

$$\frac{\partial u}{\partial x} + \frac{\partial v}{\partial y} = 0 \quad (5.42)$$

$$u \frac{\partial u}{\partial x} + v \frac{\partial u}{\partial y} = -\frac{1}{\rho} \frac{dp}{dx} + \nu \frac{\partial^2 u}{\partial y^2} \quad (5.43)$$

assuming that dp/dx is independent of y .

Using continuity Eq. (5.42), we can rewrite Eq. (5.43) as

$$\frac{\partial u^2}{\partial x} + \frac{\partial(uv)}{\partial y} = -\frac{1}{\rho} \frac{dp}{dx} + \nu \frac{\partial^2 u}{\partial y^2} \quad (5.44)$$

Integrating Eq. (5.44) with respect to y from 0 to h , there is obtained

$$-\frac{1}{\rho} \frac{dp}{dx} = \frac{1}{h} \frac{\partial}{\partial x} \int_0^h u^2 dy - \frac{\nu}{h} \left(\frac{\partial u}{\partial y} \right)_{y=h} \quad (5.45)$$

Eliminating dp/dx from Eqs. (5.43) and (5.45) and rearranging

$$\bar{u} \frac{\partial u}{\partial x} + \frac{\nu}{h} \left(\frac{\partial u}{\partial y} \right)_{y=h} - \nu \frac{\partial^2 u}{\partial y^2} = (\bar{u} - u) \frac{\partial u}{\partial x} - \nu \frac{\partial u}{\partial y} + \frac{1}{h} \frac{\partial}{\partial x} \int_0^h u^2 dy \quad (5.46)$$

The cross-sectional average of the terms on the right side of Eq. (5.46) is zero. This follows by integrating Eq. (5.46) across the section and employing that $\partial/\partial x \left(\int_0^h u dy \right)$ is zero from continuity equation. Hence, the right side is equated to zero as a linearizing approximation. The equation thus to be solved becomes

$$\nu \frac{\partial^2 u}{\partial y^2} = \bar{u} \frac{\partial u}{\partial x} + \frac{\nu}{h} \left(\frac{\partial u}{\partial y} \right)_{y=h} \quad (5.47)$$

Also, from the above analysis we obtain Targ's linearization results [106]:

$$u \frac{\partial u}{\partial x} + \nu \frac{\partial u}{\partial y} = \bar{u} \frac{\partial u}{\partial x}$$

$$\frac{1}{\rho} \frac{dp}{dx} = \frac{\nu}{h} \left(\frac{\partial u}{\partial y} \right)_{y=h}$$

Introducing the dimensionless variables, $\xi = (x/D_h)/(\bar{u}D_h/\nu)$, $\eta = y/h$, and $U = u/\bar{u}$, Eq. (5.47) becomes

$$\frac{\partial^2 U}{\partial \eta^2} = \frac{1}{16} \frac{\partial U}{\partial \xi} + \left(\frac{\partial U}{\partial \eta} \right)_{\eta=1} \quad (5.48)$$

The appropriate boundary conditions are

$$U(1, \xi) = -\frac{2-\sigma}{\sigma} 4Kn (\partial U / \partial \eta)_{\eta=1} \quad (5.49)$$

$$\left(\frac{\partial U}{\partial \eta} \right)_{\eta=0} = 0 \quad (5.50)$$

$$U(\eta, 0) = 1 \quad (5.51)$$

$$U(\eta, \infty) = U_{fd}(\eta) \quad (5.52)$$

We can write a solution of the form

$$U(\eta, \xi) = U_{fd}(\eta) + V(\eta, \xi) \quad (5.53)$$

where $V(\eta, \xi)$ is the deviation from the fully developed flow velocity distribution. It is evident that V approach zero for large ξ .

Substituting Eq. (5.53) into Eq. (5.48), we find that $U_{fd}(\eta)$ satisfies the equation

$$\frac{d^2 U_{fd}}{d\eta^2} = \left(\frac{dU_{fd}}{d\eta} \right)_{\eta=1} \quad (5.54)$$

and $V(\eta, \xi)$ satisfies the equation

$$\frac{\partial^2 V}{\partial \eta^2} = \frac{1}{16} \frac{\partial V}{\partial \xi} + \left(\frac{\partial V}{\partial \eta} \right)_{\eta=1} \quad (5.55)$$

A solution of Eq. (5.54) may be obtained using Eqs. (5.49) and (5.50) and the continuity condition $\int_0^1 U_{jd}(\eta) d\eta = 1$

$$U_{jd}(\eta) = \frac{12 \frac{2-\sigma}{\sigma} Kn}{1 + 12 \frac{2-\sigma}{\sigma} Kn} + \frac{1.5}{1 + 12 \frac{2-\sigma}{\sigma} Kn} (1 - \eta^2) \quad (5.56)$$

Equation (5.55) can be solved using separation of variables method. Thus,

$$V(\eta, \xi) = F(\xi)G(\eta) \quad (5.57)$$

Substituting Eq. (5.57) into Eq. (5.55), we obtain

$$F_i(\xi) = C_i \exp(-16\alpha_i^2 \xi) \quad (5.58)$$

$$\frac{d^2 G_i}{d\eta^2} + \alpha_i^2 G_i = \left(\frac{dG_i}{d\eta} \right)_{\eta=1} \quad (5.59)$$

where α_i are the eigenvalues.

We find that a particular solution of Eq. (5.59) is

$$G_i^p(\eta) = \frac{1}{\alpha_i^2} \left(\frac{dG_i}{d\eta} \right)_{\eta=1} \quad (5.60)$$

The solution of the homogeneous equation is

$$G_i^h(\eta) = A_i \cos(\alpha_i \eta) + B_i \sin(\alpha_i \eta) \quad (5.61)$$

In terms of Eq. (5.50), $B_i = 0$, and thus the solution of Eq. (5.59) is

$$G_i(\eta) = G_i^p(\eta) + G_i^h(\eta) = A_i \cos(\alpha_i \eta) + \frac{1}{\alpha_i^2} \left(\frac{dG_i}{d\eta} \right)_{\eta=1} \quad (5.62)$$

then

$$\left(\frac{dG_i}{d\eta} \right)_{\eta=1} = -\alpha_i A_i \sin(\alpha_i) \quad (5.63)$$

Therefore, the solution for $G_i(\eta)$ is obtained

$$G_i(\eta) = \frac{A_i}{\alpha_i} [\alpha_i \cos(\alpha_i \eta) - \sin(\alpha_i)] \quad (5.64)$$

According to boundary condition Eq. (5.49), we find the eigenvalue α_i satisfies the following equation

$$\tan(\alpha_i) = \frac{\alpha_i}{1 + 4\alpha_i^2 \frac{2-\sigma}{\sigma} Kn} \quad (5.65)$$

Also, the coefficients A_i can be chosen in order to normalize the G_i in terms of the Sturm-

Liouville orthogonality conditions, that is $\int_{-1}^1 G_i^2 d\eta = 1$

$$A_i = -\frac{1}{\sin(\alpha_i)} \left[1 + 12 \frac{2-\sigma}{\sigma} Kn + 16 \left(\alpha_i \frac{2-\sigma}{\sigma} Kn \right)^2 \right]^{-\frac{1}{2}} \quad (5.66)$$

Thus, the G_i form a complete orthonormal set.

Applying the entrance condition, Eq. (5.51),

$$V(\eta, 0) = 1 - U_{\text{fl}}(\eta) = \sum_{i=1}^{\infty} C_i G_i(\eta)$$

Using the orthonormality properties of G_i , the coefficients C_i can be determined

$$C_i = \frac{1.5}{1 + 12 \frac{2-\sigma}{\sigma} Kn} \int_1^1 \eta^2 G_i(\eta) d\eta \quad (5.67)$$

Substituting Eq. (5.64) into Eq. (5.67), we obtain

$$C_i = \frac{2A_i \sin(\alpha_i)}{\alpha_i} \quad (5.68)$$

Therefore,

$$\begin{aligned} V(\eta, \xi) &= \sum_{i=1}^{\infty} \frac{2A_i^2 \sin(\alpha_i)}{\alpha_i^2} [\alpha_i \cos(\alpha_i \eta) - \sin(\alpha_i \eta)] \exp(-16\alpha_i^2 \xi) \\ &= \sum_{i=1}^{\infty} \frac{2[\alpha_i \cos(\alpha_i \eta) - \sin(\alpha_i \eta)] \exp(-16\alpha_i^2 \xi)}{\alpha_i^2 \sin(\alpha_i) \left[1 + 12 \frac{2-\sigma}{\sigma} Kn + 16 \left(\alpha_i \frac{2-\sigma}{\sigma} Kn \right)^2 \right]} \end{aligned} \quad (5.69)$$

Finally, the complete velocity solution is

$$U(\eta, \xi) = \frac{12 \frac{2-\sigma}{\sigma} Kn}{1 + 12 \frac{2-\sigma}{\sigma} Kn} + \frac{1.5}{1 + 12 \frac{2-\sigma}{\sigma} Kn} (1 - \eta^2) \\ + \sum_{i=1}^{\infty} \frac{2[\alpha_i \cos(\alpha_i \eta) - \sin(\alpha_i)] \exp(-16\alpha_i^2 \xi)}{\alpha_i^2 \sin(\alpha_i) \left[1 + 12 \frac{2-\sigma}{\sigma} Kn + 16 \left(\alpha_i \frac{2-\sigma}{\sigma} Kn \right)^2 \right]} \quad (5.70)$$

Figure 5.5 shows the effect of ξ on the development of the velocity for $Kn^* = 0.005$.

Figure 5.6 illustrates the dimensionless entrance development length L^+ as a function of Kn ($0.001 \leq Kn \leq 0.1$). The values of L^+ corresponding to the point where $U(0, \xi) = 0.99 U_{fd}(0)$. They are fitted a simple correlation:

$$L^+ = 0.0112 \left[1 + 6.7 \frac{2-\sigma}{\sigma} Kn - 37 \left(\frac{2-\sigma}{\sigma} Kn \right)^2 \right] \quad (5.71)$$

For the continuum flow entrance length, Atkinson et al. [113] suggested a simple relationship

$$\frac{L}{D_h} = 0.3125 + 0.011 Re \quad (5.72)$$

Chen [114] proposed an equation similar to Eq. (5.32)

$$\frac{L}{D_h} = \frac{0.315}{0.0175 Re + 1} + 0.011 Re \quad (5.73)$$

The entrance length does not vanish as Re approaches zero. It still takes about 0.63 plate separation. Finally, we suggest a relationship for slip flow entrance length:

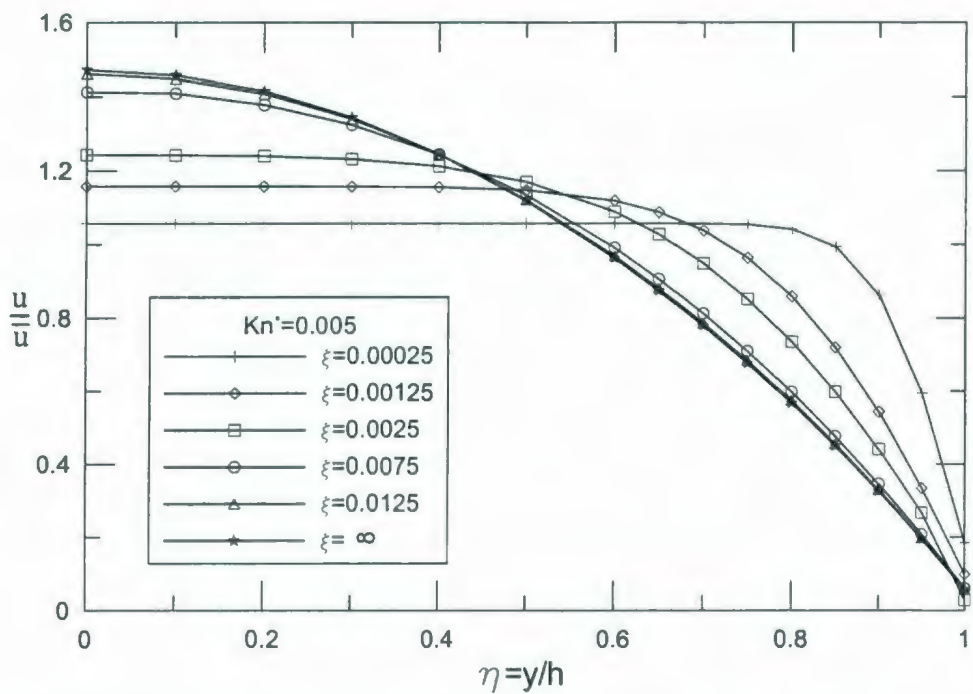


Figure 5.5 Effect of ξ on development of velocity profiles for $Kn^* = 0.005$ for parallel plates.

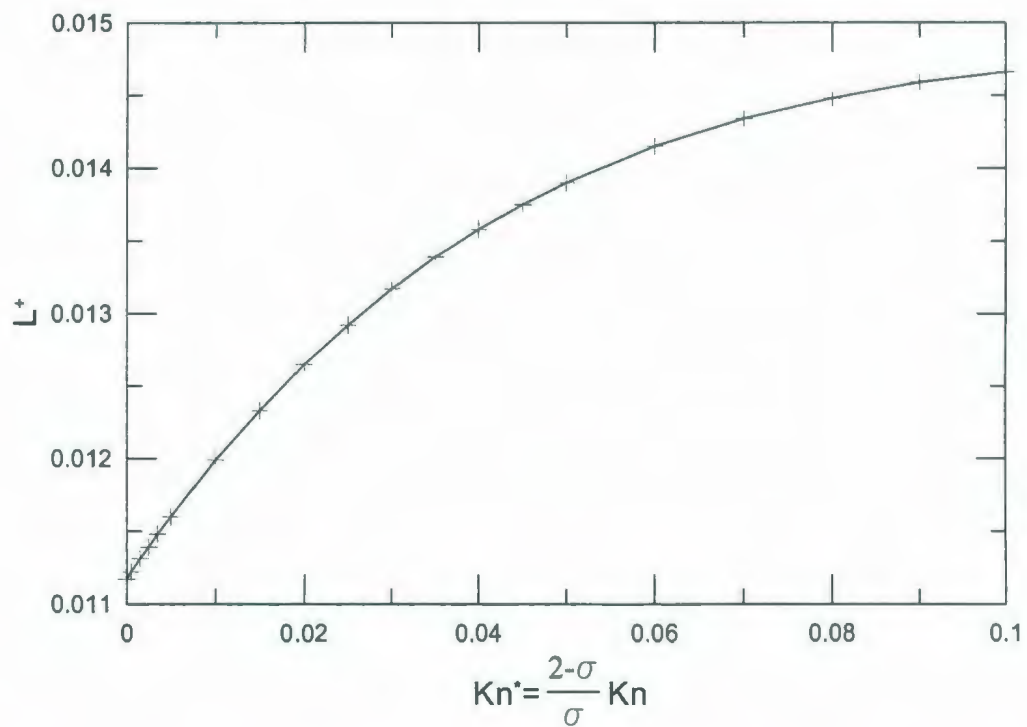


Figure 5.6 Entrance length for which $U(0,\xi) = 0.99 U_{fd}(0)$ for parallel plates.

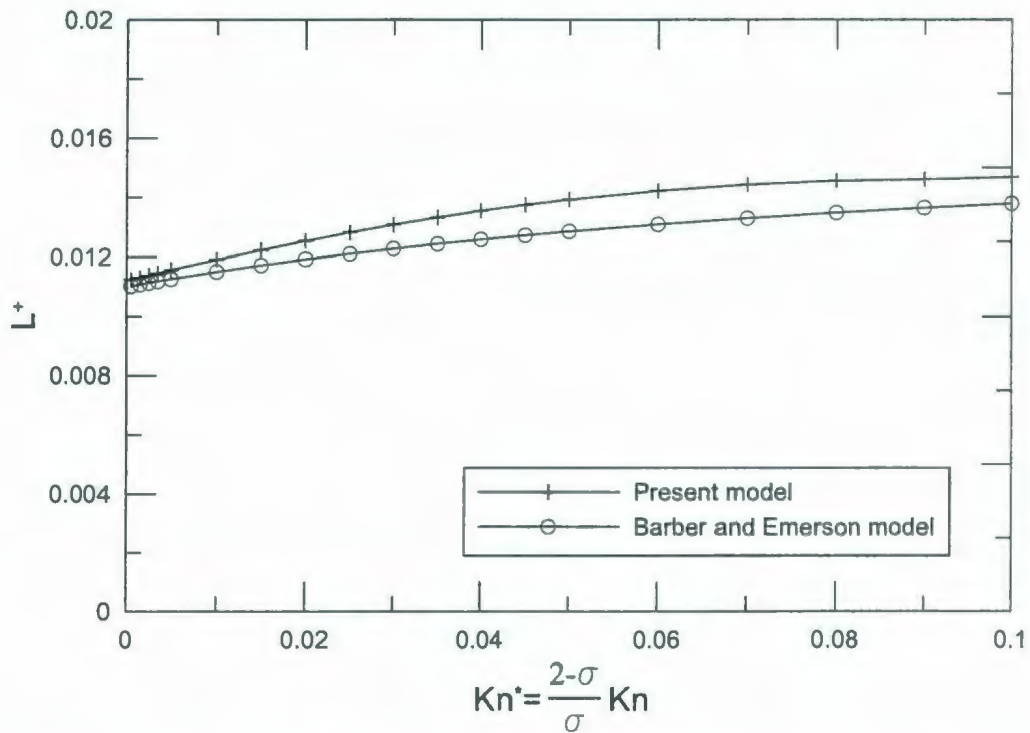


Figure 5.7 Entrance length comparison for Barber and Emerson numerical model.

$$\frac{L}{D_h} = \frac{0.315}{0.0175 \text{Re} + 1} + 0.0112 \text{Re} \left[1 + 6.7 \frac{2-\sigma}{\sigma} \text{Kn} - 37 \left(\frac{2-\sigma}{\sigma} \text{Kn} \right)^2 \right] \quad (5.74)$$

where we use the first term of Chen's development length formula, Eq. (5.73). It is seen that the effect of slip is to increase the entrance length.

Barber and Emerson [116] also suggested a curve fitted model using numerical data.

$$\frac{L}{D_h} = \frac{0.332}{0.0271 \text{Re} + 1} + 0.011 \text{Re} \left(\frac{1 + 14.78 \frac{2-\sigma}{\sigma} \text{Kn}}{1 + 9.78 \frac{2-\sigma}{\sigma} \text{Kn}} \right) \quad (5.75)$$

Figure 5.7 shows the comparison between present analytical model Eq. (5.74) and Barber and Emerson numerical model Eq. (5.75). The difference between present analytical model and Barber and Emerson numerical model is less than 8%.

The pressure drop between the entrance and any station downstream can be found by integrating the momentum equation. Equation (5.45) may be written as

$$-\frac{1}{2\left(\frac{1}{2}\rho\bar{u}^2\right)}\frac{dp}{d\xi} = \frac{\partial}{\partial\xi} \int_0^\xi U^2(\eta, \xi)d\eta - 16\left(\frac{\partial U}{\partial\eta}\right)_{\eta=1} \quad (5.76)$$

Under fully developed conditions, the inertia terms in Eq. (5.76) disappear. Therefore,

$$\frac{1}{2\left(\frac{1}{2}\rho\bar{u}^2\right)}\frac{dp}{d\xi} = 16\left(\frac{\partial U_{fd}}{\partial\eta}\right)_{\eta=1} \quad (5.77)$$

Equation (5.77) is integrated between 0 and ξ , giving

$$\frac{[p(0) - p(\xi)]_{fd}}{\frac{1}{2}\rho\bar{u}^2} = -32 \int_0^\xi \left(\frac{\partial U_{fd}}{\partial\eta}\right)_{\eta=1} d\xi = \frac{96\xi}{1 + 12\frac{2-\sigma}{\sigma}Kn} \quad (5.78)$$

Thus,

$$\frac{p(0) - p(\xi)}{\frac{1}{2}\rho\bar{u}^2} = \frac{96\xi}{1 + 12\frac{2-\sigma}{\sigma}Kn} + K(\xi) \quad (5.79)$$

Integrating Eq. (5.76) between 0 and ξ , we can obtain the following expression

$$\frac{p(0) - p(\xi)}{\frac{1}{2} \rho \bar{u}^2} = 2 \left[\int_0^1 U^2 d\eta - 1 - 16 \int_0^\xi \left(\frac{\partial U}{\partial \eta} \right)_{\eta=1} d\xi \right] \quad (5.80)$$

Therefore,

$$K(\xi) = 2 \left[\int_0^1 U^2 d\eta - 1 - 16 \int_0^\xi \left(\frac{\partial V}{\partial \eta} \right)_{\eta=1} d\xi \right] \\ = \frac{0.8}{\left(1 + 12 \frac{2-\sigma}{\sigma} Kn \right)^2} - 4 \sum_{i=1}^{\infty} \frac{\left[3 - \exp(-16\alpha_i^2 \xi) \right] \exp(-16\alpha_i^2 \xi)}{\alpha_i^2 \left[1 + 12 \frac{2-\sigma}{\sigma} Kn + 16 \left(\alpha_i^2 \frac{2-\sigma}{\sigma} Kn \right)^2 \right]} \quad (5.81)$$

From an inspection of Eq. (5.81), it is found that $K(0)$ is zero and $K(\infty)$ is given by

$$K(\infty) = \frac{0.8}{\left(1 + 12 \frac{2-\sigma}{\sigma} Kn \right)^2} \quad (5.82)$$

which is the fully developed value of incremental pressure drop factor.

Figure 5.8 shows the variation of the excess pressure drop function $K(\xi)$ with ξ for various values of Kn . It is seen that the effect of increasing Kn is to decrease $K(\xi)$. The excess pressure drop function for continuum flow and finite difference solutions from White [90] are in agreement.

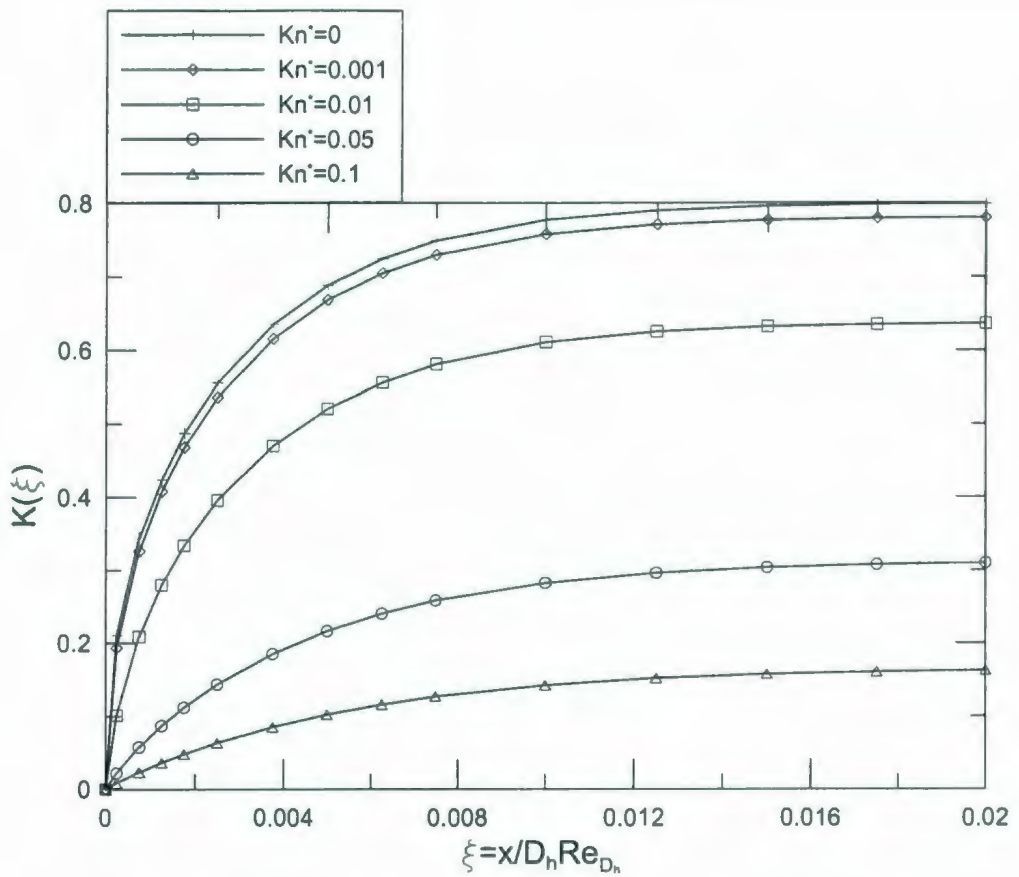


Figure 5.8 Effect of Kn^* on excess pressure drop for parallel plates.

Substituting Eq. (5.81) into Eq. (5.79), the apparent friction factor Reynolds product for parallel plates can be obtained

$$f_{app} \text{Re}_{D_h} = \frac{24}{1+12\frac{2-\sigma}{\sigma}Kn} + \frac{1}{5\xi \left(1+12\frac{2-\sigma}{\sigma}Kn\right)^2} - \sum_{i=1}^{\infty} \frac{(3 - \exp(-16\alpha_i^2 \xi)) \exp(-16\alpha_i^2 \xi)}{\alpha_i^2 \xi \left[1+12\frac{2-\sigma}{\sigma}Kn + 16\left(\alpha_i \frac{2-\sigma}{\sigma}Kn\right)^2\right]} \quad (5.83)$$

The Effect of Kn on $f_{app}Re$ for developing laminar flow is illustrated in Figure 5.9. It is seen that the effect of increasing Kn is to decrease apparent friction factor.

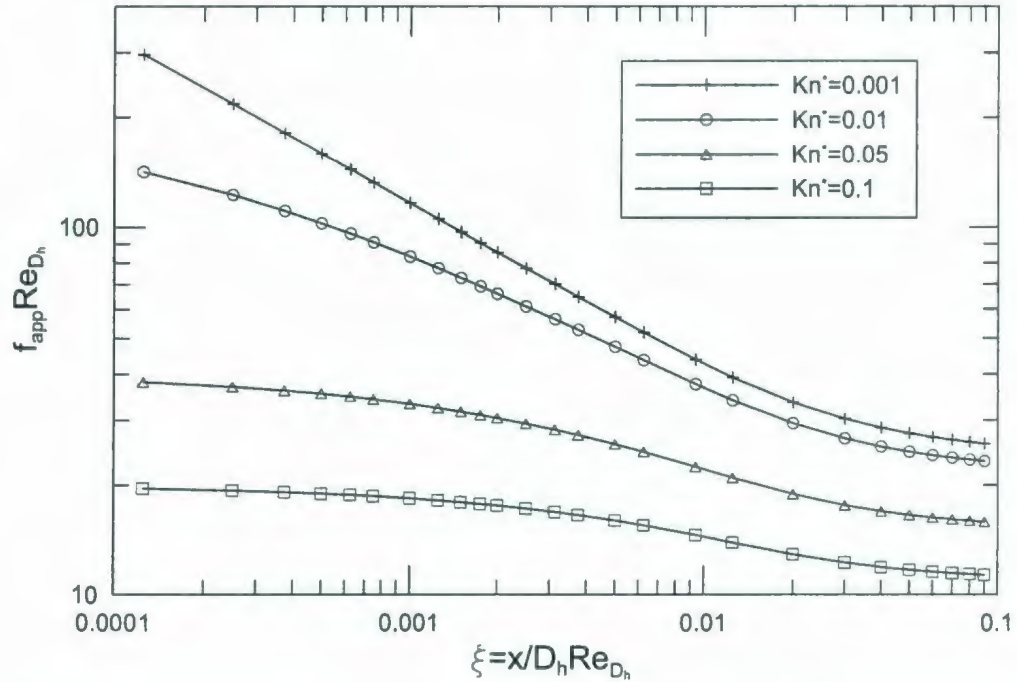


Figure 5.9 Effect of Kn^* on $f_{app}Re$ for developing laminar flow for parallel plates.

Muzychka and Yovanovich [94] showed that Eq. (5.84) may be used to compute the friction factor for the short duct of most non-circular ducts ($\xi \leq 0.001$) for continuum flow ($Kn=0$). All numerical results obtained from Eq.(5.41) or Eq.(5.83) almost reduce to their continuum limits Eq. (5.84) in the limit $Kn\rightarrow 0$.

$$(f_{app} Re_\ell)_c = \frac{3.44}{\sqrt{\xi}} \quad (5.84)$$

For slip flow, Figure 5.10 also demonstrates that very near the inlet of circular and parallel plate ducts ($\xi \leq 0.001$), $f_{app}Re$ is nearly equivalent and independent of duct shape. This is a further proof of the reliability of the proposed solutions. Therefore, Eq. (5.41) or Eq. (5.83) may be used to compute the friction factor for the very short duct of non-circular shape. As the boundary layer develops further downstream ($\xi > 0.001$), the effects of geometry become more pronounced and the solution for circular tubes and parallel plates Eq. (5.41) or Eq. (5.83) are no longer valid for non-circular ducts.

Furthermore, the asymptotic limit of $f_{app}Re$ for $\xi \rightarrow 0$ can be obtained by substituting velocity slip boundary condition into Eq. (4.1), i.e.

$$f_{app} Re = \frac{2\bar{\tau}D_h}{\mu\bar{u}} = \frac{2\frac{\mu u}{2-\sigma}D_h}{\lambda\frac{\sigma}{\mu\bar{u}}} = \frac{u}{\bar{u}} \frac{2}{Kn^*} \xrightarrow{\xi \rightarrow 0} \frac{2}{Kn^*}$$

Slip flow in the entrance region of rectangular microchannels was investigated numerically by Renksizbulut et al. [117]. Figures 5.11-5.13 demonstrate the comparison between Eq. (5.41) and Renksizbulut et al. [117] numerical data for different Reynolds numbers and Knudsen numbers. The numerical data from Shah and London [106] for continuum flow are also included in Figure 5.13. When $\xi=10^{-5}$ and $Kn^*=0.1, 0.05, 0.01$, $f_{app}Re=19.9, 39.5, 185.6$ respectively for present analysis. Therefore, present analytical results agree very well with the asymptotic limiting values, whereas the results of [117] are in poorer agreement with the asymptotic limiting values. This indicates that the

linearization method is an accurate approximation for slip flow. It is found that the Renksizbulut et al. [117] numerical data over predict the values of $f_{app}Re$.

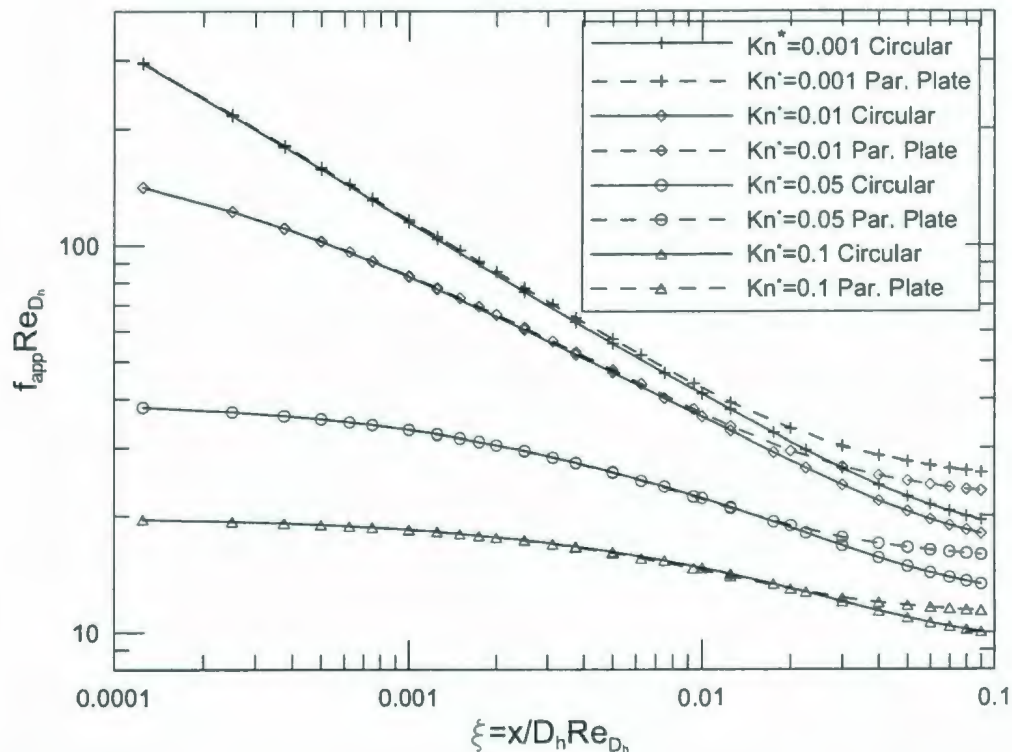


Figure 5.10 Comparison of $f_{app}Re$ for different Kn^* between circular tube and parallel plates.

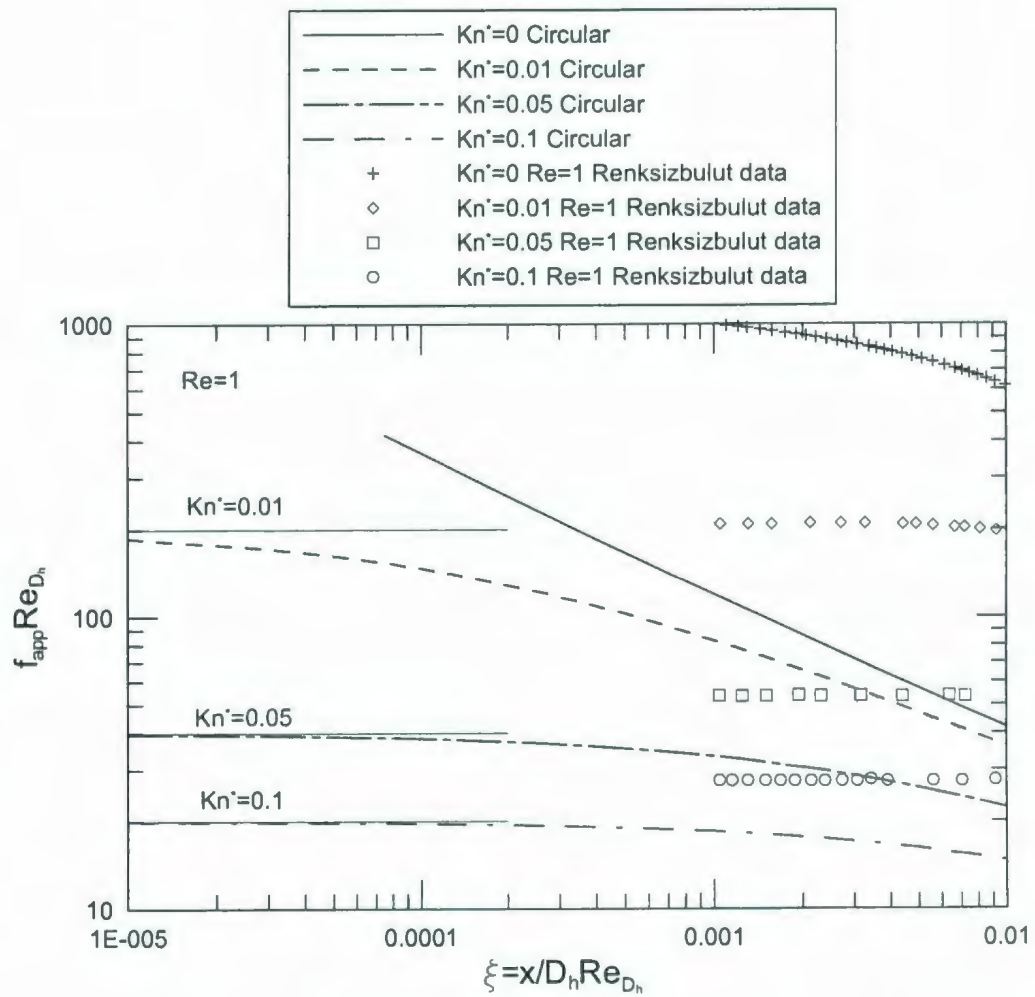


Figure 5.11 Comparison of $f_{app} Re$ for Renksizbulut et al. [117] numerical data for $Re=1$.

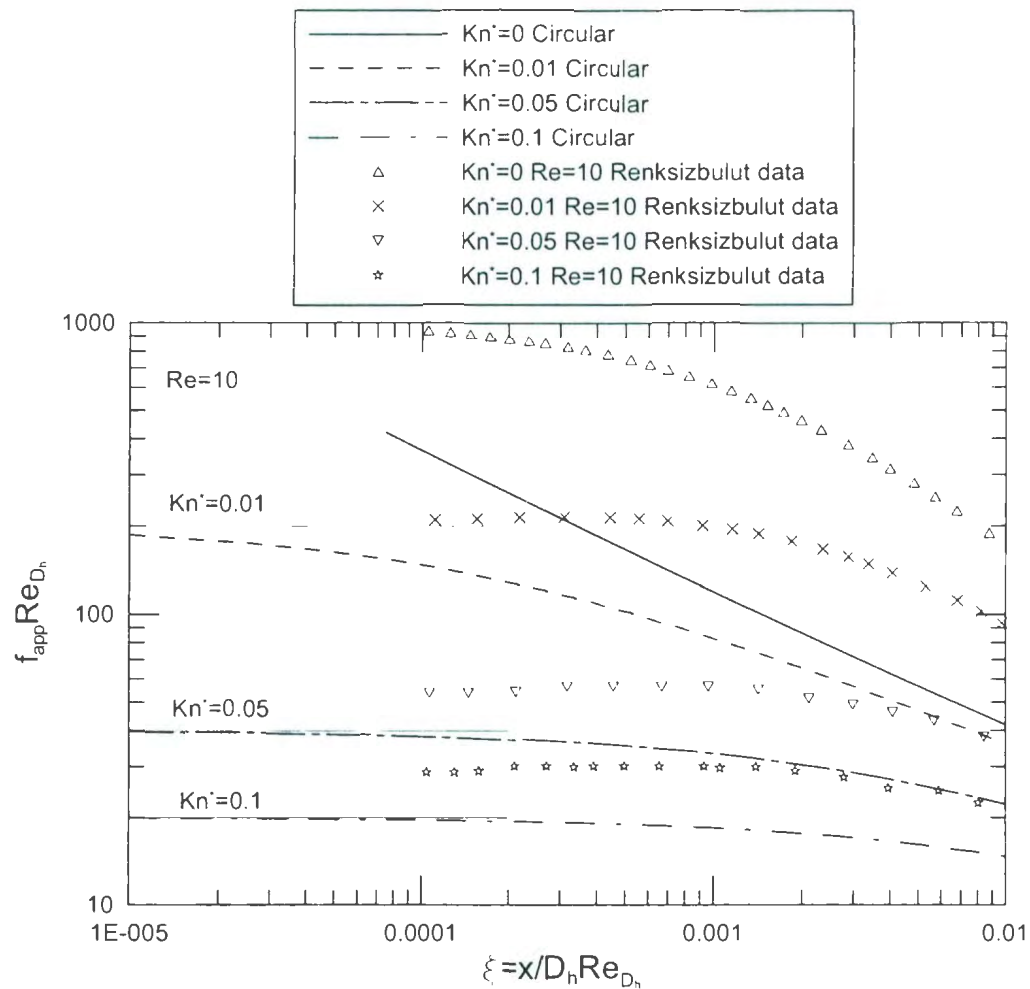


Figure 5.12 Comparison of $f_{app} Re$ for Renksizbulut et al. [117] numerical data for $Re=10$.

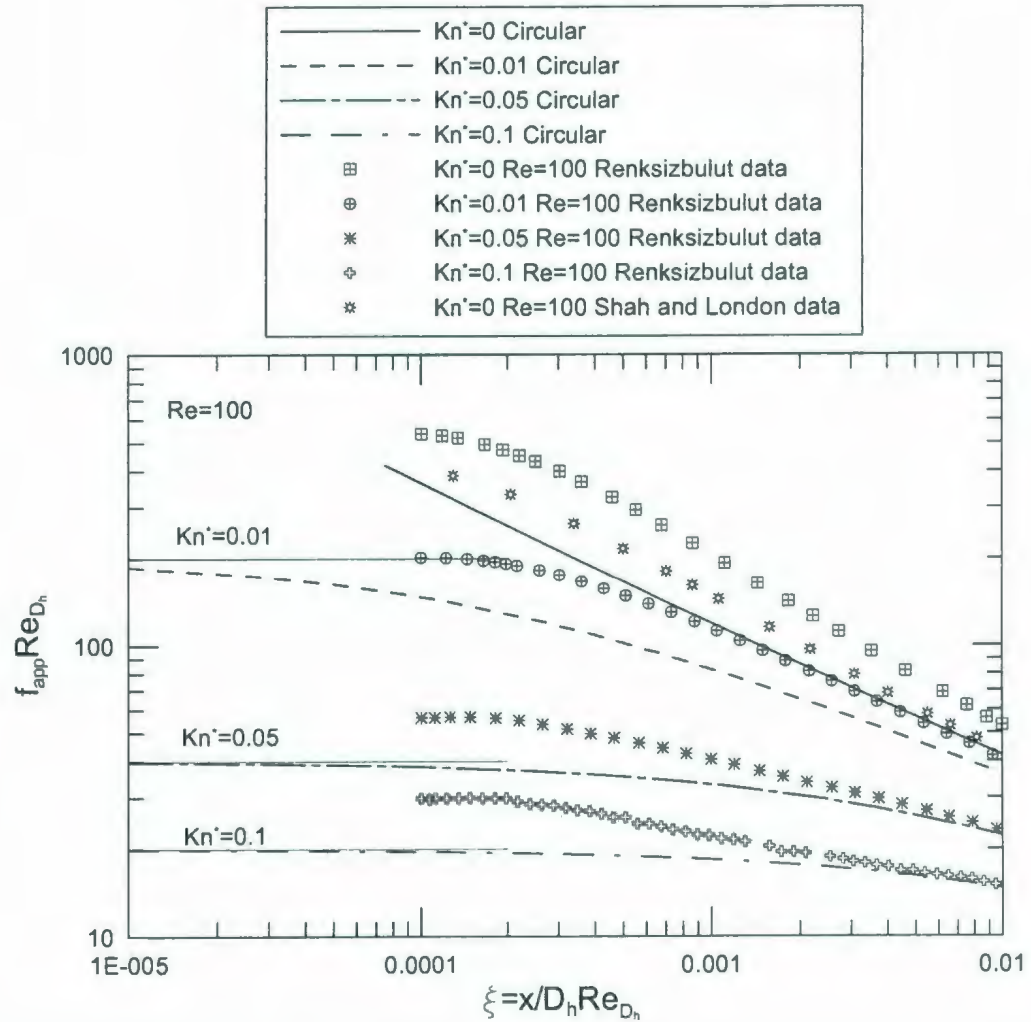


Figure 5.13 Comparison of $f_{\text{app}} \text{Re}$ for Renksizbulut et al. [117] numerical data for $\text{Re}=100$.

5.4 General Model

Muzychka and Yovanovich [94] showed that the square root of cross-sectional area is more appropriate than the hydraulic diameter for non-dimensionalizing the developing laminar continuum flow data. Duan and Muzychka [109] demonstrated that the same conclusion can be extended to the slip flow regime for fully developed flows. Muzychka and Yovanovich [94] presented the following model for predicting the friction factor Reynolds product in non-circular ducts for developing and fully developed laminar continuum flow.

$$f \text{Re}_{\sqrt{A}} = \left[\left(\frac{3.44}{\sqrt{\xi}} \right)^2 + \left(\frac{12}{\sqrt{\varepsilon}(1+\varepsilon) \left[1 - \frac{192\varepsilon}{\pi^5} \tanh\left(\frac{\pi}{2\varepsilon}\right) \right]} \right)^2 \right]^{1/2} \quad (5.85)$$

If the friction factor Reynolds product for circular tubes is recast using \sqrt{A} as a characteristic length scale in $f \text{Re}_{\sqrt{A}}$, the following relationship is obtained:

$$f_{app} \text{Re}_{\sqrt{A}} = \frac{8\sqrt{\pi}}{1 + 8\frac{2-\sigma}{\sigma} Kn} + \frac{2}{\sqrt{\pi}} \left[\frac{1}{3\xi \left(1 + 8\frac{2-\sigma}{\sigma} Kn \right)^2} - 2 \sum_{i=1}^{\infty} \frac{(3 - \exp(-\pi\alpha_i^2 \xi)) \exp(-\pi\alpha_i^2 \xi)}{\alpha_i^2 \xi \left(1 + 8\frac{2-\sigma}{\sigma} Kn + 4\left(\alpha_i \frac{2-\sigma}{\sigma} Kn\right)^2 \right)} \right] \quad (5.86)$$

where

$$\xi = \frac{x}{\sqrt{A} \operatorname{Re}_{\sqrt{A}}}$$

For short duct asymptote ($\xi < 0.001$), we only consider the second term of right hand side of Eq. (5.86)

$$f \operatorname{Re}_{\sqrt{A}} = \frac{2}{\sqrt{\pi}} \left[\frac{1}{3\xi \left(1 + 8 \frac{2-\sigma}{\sigma} Kn \right)^2} - 2 \sum_{i=1}^{\infty} \frac{(3 - \exp(-\pi\alpha_i^2 \xi)) \exp(-\pi\alpha_i^2 \xi)}{\alpha_i^2 \xi \left(1 + 8 \frac{2-\sigma}{\sigma} Kn + 4 \left(\alpha_i \frac{2-\sigma}{\sigma} Kn \right)^2 \right)} \right] \quad (5.87)$$

Equation (5.87) is independent of the duct shape and may be used to calculate the friction factor Reynolds product for the short asymptote of most non-circular ducts for slip flow.

The friction factor Reynolds product $f \operatorname{Re}$ for slip flow in long non-circular microchannels has been proposed by Duan and Muzychka [109] as follows:

$$f \operatorname{Re}_{\sqrt{A}} = \frac{1}{1 + (11.97 - 10.59\epsilon + 8.49\epsilon^2 - 2.11\epsilon^3) \frac{2-\sigma}{\sigma} Kn \sqrt{\epsilon} (1 + \epsilon) \left[1 - \frac{192\epsilon}{\pi^5} \tanh\left(\frac{\pi}{2\epsilon}\right) \right]} \quad (5.88)$$

A general model is now proposed using the Churchill and Usagi [97] asymptotic correlation method. The model takes the form:

$$f \operatorname{Re}_{\sqrt{A}} = \left[(f \operatorname{Re}_{\sqrt{A}})_{long}^n + (f_{app} \operatorname{Re}_{\sqrt{A}})_{short}^r \right]^{\frac{1}{n}} \quad (5.89)$$

where n is a superposition parameter determined by comparison with numerical and analytical data over the full range of ξ . Using the results provided by Eq. (5.87) and Eq. (5.88), and the general expression, Eq. (5.89), the following model is proposed:

$$f \operatorname{Re}_{\sqrt{A}} = \left(\frac{1}{1 + (11.97 - 10.59\varepsilon + 8.49\varepsilon^2 - 2.11\varepsilon^3) \frac{2-\sigma}{\sigma} Kn \sqrt{\varepsilon} (1+\varepsilon) \left[1 - \frac{192\varepsilon}{\pi^5} \tanh\left(\frac{\pi}{2\varepsilon}\right) \right]} \right) \\ + \left(\frac{2}{3\sqrt{\pi}\xi \left(1 + 8 \frac{2-\sigma}{\sigma} Kn \right)^2} - \frac{4}{\sqrt{\pi}} \sum_{i=1}^{\infty} \frac{(3 - \exp(-\pi\alpha_i^2\xi)) \exp(-\pi\alpha_i^2\xi)}{\alpha_i^2\xi \left(1 + 8 \frac{2-\sigma}{\sigma} Kn + 4 \left(\alpha_i \frac{2-\sigma}{\sigma} Kn \right)^2 \right)} \right) \quad (5.90)$$

Table 5.1 Eigenvalues obtained from Eq. (5.24).

| i | Eigenvalues | | | |
|-----|-------------|---------------|---------------|--------------|
| | $Kn^* = 0$ | $Kn^* = 0.01$ | $Kn^* = 0.05$ | $Kn^* = 0.1$ |
| 1 | 5.13562 | 5.03806 | 4.74142 | 4.51606 |
| 2 | 8.41724 | 8.25817 | 7.81634 | 7.54591 |
| 3 | 11.61984 | 11.40186 | 10.85911 | 10.59026 |
| 4 | 14.79595 | 14.52101 | 13.91224 | 13.66206 |
| 5 | 17.95982 | 17.62986 | 16.98106 | 16.75353 |
| 6 | 21.11700 | 20.73409 | 20.06384 | 19.85810 |
| 7 | 24.27011 | 23.83646 | 23.15780 | 22.97149 |
| 8 | 27.42057 | 26.93845 | 26.26044 | 26.09100 |
| 9 | 30.56920 | 30.04095 | 29.36979 | 29.21488 |
| 10 | 33.71652 | 33.14447 | 32.48437 | 32.34199 |
| 11 | 36.86286 | 36.24934 | 35.60308 | 35.47152 |
| 12 | 40.00845 | 39.35572 | 38.72508 | 38.60294 |
| 13 | 43.15345 | 42.46372 | 41.84973 | 41.73582 |
| 14 | 46.29800 | 45.57337 | 44.97654 | 44.86989 |
| 15 | 49.44216 | 48.68466 | 48.10514 | 48.00491 |
| 16 | 52.58602 | 51.79754 | 51.23522 | 51.14072 |
| 17 | 55.72963 | 54.91198 | 54.36656 | 54.27718 |
| 18 | 58.87302 | 58.02790 | 57.49896 | 57.41420 |
| 19 | 62.01622 | 61.14522 | 60.63226 | 60.55168 |
| 20 | 65.15927 | 64.26388 | 63.76635 | 63.68956 |

Using the available analytical data for circular tubes, and Muzychka and Yovanovich [94] model for continuum flow, it is found that the value n which minimizes the root mean square difference lies in the range $1.0 < n < 1.2$ with a convenient value $n \approx 1$. The eigenvalues α_i are given in Table 5.1. It was found that twenty eigenvalues are sufficient accurate for all values of ξ of interest. When ξ is not too small, only several terms are required. More eigenvalues should be used when ξ is very small and Knudsen number is comparatively small.

5.5 Results and Discussion

Figure 5.14 demonstrates the comparison between the proposed model Eq. (5.90) and Muzychka and Yovanovich model [94] Eq. (5.85) for continuum flow. It is found that the difference between the two models is less than 10%. Since there are no experimental results for slip flow in the hydrodynamic entrance of non-circular microchannels, it is impossible at the present to completely appraise the present model. However, experimental, analytical and numerical results for continuum flow do support the validity of the present model. Moreover, the proposed model correctly approaches the $\xi \rightarrow 0$ and $\xi \rightarrow \infty$ limits.

Furthermore, Figure 5.15 presents the comparison between the proposed model Eq. (5.90) and the analytical solution of circular ducts Eq. (5.86). The model predictions are in agreement with the analytical solution within 1%.

Niazmand et al. [118] and Renksizbulut et al. [117] numerically investigated slip flow in the entrance region of rectangular microchannels. The Reynolds number range is from

0.1 to 100. Figure 5.16 demonstrates the comparison between the proposed model and Niazmand et al. [118] numerical data for $Re=100$ and $\xi > 0.005$. It is found that the difference between the model and Niazmand et al. numerical data is from 9% to 19%. The difference decreases with an increase in Knudsen number. This indicates that the slip flow is less sensitive to analytical linearized approximations than the continuum flow. It should also be noted, however, that Niazmand et al. numerical data over predict the values of fRe .

It is found that Eq. (5.90) characterizes the developing slip flow in non-circular microchannels. The maximum deviation of exact values is approximately less than 10 percent. The friction factor Reynolds product may be predicted from Eq. (5.90), provided an appropriate definition of the aspect ratio is chosen.

5.6 Summary

A model was developed for predicting the friction factor Reynolds product in non-circular microchannels for developing slip flow. It is shown that complete problem may be easily analyzed by combining the asymptotic results for the short and long duct. The present model took advantage of the selection of a more appropriate characteristic length scale square root of flow area to develop a simple model. As for developing slip flow no solutions or tabulated data exist for most geometries, this developed model may be used to predict friction factor and pressure drop of developing slip flow in non-circular microchannels. The developed model correctly approaches the slip flow asymptote for developing flows and fully developed flows. The accuracy of the developed model was

approximately within 10 percent. It is found that slip flow is less sensitive to analytical linearized approximations than continuum flow and the linearization method is an accurate approximation for slip flow. The effects of the Knudsen number on the hydrodynamic entrance length for circular tubes and parallel plates have also been examined. Simple models were developed to predict entrance length for circular tubes and parallel plates.

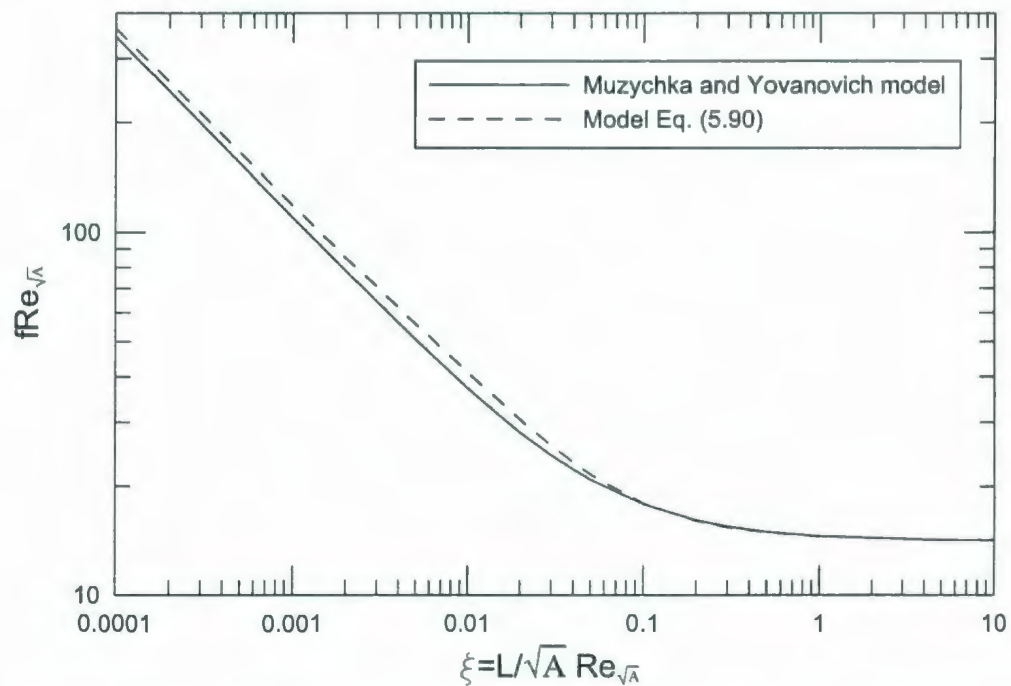


Figure 5.14 Comparison of $fRe_{\sqrt{A}}$ for Muzychka and Yovanovich [94] model.

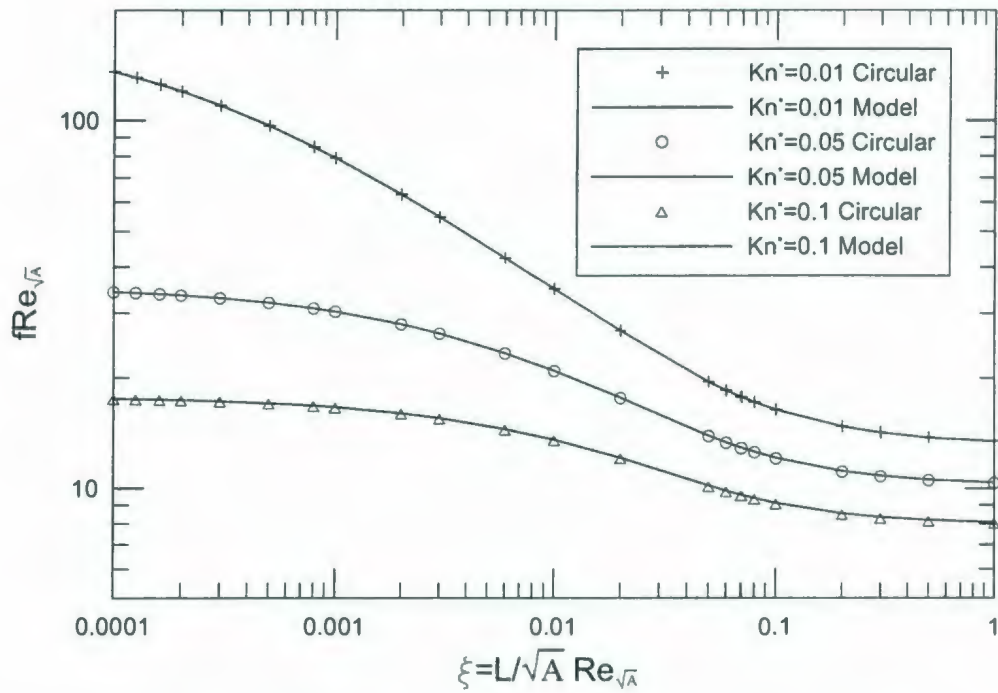


Figure 5.15 Comparison of $fRe_{\sqrt{A}}$ for circular tubes.

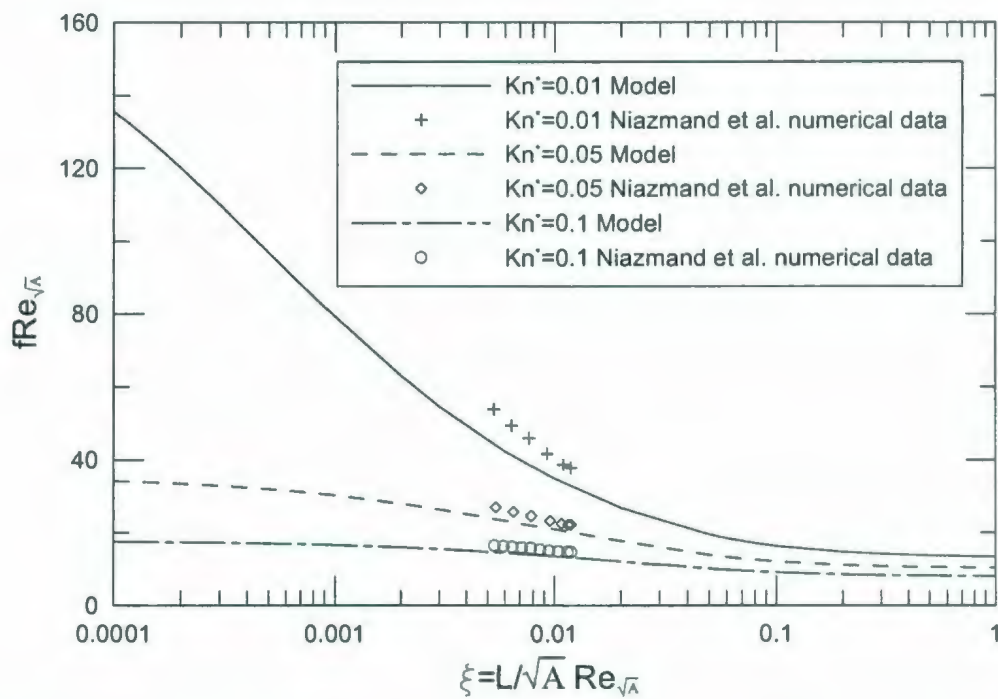


Figure 5.16 Comparison of $fRe_{\sqrt{A}}$ for Niazmand et al. [118] numerical data.

Chapter 6

Effects of Corrugated Roughness on Laminar Flow in Microtubes

6.1 Introduction

Some researchers have reported on deviations between microscale flow behavior and conventional macroscale flow theory. For laminar fully developed flow through microchannels, researchers have observed significant increases in the pressure drop from the macroscale flow theoretical values, as data appears up to 50% above the theoretical values [7-8,14,18-19,23,33-37,41-48,57,63-64,67,79,81,119]. Some publications indicate that flows on the microscale are different from that on macroscale. Several theories and models have been proposed to explain the observed deviations, but an indisputable conclusion has not yet been reached.

In macroscale flow theory, the friction factor is independent of relative roughness in the laminar region. However, some researchers proposed that the friction factor depends on the relative roughness of the walls of the microchannels also in laminar region and the relative roughness cannot be neglected for microchannels in the laminar region [7,16,41-42,46,57,60,63-64,67,72,76,80,119].

Due to limitations in current micromachining technology, the microfabricated microchannel walls typically exhibit some degree of roughness, as shown in Figure 6.1. Roughness plays an increasingly important role in microchannel flows, but it is difficult to characterize its effects theoretically or numerically. It can be characterized using stylus-type surface profilometer, optical measurement, Scanning Electron Microscope (SEM), Atomic Force Microscope (AFM), and Scanning Tunneling Microscope (STM). There is a need for a better understanding of the effects of wall roughness on fluid characteristics in microchannels.

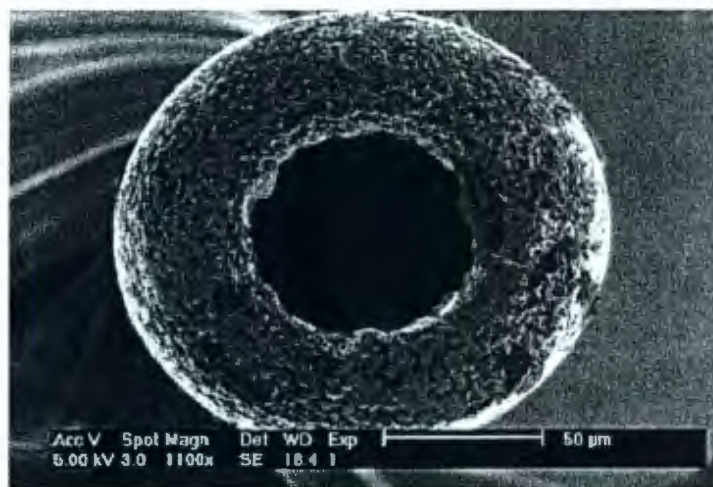


Figure 6.1 SEM image of the cross-section of a roughness microtube with a nominal internal diameter of 75 μm [62].

Bahrami et al. [119] developed a model to predict the pressure drop of the fully developed laminar continuum flows in rough microtubes. In this model, the wall roughness is assumed to possess a Gaussian isotropic distribution.

Kleinstreuer and Koo [120] proposed a numerical model to consider the effect of wall roughness on liquid continuum flow in microchannels. They modeled roughness by

considering a porous medium layer (PLM) near the wall. The porous medium layer approach is able to mimic some details of the velocity profiles and of the effect of the roughness height.

Wang et al. [121] numerically investigated the friction factors of single phase continuum flow in microchannels with various roughness elements. The two-dimensional numerical solution shows significant influence of surface roughness including the height and spacing of the roughness elements on the Poiseuille number. The Poiseuille number increases with an increase of roughness height and decreases with an increase of the roughness spacing.

Li et al. [122] studied the effects of surface roughness on the slip flow in long microtubes. The rough surface was represented as a porous film based on the Brinkman-extended Darcy model, and the core region of the flow utilized velocity slip to model the rarefaction effects. By using the appropriate matching conditions at the gas/porous interface (velocity slip and stress continuity), the governing equation of pressure distribution was derived.

Sun and Faghri [123] investigated the effects of surface roughness on nitrogen flow in a microchannel using the direct simulation Monte Carlo method. The surface roughness was modeled by an array of rectangular modules placed on two surfaces of a parallel plate channel. The effects of relative surface roughness, roughness distribution, and gas rarefaction on flow were studied. It was found that the effect of surface roughness is more pronounced at low Knudsen numbers. The roughness distribution represented by the ratio of the roughness height to spacing of the modules has a significant effect on the friction

factor. The friction factor increases not only as the roughness height increases but also as the distance between the roughness modules decreases. This is consistent with the conclusions of Wang et al. [121].

In the present chapter we examine a simple approach to modeling surface roughness in the slip flow regime.

6.2 Circumferential Corrugated Roughness

In order to simplify the roughness problem, we can consider flow inside a microtube with a rough surface which is approximately sinusoidal corrugation, $r = R + R\varepsilon \sin(\lambda\theta)$, as illustrated in Figure 6.2. Where R is the mean radius of the rough microtube and λ is the wave number ($\lambda = 2\pi R / l$), relative roughness $\varepsilon = b/R \ll 1$, b and l are the amplitude and wave length of the rough corrugated walls respectively. It is convenient to normalize the axial velocity u with $-(dp/dz)/\mu$. When the tubes are long enough ($L/D \gg 1$) and Reynolds number is relatively low, the momentum equation reduces to the Poisson equation. We will consider continuum flow first.

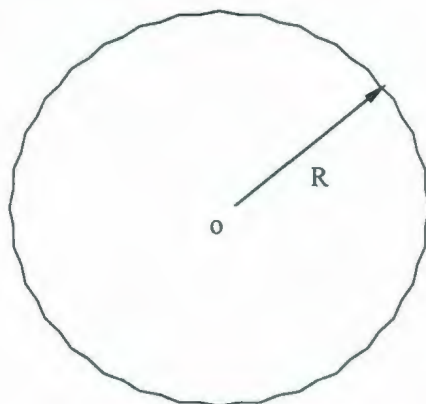


Figure 6.2 A sinusoidal wave roughness microtube.

6.2.1 Continuum Flow

$$\nabla^2 u = -1 \quad (6.1)$$

and

$$\nabla^2 = \frac{\partial^2}{\partial r^2} + \frac{1}{r} \frac{\partial}{\partial r} + \frac{1}{r^2} \frac{\partial^2}{\partial \theta^2} \quad (6.2)$$

The boundary conditions are

$$u \neq \infty \quad \text{at} \quad r = 0 \quad (6.3)$$

$$u = 0 \quad \text{at} \quad r = R + R\varepsilon \sin(\lambda\theta) \quad (6.4)$$

Using perturbation methods, we expand the velocity in terms of ε

$$u = u_0(r, \theta) + \varepsilon u_1(r, \theta) + \varepsilon^2 u_2(r, \theta) + \dots \quad (6.5)$$

Equation (6.1) yields

$$\nabla^2 u_0 = -1, \quad \nabla^2 u_1 = 0, \quad \nabla^2 u_2 = 0. \quad (6.6)$$

and for the boundary conditions we can expand $u(R + \varepsilon R \sin(\lambda\theta), \theta)$ in a Taylor series to obtain

$$u(R + \varepsilon R \sin(\lambda\theta), \theta) = u(R, \theta) + \varepsilon \left[R \sin(\lambda\theta) \frac{\partial u}{\partial r}(R, \theta) \right] + \varepsilon^2 \left[\frac{[R \sin(\lambda\theta)]^2}{2} \frac{\partial^2 u}{\partial r^2}(R, \theta) \right] + \dots = 0 \quad (6.7)$$

Substitution of Eq. (6.5) into Eq. (6.7) gives

$$\begin{aligned} u(R + \varepsilon R \sin(\lambda\theta), \theta) &= u_0(R, \theta) + \varepsilon \left[u_1(R, \theta) + \frac{\partial u_0}{\partial r}(R, \theta) R \sin(\lambda\theta) \right] \\ &\quad + \varepsilon^2 \left[u_2(R, \theta) + \frac{\partial u_1}{\partial r}(R, \theta) R \sin(\lambda\theta) + \frac{1}{2} \frac{\partial^2 u_0}{\partial r^2}(R, \theta) R^2 \sin^2(\lambda\theta) \right] + O(\varepsilon^3) = 0 \end{aligned} \quad (6.8)$$

Then, the boundary conditions become respectively

$$u_0(R, \theta) = 0 \quad (6.9)$$

$$u_1(R, \theta) + \frac{\partial u_0}{\partial r}(R, \theta) R \sin(\lambda\theta) = 0 \quad (6.10)$$

$$u_2(R, \theta) + \frac{\partial u_1}{\partial r}(R, \theta) R \sin(\lambda\theta) + \frac{1}{2} \frac{\partial^2 u_0}{\partial r^2}(R, \theta) R^2 \sin^2(\lambda\theta) = 0 \quad (6.11)$$

The solutions of this problem yields:

$$u_0 = \frac{R^2 - r^2}{4} \quad (6.12)$$

$$u_1 = \frac{1}{2} R^2 \left(\frac{r}{R} \right)^{\lambda} \sin(\lambda\theta) \quad (6.13)$$

$$u_2 = \frac{1-2\lambda}{8} R^2 - \frac{1-2\lambda}{8} R^2 \left(\frac{r}{R} \right)^{2\lambda} \cos(2\lambda\theta) \quad (6.14)$$

The total flow rate is given by

$$Q = -\frac{dp/dz}{\mu} \lambda \int_0^{2\pi/\lambda} \int_0^{R+\varepsilon R \sin(\lambda\theta)} (u_0 + \varepsilon u_1 + \varepsilon^2 u_2 + \dots) r dr d\theta = -\frac{\pi R^4 dp/dz}{8\mu} [1 - (2\lambda - 3)\varepsilon^2 + O(\varepsilon^4)] \quad (6.15)$$

It is seen that the periodic solution cannot be related to flow rate along z .

$$\frac{Q}{Q_{sm}} = 1 - (2\lambda - 3)\varepsilon^2 + O(\varepsilon^4) \quad (6.16)$$

where Q_{sm} is the flow rate for smooth microtubes. The flow rate decreases with an increase in λ . As $2\lambda - 3$ is always positive for practical applications indicating a decrease in the flow rate with wall roughness.

After integrating Eq. (6.15), the pressure drop along the length of the pipe (L) may be determined to be

$$\Delta p = \frac{8\mu L Q}{\pi R^4} \frac{1}{1 - (2\lambda - 3)\varepsilon^2 + O(\varepsilon^4)} \quad (6.17)$$

It can be also shown that the effect of wall roughness on the pressure drop is given by the following equation

$$\Delta p^* = \frac{\Delta p}{\Delta p_{sm}} = \frac{1}{1 - (2\lambda - 3)\varepsilon^2 + O(\varepsilon^4)} \quad (6.18)$$

where Δp_{sm} is the pressure drop for smooth microtubes.

Figures 6.3 and 6.4 demonstrate the effect of wave number λ and relative roughness ε on pressure drop of microtubes. As $2\lambda - 3$ is always positive, the pressure drop increases with wall roughness.

The friction factor Reynolds product can be obtained simply by substituting Eq. (6.15) into the definition of fRe .

$$fRe = \frac{2\left(-\frac{A}{P} \frac{dp}{dz}\right)D_h}{\mu \bar{u}} = \frac{2\left(-\frac{A}{P} \frac{dp}{dz}\right)D_h A}{\mu Q} = 16 \left(\frac{D_h}{2R}\right)^2 \frac{1 + \frac{1}{2}\varepsilon^2}{1 - (2\lambda - 3)\varepsilon^2 + O(\varepsilon^4)} \quad (6.19)$$

where $A = \pi R^2 \left(1 + \frac{1}{2}\varepsilon^2\right)$ and the perimeter can be evaluated numerically, see Shah and London [106]. The friction factor Reynolds product is presented in Table 6.1. The numerical value determined by conformal mapping and Green's function from Shah and London [106] is also included for comparison. It is found that Eq. (6.19) agrees with the numerical results of fRe from Shah and London. The difference decreases with a decrease in ε .

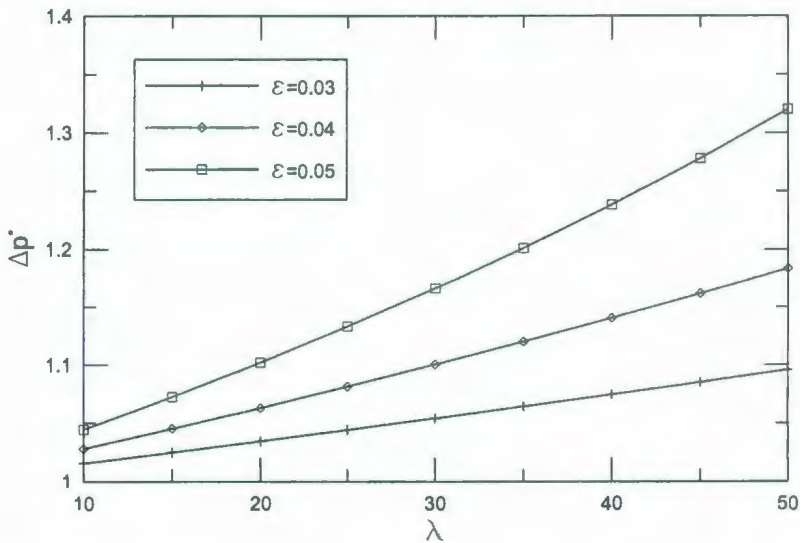


Figure 6.3 Effect of relative roughness ε and wave number λ on pressure drop of microtubes.

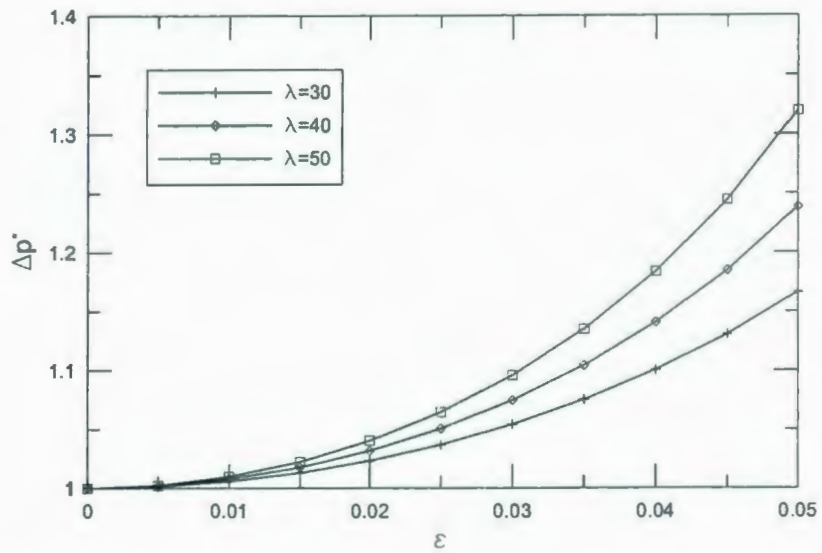


Figure 6.4 Effect of relative roughness ε and wave number λ on pressure drop of microtubes.

Table 6.1 fRe for developed laminar flow in corrugated microtubes.

| λ | ε | $D_h/2R$ | fRe | fRe [106] | Difference |
|-----------|---------------|----------|--------|-------------|------------|
| 6 | 0.02 | 0.9966 | 15.952 | 15.952 | 0.00% |
| | 0.04 | 0.9863 | 15.805 | 15.806 | 0.00% |
| | 0.06 | 0.9689 | 15.551 | 15.559 | 0.05% |
| 8 | 0.02 | 0.9938 | 15.888 | 15.887 | 0.00% |
| | 0.04 | 0.9747 | 15.536 | 15.542 | 0.04% |
| | 0.06 | 0.9418 | 14.915 | 14.943 | 0.19% |
| 12 | 0.02 | 0.9856 | 15.677 | 15.679 | 0.01% |
| | 0.04 | 0.9402 | 14.647 | 14.671 | 0.16% |
| | 0.06 | 0.8583 | 12.774 | 12.872 | 0.77% |

6.2.2 Slip Flow

We will first examine smooth microtubes. When the tubes are long enough ($L/D \gg 1$) and Reynolds number is relatively low, the continuum flow momentum equation is

$$\mu \left(\frac{d^2 u}{dr^2} + \frac{1}{r} \frac{du}{dr} \right) = \frac{dp}{dz} \quad (6.20)$$

The boundary conditions for smooth microtubes are therefore

$$u \neq \infty \quad \text{at} \quad r = 0 \quad (6.21)$$

$$u = -\lambda_f \frac{2-\sigma}{\sigma} \frac{du}{dr} \quad \text{at} \quad r = R \quad (6.22)$$

where λ_f denotes the molecular mean free path. The characteristic length scale in the present analysis is defined as the microtube mean diameter. It is convenient to introduce the Knudsen number

$$Kn = \frac{\lambda_f}{2R} \quad (6.23)$$

A solution of velocity distribution is obtained:

$$u = -\frac{1}{4\mu} \frac{dp}{dz} \left(R^2 - r^2 + \frac{2-\sigma}{\sigma} 4KnR^2 \right) \quad (6.24)$$

The mean velocity is found by integration Eq. (6.24) across the section

$$\bar{u} = \frac{1}{A} \int u dA \approx \frac{1}{\pi R^2} \int_0^R u 2\pi r dr = -\frac{R^2}{8\mu} \frac{dp}{dz} \left(1 + \frac{2-\sigma}{\sigma} 8Kn \right) \quad (6.25)$$

Then, we can obtain

$$f \text{Re} = \frac{16}{1 + \frac{2-\sigma}{\sigma} 8Kn} \quad (6.26)$$

In addition, the volume rate of flow in the microtube is given by

$$Q = \pi R^2 \bar{u} = -\frac{\pi R^4}{8\mu} \frac{dp}{dz} \left(1 + \frac{2-\sigma}{\sigma} 8Kn \right) \quad (6.27)$$

The above equation indicates that the slip velocity boundary condition increases the volume rate of flow through the microtube.

Now we will consider the coupled effects due to velocity slip and corrugated roughness on the channel walls. The only difference with no-slip case is the boundary conditions

$$u = -\lambda, \frac{2-\sigma}{\sigma} \frac{\partial u}{\partial n} \quad \text{at} \quad r = R + \varepsilon R \sin(\lambda\theta) \quad (6.28)$$

where n is the outer direction normal.

We can expand $u(R + \varepsilon R \sin(\lambda\theta), \theta)$ in a Taylor series to obtain the boundary conditions

$$\begin{aligned} u(R + \varepsilon R \sin(\lambda\theta), \theta) &= u(R, \theta) + \varepsilon \left[R \sin(\lambda\theta) \frac{\partial u}{\partial r}(R, \theta) \right] + \varepsilon^2 \left[\frac{[R \sin(\lambda\theta)]^2}{2} \frac{\partial^2 u}{\partial r^2}(R, \theta) \right] + \dots \\ &= -\lambda, \frac{2-\sigma}{\sigma} \frac{\partial u}{\partial n} \end{aligned} \quad (6.29)$$

and

$$\begin{aligned}\frac{\partial u}{\partial n} &= \frac{\partial u}{\partial r} \cos \alpha + \frac{1}{r} \frac{\partial u}{\partial \theta} \cos \beta = \frac{\nabla u \cdot \nabla[r - R - R\varepsilon \sin(\lambda\theta)]}{|\nabla[r - R - R\varepsilon \sin(\lambda\theta)]|} \\ &= \left[\frac{\partial u}{\partial r} - \frac{\partial u}{\partial \theta} \varepsilon \frac{\lambda R}{r^2} \cos(\lambda\theta) \right] \left[1 + \varepsilon^2 \frac{\lambda^2 R^2}{r^2} \cos^2(\lambda\theta) \right]^{-1/2}\end{aligned}\quad (6.30)$$

Following a procedure similar to the no-slip case (the derivation is quite space consuming and omitted here), we may obtain the solution as follows:

$$u_0 = \frac{R^2 - r^2}{4} + \frac{2 - \sigma}{\sigma} KnR^2 \quad (6.31)$$

$$u_1 = \text{periodic solution} = \dots \times (\sin(\lambda\theta)) \quad (6.32)$$

$$\begin{aligned}u_2 &= \frac{R^2}{8} \left[1 - \frac{2\lambda(1+2Kn^*) (1+4\lambda Kn^* - 2Kn^*)}{1+2\lambda Kn^*} \right] + \text{periodic solution} \\ &= \frac{R^2}{8} \left[1 - \frac{2\lambda(1+2Kn^*) (1+4\lambda Kn^* - 2Kn^*)}{1+2\lambda Kn^*} \right] + \dots \times (\cos(2\lambda\theta))\end{aligned}\quad (6.33)$$

The total flow rate is then given by

$$\begin{aligned}Q &= -\frac{dp/dz}{\mu} \lambda \int_0^{2\pi/\lambda} \int_0^{R+\varepsilon R \sin(\lambda\theta)} (u_0 + \varepsilon u_1 + \varepsilon^2 u_2 + \dots) r dr d\theta \\ &= -\frac{\pi R^4 dp/dz}{8\mu} \left[1 + 8Kn^* - \left(1 + \frac{2\lambda(1+2Kn^*) (1+4\lambda Kn^* - 2Kn^*)}{1+2\lambda Kn^*} - 4Kn^* - 4 \frac{1+2Kn^*}{1+2\lambda Kn^*} \right) \varepsilon^2 + O(\varepsilon^4) \right] \\ &= -\frac{\pi R^4 dp/dz}{8\mu} [1 - B\varepsilon^2 + O(\varepsilon^4)] (1 + 8Kn^*)\end{aligned}\quad (6.34)$$

where

$$B = \frac{1 + \frac{2\lambda(1+2Kn^*)(1+4\lambda Kn^* - 2Kn^*)}{1+2\lambda Kn^*} - 4Kn^* - 4\frac{1+2Kn^*}{1+2\lambda Kn^*}}{1+8Kn^*} \quad (6.35)$$

B is a function of wave number λ and modified Knudsen number Kn^* .

$$\frac{Q}{Q_{sm}} = [1 - B\varepsilon^2 + O(\varepsilon^4)] \left(1 + \frac{2-\sigma}{\sigma} 8Kn \right) \quad (6.36)$$

where Q_{sm} is the flow rate for continuum flow in smooth microtubes. As B is always positive indicating a decrease in the flow rate with wall roughness.

After integrating Eq. (6.34), the pressure drop for incompressible flow along the length of the pipe (L) may be determined to be

$$\Delta p = \frac{\frac{8\mu L Q}{\pi R^4}}{[1 - B\varepsilon^2 + O(\varepsilon^4)] \left(1 + \frac{2-\sigma}{\sigma} 8Kn \right)} \quad (6.37)$$

It can be also shown that the effect of wall roughness on the pressure drop is given by the following equations

$$\Delta p^* = \frac{\Delta p}{\Delta p_{sm}} = \frac{1}{[1 - B\varepsilon^2 + O(\varepsilon^4)] \left(1 + \frac{2-\sigma}{\sigma} 8Kn \right)} \quad (6.38)$$

where Δp_{sm} is the pressure drop for continuum flow in smooth microtubes.

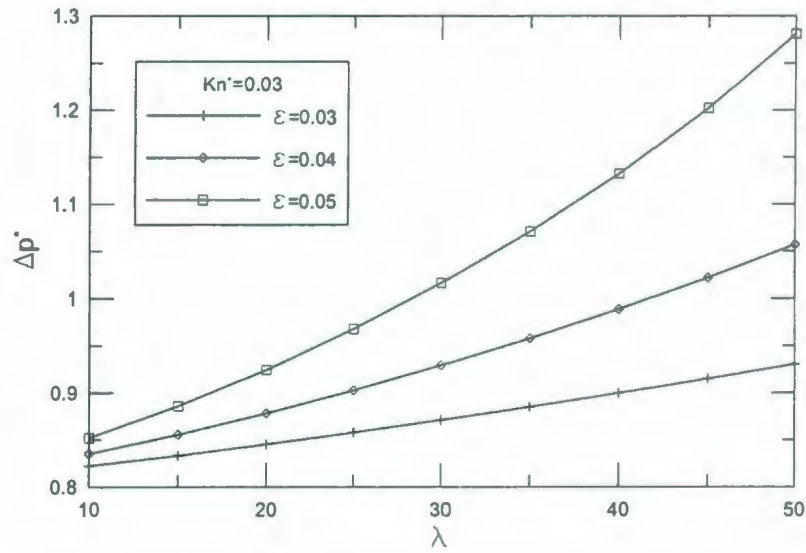


Figure 6.5 Effect of relative roughness ε , wave number λ and Knudsen number Kn on pressure drop of microtubes.

Figure 6.5 demonstrates the effect of wave number λ , relative roughness ε and Knudsen number Kn on pressure drop of microtubes. Velocity slip decreases pressure drop and corrugated roughness increases pressure drop. Pressure drop depends on ε , λ , and Kn and it can be less than, equal to or greater than unity. The coupled effects between small corrugated roughness and velocity slip proposes a possible explanation on the observed phenomenon that Chung et al. [71] and Kohl et al. [83] found, which showed that the friction factors for slip flow in microchannels can be accurately determined from conventional theory for large channels.

Using the similar procedure as continuum flow, the friction factor Reynolds product for slip flow can be obtained as follows:

$$f \operatorname{Re} = 16 \left(\frac{D_h}{2R} \right)^2 \frac{1 + \frac{1}{2} \varepsilon^2}{\left[1 - B \varepsilon^2 + O(\varepsilon^4) \right] \left(1 + \frac{2-\sigma}{\sigma} 8Kn \right)} \quad (6.39)$$

Next we consider the effects of compressibility of the gas. For compressible flow, the mass flow rate in the microtube is given by employing the equation of state $p=\rho \mathfrak{R} T$

$$\dot{m} = \rho \bar{u} A = - \frac{\pi R^4}{8 \mu \mathfrak{R} T} \left[1 - B \varepsilon^2 + O(\varepsilon^4) \right] \frac{dp}{dz} \left(p + 8 \frac{2-\sigma}{\sigma} pKn \right) \quad (6.40)$$

We can use $pKn = p_o Kn_o$ since pKn is constant for isothermal flow. Integrating Eq. (6.40), we obtain

$$\dot{m} = \rho \bar{u} A \approx \frac{\pi R^4 p_o^2}{16 \mu \mathfrak{R} T z} \left[1 - \bar{B} \varepsilon^2 + O(\varepsilon^4) \right] \left[\frac{p_i^2}{p_o^2} - \frac{p_z^2}{p_o^2} + 16 \frac{2-\sigma}{\sigma} Kn_o \left(\frac{p_i}{p_o} - \frac{p_z}{p_o} \right) \right] \quad (6.41)$$

where \bar{B} denotes the average value of $B(\lambda, Kn_i)$ and $B(\lambda, Kn_z)$.

Letting $z=L$ gives:

$$\dot{m} = \rho \bar{u} A \approx \frac{\pi R^4 p_o^2}{16 \mu \mathfrak{R} T L} \left[1 - \bar{B} \varepsilon^2 + O(\varepsilon^4) \right] \left[\frac{p_i^2}{p_o^2} - 1 + 16 \frac{2-\sigma}{\sigma} Kn_o \left(\frac{p_i}{p_o} - 1 \right) \right] \quad (6.42)$$

The continuum flow mass flow rate is given by:

$$\dot{m}_c = \rho \bar{u} A = \frac{\pi R^4 p_o^2}{16 \mu \mathfrak{R} T L} \left[1 - \bar{B} \varepsilon^2 + O(\varepsilon^4) \right] \left(\frac{p_i^2}{p_o^2} - 1 \right) \quad (6.43)$$

The effect of slip may be illustrated clearly by dividing the slip flow mass flow Eq. (6.42) by the continuum mass flow Eq. (6.43)

$$\frac{\dot{m}}{\dot{m}_c} = 1 + \frac{16 \frac{2-\sigma}{\sigma} Kn_o}{\frac{p_i}{p_o} + 1} \quad (6.44)$$

It is seen that the rarefaction increases the mass flow and that the effect of rarefaction becomes more significant when the pressure ratio decreases.

Finally, combining Eq. (6.41) and Eq. (6.42), we obtain the expression for pressure distribution:

$$\frac{p_z}{p_o} \approx -8 \frac{2-\sigma}{\sigma} Kn_o + \sqrt{\left(8 \frac{2-\sigma}{\sigma} Kn_o + \frac{p_i}{p_o}\right)^2 - \left[\frac{p_i^2}{p_o^2} - 1 + 16 \frac{2-\sigma}{\sigma} Kn_o \left(\frac{p_i}{p_o} - 1\right)\right] \frac{z}{L}} \quad (6.45)$$

The influences of circumferential corrugated surface roughness on the fully developed laminar flow in microtubes are studied and novel models are proposed to predict friction factor and pressure drop for continuum flow and slip flow. Compressibility effect has also been examined and simple models are proposed to predict the pressure distribution and mass flow rate for slip flow in corrugated rough microtubes.

It is observed that the normalized pressure drop, Δp^* , is a function of relative roughness ε and wave number λ for continuum flow, i.e. $\Delta p^* = F(\varepsilon, \lambda)$. The present model exhibits the influence of corrugated roughness. For most conventional microtubes ($\varepsilon \approx 0.03-0.05$, $\lambda = 30-50$), the present model proposes an explanation on the observed

phenomenon that pressure drop results for continuum flow have shown a striking increase (15–50%) due to roughness.

For slip flow, Δp^* is a function of relative roughness ε , wave number λ and Knudsen number Kn , i.e. $\Delta p^* = F_1(\varepsilon, \lambda, Kn)$. There exist coupled effects between velocity slip and corrugated roughness. Velocity slip decreases pressure drop and increases flow rate. Corrugated roughness increases pressure drop and decreases flow rate. These two effects can have a canceling effect in some systems.

6.3 Axial Corrugated Roughness

6.3.1 Introduction

The exact solutions of Hagen-Poiseuille flow can be obtained theoretically. However, when the radius of a tube varies with the axial distance, the flow cannot be characterized by Hagen-Poiseuille law. Langlois [124] employed the lubrication approximation to calculate the mean pressure drop. The prediction of the simple approximation method agrees well with the exact value when the tube radius varies slowly. Since Langlois' paper, some authors investigated this flow problem in tubes of slowly varying radius. Tanner and Linnett [125] extended the perturbation analysis of Blasius to predict the kinetic energy losses of viscometric capillary tubes. However, they neglected second order viscous terms in the momentum equations. Manton [126] obtained an asymptotic series solution for the low Reynolds number flow through an axisymmetric tube whose radius varies slowly in the axial direction. However, he also neglected first and second order viscous terms. Noticing this and the applications of this flow in biomechanics,

Phan-Thien [127] developed a perturbation solution and obtained an improved solution up to second order $O(\varepsilon^2)$ for the mean pressure gradient. Vasudeviah and Balamurugan [128] tried to solve the corresponding problem for slip flow. However, their derivation and result are questionable, which are discussed later. In view of the importance of this flow problem, we develop a new perturbation solution for slip flow through axially corrugated rough microtubes.

6.3.2 Theoretical Analysis

In order to simplify the roughness problem, we can consider flow inside a microtube with a rough surface which is approximately sinusoidal corrugation, $r' = R + R\varepsilon \sin(2\pi z'/l)$, as illustrated in Figure 6.6. Where R is the mean radius of the rough microtube, relative roughness $\varepsilon = b/R \ll 1$, b and l are the amplitude and wave length of the rough corrugated walls respectively. It is convenient to normalize all length variables with respect to R . When the tubes are long enough ($L/D \gg 1$) and Reynolds number is relatively low, the Stokes equation in cylindrical coordinates (r, θ, z) is

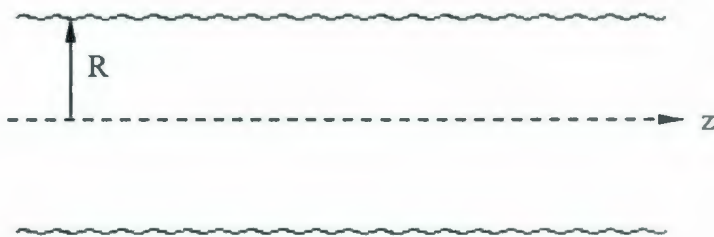


Figure 6.6 An axial sinusoidal wave rough microtube.

$$E^4\psi = 0 \quad (6.46)$$

and

$$E^2 = r \frac{\partial}{\partial r} \left(\frac{1}{r} \frac{\partial}{\partial r} \right) + \frac{\partial^2}{\partial z^2} \quad (6.47)$$

where ψ is the dimensionless stream function normalized by $(-Q/2\pi)$.

The boundary conditions are

$$\psi = 0, \quad \frac{1}{r} \frac{\partial \psi}{\partial z} = 0 \quad \text{at } r = 0 \quad (6.48)$$

$$\psi = 1, \quad \frac{1}{n} \frac{\partial \psi}{\partial n} = -\frac{\lambda_f}{R} \frac{2-\sigma}{\sigma} \frac{\partial}{\partial n} \left(\frac{1}{n} \frac{\partial \psi}{\partial n} \right) \quad \text{at } r = 1 + \varepsilon \sin(\lambda z) \quad (6.49)$$

where n is the outer direction normal and λ is the wave number ($\lambda = 2\pi R/l$). λ_f is the molecular mean free path. The characteristic length scale in the present analysis is defined as the microtube mean diameter. It is convenient to introduce the Knudsen number

$$Kn = \frac{\lambda_f}{2R} \quad (6.50)$$

Using perturbation methods, we expand ψ in terms of ε

$$\psi = \psi_0 + \varepsilon \psi_1 + \varepsilon^2 \psi_2 + \dots \quad (6.51)$$

For the boundary conditions (6.49) we can expand $\psi(1 + \varepsilon \sin(\lambda z), z)$ in a Taylor series to obtain

$$\left[\psi_0 + \varepsilon \left(\psi_1 + \sin \lambda z \frac{\partial \psi_0}{\partial r} \right) + \varepsilon^2 \left(\psi_2 + \sin \lambda z \frac{\partial \psi_1}{\partial r} + \frac{1}{2} \sin^2 \lambda z \frac{\partial^2 \psi_0}{\partial r^2} \right) \right]_{r=1} + O(\varepsilon^3) = 1 \quad (6.52)$$

and

$$\begin{aligned} \frac{\partial \psi}{\partial n} \Big|_{r=1+\varepsilon \sin \lambda z} &= \frac{\nabla \psi \cdot \nabla [r - 1 - \varepsilon \sin \lambda z]}{|\nabla [r - 1 - \varepsilon \sin \lambda z]|} = \left[\frac{\partial \psi}{\partial r} - \varepsilon \lambda \cos \lambda z \frac{\partial \psi}{\partial z} - \frac{\varepsilon^2 \lambda^2}{2} \cos^2 \lambda z \frac{\partial \psi}{\partial r} \right]_{r=1+\varepsilon \sin \lambda z} + O(\varepsilon^3) \\ &= \left[\frac{\partial \psi_0}{\partial r} + \varepsilon \left(\frac{\partial \psi_1}{\partial r} + \sin \lambda z \frac{\partial^2 \psi_0}{\partial r^2} - \lambda \cos \lambda z \frac{\partial \psi_0}{\partial z} \right) \right. \\ &\quad \left. + \varepsilon^2 \left(\frac{\partial \psi_2}{\partial r} + \sin \lambda z \frac{\partial^2 \psi_1}{\partial r^2} - \lambda \cos \lambda z \frac{\partial \psi_1}{\partial z} + \frac{1}{2} \sin^2 \lambda z \frac{\partial^3 \psi_0}{\partial r^3} - \frac{\lambda}{2} \sin 2\lambda z \frac{\partial^2 \psi_0}{\partial r \partial z} - \frac{\lambda^2}{2} \cos^2 \lambda z \frac{\partial \psi_0}{\partial r} \right) \right]_{r=1} + O(\varepsilon^3) \end{aligned} \quad (6.53)$$

and

$$\begin{aligned} \frac{\partial^2 \psi}{\partial n^2} \Big|_{r=1+\varepsilon \sin \lambda z} &= \left[\frac{\partial^2 \psi_0}{\partial r^2} + \varepsilon \left(\frac{\partial^2 \psi_1}{\partial r^2} + \sin \lambda z \frac{\partial^3 \psi_0}{\partial r^3} - 2\lambda \cos \lambda z \frac{\partial^2 \psi_0}{\partial r \partial z} \right) \right. \\ &\quad \left. + \varepsilon^2 \left(\frac{\partial^2 \psi_2}{\partial r^2} + \sin \lambda z \frac{\partial^3 \psi_1}{\partial r^3} - 2\lambda \cos \lambda z \frac{\partial^2 \psi_1}{\partial r \partial z} + \frac{1}{2} \sin^2 \lambda z \frac{\partial^4 \psi_0}{\partial r^4} - \lambda \sin 2\lambda z \frac{\partial^3 \psi_0}{\partial r^2 \partial z} \right. \right. \\ &\quad \left. \left. + \lambda^2 \cos^2 \lambda z \frac{\partial^2 \psi_0}{\partial z^2} - \lambda^2 \cos^2 \lambda z \frac{\partial^2 \psi_0}{\partial r^2} - \frac{\lambda^3}{2} \sin 2\lambda z \frac{\partial \psi_0}{\partial z} \right) \right]_{r=1} + O(\varepsilon^3) \end{aligned} \quad (6.54)$$

The solution of ψ_0 is governed by

$$E^4 \psi_0 = 0 \quad (6.55)$$

$$\psi_0 = 0, \quad \frac{1}{r} \frac{\partial \psi_0}{\partial z} = 0 \quad \text{at } r = 0 \quad (6.56)$$

$$\psi_0 = 1, \quad (1 - 2Kn^*) \frac{\partial \psi_0}{\partial r} + 2Kn^* \frac{\partial^2 \psi_0}{\partial r^2} = 0 \quad \text{at } r = 1 \quad (6.57)$$

The zeroth-order (ε^0) solution is the usual slip Poiseuille flow

$$\psi_0 = \frac{2(1 + 4Kn^*)r^2 - r^4}{1 + 8Kn^*} \quad (6.58)$$

The ε^1 -solution is governed by

$$E^4 \psi_1 = 0 \quad (6.59)$$

$$\psi_1 = 0, \quad \frac{1}{r} \frac{\partial \psi_1}{\partial z} = 0 \quad \text{at } r = 0 \quad (6.60)$$

$$\psi_1 = -\sin \lambda z \frac{\partial \psi_0}{\partial r} = -\frac{16Kn^*}{1 + 8Kn^*} \sin \lambda z \quad \text{at } r = 1 \quad (6.61)$$

$$\begin{aligned} (1 - 2Kn^*) \frac{\partial \psi_1}{\partial r} + 2Kn^* \frac{\partial^2 \psi_1}{\partial r^2} &= -\sin \lambda z \frac{\partial^2 \psi_0}{\partial r^2} + \lambda \cos \lambda z \frac{\partial \psi_0}{\partial z} - 2Kn^* \left(\sin \lambda z \frac{\partial^2 \psi_0}{\partial r^3} - 2\lambda \cos \lambda z \frac{\partial^2 \psi_0}{\partial r \partial z} \right) \\ &= \frac{8(1 + 4Kn^*)}{1 + 8Kn^*} \sin \lambda z \quad \text{at } r = 1 \end{aligned} \quad (6.62)$$

According to the boundary conditions, the ψ_1 is in the form

$$\psi_1(r, z) = \phi_1(r) \sin \lambda z \quad (6.63)$$

where

$$(D^2 - \lambda^2)^2 \phi_1 = 0, \quad D^2 \equiv r \frac{d}{dr} \left(\frac{1}{r} \frac{d}{dr} \right) \quad (6.64)$$

The solution of ϕ_1 is

$$\phi_1(r) = C_1 r I_1(\lambda r) + C_2 r^2 I_0(\lambda r) + B_1 r K_1(\lambda r) + B_2 r^2 K_0(\lambda r) \quad (6.65)$$

where $I_\nu(x)$, $K_\nu(x)$ are the modified Bessel functions of the first and second kind respectively of order ν . Due to the boundedness of the velocity field, $B_1=B_2=0$. Therefore,

$$\psi_1 = [C_1 r I_1(\lambda r) + C_2 r^2 I_0(\lambda r)] \sin \lambda z \quad (6.66)$$

Applying boundary conditions (6.61) and (6.62)

$$C_1 I_1(\lambda) + C_2 I_0(\lambda) = -\frac{16 Kn^*}{1 + 8 Kn^*} \quad (6.67)$$

$$C_1 [I_0(\lambda) + 2\lambda^2 Kn^* I_1(\lambda)] + C_2 [(2 + 2\lambda^2 Kn^*) I_0(\lambda) + \lambda(1 + 4Kn^*) I_1(\lambda)] = \frac{8(1 + 4Kn^*)}{1 + 8Kn^*} \quad (6.68)$$

Solving Eqs. (6.67) and (6.68), we have

$$C_1 = -\frac{8}{1 + 8Kn^*} \frac{(1 + 8Kn^* + 4\lambda^2 Kn^{*2}) I_0(\lambda) + 2\lambda Kn^* (1 + 4Kn^*) I_1(\lambda)}{\lambda [I_1^2(\lambda) - I_0(\lambda) I_2(\lambda)] + 4\lambda Kn^* I_1^2(\lambda)} \quad (6.69)$$

$$C_2 = \frac{8}{1 + 8Kn^*} \frac{2\lambda Kn^* I_0(\lambda) + (1 + 4Kn^* + 4\lambda^2 Kn^{*2}) I_1(\lambda)}{\lambda [I_1^2(\lambda) - I_0(\lambda) I_2(\lambda)] + 4\lambda Kn^* I_1^2(\lambda)} \quad (6.70)$$

It is seen that the first-order solution is periodic in z and cannot be related to a mean pressure gradient along z .

Next, The ε^2 -solution is governed by

$$E^4\psi_2 = 0 \quad (6.71)$$

$$\psi_2 = 0, \quad \frac{1}{r} \frac{\partial \psi_2}{\partial z} = 0 \quad \text{at } r = 0 \quad (6.72)$$

$$\begin{aligned} \psi_2 &= -\sin \lambda z \frac{\partial \psi_1}{\partial r} - \frac{1}{2} \sin^2 \lambda z \frac{\partial^2 \psi_0}{\partial r^2} \\ &= \left[-C_1 \lambda I_0(\lambda) - C_2 (2I_0(\lambda) + \lambda I_1(\lambda)) + \frac{4 - 8Kn^*}{1 + 8Kn^*} \right] \left(\frac{1 - \cos(2\lambda z)}{2} \right) \quad \text{at } r = 1 \end{aligned} \quad (6.73)$$

$$\begin{aligned} (1 - 2Kn^*) \frac{\partial \psi_2}{\partial r} + 2Kn^* \frac{\partial^2 \psi_2}{\partial r^2} &= -\sin \lambda z \frac{\partial^2 \psi_1}{\partial r^2} + \lambda \cos \lambda z \frac{\partial \psi_1}{\partial z} - \frac{1}{2} \sin^2 \lambda z \frac{\partial^3 \psi_0}{\partial r^3} + \frac{1}{2} \lambda \sin 2\lambda z \frac{\partial^2 \psi_0}{\partial r \partial z} \\ &\quad + \frac{1}{2} \lambda^2 \cos^2 \lambda z \frac{\partial \psi_0}{\partial r} - 2Kn^* \left(\sin \lambda z \frac{\partial^2 \psi_0}{\partial r^3} - 2\lambda \cos \lambda z \frac{\partial^2 \psi_1}{\partial r \partial z} + \frac{1}{2} \sin^2 \lambda z \frac{\partial^4 \psi_0}{\partial r^4} \right. \\ &\quad \left. - \lambda \sin 2\lambda z \frac{\partial^3 \psi_0}{\partial r^2 \partial z} + \lambda^2 \cos^2 \lambda z \frac{\partial^2 \psi_0}{\partial z^2} - \lambda^2 \cos^2 \lambda z \frac{\partial^2 \psi_0}{\partial r^2} - \frac{\lambda^3}{2} \sin 2\lambda z \frac{\partial \psi_0}{\partial z} \right) \\ &= -\frac{1}{2} [(C_1 \lambda + 2C_2 - 2C_1 \lambda^3 Kn^* + 2C_2 \lambda^2 Kn^*) I_0(\lambda) + (3C_2 \lambda + 2C_1 \lambda^2 Kn^* + 4C_2 \lambda Kn^* - 2C_2 \lambda^3 Kn^*) I_1(\lambda)] \\ &\quad + \frac{6(1 + 2Kn^*) - 4\lambda^2 Kn^* + 16\lambda^2 Kn^{*2}}{1 + 8Kn^*} + \dots \times (\cos(2\lambda z)) \quad \text{at } r = 1 \end{aligned} \quad (6.74)$$

The appropriate solution is in the form

$$\psi_2(r, z) = \psi_{2a}(r) + \text{periodic solution} = \psi_{2a}(r) + \dots \times (\cos(2\lambda z)) \quad (6.75)$$

It is seen that the second-order solution may cause a mean pressure gradient along z . As periodic solution does not contribute to the mean pressure gradient, only ψ_{2a} need to be determined. The ψ_{2a} solution is governed by

$$E^4 \psi_{2a} = 0 \quad (6.76)$$

$$\psi_{2a} = 0, \quad \frac{1}{r} \frac{\partial \psi_{2a}}{\partial z} = 0 \quad \text{at } r = 0 \quad (6.77)$$

$$\psi_{2a} = \frac{1}{2} \left[-C_1 \lambda I_0(\lambda) - C_2 (2I_0(\lambda) + \lambda I_1(\lambda)) + \frac{4 - 8Kn^*}{1 + 8Kn^*} \right] \quad \text{at } r = 1 \quad (6.78)$$

$$\begin{aligned} & (1 - 2Kn^*) \frac{\partial \psi_{2a}}{\partial r} + 2Kn^* \frac{\partial^2 \psi_{2a}}{\partial r^2} \\ &= -\frac{1}{2} [(C_1 \lambda + 2C_2 - 2C_1 \lambda^3 Kn^* + 2C_2 \lambda^2 Kn^*) I_0(\lambda) + (3C_2 \lambda + 2C_1 \lambda^2 Kn^* + 4C_2 \lambda Kn^* - 2C_2 \lambda^3 Kn^*) I_1(\lambda)] \\ &+ \frac{6(1 + 2Kn^*) - 4\lambda^2 Kn^* + 16\lambda^2 Kn^{*2}}{1 + 8Kn^*} \quad \text{at } r = 1 \end{aligned} \quad (6.79)$$

The solution for ψ_{2a} should be of the form

$$\psi_{2a} = C_3 r^2 - C_4 r^4 \quad (6.80)$$

In terms of boundary conditions (6.78) and (6.79), we obtain

$$C_3 = \frac{1}{2} \left[-C_1 \lambda I_0(\lambda) - C_2 (2I_0(\lambda) + \lambda I_1(\lambda)) + \frac{4 - 8Kn^*}{1 + 8Kn^*} \right] + C_4 \quad (6.81)$$

$$\begin{aligned}
C_4 &= -\frac{1}{4(1+8Kn^*)} \left[(C_1\lambda + 2C_2 + 2C_1\lambda^3 Kn^* - 2C_2\lambda^2 Kn^*) I_0(\lambda) - (C_2\lambda + 2C_1\lambda^2 Kn^* + 4C_2\lambda Kn^* - 2C_1\lambda^3 Kn^*) I_1(\lambda) \right] \\
&\quad - \frac{1+10Kn^* - 2\lambda^2 Kn^* + 8\lambda^2 Kn^{*2}}{(1+8Kn^*)^2} \\
&= \frac{1}{(1+8Kn^*)^2} \left[-1-10Kn^* + 2\lambda^2 Kn^* - 8\lambda^2 Kn^{*2} - \frac{2[\alpha_1 I_0^2(\lambda) + \alpha_2 I_0(\lambda)I_1(\lambda) + \alpha_3 I_1^2(\lambda)]}{\lambda[I_1^2(\lambda) - I_0(\lambda)I_2(\lambda)] + 4\lambda Kn^* I_1^2(\lambda)} \right]
\end{aligned} \tag{6.82}$$

where

$$\alpha_1 = \lambda \left(-1 - 4Kn^* - 2\lambda^2 Kn^* - 24\lambda^2 Kn^{*2} - 8\lambda^4 Kn^{*3} \right) \tag{6.83}$$

$$\alpha_2 = 2 + 8Kn^* - 4\lambda^2 Kn^* - 16\lambda^4 Kn^{*3} \tag{6.84}$$

$$\alpha_3 = \lambda \left(-1 - 8Kn^* - 16Kn^{*2} + 2\lambda^2 Kn^* + 8\lambda^2 Kn^{*2} + 8\lambda^4 Kn^{*3} \right) \tag{6.85}$$

The total flow rate is then given by

$$Q = \frac{2\pi R^4 dp/dz'}{\mu} \frac{2\pi}{\lambda} \frac{1}{\int_0^{\pi/\lambda} \frac{1}{r} \frac{\partial}{\partial r} (E^2 \psi) dz} = -\frac{\pi R^4 dp/dz'}{8\mu} \frac{1+8Kn^*}{1+B\epsilon^2 + O(\epsilon^4)} \tag{6.86}$$

where

$$B = (1+8Kn^*) C_4 \tag{6.87}$$

B is a function of wave number λ and modified Knudsen number Kn^* . Figure 6.7 shows the effect of λ and Kn^* on $B(\lambda, Kn^*)$. In the limit of $Kn \rightarrow 0$, Eq. (6.87) reduces to its corresponding continuum flow solution [127]:

$$B_c = -3 + \frac{4I_1^2(\lambda)}{I_1^2(\lambda) - I_0(\lambda)I_2(\lambda)} \quad (6.88)$$

For practical applications, a simple expression which is valid for $\lambda \geq 2$ can be used

$$B_c = 3.92\lambda - 1.76 \quad (6.89)$$

It is seen that the periodic solution cannot be related to the mean pressure gradient along z as its contribution to the integral is zero. Only ψ_0 and ψ_{2a} contribute to the mean pressure gradient.

$$\frac{Q}{Q_{sm}} = \frac{1 + 8Kn^*}{1 + B\varepsilon^2 + O(\varepsilon^4)} \quad (6.90)$$

where Q_{sm} is the flow rate for continuum flow in smooth microtubes. The flow rate decreases with an increase in λ . As B is always positive indicating a decrease in the flow rate with wall roughness.

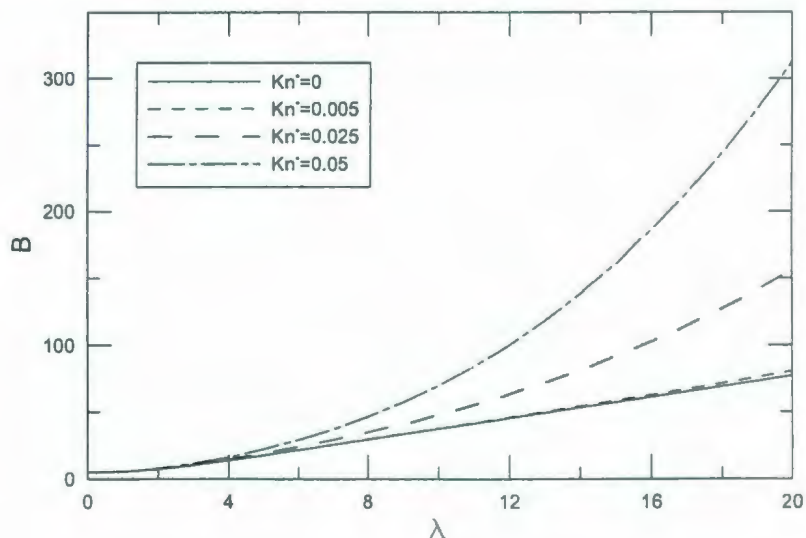


Figure 6.7 $B(\lambda, Kn^*)$ as a function of λ and Kn^* .

Setting $\varepsilon = 0$ in Eq. (6.90), we obtain the corresponding expression for the flow rate in smooth microtubes as $Q/Q_{sm} = 1 + 8Kn^*$. However, Vasudeviah and Balamurugan [128] gave the following inaccurate expression:

$$\frac{Q}{Q_{sm}} \approx \frac{1 + 10Kn^*}{1 + 2Kn^*} \quad (6.91)$$

After integrating Eq. (6.86), the pressure drop along the length of the pipe (L) may be determined to be

$$\Delta p = \frac{8\mu L Q}{\pi R^4} \frac{1 + B\varepsilon^2 + O(\varepsilon^4)}{1 + 8Kn^*} \quad (6.92)$$

It can be also shown that the effect of wall roughness on the pressure drop is given by the following equations

$$\Delta p^* = \frac{\Delta p}{\Delta p_{sm}} = \frac{1 + B\varepsilon^2 + O(\varepsilon^4)}{1 + 8Kn^*} \quad (6.93)$$

where Δp_{sm} is the pressure drop for continuum flow in smooth microtubes.

Figures 6.8 and 6.9 demonstrate the effect of wave number λ and relative roughness ε on pressure drop of microtubes for continuum flow. As B is always positive, the pressure drop increases with wall roughness.

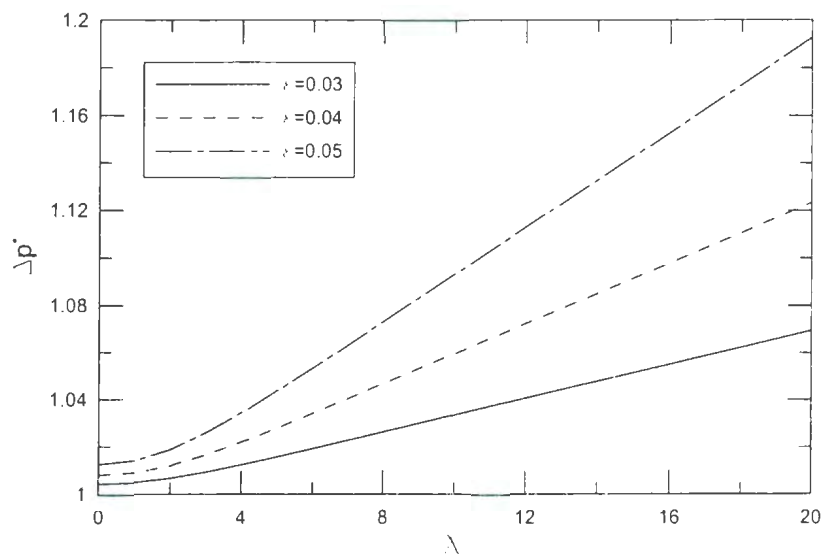


Figure 6.8 Effect of relative roughness ε and wave number λ on pressure drop of microtubes for continuum flow.

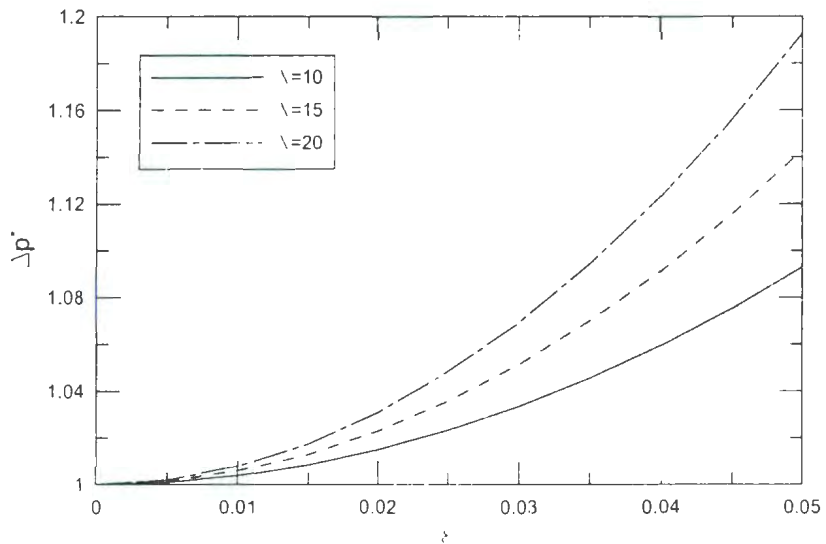


Figure 6.9 Effect of relative roughness ε and wave number λ on pressure drop of microtubes for continuum flow.

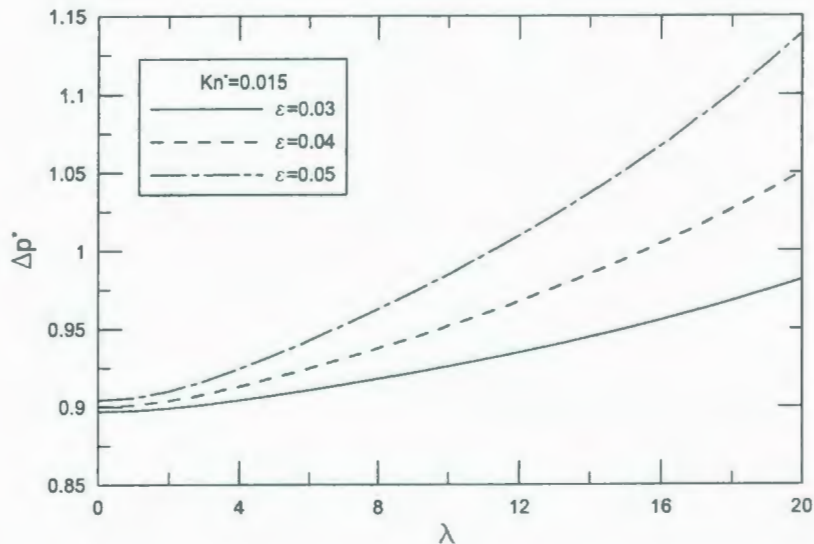


Figure 6.10 Effect of relative roughness ε , wave number λ and Knudsen number Kn on pressure drop of microtubes for slip flow.

Figure 6.10 demonstrates the effect of wave number λ , relative roughness ε and Knudsen number Kn on pressure drop of microtubes for slip flow. Velocity slip decreases pressure drop and corrugated roughness increases pressure drop. Pressure drop depends on ε , λ , and Kn and it can be less than, equal to or greater than unity. The coupled effects between small corrugated roughness and velocity slip proposes a possible explanation on the observed phenomenon that Chung et al. [71] and Kohl et al. [83] found, which showed that the friction factors for gas flow in microchannels can be accurately determined from conventional theory for large channels.

The mean friction factor Reynolds product can be obtained simply by substituting Eq. (6.86) into the definition of fRe .

$$f \operatorname{Re} = \frac{2 \left(-\frac{A}{P} \frac{dp}{dz'} \right) D_h}{\mu \bar{u}} = \frac{2 \left(-\frac{A}{P} \frac{dp}{dz'} \right) D_h A}{\mu Q} = \frac{16 [1 + B\varepsilon^2 + O(\varepsilon^4)]}{(1 + 8Kn^*)} \quad (6.94)$$

The above analysis is carried out for constant fluid properties. We may now consider compressibility of the gas. For compressible flow, the mass flow rate in the microtube is given by employing the equation of state $p=\rho \mathcal{R} T$

$$\dot{m} = \rho \bar{u} A = -\frac{\pi R^4}{8 \mu \mathcal{R} T} [1 - B\varepsilon^2 + O(\varepsilon^4)] \frac{dp}{dz} \left(p + 8 \frac{2-\sigma}{\sigma} p Kn \right) \quad (6.95)$$

We can use $pKn = p_o Kn_o$ since pKn is constant for isothermal flow. Integrating Eq. (6.95), we obtain

$$\dot{m} = \rho \bar{u} A \cong \frac{\pi R^4 p_o^2}{16 \mu \mathcal{R} T z} [1 - \bar{B} \varepsilon^2 + O(\varepsilon^4)] \left[\frac{p_i^2}{p_o^2} - \frac{p_z^2}{p_o^2} + 16 \frac{2-\sigma}{\sigma} Kn_o \left(\frac{p_i}{p_o} - \frac{p_z}{p_o} \right) \right] \quad (6.96)$$

where \bar{B} denotes the average value of $B(\lambda, Kn_i)$ and $B(\lambda, Kn_z)$.

Letting $z=L$ gives:

$$\dot{m} = \rho \bar{u} A \cong \frac{\pi R^4 p_o^2}{16 \mu \mathcal{R} T L} [1 - \bar{B} \varepsilon^2 + O(\varepsilon^4)] \left[\frac{p_i^2}{p_o^2} - 1 + 16 \frac{2-\sigma}{\sigma} Kn_o \left(\frac{p_i}{p_o} - 1 \right) \right] \quad (6.97)$$

The continuum flow mass flow rate is given by:

$$\dot{m}_c = \rho \bar{u} A = \frac{\pi R^4 p_o^2}{16 \mu \mathcal{R} T L} [1 - \bar{B} \varepsilon^2 + O(\varepsilon^4)] \left(\frac{p_i^2}{p_o^2} - 1 \right) \quad (6.98)$$

The effect of slip may be illustrated clearly by dividing the slip flow mass flow Eq. (6.97) by the continuum mass flow Eq. (6.98)

$$\frac{\dot{m}}{\dot{m}_c} \approx 1 + \frac{16 \frac{2-\sigma}{\sigma} Kn_o}{\frac{p_i}{p_o} + 1} \quad (6.99)$$

It is seen that the rarefaction increases the mass flow and that the effect of rarefaction becomes more significant when the pressure ratio decreases.

Combining Eq. (6.96) and Eq. (6.97), we obtain the expression for pressure distribution:

$$\frac{p_z}{p_o} \approx -8 \frac{2-\sigma}{\sigma} Kn_o + \sqrt{\left(8 \frac{2-\sigma}{\sigma} Kn_o + \frac{p_i}{p_o}\right)^2 - \left[\frac{p_i^2}{p_o^2} - 1 + 16 \frac{2-\sigma}{\sigma} Kn_o \left(\frac{p_i}{p_o} - 1\right)\right] \frac{z}{L}} \quad (6.100)$$

The influences of axial corrugated surface roughness on the fully developed laminar flow in microtubes are studied and novel models are proposed to predict friction factor and pressure drop for continuum flow and slip flow. Compressibility effect has also been examined and simple models are proposed to predict the pressure distribution and mass flow rate for slip flow in corrugated rough microtubes.

It is observed that the normalized pressure drop, Δp^* , is a function of relative roughness ε and wave number λ for continuum flow, i.e. $\Delta p^* = F(\varepsilon, \lambda)$. The present model exhibits the influence of corrugated roughness. For most conventional microtubes ($\varepsilon \approx 0.03-0.05$, $\lambda = 10-20$), the present model proposes an explanation on the observed

phenomenon that pressure drop results for continuum flow have shown an increase due to roughness.

For slip flow, Δp^* is a function of relative roughness ε , wave number λ and Knudsen number Kn , i.e. $\Delta p^* = F_1(\varepsilon, \lambda, Kn)$. There exist coupled effects between velocity slip and corrugated roughness. Velocity slip decreases pressure drop and increases flow rate. Corrugated roughness increases pressure drop and decreases flow rate.

6.4 Summary

The effects of corrugated surface roughness on fully developed laminar flow in microtubes are investigated. Novel analytical models are developed to predict friction factor and pressure drop in corrugated roughness microtubes for continuum flow and slip flow. The developed model for slip flow illustrates the coupled effects between velocity slip and corrugated roughness.

The Poiseuille number depends on the relative roughness of the walls of the microchannels also in laminar region and the relative roughness cannot be neglected for microchannels in the laminar region.

The Poiseuille number increases not only as the roughness height increases but also as the roughness spacing decreases.

The presented simple models for circumferential and longitudinal corrugated roughness in this chapter may be used to approximately estimate roughness and velocity slip effects for the design and application of microtubes.

Chapter 7

Slip Flow Heat Transfer in Annular Microchannels with Constant Heat Flux

7.1 Introduction

Slip flow heat transfer in circular tubes was investigated by Sparrow and Lin [129], Barron et al. [130], Ameel et al. [51], Larrode et al. [131], and Simek and Hadjiconstantinou [132]. Yu and Ameel [133, 134], Tung and Bayazitoglu [135] and Renksizbulut et al. [117] studied slip flow heat transfer in rectangular microchannels. In these analyses both uniform wall temperature and uniform wall heat flux boundary conditions were considered. Convection heat transfer in annular macrochannels has been extensively investigated by numerical and analytical methods over the years [106]. However, no attempt has been made for solving the same problem in microchannels. With the development of microscale thermal fluid systems, there is a need to investigate slip flow heat transfer in annular microchannels. In particular such a model is useful as it contains both the tube and channel as special limits.

7.2 Theoretical Analysis

It is necessary to first examine the velocity problem since the heat transfer analysis requires knowing velocity distributions. A schematic diagram of the annular duct section

is provided in Figure 7.1. When the microchannels are long enough ($L/D_h \gg 1$) and Reynolds number is relatively low, the momentum equation reduces to the form

$$\mu \left(\frac{d^2 u}{dr^2} + \frac{1}{r} \frac{du}{dr} \right) = \frac{dp}{dx} \quad (7.1)$$

The velocity distribution must satisfy the slip boundary condition at the walls. The local slip velocity is proportional to the local velocity gradient normal to the wall. The corresponding slip boundary conditions are therefore

$$u = \lambda \frac{2-\sigma}{\sigma} \frac{du}{dr} \quad \text{at} \quad r = b \quad (7.2)$$

$$u = -\lambda \frac{2-\sigma}{\sigma} \frac{du}{dr} \quad \text{at} \quad r = a \quad (7.3)$$

The characteristic length scale in the present analysis is defined as the hydraulic diameter, such that

$$Kn = \frac{\lambda}{D_h} = \frac{\lambda}{2(a-b)} \quad (7.4)$$

A solution of these equations yields

$$u = -\frac{a^2}{4\mu} \frac{dp}{dx} \left\{ 1 - \frac{r^2}{a^2} + 4(1-\varepsilon) \frac{2-\sigma}{\sigma} Kn - \frac{\varepsilon(1-\varepsilon^2) \left[1 + 4 \frac{2-\sigma}{\sigma} Kn \right] \left[(1-\varepsilon) \frac{2-\sigma}{\sigma} 2Kn - \ln \frac{r}{a} \right]}{(1-\varepsilon^2) \frac{2-\sigma}{\sigma} 2Kn - \varepsilon \ln \varepsilon} \right\} \quad (7.5)$$

where $\varepsilon = b/a$. The mean velocity is found by integration of Eq. (7.5) across the section of the duct:

$$\begin{aligned}\bar{u} &= \frac{1}{A} \int u dA = \frac{1}{\pi(a^2 - b^2)} \int u 2\pi r dr \\ &= -\frac{a^2}{8\mu} \frac{dp}{dx} \left[1 + \varepsilon^2 + 8(\varepsilon^2 - \varepsilon + 1) \frac{2-\sigma}{\sigma} Kn + \frac{\varepsilon(1-\varepsilon^2) \left(1 + 4 \frac{2-\sigma}{\sigma} Kn \right)^2}{\varepsilon \ln \varepsilon - 2(1-\varepsilon^2) \frac{2-\sigma}{\sigma} Kn} \right] \quad (7.6)\end{aligned}$$

With the velocity solution, we may now consider the heat transfer problem.

7.2.1 Case (i) uniform wall heat flux on the inner wall, adiabatic on the outer wall ($q_i = q$, $q_o = 0$)

A schematic diagram of the annular tube cross section is pictured in Figure 7.1. The starting point of the analysis is the law of conservation of energy. For fully developed laminar flow, the energy equation takes the form

$$\rho c_p u \frac{\partial T}{\partial x} = \frac{k}{r} \frac{\partial}{\partial r} \left(r \frac{\partial T}{\partial r} \right) \quad (7.7)$$

For thermally fully developed flow with uniform wall heat flux, $\partial T/\partial x = dT/dx$ is a constant. From an energy balance on a length of duct dx , it follows that

$$q 2\pi b dx = \rho \pi (a^2 - b^2) \bar{u} c_p dT \quad (7.8)$$

Solving for dT/dx and substituting into Eq. (7.7) gives

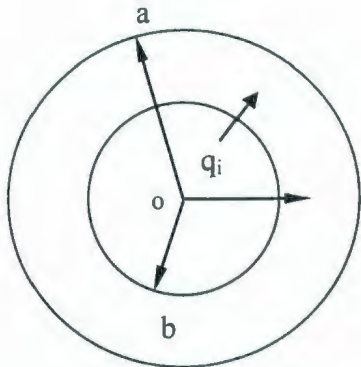


Figure 7.1 A concentric circular annular duct with uniform wall heat flux on the inner wall, adiabatic on the outer wall.

$$\frac{2qb}{(a^2 - b^2)} \bar{u} = \frac{k}{r} \frac{\partial}{\partial r} \left(r \frac{\partial T}{\partial r} \right) \quad (7.9)$$

Due to effect of rarefaction, there is a temperature jump between the wall surface temperature T_w and the contiguous gas temperature T . The appropriate boundary conditions are

$$\frac{dT}{dr} = 0 \quad \text{at} \quad r = a \quad (7.10)$$

$$T - T_w = \frac{2 - \sigma_T}{\sigma_T} \frac{2\gamma}{\gamma + 1} \Pr \frac{dT}{dr} \quad \text{at} \quad r = b \quad (7.11)$$

in which σ_T represents a thermal accommodation coefficient measuring the extent to which the energies of molecules impinging on a surface are affected by contact with the surface. σ_T is usually between 0.32 and 1 [102] and close to unity for typical engineering surfaces, but it may reduce to the order of 10^{-1} for especially clean surfaces. \Pr and γ

denote the Prandtl number and specific heat ratio respectively. With these boundary conditions, the temperature distribution can be obtained. In order to determine the local heat transfer coefficient and Nusselt number, the bulk temperature T_b is needed and may be obtained as follows

$$T_b = \frac{\int_b^r 2\pi r u T dr}{\int_b^r 2\pi r u dr} \quad (7.12)$$

After integration we can obtain the Nusselt number as

$$Nu_{ii} = \frac{q_i D_h}{k(T_w - T_b)} \quad (7.13)$$

The solution requires many pages to show the complete Nusselt number expression. It is very space consuming and therefore must be omitted here. In the limit of $Kn \rightarrow 0$, Eq. (7.13) reduces to its continuum flow solution:

$$Nu_n = \frac{144(\varepsilon - 1)(\varepsilon^2 - 1)^2 [\varepsilon^2 \ln \varepsilon - \varepsilon^2 + \ln \varepsilon + 1]}{\left[45\varepsilon^9 - 234\varepsilon^7 + 432\varepsilon^5 - 342\varepsilon^3 + 99\varepsilon + 72\varepsilon(\ln \varepsilon)^3 + (33\varepsilon^9 - 108\varepsilon^5 - 144\varepsilon^3 + 219\varepsilon)(\ln \varepsilon)^2 \right] + (-76\varepsilon^9 + 184\varepsilon^7 + 108\varepsilon^5 - 464\varepsilon^3 + 248\varepsilon)\ln \varepsilon} \quad (7.14)$$

Assuming $\sigma = 1$, $\sigma_T = 1$, $Pr = 0.71$, $\gamma = 1.4$, we can obtain the relationship of Nu and Kn . Figure 7.2 shows the variation of Nusselt numbers for uniform wall heat flux on the inner wall, adiabatic on the outer wall for annular ducts, where the Nusselt number data have been normalized with the continuum flow Nusselt number. It is seen that the Nu/Nu_c

values decrease as the Knudsen number increases for the same radii ratio. The Nu/Nu_c values also decrease with a decrease of ε for the same Kn . The fully developed Nusselt numbers for different Knudsen numbers are presented in Table 7.1. It is noted that Eq. (7.13) reduces to its corresponding continuum flow results [106] in the limit of $Kn \rightarrow 0$.

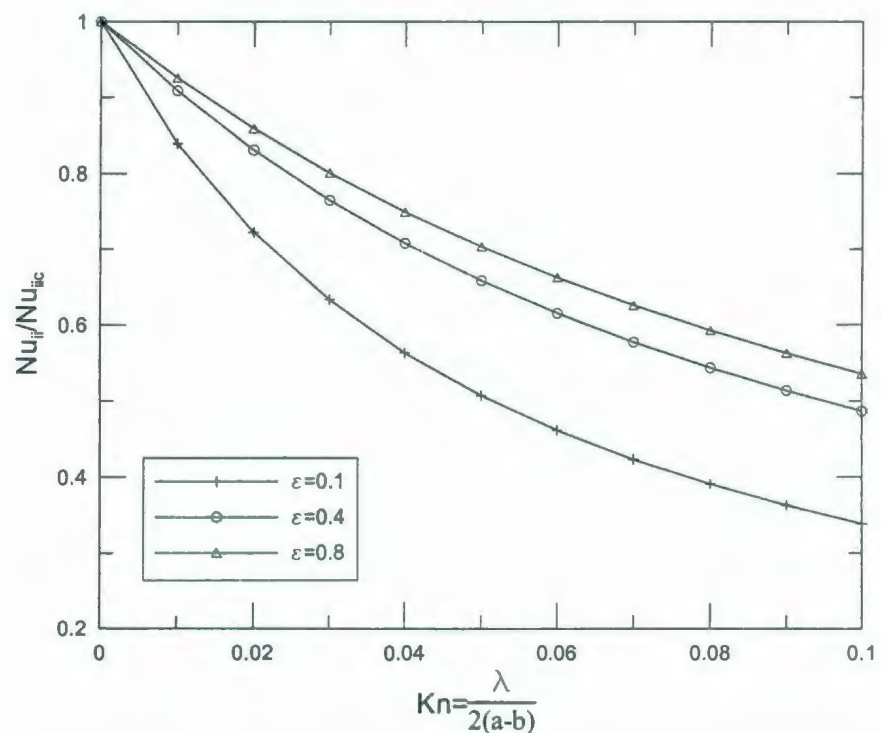


Figure 7.2 Variation of Nusselt number for uniform wall heat flux on the inner wall, adiabatic on the outer wall.

Table 7.1 Fully developed Nusselt numbers (i) for different Knudsen numbers.

| b/a | $Nu Kn^*=0$ | $Nu Kn^*=0.01$ | $Nu Kn^*=0.04$ | $Nu Kn^*=0.07$ | $Nu Kn^*=0.1$ |
|-------|-------------|----------------|----------------|----------------|---------------|
| 0 | ∞ | ∞ | ∞ | ∞ | ∞ |
| 0.001 | 337.04414 | 51.58819 | 14.55661 | 8.47398 | 5.97672 |
| 0.01 | 54.01669 | 28.69024 | 11.87604 | 7.48470 | 5.46457 |
| 0.02 | 32.70512 | 21.33320 | 10.39371 | 6.86479 | 5.12490 |
| 0.04 | 20.50925 | 15.38538 | 8.75035 | 6.10532 | 4.68769 |
| 0.05 | 17.81128 | 13.82053 | 8.22319 | 5.84363 | 4.53139 |
| 0.06 | 15.93349 | 12.66667 | 7.80261 | 5.62800 | 4.40034 |
| 0.08 | 13.46806 | 11.06362 | 7.16737 | 5.29021 | 4.19083 |
| 0.10 | 11.90578 | 9.99206 | 6.70573 | 5.03512 | 4.02914 |
| 0.15 | 9.68703 | 8.38991 | 5.95260 | 4.60069 | 3.74676 |
| 0.20 | 8.49892 | 7.49106 | 5.49354 | 4.32437 | 3.56254 |
| 0.25 | 7.75347 | 6.91204 | 5.18291 | 4.13239 | 3.43250 |
| 0.30 | 7.24115 | 6.50739 | 4.95876 | 3.99143 | 3.33602 |
| 0.40 | 6.58330 | 5.98007 | 4.65823 | 3.79954 | 3.20353 |
| 0.50 | 6.18102 | 5.65372 | 4.46803 | 3.67676 | 3.11830 |
| 0.60 | 5.91171 | 5.43397 | 4.33869 | 3.59301 | 3.06018 |
| 0.70 | 5.72036 | 5.27750 | 4.24631 | 3.53339 | 3.01894 |
| 0.80 | 5.57849 | 5.16183 | 4.17839 | 3.49089 | 2.98868 |
| 0.90 | 5.46988 | 5.10665 | 4.12284 | 3.45118 | 2.95475 |

7.2.2 Case (ii) uniform wall heat flux on the outer wall, adiabatic on the inner wall ($q_i = 0, q_o = q$)

A schematic diagram of the annular tube cross section is given in Figure 7.3. For fully developed laminar flow, the energy equation can be expressed as

$$\rho c_p u \frac{\partial T}{\partial x} = \frac{k}{r} \frac{\partial}{\partial r} \left(r \frac{\partial T}{\partial r} \right) \quad (7.15)$$

For thermally fully developed condition with uniform wall heat flux, from an energy balance on a length of duct dx , it follows

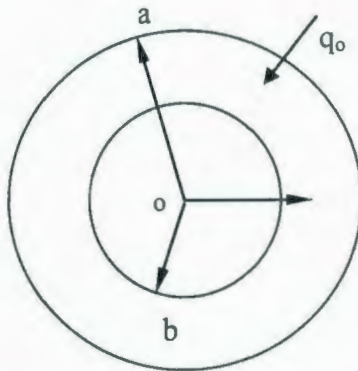


Figure 7.3 A concentric circular annular duct with uniform wall heat flux on the outer wall, adiabatic on the inner wall.

$$q2\pi adx = \rho\pi(a^2 - b^2)\bar{u}c_p dT \quad (7.16)$$

Eliminating $\partial T/\partial x$ from Eqs. (7.15) and (7.16) and rearranging

$$\frac{2qa}{(a^2 - b^2)} \frac{u}{\bar{u}} = \frac{k}{r} \frac{\partial}{\partial r} \left(r \frac{\partial T}{\partial r} \right) \quad (7.17)$$

Due to effect of rarefaction, the appropriate boundary conditions are

$$\frac{dT}{dr} = 0 \quad \text{at } r = b \quad (7.18)$$

$$T - T_w = -\frac{2 - \sigma_r}{\sigma_r} \frac{2\gamma}{\gamma + 1} \text{Pr} \frac{\lambda}{dr} \frac{dT}{dr} \quad \text{at } r = a \quad (7.19)$$

With these boundary conditions, the temperature distribution can be obtained in the same manner as the previous case.

After integration the bulk temperature T_b using Eq. (7.12) we can obtain the Nusselt number as

$$Nu_{oo} = \frac{q_o D_h}{k(T_w - T_b)} \quad (7.20)$$

As before the solution requires many pages to show the complete Nusselt number expression. In the limit of $Kn \rightarrow 0$, Eq. (7.20) reduces to its continuum flow solution:

$$Nu_{oo} = \frac{144(\varepsilon - 1)(\varepsilon^2 - 1)^2 [\varepsilon^2 \ln \varepsilon - \varepsilon^2 + \ln \varepsilon + 1]^2}{[-99\varepsilon^8 + 342\varepsilon^6 - 432\varepsilon^4 + 234\varepsilon^2 - 45 + 72\varepsilon^8 (\ln \varepsilon)^3 + (-219\varepsilon^8 + 144\varepsilon^6 + 108\varepsilon^4 - 33)(\ln \varepsilon)^2] \\ + (248\varepsilon^8 - 464\varepsilon^6 + 108\varepsilon^4 + 184\varepsilon^2 - 76)\ln \varepsilon} \quad (7.21)$$

Moreover, the limit of Eq. (7.20) which corresponds to a circular tube for $\varepsilon \rightarrow 0$ is [129]:

$$Nu_{oo} = \frac{q_o D_h}{k(T_w - T_b)} = \frac{48}{11 + 128 \frac{2-\sigma}{\sigma} Kn + 384 \left(\frac{2-\sigma}{\sigma} Kn \right)^2 + 48 \frac{2-\sigma_T}{\sigma_T} \frac{2\gamma}{\gamma+1} \frac{Kn}{Pr}} \quad (7.22)$$

Assuming $\sigma = 1$, $\sigma_T = 1$, $Pr = 0.71$, $\gamma = 1.4$, we can obtain the relationship of Nu and Kn . Figure 7.4 shows the variation of Nusselt numbers for uniform wall heat flux on the outer wall, adiabatic on the inner wall for annular ducts. It is seen that the Nu/Nu_c values decrease as the Knudsen number increases for the same radii ratio. The Nu/Nu_c values increase with a decrease of ε for the same Kn . The fully developed Nusselt numbers for

different Knudsen numbers are demonstrated in Table 7.2. It is seen that Eq. (7.20) reduces to its corresponding continuum flow results [106] in the limit of $Kn \rightarrow 0$.

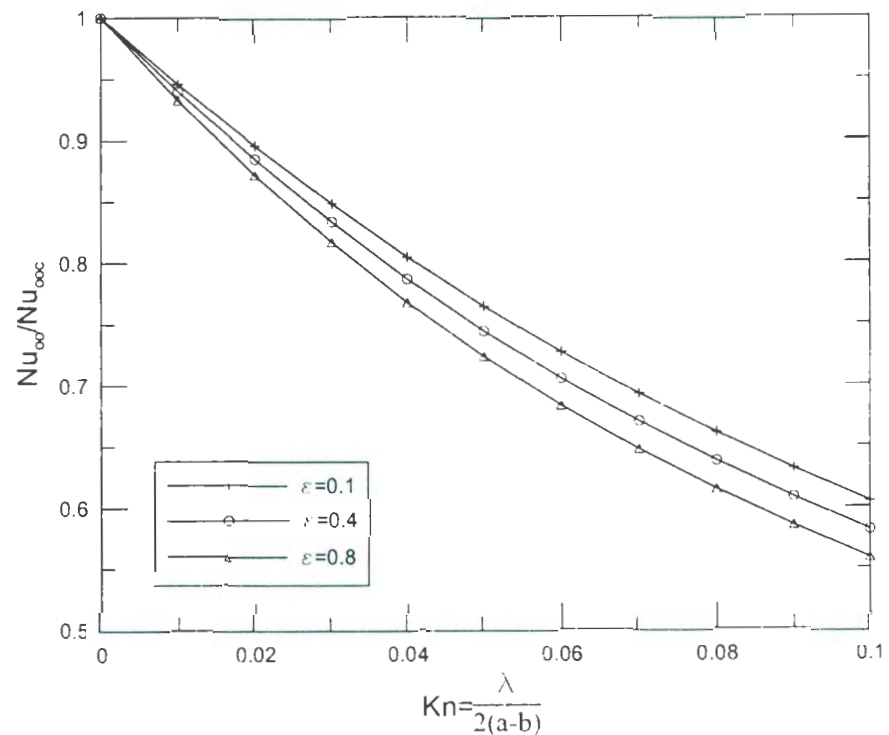


Figure 7.4 Variation of Nusselt number for uniform wall heat flux on the outer wall, adiabatic on the inner wall.

Table 7.2 Fully developed Nusselt numbers (ii) for different Knudsen numbers.

| b/a | $Nu \text{ Kn}^*=0$ | $Nu \text{ Kn}^*=0.01$ | $Nu \text{ Kn}^*=0.04$ | $Nu \text{ Kn}^*=0.07$ | $Nu \text{ Kn}^*=0.1$ |
|-------|---------------------|------------------------|------------------------|------------------------|-----------------------|
| 0 | 4.36364 | 4.22916 | 3.76201 | 3.31123 | 2.92359 |
| 0.001 | 4.58657 | 4.27301 | 3.76998 | 3.31379 | 2.92445 |
| 0.01 | 4.69234 | 4.41098 | 3.81332 | 3.32884 | 2.92923 |
| 0.02 | 4.73424 | 4.46555 | 3.83847 | 3.33786 | 2.93144 |
| 0.04 | 4.77803 | 4.51708 | 3.86441 | 3.34621 | 2.93172 |
| 0.05 | 4.79198 | 4.53214 | 3.87177 | 3.34796 | 2.93083 |
| 0.06 | 4.80323 | 4.54373 | 3.87711 | 3.34882 | 2.92957 |
| 0.08 | 4.82070 | 4.56063 | 3.88403 | 3.34887 | 2.92642 |
| 0.10 | 4.83421 | 4.57269 | 3.88802 | 3.34770 | 2.92290 |
| 0.15 | 4.86026 | 4.59354 | 3.89256 | 3.34296 | 2.91414 |
| 0.20 | 4.88259 | 4.60981 | 3.89496 | 3.33840 | 2.90669 |
| 0.25 | 4.90475 | 4.62560 | 3.89787 | 3.33524 | 2.90100 |
| 0.30 | 4.92801 | 4.64233 | 3.90215 | 3.33379 | 2.89707 |
| 0.40 | 4.97917 | 4.68022 | 3.91551 | 3.33583 | 2.89394 |
| 0.50 | 5.03653 | 4.72413 | 3.93480 | 3.34352 | 2.89597 |
| 0.60 | 5.09922 | 4.77322 | 3.95897 | 3.35566 | 2.90194 |
| 0.70 | 5.16618 | 4.82649 | 3.98695 | 3.37121 | 2.91092 |
| 0.80 | 5.23654 | 4.88378 | 4.01949 | 3.38944 | 2.92227 |
| 0.90 | 5.30955 | 4.94356 | 4.05602 | 3.40928 | 2.93510 |

7.2.3 Case (iii) uniform wall heat flux on both walls ($q_i \neq 0, q_o \neq 0$)

A schematic diagram of the annular tube cross section is pictured in Figure 7.5. For fully developed laminar flow, the energy equation may be written as

$$\rho c_p u \frac{\partial T}{\partial x} = \frac{k}{r} \frac{\partial}{\partial r} \left(r \frac{\partial T}{\partial r} \right) \quad (7.23)$$

The boundary conditions are

$$-k \frac{\partial T}{\partial r} = q_i \quad r = b \quad (7.24)$$

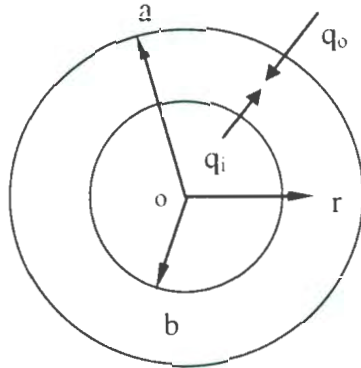


Figure 7.5 A concentric circular annular duct with uniform wall heat flux on both walls.

$$k \frac{\partial T}{\partial r} = q_o \quad r = a \quad (7.25)$$

As the boundary conditions are nonhomogeneous, solutions for these boundary conditions can be obtained by the principle of superposition once the solutions for each boundary condition are derived. Considering the problem as two components (1 and 2):

Problem 1

$$\rho c_p u \frac{\partial T_1}{\partial x} = \frac{k}{r} \frac{\partial}{\partial r} \left(r \frac{\partial T_1}{\partial r} \right) \quad (7.26)$$

The boundary conditions are:

$$-k \frac{\partial T_1}{\partial r} = q_i \quad r = b \quad (7.27)$$

$$\frac{\partial T_1}{\partial r} = 0 \quad r = a \quad (7.28)$$

Problem 2

$$\rho c_p u \frac{\partial T_2}{\partial x} = \frac{k}{r} \frac{\partial}{\partial r} \left(r \frac{\partial T_2}{\partial r} \right) \quad (7.29)$$

The boundary conditions are:

$$\frac{\partial T_2}{\partial r} = 0 \quad r = b \quad (7.30)$$

$$k \frac{\partial T_2}{\partial r} = q_o \quad r = a \quad (7.31)$$

Due to effect of rarefaction, there is a temperature jump between the wall surface temperature T_w and the contiguous gas temperature T . In mathematical terms, the boundary conditions are as follows:

$$T_1 - T_{w1} = \frac{2 - \sigma_T}{\sigma_T} \frac{2\gamma}{\gamma + 1} \text{Pr} \frac{dT_1}{dr} \quad \text{at } r = b \quad (7.32)$$

$$T_2 - T_{w2} = \frac{2 - \sigma_T}{\sigma_T} \frac{2\gamma}{\gamma + 1} \text{Pr} \frac{dT_2}{dr} \quad \text{at } r = b \quad (7.33)$$

$$T_1 - T_{wo1} = -\frac{2 - \sigma_T}{\sigma_T} \frac{2\gamma}{\gamma + 1} \text{Pr} \frac{dT_1}{dr} \quad \text{at } r = a \quad (7.34)$$

$$T_2 - T_{wo2} = -\frac{2 - \sigma_T}{\sigma_T} \frac{2\gamma}{\gamma + 1} \text{Pr} \frac{dT_2}{dr} \quad \text{at } r = a \quad (7.35)$$

applying the principle of superposition

$$T = T_1 + T_2 \quad (7.36)$$

$$T_b = T_{b1} + T_{b2} \quad (7.37)$$

$$T_{wi} = T_{wi1} + T_{wi2} \quad (7.38)$$

$$T_{wo} = T_{wo1} + T_{wo2} \quad (7.39)$$

The solutions of problems 1 and 2 have been correspondingly obtained from the above cases (i, ii), therefore superposition of these solutions is the solution of original problem. Nu_i and Nu_o are evaluated at the inner and outer walls respectively. For convenience, we may define two parameters $\varepsilon_i, \varepsilon_o$

$$\varepsilon_i = \frac{T_{wi1} - T_{b1}}{T_{wi1} + T_{wi2} - T_{b1} - T_{b2}} \quad (7.40)$$

$$Nu_i = \frac{q_i D_h}{k(T_{wi} - T_b)} = Nu_{ii} \varepsilon_i \quad (7.41)$$

$$\varepsilon_o = \frac{T_{wo2} - T_{b2}}{T_{wo1} + T_{wo2} - T_{b1} - T_{b2}} \quad (7.42)$$

$$Nu_o = \frac{q_o D_h}{k(T_{wo} - T_b)} = Nu_{oo} \varepsilon_o \quad (7.43)$$

The solutions for Nu_i and Nu_o are quite involved. The program Maple was used to assist in the computation. It is quite space consuming and therefore must be omitted here. However, they are available from the author upon request.

Moreover, when $q_i=q_o$, the limit of Eqs. (7.41) and (7.43) which corresponds to a parallel-plate channel for $\varepsilon \rightarrow 1$ is [136]:

$$Nu_i = Nu_o = \frac{qD_h}{k(T_w - T_b)} = \frac{140}{\frac{17 + 336 \frac{2-\sigma}{\sigma} Kn + 1680 \left(\frac{2-\sigma}{\sigma} Kn \right)^2}{\left(1 + 12 \frac{2-\sigma}{\sigma} Kn \right)^2} + 140 \frac{2-\sigma_T}{\sigma_T} \frac{2\gamma}{\gamma+1} \Pr}$$

(7.44)

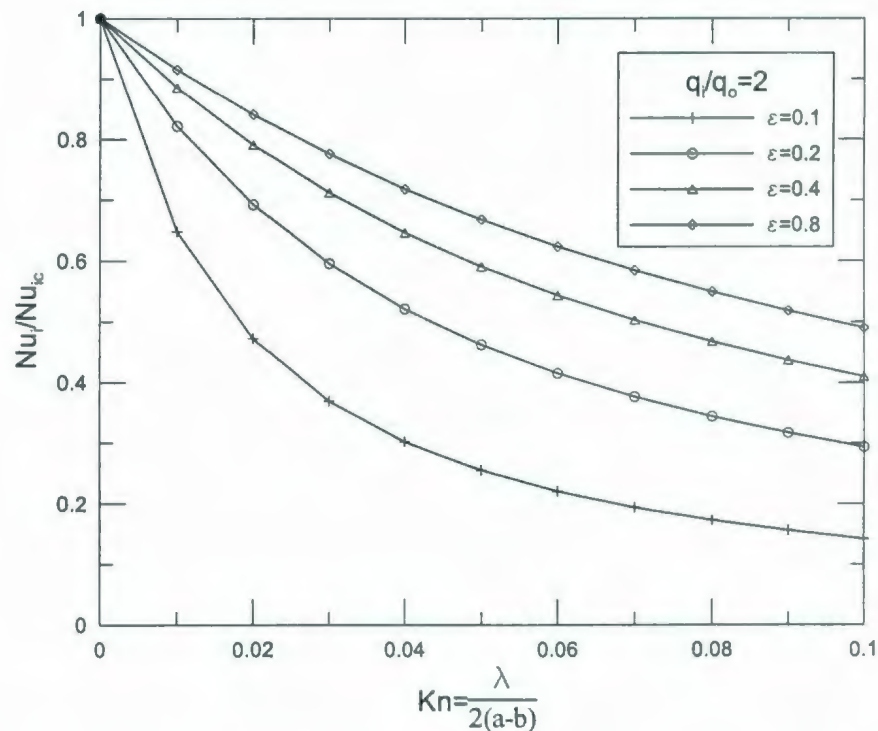


Figure 7.6 Variation of Nu_i for uniform wall heat flux on both walls.

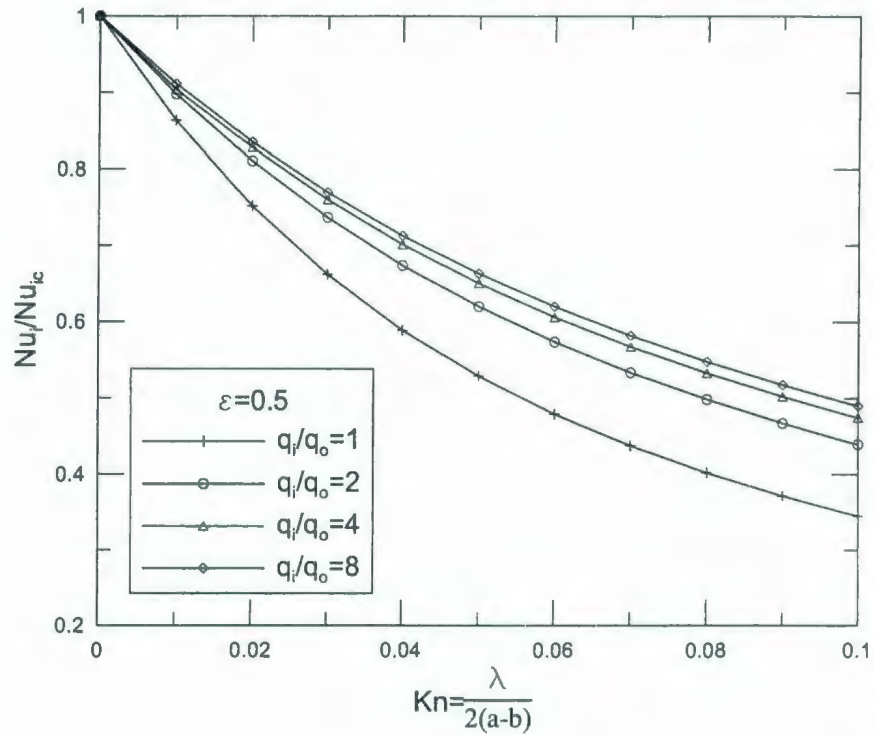


Figure 7.7 Effects of q_i/q_o for Nu_i for uniform wall heat flux on both walls.

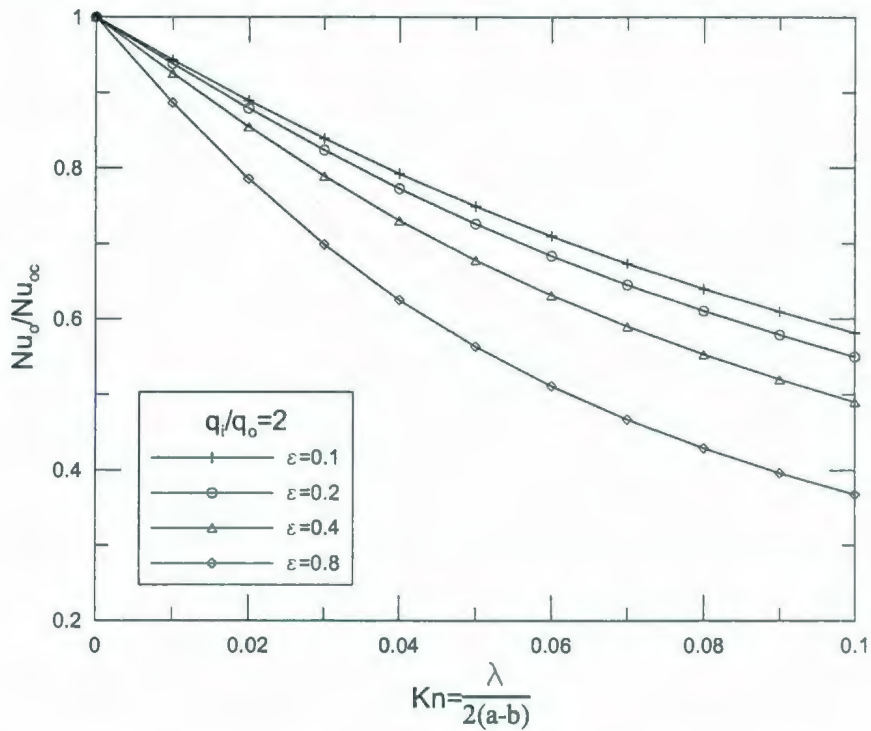


Figure 7.8 Variation of Nu_o for uniform wall heat flux on both walls.

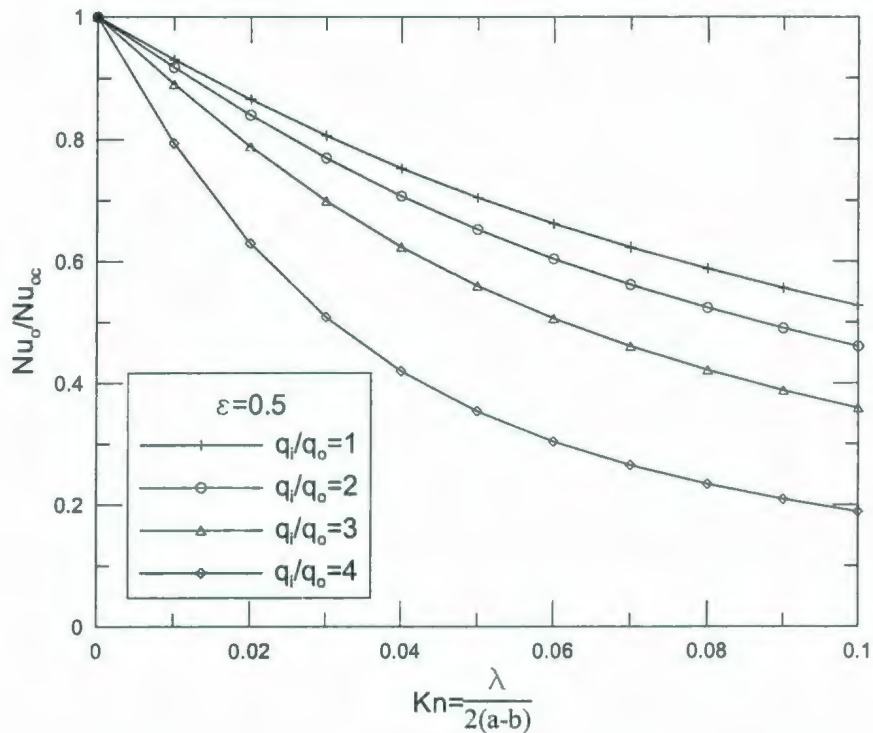


Figure 7.9 Effects of q_i/q_o for Nu_o for uniform wall heat flux on both walls.

Assuming $\sigma = 1$, $\sigma_T = 1$, $Pr = 0.71$, $\gamma = 1.4$, we can obtain the relationship of Nu and Kn .

Figure 7.6 shows the variation of Nu_i for uniform wall heat flux on both walls for annular ducts. It is seen that the Nu/Nu_{ic} values decrease as the Knudsen number increases for the same ε and q_i/q_o . The Nu/Nu_{ic} values increase with an increase of ε for the same Kn and q_i/q_o . Figure 7.7 demonstrates the effects of q_i/q_o for Nu_i for uniform wall heat flux on both walls for annular ducts. The Nu/Nu_{ic} values increase with an increase of q_i/q_o for the same Kn and ε .

Figure 7.8 shows the variation of Nu_o for uniform wall heat flux on both walls for annular ducts. It is seen that the Nu_o/Nu_{oc} values decrease as the Knudsen number increases for the same ε and q_i/q_o . The Nu_o/Nu_{oc} values increase with a decrease of ε for the same Kn and q_i/q_o . Figure 7.9 illustrates the effects of q_i/q_o for Nu_o for uniform wall heat flux on both walls for annular ducts. The Nu_o/Nu_{oc} values decrease with an increase of q_i/q_o for the same Kn and ε .

Now, we consider two special cases of specified constant wall heat fluxes in order to compare with the available continuum flow results in the open literature [106]. Two special cases of specified constant wall heat fluxes are (A) constant and equal axial heat fluxes specified on both walls such that at any axial location the peripheral wall temperatures are constant but different at the inner and outer walls; (B) constant but different wall heat fluxes specified on both walls such that at any axial location the peripheral wall temperatures at the inner and outer walls are constant and equal. Note that the heat flux is specified as positive if the heat transfer is from the wall to the fluid. The fully developed Nusselt numbers for both these cases are presented in Tables 7.3-7.6. It is noted that Eqs. (7.41) and (7.43) reduce to its corresponding continuum flow results [106] in the limit of $Kn \rightarrow 0$.

Table 7.3 Fully developed Nusselt numbers at the inner walls (iii)(A) for different Kn .

| b/a | $Nu Kn^*=0$ | $Nu Kn^*=0.01$ | $Nu Kn^*=0.04$ | $Nu Kn^*=0.07$ | $Nu Kn^*=0.1$ |
|--------|-------------|----------------|----------------|----------------|---------------|
| 0 | 0 | 0 | 0 | 0 | 0 |
| 0.0001 | -7.222 | -7.775 | -12.753 | -36.118 | 43.424 |
| 0.001 | -7.507 | -8.045 | -13.262 | -40.165 | 38.867 |
| 0.01 | -8.912 | -9.826 | -17.639 | -133.195 | 23.535 |
| 0.02 | -10.270 | -11.593 | -23.670 | 161.919 | 17.945 |
| 0.04 | -13.269 | -15.695 | -48.714 | 36.963 | 13.153 |
| 0.05 | -15.055 | -18.300 | -85.684 | 28.059 | 11.847 |
| 0.06 | -17.128 | -21.500 | -270.336 | 23.046 | 10.871 |
| 0.08 | -22.569 | -30.941 | 97.476 | 17.540 | 9.494 |
| 0.10 | -31.036 | -49.601 | 44.947 | 14.545 | 8.558 |
| 0.15 | -128.740 | 228.507 | 21.509 | 10.804 | 7.129 |
| 0.20 | 88.712 | 42.656 | 15.302 | 8.999 | 6.307 |
| 0.25 | 37.359 | 25.680 | 12.394 | 7.922 | 5.765 |
| 0.30 | 25.166 | 19.267 | 10.695 | 7.201 | 5.378 |
| 0.40 | 16.555 | 13.786 | 8.779 | 6.290 | 4.860 |
| 0.50 | 13.111 | 11.316 | 7.720 | 5.734 | 4.525 |
| 0.60 | 11.248 | 9.905 | 7.045 | 5.358 | 4.291 |
| 0.70 | 10.077 | 8.989 | 6.576 | 5.087 | 4.118 |
| 0.80 | 9.272 | 8.348 | 6.229 | 4.881 | 3.984 |
| 0.90 | 8.684 | 7.867 | 5.960 | 4.716 | 3.875 |
| 1.00 | 8.235 | 7.501 | 5.755 | 4.590 | 3.791 |

Table 7.4 Fully developed Nusselt numbers at the inner walls (iii)(B) for different Kn .

| b/a | $Nu Kn^*=0$ | $Nu Kn^*=0.01$ | $Nu Kn^*=0.04$ | $Nu Kn^*=0.07$ | $Nu Kn^*=0.1$ | q_i/q_o |
|--------|-------------|----------------|----------------|----------------|---------------|-----------|
| 0 | ∞ | ∞ | ∞ | ∞ | ∞ | ∞ |
| 0.0001 | 4051.526 | 59.989 | 15.159 | 8.675 | 6.077 | 847.448 |
| 0.001 | 563.701 | 55.171 | 14.829 | 8.565 | 6.021 | 114.141 |
| 0.01 | 91.097 | 37.065 | 13.144 | 7.970 | 5.718 | 17.348 |
| 0.02 | 55.320 | 29.525 | 12.094 | 7.573 | 5.509 | 10.236 |
| 0.04 | 34.772 | 22.595 | 10.804 | 7.054 | 5.230 | 6.206 |
| 0.05 | 30.209 | 20.627 | 10.357 | 6.866 | 5.127 | 5.319 |
| 0.06 | 27.026 | 19.131 | 9.988 | 6.706 | 5.038 | 4.703 |
| 0.08 | 22.833 | 16.988 | 9.406 | 6.447 | 4.893 | 3.893 |
| 0.10 | 20.162 | 15.505 | 8.962 | 6.243 | 4.777 | 3.379 |
| 0.15 | 16.334 | 13.204 | 8.196 | 5.878 | 4.567 | 2.642 |
| 0.20 | 14.253 | 11.853 | 7.696 | 5.630 | 4.421 | 2.240 |
| 0.25 | 12.924 | 10.953 | 7.338 | 5.448 | 4.314 | 1.981 |
| 0.30 | 11.993 | 10.302 | 7.067 | 5.307 | 4.229 | 1.798 |
| 0.40 | 10.764 | 9.418 | 6.680 | 5.102 | 4.106 | 1.551 |
| 0.50 | 9.979 | 8.837 | 6.413 | 4.957 | 4.018 | 1.389 |
| 0.60 | 9.429 | 8.423 | 6.216 | 4.849 | 3.951 | 1.272 |
| 0.70 | 9.020 | 8.111 | 6.064 | 4.764 | 3.899 | 1.182 |
| 0.80 | 8.701 | 7.864 | 5.941 | 4.695 | 3.856 | 1.110 |
| 0.90 | 8.446 | 7.665 | 5.850 | 4.638 | 3.820 | 1.050 |
| 1.00 | 8.235 | 7.501 | 5.755 | 4.590 | 3.791 | 1.000 |

Table 7.5 Fully developed Nusselt numbers at the outer walls (iii)(A) for different Kn .

| b/a | $Nu Kn^*=0$ | $Nu Kn^*=0.01$ | $Nu Kn^*=0.04$ | $Nu Kn^*=0.07$ | $Nu Kn^*=0.1$ |
|--------|-------------|----------------|----------------|----------------|---------------|
| 0 | 4.364 | 4.229 | 3.762 | 3.311 | 2.924 |
| 0.0001 | 4.526 | 4.235 | 3.763 | 3.312 | 2.924 |
| 0.001 | 4.589 | 4.276 | 3.772 | 3.315 | 2.926 |
| 0.01 | 4.721 | 4.438 | 3.834 | 3.345 | 2.941 |
| 0.02 | 4.792 | 4.519 | 3.880 | 3.369 | 2.956 |
| 0.04 | 4.894 | 4.625 | 3.947 | 3.409 | 2.980 |
| 0.05 | 4.937 | 4.666 | 3.974 | 3.426 | 2.991 |
| 0.06 | 4.977 | 4.705 | 4.000 | 3.442 | 3.001 |
| 0.08 | 5.052 | 4.774 | 4.047 | 3.472 | 3.021 |
| 0.10 | 5.122 | 4.839 | 4.090 | 3.500 | 3.040 |
| 0.15 | 5.288 | 4.988 | 4.190 | 3.566 | 3.085 |
| 0.20 | 5.449 | 5.130 | 4.284 | 3.630 | 3.129 |
| 0.25 | 5.608 | 5.270 | 4.377 | 3.692 | 3.172 |
| 0.30 | 5.767 | 5.409 | 4.468 | 3.753 | 3.215 |
| 0.40 | 6.089 | 5.689 | 4.649 | 3.875 | 3.300 |
| 0.50 | 6.419 | 5.973 | 4.831 | 3.995 | 3.385 |
| 0.60 | 6.759 | 6.263 | 5.013 | 4.115 | 3.468 |
| 0.70 | 7.109 | 6.561 | 5.197 | 4.235 | 3.550 |
| 0.80 | 7.472 | 6.864 | 5.380 | 4.354 | 3.632 |
| 0.90 | 7.847 | 7.188 | 5.571 | 4.472 | 3.712 |
| 1.00 | 8.235 | 7.501 | 5.755 | 4.590 | 3.791 |

Table 7.6 Fully developed Nusselt numbers at the outer walls (iii)(B) for different Kn .

| b/a | $Nu Kn^*=0$ | $Nu Kn^*=0.01$ | $Nu Kn^*=0.04$ | $Nu Kn^*=0.07$ | $Nu Kn^*=0.1$ | q_i/q_o |
|--------|-------------|----------------|----------------|----------------|---------------|-----------|
| 0 | 4.364 | 4.229 | 3.762 | 3.311 | 2.924 | ∞ |
| 0.0001 | 4.781 | 4.468 | 3.945 | 3.450 | 3.030 | 847.448 |
| 0.001 | 4.939 | 4.595 | 4.019 | 3.503 | 3.070 | 114.141 |
| 0.01 | 5.251 | 4.926 | 4.205 | 3.624 | 3.154 | 17.348 |
| 0.02 | 5.404 | 5.084 | 4.307 | 3.690 | 3.199 | 10.236 |
| 0.04 | 5.603 | 5.279 | 4.438 | 3.775 | 3.257 | 6.206 |
| 0.05 | 5.679 | 5.351 | 4.488 | 3.807 | 3.279 | 5.319 |
| 0.06 | 5.747 | 5.415 | 4.531 | 3.836 | 3.298 | 4.703 |
| 0.08 | 5.865 | 5.523 | 4.604 | 3.884 | 3.331 | 3.893 |
| 0.10 | 5.967 | 5.616 | 4.666 | 3.924 | 3.359 | 3.379 |
| 0.15 | 6.182 | 5.807 | 4.790 | 4.005 | 3.413 | 2.642 |
| 0.20 | 6.363 | 5.966 | 4.891 | 4.070 | 3.456 | 2.240 |
| 0.25 | 6.524 | 6.104 | 4.976 | 4.124 | 3.492 | 1.981 |
| 0.30 | 6.672 | 6.230 | 5.052 | 4.171 | 3.524 | 1.798 |
| 0.40 | 6.941 | 6.455 | 5.185 | 4.253 | 3.577 | 1.551 |
| 0.50 | 7.185 | 6.657 | 5.300 | 4.323 | 3.622 | 1.389 |
| 0.60 | 7.414 | 6.844 | 5.405 | 4.386 | 3.662 | 1.272 |
| 0.70 | 7.631 | 7.020 | 5.501 | 4.442 | 3.698 | 1.182 |
| 0.80 | 7.840 | 7.185 | 5.591 | 4.495 | 3.731 | 1.110 |
| 0.90 | 8.040 | 7.348 | 5.676 | 4.545 | 3.762 | 1.050 |
| 1.00 | 8.235 | 7.501 | 5.755 | 4.590 | 3.791 | 1.000 |

7.3 Results and Discussion

Due to the temperature jump boundary condition, the bulk gas temperature of slip flow is lower than the gas temperature of continuum flow. The temperature jump is equivalent to a thermal contact resistance between the wall and gas, while the slip velocity acts to decrease the thermal contact resistance. The velocity slip and temperature jump bring about opposite effects on the temperature difference between the gas and the wall; the velocity slip tends to decrease the temperature difference between the gas and the wall, while the temperature jump tends to increase the difference. It is clear that the effects of velocity slip would tend to increase the Nusselt number, while the temperature jump would act to decrease the Nusselt number.

Larrode et al. [131] studied slip flow heat transfer in circular tubes and Yu and Ameel [133, 134] investigated slip flow heat transfer in rectangular microchannels. They proposed that heat transfer could be increased or decreased compared to continuum flow conditions depending on β and Knudsen number. Where β is defined as

$$\beta = \frac{\frac{2 - \sigma_r}{\sigma_r} \frac{2\gamma}{\gamma + 1} \text{Pr}}{\frac{2 - \sigma}{\sigma}} \quad (7.45)$$

and includes all of the parameters associated with the gas and wall interaction.

Actually, only when β and Knudsen number are very small (such as $\beta < 0.3$ for parallel plates and $\beta < 0.8$ for circular tubes) does it appear possible for the effects of velocity slip to win out over the opposite effects of the temperature jump and thus make a Nusselt

number greater than the continuum flow value. Or, when the tangential momentum accommodation coefficient is significantly smaller than thermal accommodation coefficient, the Nusselt number will be greater than the continuum flow value. However, for practical engineering applications, it is extremely difficult to realize and heat transfer is always reduced when slip flow occurs.

For small β , the velocity slip dominates and heat transfer is enhanced. At large β , the temperature jump dominates and heat transfer is weakened. When the temperature jump at the wall is neglected ($\beta=0$), in other words, only the velocity slip at the wall is considered, the Nusselt number increases with an increase of Knudsen numbers. The same results were found by several researchers [51, 129-133]. Ignoring temperature jump will lead to significant overprediction of heat transfer.

7.4 Summary

Slip flow heat transfer in annular microchannels with constant heat flux under hydrodynamically and thermally fully developed condition is investigated. The analysis is carried out for both uniform wall heat flux on one wall, adiabatic on the other wall, and uniform wall heat flux on both walls. The results indicate that the slip flow Nusselt numbers are lower than those for continuum flow and decrease with an increase in Knudsen number for practical engineering applications. Only when β are very small is it possible for the effects of velocity slip to override the opposite effects of the temperature jump and thus make a Nusselt number greater than the continuum flow value. The effects

of Knudsen number, radii ratio and heat flux ratio on heat transfer characteristics are discussed respectively.

Chapter 8

Summary

8.1 Summary

Analytical models have been developed to provide a means of predicting flow characteristics, such as volumetric flow rate or average velocity, friction factor, and pressure distribution for fluids operating in microchannels. The developed models address: (i) fully developed slip flow in non-circular microchannels, (ii) hydrodynamically developing slip flow in non-circular microchannels, (iii) compressibility effects, (iv) surface roughness effects, and (v) slip flow heat transfer in annular microchannels. The studies help understand the behavior of fluids in microchannels. The simple models developed are general and robust, and may be used by the research community for the practical engineering design of microchannel flow systems.

An analytical solution of Poiseuille number was first obtained using separation of variables in elliptic cylinder coordinates. Fully developed slip flow in non-circular microchannels has been investigated and a model was proposed to predict the friction factor Reynolds product fRe for slip flow in most non-circular microchannels. The developed model took advantage of the selection of a more appropriate characteristic length scale square root of the cross-sectional flow area to develop a simple model. The

accuracy of the developed model was found to be within 10 percent, with most data for practical configurations within 5 percent.

Compressibility effects on slip flow in non-circular microchannels have been examined and simple models were proposed to predict the pressure distribution and mass flow rate for slip flow in most non-circular microchannels.

Hydrodynamically developing slip flow in non-circular microchannels has been investigated and a model was proposed to predict the friction factor Reynolds product fRe for slip flow in most non-circular microchannels. The developed model correctly approaches the slip flow asymptote for developing flows and fully developed flows. It is found that the linearization method to solve the Navier-Stokes equations is an accurate approximation for developing slip flows. The effects of the Knudsen number on the hydrodynamic entrance length for circular tubes and parallel plates have also been examined and simple models were developed to predict entrance length for circular tubes and parallel plates.

The developed simple models may be used to predict results for non-circular microducts for which no solutions or tabulated data exist such as rectangular, annular, elliptical, trapezoidal, double-trapezoidal, triangular, rhombic, hexagonal, octagonal, circular segment microchannels. The developed models are simple and founded on theory, and the accuracy of the developed models has been examined with some experimental measurements and numerical analysis.

The effects of corrugated surface roughness on fully developed laminar flow in microtubes were investigated. Novel analytical models were developed to predict friction

factor and pressure drop in corrugated roughness microtubes for continuum flow and slip flow. The developed model for slip flow illustrates the coupled effects between velocity slip and corrugated roughness. The Poiseuille number depends on the relative roughness of the walls of the microchannels also in laminar region and the relative roughness cannot be neglected for microchannels in the laminar region. The Poiseuille number increases not only as the relative roughness increases but also as the roughness spacing decreases.

Slip flow heat transfer in annular microchannels has been examined. The effects of Knudsen number, radii ratio and heat flux ratio on heat transfer characteristics were discussed. The results indicate that the slip flow Nusselt numbers are lower than those for continuum flow and decrease with an increase in Knudsen number for practical engineering applications.

8.2 Future Research

The developed models could be extended to the early transition regime by employing the second-order slip boundary conditions. The second-order models may improve predictions for high Knudsen numbers.

Further work may include numerical investigation on slip flow in short non-circular microchannels. Velocity slip is very large near the channel entrance due to the existence of large gradients.

Another area of future study involves slip flow heat transfer in non-circular ducts under constant wall temperature and heat flux conditions as similar numerical works are only confined to simple geometries. Heat transfer in microflows has important

engineering applications. In particular the entrance region should be investigated, where the major heat transfer occurs in short channels that are frequently encountered in various types of microfluidic devices found in MEMS.

Due to the lack of molecular-based theory of liquids, a nondimensional number similar to the Knudsen number is not commonly used. In liquid flows, slip is detectable only when the characteristic dimension is approximately 1 μm . Slip in liquids is on the order of 10 to 100 nm. Furthermore, there is no slip if the walls are rough. Other important influences on slip are the chemical characteristics of the wall and liquid, and residual gases effects. The physics of liquid slip is complicated and not well understood. If a nondimensional number similar to the Knudsen number is defined for liquid slip flow, the present developed models can be utilized.

Benchmark studies, which carefully examine pressure drop, friction factor, entrance and exit effects, and roughness effects for liquid flow over a wider Reynolds number range in microchannels are strongly needed. These studies will determine if the conventional theory applies or if there needs to be new fundamental flow theories formulated especially for liquid flow in microchannels.

References

- [1] G.E. Karniadakis, A. Beskok, N. Aluru, *Microflows and Nanoflows*, Springer, 2005.
- [2] M. Ged-el-Hak, *MEMS Handbook*, CRC Press, 2001.
- [3] N.T. Nguyen, S.T. Wereley, *Fundamentals and Applications of Microfluidics*, Artech House, 2003.
- [4] S.G. Kandlikar, S.V. Garimella, D. Li, S. Colin, M. King, *Heat Transfer and Fluid Flow in Minichannels and Microchannels*, Elsevier, 2006.
- [5] P. Tabeling, *Introduction to Microfluidics*, Oxford University Press, 2005.
- [6] D.B. Tuckerman and R.F.W. Pease, "High-performance heat sinking for VLSI," *Institute of Electrical and Electronics Engineering Electron Device Letters*, Electron Device Letters – 2, pp. 126-129, 1981.
- [7] P. Wu and W.A Little, "Measurement of Friction Factors for Flows of Gases in Very Fine Channels Used for Microminiature Joule-Thompson Refrigerators," *Cryogenics*, Vol. 23, pp. 273-277, 1983.
- [8] P. Wu and W.A. Little, "Measurement of the heat transfer characteristics of gas flow in fine channel heat exchangers used for microminiature refrigerators," *Cryogenics*, Vol. 24, pp. 415-420, 1984.
- [9] J. Pfahler, J. Harley, H. Bau, and J.N. Zemel, "Gas and Liquid Flow in Small Channels," *Micromechanical Sensors, Actuators, and Systems ASME*, Vol. 32, pp. 49-58, 1991.
- [10] J. Pfahler, J. Harley, H. Bau, and J.N. Zemel, "Gas and liquid transport in small channels," *Microstructures, Sensors and Actuators, ASME*, Vol. 19, pp. 149-157, 1990.
- [11] J. Pfahler, J. Harley, H. Bau, "Liquid transport in micron and submicron channels," *Sensors and Actuators*, Vol. A21-23, pp. 431-434, 1990.
- [12] J.C. Harley, Y. Huang, H. Bau, and J.N. Zemel, "Gas Flows in Micro-Channels," *Journal of Fluid Mechanics*, Vol. 284, pp. 257-274, 1995.

- [13] J. Harley, J. Pfahler, H. Bau, and J.N. Zemel, "Transport processes in micron and submicron channels," *ASME Heat Transport Processes*, Vol. HTD-116, pp. 1-5, 1989.
- [14] J. Harley, H. Bau, J.N. Zemel, and V. Dominko, "Fluid flow in micron and submicron size channels," in *Proceedings Workshop on Micro Electro Mechanical Systems*, Salt Lake City, UT, February 20-22, 1989, pp. 25-28.
- [15] S.B. Choi, R.F. Barron, and R.O. Warrington, "Fluid Flow and Heat Transfer in Microtubes," *Micromechanical Sensors, Actuators, and Systems ASME*, Vol. 32, pp.123-134, 1991.
- [16] D. Yu, R. Warrington, R. Barron, and T. Ameel, "Experimental and Theoretical Investigation of Fluid Flow and Heat Transfer in Microtubes," *Proceedings of the 1995 ASME/JSME Thermal Engineering Joint Conference*, Maui, Hawaii, Vol. 1, pp. 523-530, 1995.
- [17] X.F. Peng, G.P. Peterson, and B.X. Wang, "Heat Transfer Characteristics of Water Through Microchannels, *Experimental Heat Transfer*, Vol. 7, pp. 265-283, 1994.
- [18] X.F. Peng, G.P. Peterson, "Convective Heat Transfer and Flow Friction for Water Flow in Microchannel Structures," *International Journal of Heat and Mass Transfer*, Vol. 39, pp. 2599-2608, 1996.
- [19] X.F. Peng, G.P. Peterson, and B.X. Wang, "Frictional Flow Characteristics of Water Flowing Through Rectangular Microchannels," *Experimental Heat Transfer*, Vol. 7, pp. 249-264, 1994.
- [20] H.B. Ma and G.P. Peterson, "Laminar Friction Factor in Microscale Ducts of Irregular Cross Section," *Microscale Thermophysical Engineering*, Vol. 1, pp. 253-265, 1997.
- [21] B.X. Wang, X.F. Peng, "Experimental investigation on liquid forced convection heat transfer through microchannels," *International Journal of Heat and Mass Transfer Suppl.* 37(1), pp. 73-82, 1994.
- [22] X.F. Peng, G.P. Peterson, "The effect of thermofluid and geometrical parameters on convection of liquids through rectangular microchannels," *International Journal of Heat and Mass Transfer*, Vol. 38, pp. 755-758, 1995.
- [23] P. Wilding, M.A. Shoffner, and L.J. Kircka, "Manipulation and flow of biological fluids in straight channels micromachined in silicon," *Clin. Chem.*, Vol. 40, pp. 43-47, 1994.

- [24] X.N. Jiang, Z.Y. Zhou, J. Yao, Y. Li and X.Y. Ye, "Micro-fluid flow in microchannel," in *Proc. Transducers '95*, Stockholm, Sweden, June 25-29, 1995, pp. 317-320.
- [25] X.N. Jiang, Z.Y. Zhou, X.Y. Huang, and C.Y. Liu, "Laminar Flow Through Microchannels Used for Microscale Cooling Systems," *IEEE/CPMT Electronic Packaging Technology Conference*, pp. 119-122, 1997.
- [26] E.R. Arkilic, K.S. Breuer, and M.A. Schmidt, "Gaseous flow in microchannels," *ASME Application of Microfabrication Fluid Mechanics*, Vol. FED-197, pp. 57-66, 1994.
- [27] E.R. Arkilic, K.S. Breuer, and M.A. Schmidt, "Gaseous slip flow in long microchannels," *Journal of Microelectromechanical Systems*, Vol. 6, pp. 167-178, 1997.
- [28] S.A. Schaaf, and P.L. Chambre, *Flow of Rarefied Gases*, Princeton Univ. Press, 1958.
- [29] K. Pong, C. Ho, J. Liu, and Y. Tai, "Nonlinear pressure distribution in uniform microchannels," *ASME Application of Microfabrication to Fluid Mechanics*, Vol. FED-197, pp. 51-56, 1994.
- [30] J. Liu, Y.-C. Tai, and C.-M. Ho, "MEMS for pressure distribution studies of gaseous flows in microchannels," in *Proceedings of IEEE International Conference on Micro Electro Mechanical Systems*, Amsterdam, The Netherlands, Jan. 29-Feb. 2, 1995, pp. 209-215.
- [31] J.C. Shih, C. Ho, J. Liu, and Y. Tai, "Monatomic and Polyatomic Gas Flow Through Uniform Microchannels," *ASME Microelectromechanical Systems (MEMS)*, Vol. DSC-59, pp. 197-203, 1996.
- [32] C. Ho and Y. Tai, "Micro-Electro-Mechanical Systems (MEMS) and Fluid Flows," *Annual Review Fluid Mechanics*, Vol. 30, pp. 579-612, 1998.
- [33] S. Wu, J. Mai, Y. Zohar, Y.C. Tai, and C.M. Ho, "A suspended microchannel with integrated temperature sensors for high pressure flow studies," in *Proc. IEEE Workshop on Micro Electro Mechanical Systems*, Heidelberg, Germany, Jan. 25-29, 1998, pp. 87-92.
- [34] W. Urbanek, J.N. Zemel, and H. Bau, "An Investigation of the Temperature Dependence of Poiseuille Numbers in Microchannel Flow," *Journal of Micromechanics and Microengineering*, Vol. 3, pp. 206-209, 1993.
- [35] I. Papautsky, J. Brazzle, T.A. Ameel, and A.B. Frazier, "Laminar Fluid Behavior in Microchannels Using Micropolar Fluid Theory," *Sensors and Actuators, Physical*

Proceedings of the 1998 11th IEEE International Workshop on Micro Electro Mechanical Systems, MEMS, Heidelberg, Germany, Vol. 73, pp. 101-108, 1998.

- [36] I. Papautsky, J. Brazzle, T.A. Ameel, and A.B. Frazier, "Microchannel Fluid Behavior Using Micropolar Fluid Behavior," *Proceedings of the 1998 IEEE 11th Annual International Workshop on Micro Electro Mechanical Systems*, Heidelberg, Germany, pp. 544-549, 1998.
- [37] I. Papautsky, B.K. Gale, S. Mohantry, T.A. Ameel, and A.B. Frazier, "Effects of Rectangular Microchannel Aspect Ratio on Laminar Friction Constant," *Proceedings of SPIE – The International Society for Optical Engineering, Proceedings of the 1999 Microfluidic Devices and Systems II*, Santa Clara, CA, Vol. 3877, pp. 147-158, 1999.
- [38] S.F. Choquette, M. Faghri, E.J. Kenyon, and B. Sunden, "Compressible Fluid Flow in Micro Sized Channels," *National Heat Transfer Conference*, Vol. 5, pp. 25-32, 1996.
- [39] T.M. Harms, M. Kazmierczak, F.M. Gerner, A. Holke, H.T. Henderson, J. Pilchowski, and K. Baker, "Experimental Investigation of Heat Transfer and Pressure Drop Through Deep Microchannels in a (110) Silicon Substrate," *Proceedings of the ASME Heat Transfer Division*, Vol. 1, pp. 347-357, 1997.
- [40] R.L. Webb and M. Zhang, "Heat Transfer and Friction in Small Diameter Channels," *Microscale Thermophysical Engineering*, Vol. 2, pp. 189-202, 1998.
- [41] D. Pfund, D. Rector, A. Shekariz, A. Popescu, and J. Welty, "Pressure Drop Measurements in a Microchannel," *Proceedings of the 1998 ASME International Mechanical Engineering Congress and Exposition: DSC Micro-Electro-Mechanical Systems*, Vol. 66, pp. 193-198, 1998.
- [42] D. Pfund, A. Shekariz, A. Popescu, and J.R. Welty, "Pressure Drop Measurements in a Microchannel," *AICHE J.*, Vol. 46, pp. 1496-1507, 2000.
- [43] G.M. Mala, D. Li, and J.D. Dale, "Heat Transfer and Fluid Flow in Microchannels," *International Journal of Heat and Mass Transfer*, Vol. 40, pp. 3079-3088, 1997.
- [44] G.M. Mala, C. Yang, D. Li, "Electrical Double Layer Potential in a Rectangular Microchannel," *Colloids and Surfaces*, Vol. 135, pp. 109-116, 1998.
- [45] G.M. Mala, D. Li, C. Werner, H.J. Jacobasch, and Y.B. Ning, "Flow Characteristics of Water Through a Microchannel Between Two Parallel Plates with Electrokinetic Effects," *International Journal of Heat and Fluid Flow*, Vol. 18, pp. 489-496, 1997.

- [46] W. Qu, G.M. Mala, and D. Li, "Pressure-driven Flows in Trapezoidal Silicon Microchannels," *International Journal of Heat and Mass Transfer*, Vol. 43, pp. 353-364, 2000.
- [47] G.M. Mala, D. Li, "Flow characteristics of water in microtubes," *International Journal of Heat and Fluid Flow*, Vol. 20, pp. 142-148, 1999.
- [48] L. Kulinsky, Y. Wang, and M. Ferrari, "Electroviscous Effects in Microchannels," *SPIE Conference on Micro and Nanofabricated Structures and Devices for Biomedical Environment Applications II*, San Jose, CA, Vol. 3606, pp. 158-168, 1999.
- [49] N.P. Migun and P.P. Prokhorenko, "Measurement of the Viscosity of Polar Liquids in Microcapillaries," *Colloid Journal of the USSR*, Vol. 49, pp. 894-897, 1987.
- [50] A. Beskok, G.E. Karniadakis, and W. Trimmer, "Rarefaction and Compressibility Effects in Gas Microflows," *Journal of Fluids Engineering*, Vol. 118, pp. 448-455, 1996.
- [51] T.A. Ameel, X. Wang, R.F. Barron, and R.O. Warrington, "Laminar Forced Convection in a Circular Tube With Constant Heat Flux and Slip Flow," *Microscale Thermophysical Engineering*, Vol. 1, pp. 303-320, 1997.
- [52] Z.Y. Guo and X.B. Wu, "Compressibility Effects on the Gas Flow and Heat Transfer in a Microtube," *International Journal of Heat and Mass Transfer*, Vol. 40, pp. 3251-3254, 1997.
- [53] S.M. Flockhart and R.S. Dhariwal, "Experimental and numerical investigation into the flow characteristics of channels etched in <100> silicon," *Journal of Fluids Engineering*, Vol. 120, pp. 291-295, 1998.
- [54] B. Xu, K.T. Ooi, N.T. Wong, C.Y. Liu, W.K. Choi, "Liquid flow in microchannels," *Proceedings of the 5th ASME/JSME Joint Thermal Engrg. Conference*, San Diego, CA, 1999, pp. 150-158.
- [55] B. Xu, K.T. Ooi, N.T. Wong, W.K. Choi, "Experimental investigation of flow friction for liquid flow in microchannels," *Internat. Comm. Heat Mass Transfer*, Vol. 27, pp. 1165-1176, 2000.
- [56] K.V. Sharp, R.J. Adrian, D.J. Beebe, "Anomalous transition to turbulent in microtubes," *Proceedings of Int. Mech. Eng. Cong. Expo., 5th Micro-Fluidic Symp.*, Orlando, FL, 2000, pp. 150-158.
- [57] L.S. Ding, H. Sun, X.L. Sheng, B.D. Lee, "Measurement of friction factor for R134a and R12 through microchannels," *Proceedings of Symposium on Energy Engrg. In the 21st Century*, Vol. 2, 2000, pp. 650-657.

- [58] T. Araki, M.S. Kim, I. Hiroshi, K. Suzuki, "An experimental investigation of gaseous flow characteristics in microchannels," *G.P. Celata et al.(Eds.), Proceedings of International Conference on Heat Transfer and Transport Phenomena in Microscale*, Begell House, New York, USA, 2000, pp. 155-161.
- [59] M.S. Kim, T. Araki, K. Inaoka, K. Suzuki, "Gas flow characteristics in microtubes," *JSME International Journal, Series B*, Vol. 43, No. 4, pp. 634-639, 2000.
- [60] G.P. Celata, M. Cumo, M. Guglielmi, G. Zummo, "Experimental investigation of hydraulic and single phase heat transfer in 0.130 mm capillary tube," *G.P. Celata et al.(Eds.), Proceedings of International Conference on Heat Transfer and Transport Phenomena in Microscale*, Begell House, New York, USA, 2000, pp. 108-113.
- [61] J. Judy, D. Maynes, B.W. Webb, "Liquid flow pressure drop in microtubes," *G.P. Celata et al.(Eds.), Proceedings of International Conference on Heat Transfer and Transport Phenomena in Microscale*, Begell House, New York, USA, 2000, pp. 149-154.
- [62] J. Judy, D. Maynes, B.W. Webb, "Characteristics of frictional pressure drop for liquid flows through microchannels," *International Journal of Heat and Mass Transfer*, Vol. 45, pp. 3477-3489, 2002.
- [63] Z.X. Li, D.X. Du, Z.Y. Guo, "Characteristics of frictional resistance for gas flow in microtubes," *Proceedings of Symposium on Energy Engrg. In the 21st Century*, Vol. 2, 2000, pp. 658-664.
- [64] Z.X. Li, D.X. Du, Z.Y. Guo, "Experimental study on flow characteristics of liquid in circular microtubes," *G.P. Celata et al.(Eds.), Proceedings of International Conference on Heat Transfer and Transport Phenomena in Microscale*, Begell House, New York, USA, 2000, pp. 162-168.
- [65] C.Y. Yang, H.T. Chien, S.R. Lu, R.J. Shyu, "Friction characteristics of water, R134a and air in small tubes," *G.P. Celata et al.(Eds.), Proceedings of International Conference on Heat Transfer and Transport Phenomena in Microscale*, Begell House, New York, USA, 2000, pp. 168-174.
- [66] S.E. Turner, H. Sun, M. Faghri, O.J. Gregory, "Compressible gas flow through smooth and rough microchannels," *Proceedings of IMECE 2001*, New York, USA, 2001, HTD-24145.
- [67] S.G. Kandlikar, S. Joshi, S. Tian, "Effect of channel roughness on heat transfer and fluid flow characteristics at low Reynolds numbers in small diameter tubes," *Proc. of 35th National Heat Transfer Conference*, Anaheim CA, USA, 2001, paper 12134.

- [68] P. Gao, S. LePerson, M. Favre-Marinet, "Scale effects on hydrodynamics and heat transfer in two-dimensional mini and microchannels," *International Journal of Thermal Sciences*, Vol. 41, pp. 1017-1027, 2002.
- [69] G.R. Warrier, V.K. Dhir, L.A. Momoda, "Heat transfer and pressure drop in narrow rectangular channels," *Exp. Thermal Fluid Sci.*, Vol. 26, pp. 53-64, 2002.
- [70] H.E. Hegab, A. Bari, T. Ameel, "Friction and convection studies of R134a in microchannels within the transition and turbulent flow regimes," *Exp. Heat Transfer*, Vol. 15, pp. 245-259, 2002.
- [71] P. Chung, M. Kawaji, A. Kawahara, "Characteristics of single-phase flow in microchannels," *Proceedings of ASME 2002 Fluids Engineering Division Summer Meeting*, Montreal, Canada, July 14-18, 2002.
- [72] A. Bucci, G.P. Celata, M. Cumo, E. Serra, G. Zummo, "Fluid flow and single-phase flow heat transfer of water in capillary tubes," *Proceedings of the Int. Conference on Minichannels and Microchannels*, Rochester, USA, 2003, paper ICMM-1037.
- [73] H.Y. Wu, P. Cheng, "Friction factors in smooth trapezoidal silicon microchannels with different aspect ratios," *International Journal of Heat and Mass Transfer*, Vol. 46, pp. 2529-2525, 2003.
- [74] J. Maurer, P. Tabeling, P. Joseph, H. Willaime, "Second-order slip laws in microchannels for helium and nitrogen," *Physics of Fluids*, Vol. 15, pp. 2613-2621, 2003.
- [75] J.T. Teng, J.C. Chu, J.J. Chen, C.C. Wang, C.H. Lin, and R. Greif, "A study on the behavior of the pressure drop for the fluid flow in a triangular microchannel," *Proceedings of 7th Biennial Conference on Engineering Systems Design and Analysis*, Manchester, UK, July 19-22, 2004.
- [76] X. Tu and P. Hrnjak, "Experimental investigation of single-phase flow pressure drop through rectangular microchannels," *Proceedings of the Int. Conference on Minichannels and Microchannels*, Rochester, USA, 2003, paper ICMM-1028.
- [77] J.Y. Jung and H.Y. Kwak, "Fluid flow and heat transfer in microchannels with rectangular cross section," *Proceedings of the Int. Conference on Minichannels and Microchannels*, Rochester, USA, 2003, paper ICMM-1032.
- [78] A. Bari, J.M. Koo, L.N. Jiang, J. Paidipati, and K. Goodson, "Frictional characteristics of microchannel gas flow," *Proceedings of the Int. Conference on Minichannels and Microchannels*, Rochester, USA, 2003, paper ICMM-1034.

- [79] D. Brutin and L. Tadrist, "Experimental friction factor of a liquid flow in microtubes," *Physics of Fluids*, Vol. 15, pp. 653-661, 2003.
- [80] R. Baviere, F. Ayela, S. Le Person and M. Favre-Marinet, "An experimental study of water flow in smooth and rough rectangular micro-channels," *Proceedings of the Second Int. Conference on Minichannels and Microchannels*, Rochester, USA, 2004, paper ICMM2004-2338.
- [81] S.S. Hsieh, C.Y. Lin, C.F. Huang and H.H. Tsai, "Liquid flow in a micro-channel," *Journal of Micromechanics and Microengineering*, Vol. 14, pp. 436-445, 2004.
- [82] D. Liu and S. Garimella, "Investigation of liquid flow in microchannels," *Journal of Thermophysics and Heat Transfer*, Vol. 18, pp. 65-72, 2004.
- [83] M.J. Kohl, S.I. Abdel-Khalik, S.M. Jeter, and D.I. Sadowski, "An experimental investigation of microchannel flow with internal pressure measurements," *International Journal of Heat and Mass Transfer*, Vol. 48, pp. 1518-1533, 2005.
- [84] C. Aubert, S. Colin, "High-order boundary conditions for gaseous flows in rectangular microducts," *Microscale Thermophysical Engineering*, Vol. 5, pp. 41-54, 2001.
- [85] R.G. Deisler, "An analysis of second-order slip flow and temperature-jump boundary conditions for rarefied gases," *International Journal of Heat and Mass Transfer*, Vol. 7, pp. 681-694, 1964.
- [86] S. Colin, P. Lalonde, R. Caen, "Validation of a second-order slip flow model in rectangular microchannels," *Heat Transfer Engineering*, Vol. 25, pp. 23-30, 2004.
- [87] R.W. Barber, D.R. Emerson, "Challenges in modeling gas-phase flow in microchannels: from slip to transition," *Heat Transfer Engineering*, Vol. 27, pp. 3-12, 2006.
- [88] E. Kennard, *Kinetic Theory of Gases*, New York, NY: McGraw-Hill, 1938.
- [89] A. Beskok, G.E. Karniadakis, "Simulation of slip-flows in complex micro-geometries," in *Proc. ASME*, Vol. DSC-40, pp. 355-370, 1992.
- [90] F.M. White, *Viscous Fluid Flow*, 2nd ed. New York, NY: McGraw-Hill, 1991.
- [91] R.L. Panton, *Incompressible Flow*, 3rd ed. New York, NY: John Wiley and Sons, 2005.
- [92] H. Schlichting, *Boundary Layer Theory*, 7th ed. New York, NY: McGraw-Hill, 1979.

- [93] F.W. Schmidt and B. Zeldin, "Laminar flows in inlet sections of tubes and ducts," *American Institute of Chemical Engineers Journal*, Vol. 15, pp. 612-614, 1969.
- [94] Y.S. Muzychka, and M.M. Yovanovich, 2002. "Laminar Flow Friction and Heat Transfer in Non-Circular Ducts and Channels: Part I-Hydrodynamic Problem," *Compact Heat Exchangers*, A Festschrift on the 60th Birthday of Ramesh K. Shah, Grenoble, France, August 24, pp. 123-130.
- [95] M.M. Yovanovich, and Y.S. Muzychka, 1997. "Solution of Poisson Equation within Singly and Doubly Connected Domains," *AIAA Paper 97-3880, presented at the National Heat Transfer Conference*, Baltimore MD.
- [96] A. Bejan, *Convection Heat Transfer*, 3rd ed., Wiley, 2004.
- [97] S.W. Churchill, and R. Usagi, "A general expression for the correlation of rates of transfer and other phenomena," *American Institute of Chemical Engineers*, Vol. 18, pp. 1121-1128, 1972.
- [98] Y.S. Muzychka, Analytical and Experimental Study of Fluid Friction and Heat Transfer in Low Reynolds Number Flow Heat Exchangers, Ph.D. Thesis, University of Waterloo, 1999.
- [99] W.A. Ebert, E.M. Sparrow, "Slip flow in rectangular and annular ducts," *Journal of Basic Engineering*, Vol. 87, pp. 1018-1024, 1965.
- [100] P. Moon, D. Spencer, *Field Theory for Engineers*, Van Nostrand, Princeton Univ. Press., 1961.
- [101] P. Moon, D. Spencer, *Field Theory Handbook*, 2nd edition, Springer-Verlag., 1971.
- [102] W.M. Rohsenow, H.Y. Choi, *Heat, Mass, and Momentum Transfer*, Prentice-Hall Inc., 1961.
- [103] M. Abramowitz, I.A. Stegun, *Handbook of Mathematical Functions*, Courier Dover Publications, 1965.
- [104] N.M. Lebedev, I.P. Skalskaya, Y.S. Uflyand, *Worked Problems in Applied Mathematics*, Courier Dover Publications, 1965.
- [105] Maple 9, Waterloo Maple Software, Waterloo, Canada, 2003.
- [106] R.K. Shah, A.L. London, *Laminar Flow Forced Convection in Ducts*, Academic Press., 1978.

- [107] Z.P. Duan, Y.S. Muzychka, "Slip flow in elliptic microchannels," *International Journal of Thermal Sciences*, Vol. 46, No. 11, pp. 1104-1111, 2007.
- [108] G.L. Morini, M. Lorenzini, M. Spiga, "A criterion for experimental validation of slip-flow models for incompressible rarefied gases through microchannels," *Microfluidics Nanofluidics*, Vol. 1, pp. 190-196, 2005.
- [109] Z.P. Duan, Y.S. Muzychka, "Slip flow in non-circular microchannels," *Microfluidics and Nanofluidics*, Vol. 3, No. 4, pp. 473-484, 2007.
- [110] A. Sceekanth, "Slip Flow through Long Circular Tubes," *Proceedings of the Sixth International Symposium on Rarefied Gas Dynamics*, eds. L. Trilling and H.Y. Wachman, Academic Press, pp. 667-680, 1969.
- [111] J. Jang and S. T. Wereley, "Pressure Distributions of Gaseous Slip Flow in Straight and Uniform Rectangular Microchannels," *Microfluidics and Nanofluidics*, Vol. 1, pp. 41-51, 2004.
- [112] E.M. Sparrow, T.S. Lundgren, S.H. Lin, 1962. "Slip flow in the entrance region of a parallel plate channel," In: *Proceedings of the Heat Transfer and Fluid Mechanics Institute*, Stanford University Press, pp. 223-238.
- [113] B. Atkinson, M.P. Brocklebank, C.C.H. Card, J.M. Smith, "Low Reynolds number developing flows," *AIChE Journal*, Vol. 15, pp. 548-553, 1969.
- [114] R.Y. Chen, "Flow in the entrance region at low Reynolds numbers," *Journal of Fluids Engineering*, Vol. 95, pp. 153-158, 1973.
- [115] M. Friedmann, J. Gillis, N. Liron, "Laminar flow in a pipe at low and moderate Reynolds numbers," *Applied Scientific Research*, Vol. 19, pp. 426-438, 1968.
- [116] R.W. Barber, D.R. Emerson, 2001. "A numerical investigation of low Reynolds number gaseous slip flow at the entrance of circular and parallel plate microchannels," In: *ECCOMAS Computational Fluid Dynamics Conference*, Swansea, Wales, UK.
- [117] M. Renksizbulut, H. Niazmand, G. Tercan, "Slip-flow and heat transfer in rectangular microchannels with constant wall temperature," *International Journal of Thermal Sciences*, Vol. 45, pp. 870-881, 2006.
- [118] H. Niazmand, G. Tercan, M. Renksizbulut, 2005. Entrance region flows in rectangular microchannels with constant wall temperature. In: *Proceedings of the 3rd Int. Conference on Minichannels and Microchannels*, Toronto, Canada, paper ICMM2005-75064.

- [119] M. Bahrami, M.M. Yovanovich, and J.R. Culham, "Pressure Drop of Fully Developed, Laminar Flow in Rough Microtubes," *Journal of Fluids Engineering*, Vol. 128, pp. 632-637, 2006.
- [120] C. Kleinstreuer, and J. Koo, "Computational Analysis of Wall Roughness Effects for Liquid Flow in Micro-Conduits," *Journal of Fluid Engineering*, Vol. 126, pp. 1-9, 2004.
- [121] X.Q. Wang, C. Yap, and A.S. Mujumdar, "Effects of Two-Dimensional Roughness in Flow in Microchannel," *Journal of Electronic Packaging*, Vol. 127, pp. 357-361, 2005.
- [122] W.L. Li, J.W. Lin, S.C. Lee, and M.D. Chen, "Effects of roughness on rarefied gas flow in long microtubes," *Journal of Micromechanics and Microengineering*, Vol. 12, pp. 149-156, 2002.
- [123] H. Sun, and M. Faghri, "Effects of surface roughness on nitrogen flow in a microchannel using the direct simulation Monte Carlo method," *Numerical Heat Transfer, Part A*, Vol. 43, pp. 1-8, 2003.
- [124] W.E. Langlois, 1958, "Creeping Viscous Flow through a Two-Dimensional Channel of Varying Gap," *Proceedings of 3rd National Congress of Applied Mechanics*, pp. 777-783.
- [125] R.I. Tanner, and I.W. Linnett, 1965, *2nd Australian Conference on Hydraulics and Fluid Mech. A*, pp. 159-166.
- [126] M.J. Manton, "Low Reynolds Number Flow in Slowly Varying Axisymmetric Tubes," *Journal of Fluid Mechanics*, Vol. 49, pp. 451-459, 1971.
- [127] N. Phan-Thien, "On the Stokes Flow of Viscous Fluids through Corrugated Pipes," *Journal of Applied Mechanics*, Vol. 47, pp. 961-963, 1980.
- [128] M. Vasudeviah, and K. Balamurugan, "Stokes Slip Flow in a Corrugated Pipe," *International Journal of Engineering Science*, Vol. 37, pp. 1629-1641, 1999.
- [129] E.M. Sparrow, and S.H. Lin, "Laminar Heat Transfer in Tubes under Slip Flow Conditions," *Journal of Heat Transfer*, Vol. 84, pp. 363-369, 1962.
- [130] R.F. Barron, X.M. Wang, T.A. Ameel, and R.O. Warrington, "The Graetz Problem Extended to Slip Flow," *International Journal of Heat and Mass Transfer*, Vol. 40, pp. 1817-1823, 1997.
- [131] F.E. Larrode, C. Housiadas, and Y. Drossinos, "Slip Flow Heat Transfer in Circular Tubes," *International Journal of Heat and Mass Transfer*, Vol. 43, pp. 2669-2680, 2000.

- [132] O. Simek, and N.G. Hadjiconstantinou, 2001, "Slip Flow Constant-Wall-Temperature Nusselt Number in Circular Tubes in the Presence of Axial Heat Conduction," *Proceedings of ASME International Mechanical Engineering Congress and Exposition*, New York, IMECE2001/HTD-24106.
- [133] S.P. Yu, and T.A. Ameel, "Slip Flow Heat Transfer in Rectangular Microchannels," *International Journal of Heat and Mass Transfer*, Vol. 44, pp. 4225-4234, 2001.
- [134] S.P. Yu, and T.A. Ameel, "Slip Flow Convection in Isoflux Rectangular Microchannels," *Journal of Heat Transfer*, Vol. 124, pp.346-355, 2002.
- [135] G. Tunc, and Y. Bayazitoglu, "Heat Transfer in Rectangular Microchannels," *International Journal of Heat and Mass Transfer*, Vol. 45, pp. 765-773, 2002.
- [136] R.M. Inman, "Laminar slip flow heat transfer in a parallel plate channel or a round tube with uniform wall heating," Technical report, NASA, Report D-2393, 1964.





